5-20-2005

Development of Mass Spectrometric Methods for the Analysis of Components and Complex Interactions in Biological Systems

Bryan Melvin Ham
University of New Orleans

Recommended Citation

Ham, Bryan Melvin, "Development of Mass Spectrometric Methods for the Analysis of Components and Complex Interactions in Biological Systems" (2005). *University of New Orleans Theses and Dissertations*. 263.
https://scholarworks.uno.edu/td/263

DEVELOPMENT OF MASS SPECTROMETRIC METHODS FOR THE ANALYSIS OF COMPONENTS AND COMPLEX INTERACTIONS IN BIOLOGICAL SYSTEMS

A Dissertation

Submitted to the Graduate Faculty of the
University of New Orleans
in partial fulfillment of the
requirements for the degree of

Doctor of Philosophy
in
The Department of Chemistry

by

Bryan Melvin Ham

B.A., University of New Orleans, 1989

May, 2005

ACKNOWLEDGEMENTS

This dissertation is dedicated to my wonderful and lovely wife whose love and support helped me through uncountable times of trials and testing to get to this final point. I also want to dedicate this dissertation to my parents who have always been there for me through the many years of my work and studies.

I would like to thank my advisor, Professor Richard Cole for his help, support, advice, and his sense of student freedom to pursue directions and interest without which I could not have achieved what I have.

I want to thank Professor Matthew Tarr, Professor Ronald Evilia, and Professor Zeev Rosenzweig for being on my graduate committee and giving me helpful advice and very insightful discussions concerning my projects. I also want to thank Professor Kevin Boyd for our productive discussions concerning my work, Professor Guijun Wang for advice, Professor Edwin Stevens for consultation and guidance, and finally Harry Reese for his time and expertise in instrumental troubleshooting and repair.

I want to thank Professor Jean Jacob from the Louisiana State University Health Sciences Center Department of Ophthalmology for being on my committee, for samples pertaining to my research projects, and for extensive advice, guidance, and contributions to the interpretation of the studies that I completed.

I would like to thank my friends Lingu Du for very helpful discussions concerning my work, and Dr. Yuguang Ma for helpful discussions and friendship.

Finally, I would like to thank the group members I have worked with in my group, and others, which has made this an enjoyable learning experience and journey.

Financial support was provided by The Louisiana Board of Regents through grant no. LEQSF (2001-04)-RD-B-11, and from the National Eye Institute through NEI/R03 EY14021.

TABLE OF CONTENTS

LIST OF TABLES

LIST OF FIGURES

ABSTRACT

The anti-cancer agent 4,4-dihydroxybenzophenone-2,4-dinitrophenylhydrazone (A007) forms complexes with π-delocalized lymphangitic dyes that allow its penetration through the skin effectively delivering it to a meta-stable type cancerous site. Previous *in vitro* studies, combined with gas phase mass spectrometry studies, have shown that a stronger binding affinity equates to a greater efficacy of the drug. For the determination of drug:dye complex binding strength coefficients in solution, two methods have been developed by affinity capillary electrophoresis (ACE), and cation exchange liquid chromatography (CELC). The methods demonstrated that A007 non-covalent binding strength was greatest for methylene green, followed by methylene blue, and lastly toluidine blue.

Bond dissociation energies and apparent reaction enthalpies for the fragmentation pathways of lithiated acylglycerols were experimentally determined by collision activation in a triple quadrupole mass spectrometer. A developed novel derived effective path length approach for predicting bond dissociation energies (BDE) for electrostatic complex's alkali metal adducts (Li^+), and halide adducts (Cl^-) of acylglycerols was applied to the major fragmentation product ions of a lithiated mono-acylglycerol, a 1,2-diacylglycerol, and a 1,3-diacylglycerol, to predict the covalent bond dissociation energies involved in fragmentation pathways. The model's calculated apparent reaction enthalpies are used in conjunction with the energy-resolved mass spectrometry method of breakdown graphs to give a more complete quantitative aspect to the interpretation of the fragmentation processes.

The dry eye condition affects millions of individuals world wide. The symptoms can be a result of simple irritation to the eye or a serious disease state. A dry eye model was developed using rabbits in order to study the compositional makeup of the tear components in hopes of identifying an underlying cause, or expressed effect of the dry eye condition. The major non-polar lipids of the tear were identified by mass spectrometry as mono and diacylglycerols, with a smaller extent of triacylglycerols. The major polar phosphorylated lipids were identified in the tear extract revealing that sphingomyelin based species were being expressed in the dry eye condition. The major proteins were determined to be the lower molecular weight lipid binding proteins where two specific species were found to increase in expression for the dry eye condition.

CHAPTER I: INTRODUCTION

1.1 Objectives and Aims

Previous work in measuring and identifying biological compounds from complicated extracts has had difficulty in the ability to achieve detection, identification and quantitation of the low nano to picogram levels that are found in tears. Also, specialized mass spectrometers that are not readily available to most laboratories are typically used for complex biological compound interactions. Therefore, the main objective of my work was to develop new and improved mass spectrometric methods for the measurement of biological compounds and their complex interactions using common mass spectrometer instrumentation. The specific aims of my work were to develop advanced mass spectrometric methodology for: a) the measurement of complex biological interactions in the solution-phase, b) the measurement of complex biological interactions in the gas-phase c) the identity and comparison of nonpolar and polar lipids in a rabbit dry eye tear model, and d) the identity and comparison of the major proteins in a rabbit dry eye tear model.

1.2 Significance and Impact

The use of mass spectrometry has become a powerful analytical tool for gas phase thermochemistry studies, for structural elucidation of organic compounds, and for composition studies of complex biological samples. The high sensitivity of mass spectrometers has also allowed the measurement of biological extracts that contain very low levels of the analytes of interest such as tear film extracts. Previous investigations into molecular changes in tear film structure have been hampered by the need to pool tears to make up a sample large enough to undergo analytical methods such as one- or two-dimensional electrophoresis. Another problem is the requirement that the tear components be derivatized before they are subjected to gas chromatography, mass spectrometry, or both. Finally, the total chloroform extract of the tear layer constitutes a complex mixture of biological compounds that includes non-polar and polar lipids and some lipoproteins. The polar lipid components make up a very small fraction of the total extract, rendering their analysis difficult by mass spectrometry alone. Therefore, there is a need to develop new methodology that combines optimized sample pretreatment in conjunction with mass spectral instrumental analysis. In response to this, we have developed methodologies for enhanced lipid and protein analysis that includes sample pretreatment such as clean-up chromatography, cationizing agents, washing solutions, wax plating MALDI Voyager plates, and enhanced MALDI matrices. The methodologies that have been developed have generated significant improvements such as increased sensitivities, enhanced signal responses, and lower detection limits.

The study of noncovalent bond dissociation energies by mass spectrometry has been investigated for well over 25 years, generating very accurate and reliable values. However, the type of mass spectrometer used is highly specialized and not readily accessible to most research laboratories, and is primarily limited to small molecular weight systems such as solvent/metal adducts. In response to this, we have developed a mass spectrometric method for the measurement of bond dissociation energies for both small molecular weight systems such as solvent/metal adducts, and larger molecular weight systems such as lipid/metal adducts. We have also extended the method to calculate "covalent" bond dissociation energies as well as noncovalent using a mass spectrometer that is fairly common in many research laboratories. This methodology in effect enables a broader scope to the measurement of dissociation energies by mass spectrometry that is more accessible to researchers.

The analysis of the components of tears has been reported upon for more than 40 years primarily using methods that required compositing samples, special pretreatment of samples, and were not as sensitive as that needed for very low levels of analytes. With the advancements in mass spectrometric instrumentation, ionization sources, and preparation techniques, there has been a tremendous growth in applications towards the analysis of complex biological samples. However, there are still many obstacles that are encountered when analyzing these complex biological samples. For the tear composition studies, these included very low levels of lipids in the nano to picogram levels that were suffering from suppression from other analytes present, and proteins that have been challenging to compare a normal to a diseased state expression. The developed methodology presented here shows for the first time the observance of single lipid species in the tear thus allowing the observance of an expression differential. The developed methodology has also allowed an expression study differential to be observed with the tear proteins. These studies may be able to identify causes to, or signaling agents of the dry eye diseased state.

In order to fully understand the results presented in Chapters III through VIII, it is necessary to be familiar with some of the basic concepts of the applied methodologies used in each study. Therefore, the following sections provide a brief introduction and overview of the instrumental methods used in the research studies reported upon in this dissertation.

1.3 Overview of High Performance Liquid Chromatography (HPLC) and Capillary Zone Electrophoresis (CZE)

High performance liquid chromatography (HPLC), and capillary zone electrophoresis (CZE) are two analytical separation techniques that have been used as individual approaches for compound separations, and as complimentary approaches. HPLC is a separation technique that utilizes a compound's affinities for either a stationary phase, or a mobile phase, in order to perform a chromatographic separation. In reverse phase HPLC (RP-HPLC), typically the stationary phase is composed of a long chain non-aromatic, aliphatic hydrocarbon (e.g. C18, for an 18-carbon chain) that is covalently bound to silica or polymer beads packed into a cylinder stainless steel tube. The mobile phase typically consists of mixtures of H_2O, methanol (MeOH), and acetonitrile (ACN) that are all three completely miscible in all molar fraction ratios. The sample is loaded onto the C18 column with a high H_2O ratio in the mobile phase where the affinity of organic compounds are greatest for the C18 stationary phase. The mobile phase is changed in a gradient fashion where the organic solvent (MeOH or ACN) is gradually increased. The affinity for the organic molecules now increases in the mobile phase which helps to carry them along through the column. The separation of the individual organic constituents now takes place due to their different affinities for the stationary and mobile phases.

Strong ion exchange high performance liquid chromatography works upon similar principles as RP-HPLC, except that the compound of interest now has a strong ionic, electrostatic, non-covalent affinity for the stationary phase. This approach works well for compound that posses a permanent charge such as an acid in basic solution, or a base in acidic solution. Strong cation exchange high performance liquid chromatography (SCEX-HPLC) uses an organically bound sulfonic acid group that has a high affinity for compounds that contain permanent positive charges. Due to the aromatic backbone of strong cation exchange stationary phases, there is also a slight reverse phase interaction that can also take place. For the chromatographic elution of the compound of interest from the strong cation exchange column, typically a salt gradient is used which displaces the analyte from the poly-sulfonic acid stationary phase.

Capillary zone electrophoresis (CZE) is another very useful separation technique which has traditionally been applied primarily to analytes of interest which also posses a permanent charge, just as is the case with strong ion exchange chromatography. Unlike liquid chromatography, capillary zone electrophoresis does not separate analytes according to their respective affinities for mobile and stationary phases, rather the separation is achieved based off of analytes electrophoretic mobilities in an electric field. In positive mode electrophoresis, positively charged analytes move from the anodic (positive electrode) region of the separation phase, to a cathodic (negative electrode) region of the separation phase, through a narrow bore, short fused silica tube. In general, small highly charged analytes have the greatest mobilities, followed by higher molecular weight similarly charged analytes, followed by neutrals, which travel through the separation capillary due to a phenomenon known as electroosmotic flow (EOF), and lastly, oppositely charged ions. The forces acting upon the analytes are vectors, therefore they are additive, and result in the separation of analytes based upon their mass to charge ratios. Electroosmotic flow results from bulk movement of the separation phase through the fused silica capillary due to the charged silano groups of the fused silica wall. EOF can be influenced through pH changes (high pH produces deprotonated, charged silano groups resulting in higher EOF, while low pH results in protonated silano groups thus decreasing EOF), organic modifiers in the separation phase (a higher organic modifier such as MeOH reduces EOF), and also through neutral coating of the fused silica wall such as with polymers, which can reduce or eliminate EOF.

Since its early introduction(1-4), capillary zone electrophoresis is an analytical technique that has become an indispensable tool in many modern laboratories, especially in the pharmaceutical industry(5). The application of capillary electrophoresis to the study of complexes, known as affinity capillary electrophoresis (ACE), has recently experienced a large growth. This methodology has been used to study the electrophoretic mobility and separation of various complexes(6), complex electrostatic interactions(7), complex binding and disassociation constants(8,9), and complex stoichiometry(10). In most studies, affinity CE ideally involves the measurement of a complex that stays bound throughout the electrophoretic separation(11). The complexes that were evaluated by this study involve a purely electrostatic binding between the dye carrier compound, and the anti-cancer agent A007, which have estimated high disassociation constants.

1.4 Overview of Electrospray Triple Quadrupole Mass Spectrometry

Electrospray ionization (ESI) is a process that enables the transfer of compounds in solution phase to the gas phase in an ionized state thus allowing their measurement by mass spectrometry. The use of ESI coupled to mass spectrometry was pioneered by Fenn et al.(12,13), in 1985, by extending the work of Dole et al.(14) who demonstrated the production of gas phase ions by spraying macromolecules through a steel capillary that was electrically charged, and subsequently monitoring the ions with an ion-drift spectrometer. The process by which ESI works has received much theorization, study, and debate(15-21), in the scientific community, especially the formation of the ions from the Taylor(22) cone droplets and offspring droplets. The electrospray process is achieved by placing a potential difference between the capillary and a flat counter electrode. The generated electric field will penetrate into the liquid meniscus and create an excess abundance of charge at the surface. The meniscus becomes unstable and protrudes out forming a Taylor cone. At the end of the Taylor cone a jet of emitting droplets (number of drops estimated at 51,250 with radius of 1.5 μm) will form that contain an excess of charge. As the droplets move towards the counter electrode, a few processes take place. The drop shrinks due to evaporation thus increasing the surface charge until columbic repulsion is great enough that offspring droplets are produced. This is known as the Rayleigh limit producing a columbic explosion. The produced offspring droplets have 2% of the parent droplets mass and 15% of the parent droplets charge. This process will continue until the drop contains one molecule of analyte and charges that are associated with basic sites (positive mode). This is referred to as the "charged residue model" that is most important for large molecules such as proteins. As the droplets move towards the counter electrode a second process also take place known as the "ion evaporation model." In this process the offspring droplet will allow evaporation of an analyte molecule from its surface along with charge when the charge repulsion of the analyte with the solution is great enough to allow it to leave the surface of the drop. This usually takes place for droplets with a radius that is less than 10 nm. This type of ion formation is most important for small molecules.

In the ensuring years since its introduction, electrospray mass spectrometry has been used for structural elucidation and fragment information(23-25), and non-covalent complex studies(26,27), just to name a few recent examples of its overwhelmingly wide range of applications.

Electrospray(28-31) is an ionization method that is now well known to produce intact gas phase ions with very minimal, if any, fragmentation being produced during the ionization process. In the transfer process of the ions from the condensed phase to the gas phase, several types of “cooling” processes of the ions are taking place in the source: (1) cooling during the desolvation process through vibrational energy transfer from the ion to the departing solvent molecules, (2) adiabatic expansion of the electrospray as it enters the first vacuum stage, (3) evaporative cooling, and (4) cooling due to low energy dampening collisions with ambient gas molecules. The combination of these effects, and the fact that electrospray can effectively transfer a solution phase complex to the gas phase with minimal interruption of the complex, makes the study of non-covalent complexes from solution by electrospray ionization mass spectrometry attractive.

The ESI source is coupled to a triple quadrupole mass spectrometer for detection of the ions produced from the electrospray process. The triple quadrupole mass spectrometer is a versatile tool in structural analysis of components of complex matrices. The instrument is comprised of three quadrupoles, in tandem, which two (the first and third) have individual detectors, while the middle quadrupole (actually a hexapole), known as the collision gas cell, is RF only with no detector. Figure 1.2.4 shows the arrangement in space of the quadrupoles. Having the quadrupoles aligned in tandem allows approaches to compound isolation, and subsequent identification by using the quadrupoles as mass filters(32). A quadrupole is made up of four rods that are placed precisely parallel to each other. One set of opposite poles have a DC voltage (U) supply connected while the other two have a radio frequency (rf) voltage (V) connected(33). Ions are accelerated into the quadrupole by a small voltage of 5 V, and under the influence of the combination of electric fields, the ions follow a complicated trajectory path. If the oscillation of the ions in the quadrupole have finite amplitude it will be stable and pass through. If they are infinite, they will be unstable and the ion will collide with the rods. At a certain range of DC voltage U and radio frequency potential V, the ion of interest will have a stable region. A plot of U versus V is used to scan mass to charge ratios (m/z) with the quadrupoles allowing the measurement of a range of masses, typically up to 4000 Da. The slope of the line is a fixed ratio of U to V. As U and V are varied, the scan follows the scan line and subsequent m/z values are recorded. Due to this functionality the quadrupoles are called mass filters, however, they are still dependent upon a mass to charge ratio. The mass spectrometry methods used in the lipid analyses included single stage analysis (ESI-MS) where the first quadrupole is scanned and the first detector is used. This is used for compound molecular mass. A second method used was neutral loss scanning (NL). This is used to determine the initial molecule that losses a certain neutral mass upon fragmentation induced in the central hexapole collision cell. In this procedure the first and third quadrupoles are scanned at a differential equal to the neutral loss value. For example, if the NL value is 50 then when Q1 is at 200 m/z, Q3 is scanning at 150 m/z. When 150 m/z is registered by detector 2, the Q1 value is recorded along with the intensity recorded with detector 2. A third method used was precursor ion scanning. This is used to determine the initial molecule that produces a specific product ion. Here Q3 is held static at the ion fragment m/z of interest and Q1 is scanned over an m/z range. When the ion is detected by Q3 the m/z value in Q1 is recorded in conjunction with the intensity recorded by detector 2. Finally, a fourth method used was product ion scanning(33). This is a scan for product ions produced from a single precursor ion which is allowed to pass through Q1. This is used for structural elucidation.

1.5 Overview of Matrix Assisted Laser Desorption Ionization (MALDI) Time-of-Flight (TOF) Mass Spectrometry

Matrix assisted laser desorption ionization (MALDI) is a process that enables the transfer of compounds in a solid, crystalline phase to the gas phase in an ionized state thus allowing their measurement by mass spectrometry(34-36). The process involves mixing the analyte of interest with a strongly ultra-violet absorbing organic compound, applying the mixture to a surface and then allowing it to dry. Examples of typical organic matrix compounds used are 2,5-dihydroxybenzoic acid (DHB), 3,5-dimethoxy-4-hydroxy-trans-cinnamic acis (sinapic or sinapinic acid), and α-cyano-4-hydroxy-trans-cinnamic acid (α-CHCA). There are many techniques described for applying the matrix to the target such as the "dried droplet" method(36,37), and the "thin film" method(38). The dried crystalline mixture "film" or "spot" is then irradiated with a nitrogen laser (337 nm), or an Nd-YAG laser (266 nm). The strongly UV absorbing species accepts energy from the laser and desorbs from the surface carrying along any analyte that is mixed with it. The analyte is cationized in the plume above the crystalline surface with, in the positive mode, either a hydrogen proton or a metal cation such as sodium.

The desorbed, ionized compounds from the matrix assisted laser desorption ionization process are then introduced into a mass spectrometer for analysis. The most common mass spectrometer that is coupled to MALDI is the time-of-flight mass spectrometer (TOF MS)(39,40). The TOF mass spectrometer separates compounds according to their mass to charge ratios (m/z) through a direct relationship between a compounds drift time through a predetermined drift pathlength and its mass to charge ratio (m/z). Initially, all the ions have similar kinetic energies imparted to them from the draw-out pulse (representing time zero) which accelerates them into the flight tube. Because the compounds have different masses their velocities will be different according to the relationship between kinetic energy and mass represented by: KE = eV = $1/2mv^2$. From this expression, the mass to charge ratio is related to the ions flight time by the following expression: $m/z = 2vt^2/L^2$. There is a high transmission efficiency of the ions into and through the drift tube which equates to very low levels of detection limits which are in the femtamole to atamole ranges. Theoretically, the mass range of the spectrometer is unlimited due to the relationship of drift time for mass measurement. In practice though, the sensitivity needed to detect a very slow moving large molecular weight compound limits the TOF-MS to 1 to 2 million Daltons or so.

The early designs of time of flight mass spectrometers suffered from poor resolution which is the ability of the mass spectrometer to separate ions. This is usually expressed as resolution = $m/\Delta m$ where m is the mass of the peak of interest and Δm is the difference between this mass and the next closest peak. The poor resolution was due to nonuniform initial spatial and energy distributions of the formed ions in the mass spectrometer's ionization source. Due to the distribution spreads the mass resolution was directly dependant upon the initial velocity of the formed ions. Early work reported by Wiley et al.(41) reported upon the correction for initial velocity distributions using a technique they described as "time-lag energy focusing" where the ions were produced in a field-free region, then after a preset time a pulse was applied to the region to extract the formed ions. They also reported upon a way to correct for initial special distributions through a two field pulsed ion source. They demonstrated though that correction can only be made for one of the distributions at a time. In MALDI, the spatial distribution spread is not a significant problem, therefore "delayed extraction" of the ions from the field free source region should correct for the initial energy distribution spread of the formed ions(42). With this correction, the resolution should be directly dependent upon the total flight time ratioed to the error in the time measurement, thus an increase in the length of the flight path should equate to a higher resolution. The resolution enhancement due to the delayed extraction initial energy focusing and flight path was demonstrated in a study reported by Vestal et al.(42) using a MALDI-TOF mass spectrometer.

A second modification of time of flight mass spectrometers involves time focusing of the ions while they are in flight through the use of an electrostatic mirror at the end of the flight tube(43,44). The electrostatic mirror focusing the ions with the same mass to charge ratio but slightly different kinetic energies by allowing a slightly longer path for the higher KE containing ion compared to a slightly lower KE ion thus allowing the ions to catch up to one another. The electrostatic mirror also increases the flight path length of the mass spectrometer, thus providing a double focusing effect. All recent TOF-mass spectrometers employ both delayed extraction and the reflectron electrostatic mirror for analysis of compounds below 10 kDa. For compounds greater than 10 kDa a linear mode is typically used where the electrostatic mirror is turned off.

1.6 References

1. Mikkers, F.E.P., Everaerts, F.M., and Verheggen, Th.P.E.M. . *J. Chromatogr.,* **1979,** *169*, 11.
2. Jorgenson, J. W.; Lukacs, K. D. *Anal. Chem.* **1981**, *53*, 1298-1302.
3. Terabe, S., Otsuka, K., Ichikawa, K., Tsuchiya, A., and Ando, T. *Anal. Chem.* **1984**, *56*, 111.
4. Hjerten, S. *J. Chromatogr.,* **1985,** *347*, 191.
5. Hadley, M.; Gilges, M.; Senior, J.; Shah, A.; Camilleri, P. *J. Chromatogr., B* **2000**, *745*, 177-188.
6. Chu, Y. H.; Dunayevskiy, Y. M.; Kirby, D. P.; Vouros, P.; Karger, B. L. *J. Am. Chem. Soc.* **1996**, *118*, 7827-7835.
7. Rao, J.; Colton, I. J.; Whitesides, G. M. *J. Am. Chem. Soc.* **1997,** *119*, 9336-9340.
8. Rundlett, K. L.; Armstrong, D. W. *J. Chromatogr., A* **1996,** *721*, 173-186.
9. Dunayevskiy, Y. M.; Lyubarskaya, Y. V.; Chu, Y. H.; Vouros, P.; Karger, B. L. *J. Med. Chem.* **1998,** *41,* 1201-1204.
10. Okun, V. M.; Moser, R.; Blaas, D.; Kenndler, E. *Anal. Chem.* **2001,** *73,* 3900-3906.
11. Wan, Q. H.; Le, X. C. *Anal.Chem.* **1999,** *71*, 4183-4189.
12. Whitehouse, C.M., Dryer, R.N., Yamashita, M., and Fenn, J.B. *Anal. Chem.* **1985,** *57,* 675.
13. Fenn, J.B. *J. Am. Soc. Mass. Spectrom.* **1993,** *4*, 524.

14. Dole, M., Hines, R.L., Mack, R.C., Mobley, R.C., Ferguson, L.D., and Alice, M.B. *J. Chem. Phys.* **1968,** *49*, 2240.
15. Kebarle, P., Ho, Y. In *Electrospray Ionization Mass Spectrometry;* Cole, R.B., Ed.; Wiley: New York, 1997; p. 17.
16. Cole, R.B. *J. Mass Spectrom.* **2000,** *35,* 763-772.
17. Cech, N.B., and Enke, C.G. *Mass Spectrometry Reviews,* **2001,** *20,* 362-387.
18. Gaskell, S.J. *J. Mass Spectrom.*, **1997,** *32,* 677-688.
19. Cech, N.B., and Enke, C.G. *Anal. Chem.,* **2000,** *72,* 2717-2723.
20. Sterner, J.L., Johnston, M.V., Nicol, G.R., and Ridge, D.P. *J. Mass Spectrom.* **2000,** *35,* 385-391.
21. Cech, N.B., and Enke, C.G. *Anal. Chem.,* **2001,** *73,* 4632-4639.
22. Taylor, G.I. *Proc. R. Soc. London, Ser. A,* **1964**, *280*, 383.
23. Cao, P., and Stults, J.T. *Rapid Commun. Mass Spectrom.* **2000**, *14,* 1600-1606.
24. Ho, Y.P., Huang, P.C., and Deng, K.H. *Rapid Commun. Mass Spectrom.* **2003**, *17,* 114-121.
25. Kocher, T., Allmaier, G., and Wilm, M. *J. Mass Spectrom.* **2003,** *38,* 131-137.
26. Lorenz, S.A., Maziarz, E.P., and Wood, T.D. *J. Am Soc Mass Spectrom* **2001**, *12,* 795-804.
27. Daniel, J.M., Friess, S.D., Rajagopalan, S., Wendt, S., and Zenobi, R. *International Journal of Mass Spectrometry* **2002,** *216,* 1-27.
28. C. M. Whitehouse, R. N. Dreyer, M. Yamashita and J. B. Fenn, *Anal. Chem.* **57**, 675 (1985).
29. J. B. Fenn, *J Am Soc Mass Spectrom* **4**, 524, (1993).
30. R. B. Cole, *J. Mass Spectrom.* **35**, 763 (2000).
31. N. B. Cech and C. G. Enke, *Mass Spec Rev* **20**, 362 (2001).
32. Johnstone, R.A.W.; Rose, M.E. Mass Spectrometry for Chemists and Biochemists, 2nd ed.; Cambridge University Press: New York, 1996; Chapter 2.
33. Micromass Quattro II User's Guide, Micromass UK Limited, March 1996, 19-26.
34. Karas, M.; Bachmann, D.; Bahr, U.; Hillenkamp, F. *Int. J. Mass Spectrom. Ion Processes* **1987**, *78*, 53.
35. Tanaka, K.; Waki, H.; Ido, Y.; Akita, S.; Yoshida, Y.; Yoshida, T. *Rapid Commun. Mass Spectrom.* **1988**, *2*, 151-153.
36. Karas, M.; Hillenkamp, F. *Anal Chem* **1988**, *60*, 2299.
37. Xiang, F,; Beavis, R. C. *Org. Mass Spectrom.* **1993**, *28*, 1424.
38. Xiang, F,; Beavis, R. C. *Rapid Commun. Mass Spectrom.* **1994**, *8*, 199-204.
39. Hillenkamp, F.; Unsold, E.; Kaufmann, R.; Nitsche, R. *Appl. Phys.* **1975**, *8*, 341-348.
40. Van Breemen, R. B.; Snow, M.; Cotter, R. J. *Int. J. Mass Spectrom. Ion Phys.* **1983**, *49*, 35-50.
41. Wiley, W. C.; McLaren, I. H. Time-of-Flight Mass Spectrometer with Improved Resolution *Rev. Sci. Instrum.* **1955**, *26*, 1150-1156.
42. Vestal, M. L.; Juhasz, P.; Martic, S. A. Delayed Extraction Matrix-assisted Laser Desorption Time-of-Flight Mass Spectrometry *Rapid Commun. Mass Spectrom.* **1995**, *9*, 1044-1050.
43. Mamyrin, B. A.; Karateev, V. I.; Shmikk, D. V.; Zagulin, V. A. *Sov. Phys. JETP* **1973**, *37*, 45.
44. Della Negra, S.; Le Beyec, Y. *Int. J. Mass Spectrom. Ion Processes* **1984**, *61*, 21.

CHAPTER II: DETERMINATION OF RELATIVE BINDING CONSTANTS BETWEEN π-DELOCALIZED LYMPHANGITIC DYES AND AN ANTI-CANCER AGENT BY CATION EXCHANGE LIQUID CHROMATOGRAPHY AND AFFINITY CAPILLARY ZONE ELECTROPHORESIS

2.1 Introduction

One of the major problems with anti-cancer therapy is the effective delivery of the anti-cancer agent to the tumor site. Skin permeability studies have demonstrated that the coupling of the anti-cancer agent A007 with a carrier dye molecule (methylene green, MEG, methylene blue, MEB, and toluidine blue, TB, see Figure 2.1 for structures) increases A007's therapeutic activity(1), with a rating from most effective, to least, as MEG>MEB>TB. Electrospray ionization tandem mass spectrometry(2-5) (ESI-MS/MS) has been used in our lab (results unpublished) to study the characteristics and relative binding strengths of the three dyes MEG, MEB, and TB, complexed with A007. The gas phase binding strengths of the three complexes, determined by ESI-MS/MS, were ranked in the following order: MEG>MEB>TB, which indicates that a stronger binding between the carrier and anti-cancer agent directly correlates to a greater efficacy. A high performance liquid chromatography (HPLC) method has been developed for the determination of A007 in plasma(6), but not for the complexes that are formed between A007 and carrier compounds. A cation exchange chromatography (CEC) method has been developed in our lab (results unpublished) in order to rank the binding strengths of carrier:A007 complexes. The CEC method determined binding strengths with the same trend as was determined by ESI-MS/MS, namely MEG>MEB>TB. This effectively gave a "solution phase" ranking of binding strengths.

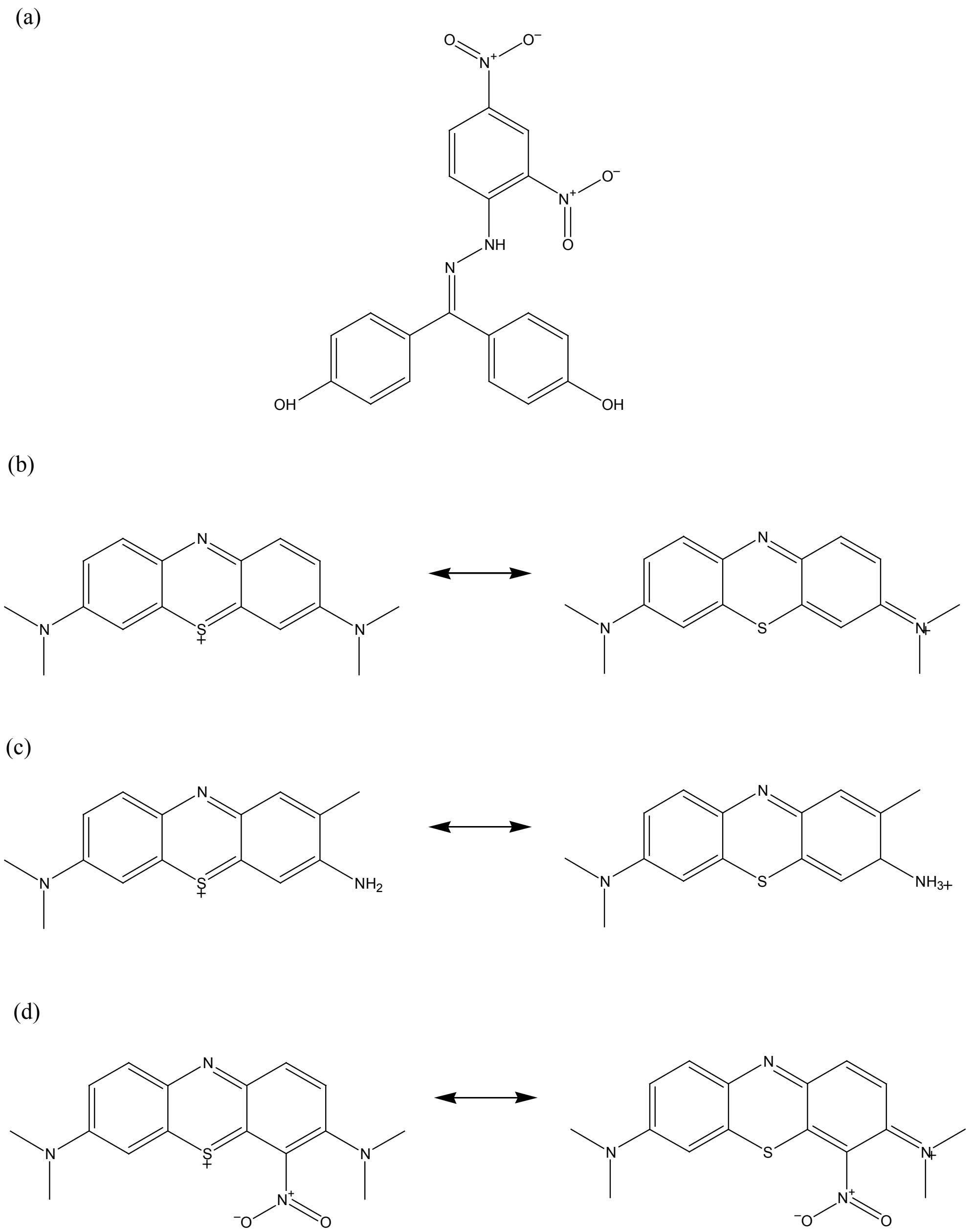

Figure 2.1. Structures of (a) 4,4'-Dihydroxybenzophenone-2,4-dinitrophenylhydrazone (A007)(1), (b) methylene blue (MEB), (c) toluidine blue (TB), and (d) methylene green (MEG).

The ACE method developed ranked the binding strengths of the carrier:A007 complexes, in the solution phase at an adjusted physiological pH (7.4), as MEG>MEB>TB. These results are in agreement with the ESI-MS/MS, and cation exchange chromatography rankings that were previously determined.

2.2 Experimental

The UV/VIS experiments were performed with a PC controlled CARY 500 Scan UV-Vis-NIR Spectrophotometer (Varian Australia Pty. Ltd.).

The fluorescence experiments were performed with a PC controlled Photon Technology International Fluorometer (PTI, Canada).

The CE experiments were performed with a BioFocus 2000 Capillary Electrophoresis System (BIO-RAD, Hercules, California) with a UV/VIS variable wavelength detector. Uncoated fused-silica capillaries were used with a total length of 56 cm, effective length 50 cm, and 50 um i.d. The capillaries were maintained at a temperature of 25 ^{o}C. The injection time was 30 psi*sec pressure. All runs were made in a constant voltage mode with a running voltage of 30 kV. The polarity was + to – (positive polarity mode where the negative pole is at the capillary outlet). Between runs, the CE capillary was conditioned through a series of washes comprised of 13 min. 1 M NaOH, followed by 13 min. of separation phase. The separation phase consisted of (1) 50% MeOH/50% H_2O buffered with 25 mM mono and dibasic hydrogen phosphate at a pH of 7.4 (adjusted), or (2) 50% MeOH/50% H_2O, 25 mM phosphate buffer at 7.4 pH (adjusted) and spiked with either MEG, MEB, or TB.

The HPLC experiments were performed with an 1100 Series HPLC (Agilent Technologies, Palo Alta, CA) comprised of a vacuum degasser, a quarternary pump, and a diode array detector. The column used was a 150 x 1.0 mm, 5 micrometer, 300-A, PolySULFOETHYL A column (PolyLC, Columbia, MD). Instrumental parameters consisted of a 0.1 ml per minute flow, 10 microliter injection loop, and ambient column temperature. Mobile phases consisted of (1) 50% MeOH/50% H_2O, buffered at 7.4 pH (adjusted) with 15 mM triethylamine phosphate (TEAP), (2) 50% MeOH/50% H_2O, buffered at 7.4 pH (adjusted) with 15 mM TEAP, and spiked with either 5×10^{-5} M MEG, 5×10^{-5} M MEB, or 5×10^{-5} M TB, or (3) 50% MeOH/50% H_2O, buffered at 7.4 pH (adjusted) with 15 mM triethylamine phosphate and 0.5 M NaCl.

To mimic physiological conditions, all solutions are at a pH of 7.4, but adjusted due to the change in H^+ activity for a 50 % methanol and 50 % water mixture(18,19).

2.3 Results and Discussion

2.3.1 UV/Vis Study of the Compounds and Complexes

Figure 2.2 illustrates UV/Vis spectra of the complexes formed between the three dyes and A007. What's observed from the spectra is that each compound contains a unique absorbance peak which can be used to detect and monitor the compounds and complexes without interference. The three dyes used in the study, methylene green, methylene blue, and toluidine blue, have unique absorbance maximums at 656 nm, 662 nm, and 630 nm, respectively. The anti-cancer agent A007 has an absorbance maximum between 398 nm, and 405 nm. Both dye and A007 peaks are found in the complexes, and the A007 max at 398 nm was used to detect the complex for mobility calculations and migration times (ACE), and retention times (CELC).

2.3.2 Flourescence Study of the Dye-A007 Complexes

The dyes used in the study naturally fluoresce at specific wavelengths. It was initially felt that the complex between the dyes and the anti-cancer agent A007 enhanced this fluorescence. Using the method of continuous variation(20,21), a fluorescence maximum was obtained for each dye-A007 complex versus mole fraction. These dyes however are known to produce dimers in the liquid phase(22), where the production of the dimer will quench the fluorescence. Further spectroscopic experiments showed that only one species of complex was being formed in solution between A007 and the dyes, but the enhancement in fluorescence was attributable to the decrease in dye dimer only, and not to the formation of the A007:dye complex.

2.3.3 Cation Exchange Liquid Chromatography Results.

A binding coefficient (BC) equation (see equation 1) was derived based on the retention times of the dyes, the A007:dye complexes, and the anti-cancer agent A007, in order to rank the binding strengths of the A007:dye complexes. The scale spans a BC value from approximately 0.1, representing a weak binding, to 1.0, representing the strongest binding.

$$BC = (t_{drug(carrier)} - t_{drug})/(t_{carrier} - t_{drug}) \qquad (1)$$

Figure 2.3 contains the CELC chromatograms illustrating the retention times used for the calculation of the binding constants. It is felt that this approach gives a direct measurement of

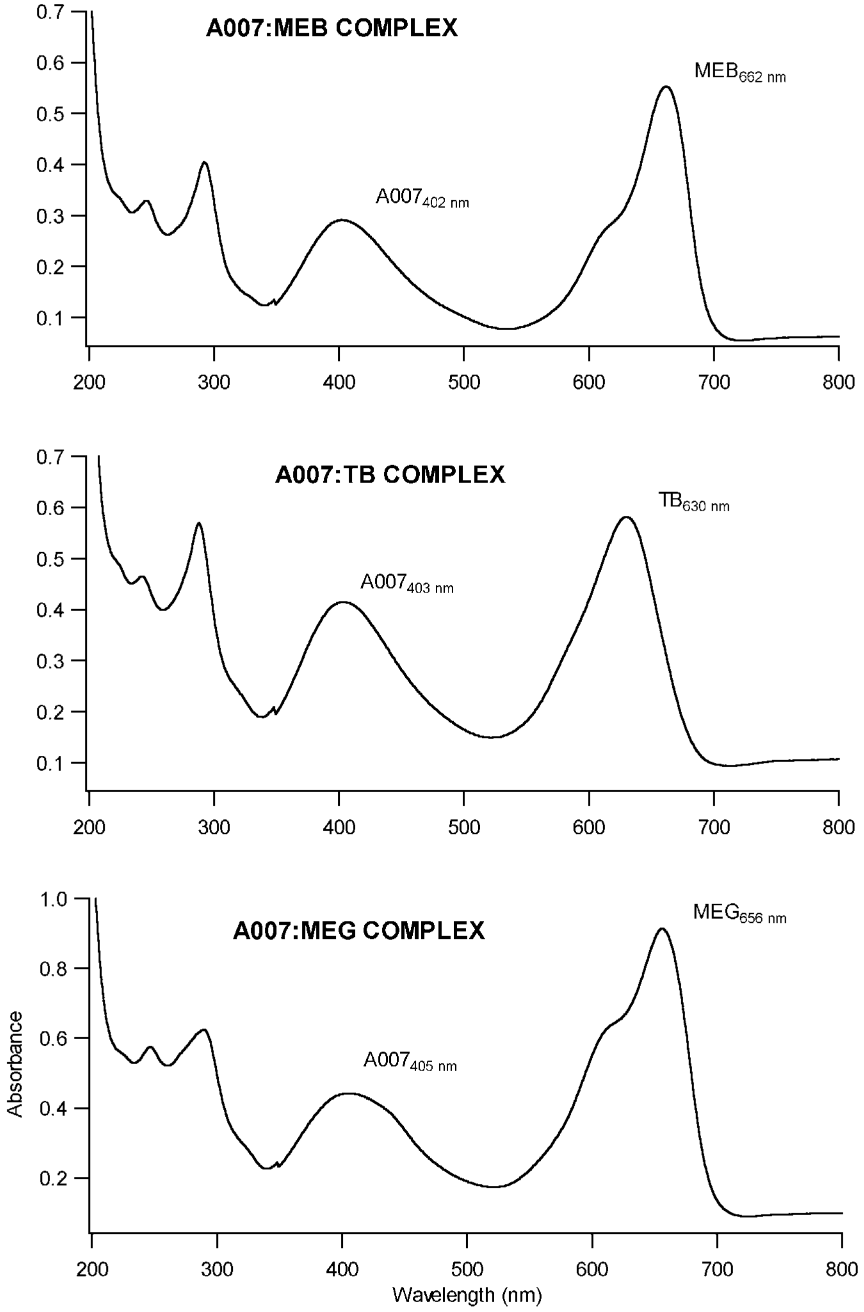

Figure 2.2. UV/Vis absorbance spectrums of A007:Dye complexes illustrating absorbance maximums of (a) 405 nm for A007, 662 nm for MEB, (b) 630 nm for TB, and (c) 656 nm for MEG.

the binding strength between the dyes and A007. The binding method is achieved through a kind of pseudo stationary phase that is produced in the cation exchange column between the dye in the mobile phase, and the sulfoethyl A stationary phase. With a stronger binding between the dye and A007, A007 will have a longer elution time, as is observed in the chromatograms contained in Figure 1. The binding strength scale of the three dyes was determined to be methylene green > methylene blue > toluidine blue, with calculated BC's of 0.54 ± 0.05, 0.24 ± 0.02, and 0.18 ± 0.02, respectively (BC values are the average plus or minus one standard deviation of at least three determinations).

2.3.4 Capillary Electrophoresis Results

Figure 2.4 illustrates the results of the change in mobilities of A007 versus increasing concentrations of the dye ligands titrated into the separation phase. There are initial similarities in the effective mobilities of A007 observed between the three systems at a dye ligand concentration of 5×10^{-5} M (MEG dye A007 mobility of 14.9 $cm^2kV^{-1}min^{-1}$, MEB dye A007 mobility of 14.3 $cm^2kV^{-1}min^{-1}$, and TB dye A007 mobility of 14.9 $cm^2kV^{-1}min^{-1}$). Following this there is a subsequent decreasing mobility trend as the dye concentration is increased to 8×10^{-4} M. This suggests that the change in mobility could be attributed to a decrease in the electroosmotic flow with increasing background electrolyte(23-25). This type of effect is also observed with increasing percentages of organic solvent in the separation phase(26-30). Salomon et al.(23) derived an expression which describes the change in electroosmotic mobility as a function of buffer (electrolyte) concentration:

$$\mu_{eo} = (Q_0/n(1 + K_{wall}[M^+]))(d_0 + 1/(K'([M^+])^{1/2})) \qquad (2)$$

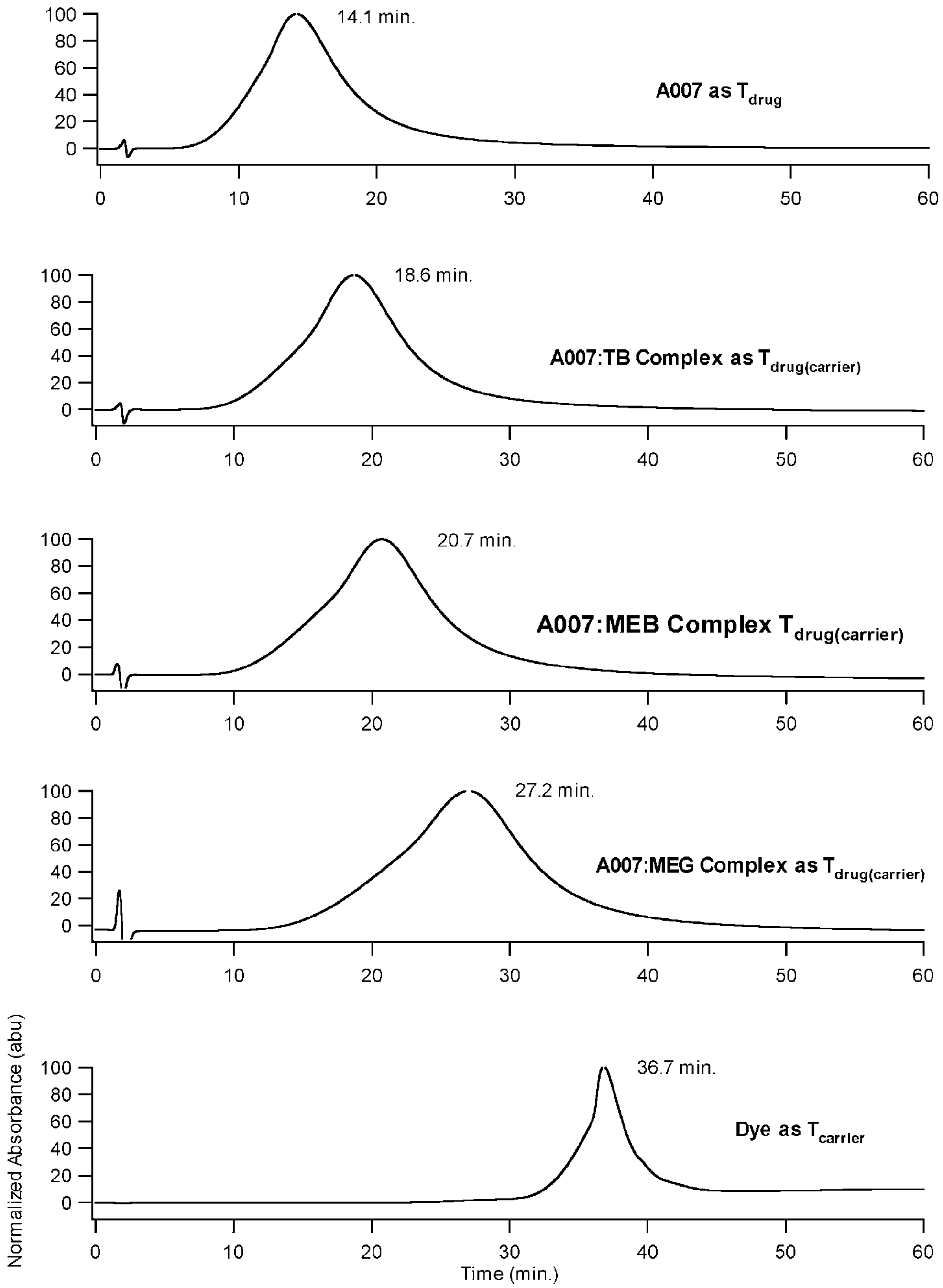

Figure 2.3. Typical CELC chromatograms of A007 (T_{drug}) at 5x10^{-5} M A007, A007:TB Complex ($T_{drug(carrier)}$) at 5x10^{-5} M TB and A007, A007:MEB Complex ($T_{drug(carrier)}$) at 5x10^{-5} M MEB and A007, A007:MEG Complex ($T_{drug(carrier)}$) at 5x10^{-5} M MEG and A007, and Dye ($T_{carrier}$).

The μ_{eo} is inversely proportional to both the ionic strength of the solution [M^+], and to the association of the cations to the silica wall (K_{wall}). An increase in either of these leads to a decrease in the mobility. The studies reported by Salomon measured the change in electroosmotic mobilities for buffer concentrations ranging from approximately 2 mM to 40 mM. The mobility change experiments performed on the A007:dye complexes reported here ranged from 25.05 mM ionic to 25.8 mM ionic. This is a much lower change in ionic strength of the separation phases suggesting perhaps a negligible contribution. The anti-cancer agent A007 at a pH of 7.4 is neutral, therefore its mobility in buffer alone would represent the electroosmotic flow of the system before titrating the separation phase with the dye ligand. A007's mobility in buffer alone was measured at 13.5 $cm^2kV^{-1}min^{-1}$. This result is very similar to the mobilities measured for A007 when $5x10^{-5}$ M dye (first data point, Figure 2.3) had been titrated into the separation phases (MEG dye A007 mobility of 14.9 $cm^2kV^{-1}min^{-1}$, MEB dye A007 mobility of 14.3 $cm^2kV^{-1}min^{-1}$, and TB dye A007 mobility of 14.9 $cm^2kV^{-1}min^{-1}$). Notice the slight increase in mobility of A007 in separation phases containing $5x10^{-5}$ M dye versus the mobility of A007 in buffer alone. The three dyes MEG, MEB, and TB are very similar in structure (see Figure 2.1), and all possess a permanent positive charge. Therefore, the change in EOF due to increasing concentrations of the dye ligands in the separation phase would be expected to be of similar magnitude for the three systems, as was observed with the mobility of A007 with the titration of $5x10^{-5}$ M dye into the separation phases. As higher dye concentrations are titrated into the separation phase, the mobilities of A007 are observed to decrease. This is attributed to the higher

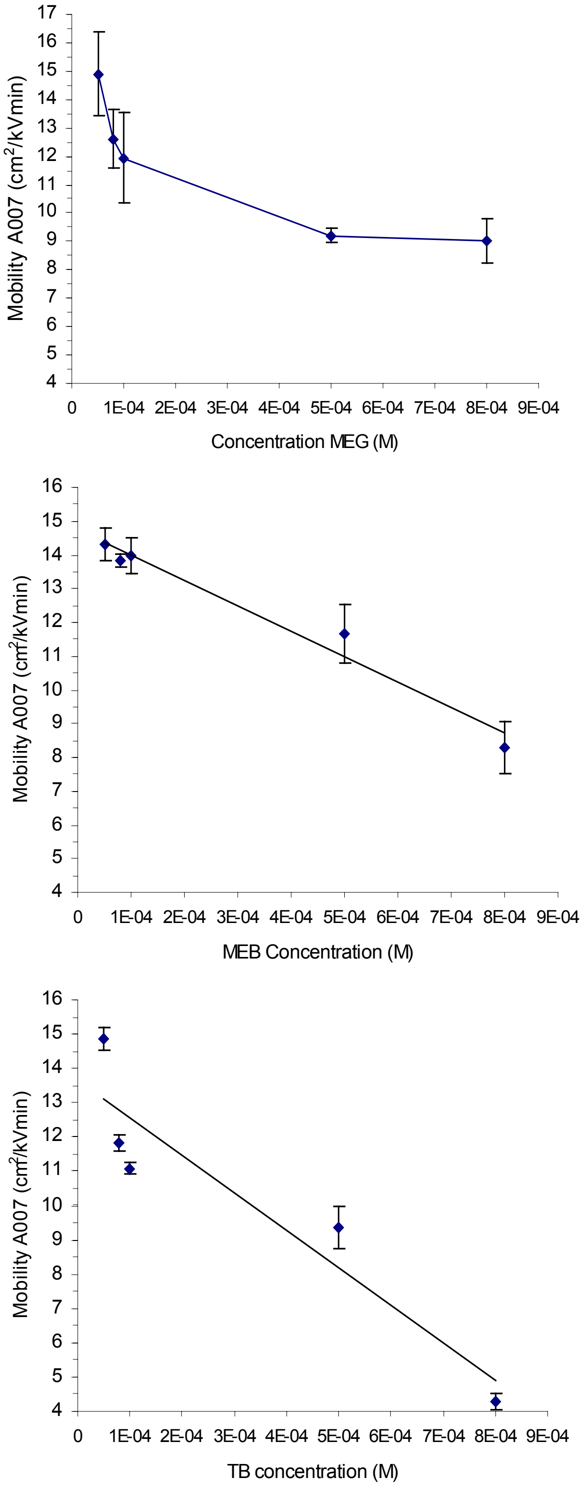

Figure 2.4. Plots of the mobility of A007 in increasing concentrations of methylene green, methylene blue, and toluidine blue.

background electrolyte effect described by eq 2. However, as the dye ligand is titrated into the separation phase, the A007:dye electrostatic interaction is strong enough to produce a difference in the mobility of A007 when comparing the three systems (e.g., A007 mobilities at 8×10^{-4} M dye ligand: 4.03 ± 0.24 $cm^2kV^{-1}min^{-1}$ for TB, 8.30 ± 0.76 $cm^2kV^{-1}min^{-1}$ for MEB, and 9.04 ± 0.78 $cm^2kV^{-1}min^{-1}$ for MEG). This illustrates that the dye ligand is playing an influential role in the change in A007 mobilities through a direct electrostatic interaction in addition to EOF changes due to high electrolyte background (see Figure 2.3). It was at the 8×10^{-4} M concentration of the dye ligand in the separation phase that the ranking of the relative binding strength coefficients of the A007:dye complexes was calculated.

A binding strength coefficient (BC), eq 3, was derived based on the ratio of the electrophoretic mobility of A007 in the presence of ligand, to that of the mobility of the free A007. A BC of approximately 0.1 would indicate a weak binding, while a BC of 1 would indicate the strongest binding. A similar ratio relationship was derived by Srinivasan et al.(31) to directly calculate disassociation constants for noncovalent complexes between cyclodextrin and barbiturates. The relationship derived and used for the BC ranking is as follows:

$$BC = \mu_{complex}/\mu_{drug} \qquad (3)$$

Figure 2.5 is a series of electropherograms illustrating the migration times of the dyes, and A007 as sample in separation phases containing the dye ligands MEG, MEB, and TB. The effective electrophoretic mobility, in the presence of electroosmotic flow, of component i was calculated using the following equation(32):

$$u_i = v_i/E = v_i \cdot L_t/V \quad [cm^2 \cdot kV^{-1} \cdot min^{-1}] \qquad (4)$$

where:

$$v_i = v_{i(net)} - v_{eo} = L_D/t_i - L_D/t_{eo} \quad [cm \cdot min^{-1}] \qquad (5)$$

Combining equations 3 and 4 gives the standard mobility equation:

$$u_i = (L_D/t_i - L_D/t_{eo})\cdot L_T/V \quad [\mathrm{cm^2\cdot kV^{-1}\cdot min^{-1}}] \qquad (6)$$

Equation (5) was further simplified, due to the absence of a measurable EOF, to:

$$u_i = L_D L_T t_i^{-1} V^{-1} \quad [\mathrm{cm^2\cdot kV^{-1}\cdot min^{-1}}] \qquad (7)$$

The calculated binding strength coefficients by ACE are listed in Table 2.1 along with the BC values calculated from the CELC results.

Compound	ACE BC	CEC BC
Methylene green	0.67 ± 0.06	0.54 ± 0.05
Methylene blue	0.62 ± 0.06	0.24 ± 0.02
Toluidine blue	0.32 ± 0.02	0.18 ± 0.02

Table 2.1 Binding constant values for the methylene green, methylene blue, and toluidine blue complexes with A007 by affinity capillary electrophoresis (ACE), and cation exchange chromatography (CEC).

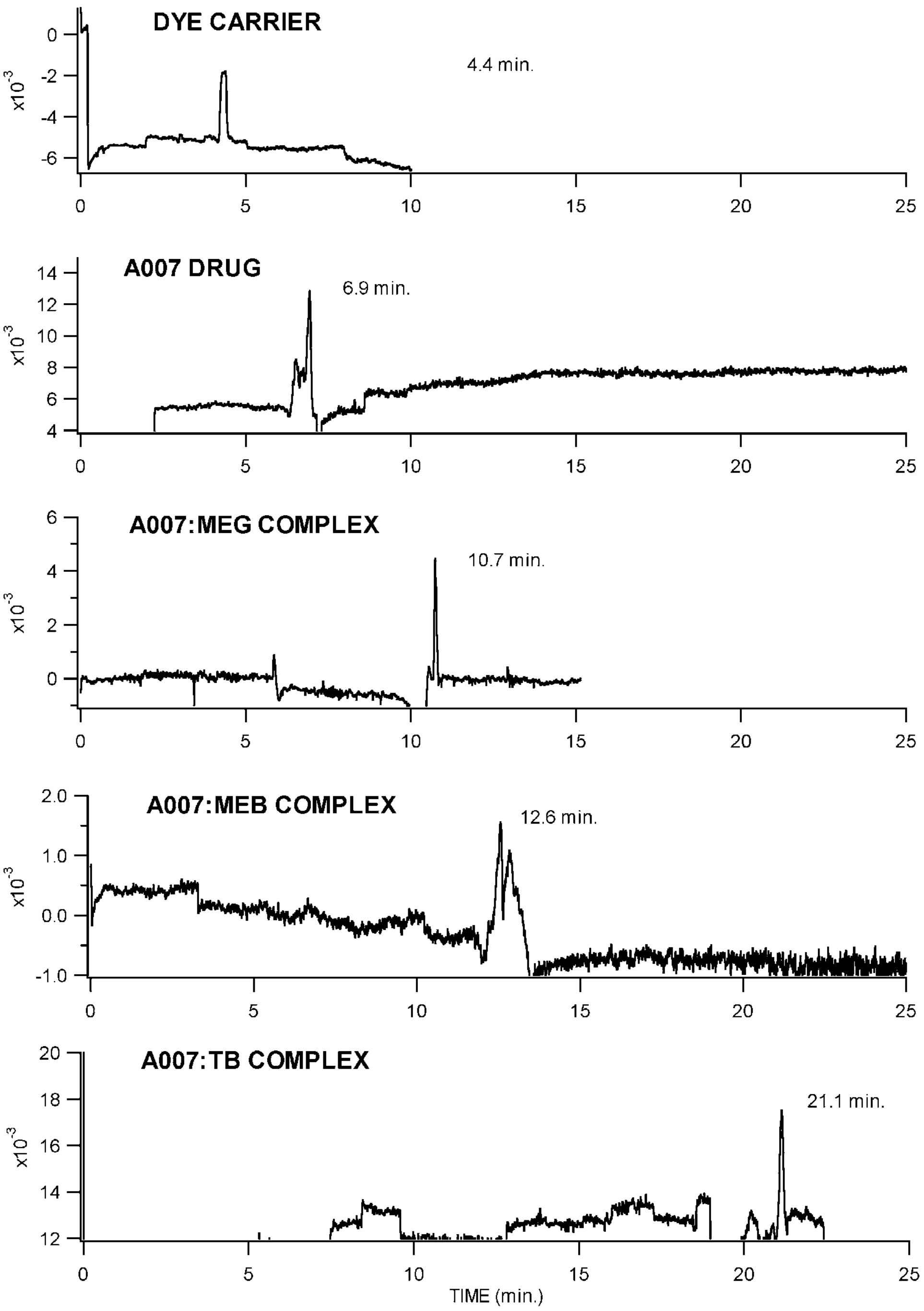

Figure 2.5. Electropherograms of (a) the three dyes (co-migration), (b) the anti-cancer agent A007, (c) A007:MEG complex, (d) A007:MEB complex, and (e) A007:TB complex.

2.3.5 Comparison of Methods

As illustrated in Table 2.1, the ACE results show that MEG and MEB have very similar binding coefficients, while TB was well differentiated. The ranking by CELC shows binding coefficients that are more differentiated between the three, probably due to a much more direct electrostatic binding strength determination than what is measured with the ACE approach.

The affinity capillary electrophoresis, ACE, method does have some general advantages over the other two methods. The ES-MS/MS method describes a relative binding strength between the complexes in the gas phase only. In general, gas phase binding strengths vary greatly in agreement with solution phase binding strengths, always dependent on the system being studied. In this work, a solution phase analytical method for binding strength determination was needed. The cation exchange chromatography, CEC, approach gives a good separation between the ranking values for the complexes, but the method requires considerable column equilibration time with the changing of each mobile phase ligand (approximately 2 to 3 hours). In comparison the ACE method is fast (analysis completed between 10 to 30 minutes), and requires little treatment between the changing of ligand separation phases (13 minute caustic wash, followed by a 13 minute separation phase wash). A further advantage is that typical ACE methods generally require samples in the nanomolar to micromolar concentration ranges, as compared to millimolar levels as used in chromatographic methods such as the CELC method(33). In general use, the ACE method would be utilized as a rapid screening determination of binding strengths, while the CELC method would act as a more accurate, confirmation method.

2.4 Conclusions

Affinity capillary electrophoresis has become a versatile tool in the study of many descriptive parameters of complexes. Though this methodological approach has generally been used for high affinity complexes, it can also be successfully used for complexes of low affinity, or high disassociation, as demonstrated through the application to this dye-anti cancer agent complex. The ACE method offers an alternative approach in the determination of binding strength coefficients of complexes, with advantages over the other two methods studied, ES-MS/MS and cation exchange liquid chromatography, respectively. The ACE method requires less time for analysis, and also smaller sample sizes as compared to ES-MS/MS and CELC. The cost for ES-MS/MS instrumentation can also be prohibitive for some laboratories. The ACE method is robust, and can be applied as a general method for the determination of binding strengths of non-covalent complexes. In its specific use for the dye:A007 system, the ACE method would be utilized as a rapid screening determination of binding strengths, while the CELC method would act as a more precise, confirmation method.

2.5 References

1. Morgan, L. R.; Rodgers, A. H.; LeBlanc, B. W.; Boue, S. M.; Yang, Y.; Jursic, B. S.; Cole, R. B. *Bioorganic & Medicinal Chemistry Letters* **2001**, *11*, 2193-2195.
2. Whitehouse, C.M., Dryer, R.N., Yamashita, M., and Fenn, J.B. *Anal. Chem.* **1985,** *57,* 675.
3. Fenn, J.B. *J. Am. Soc. Mass. Spectrom.* **1993,** *4*, 524.
4. Kebarle, P., Ho, Y. In *Electrospray Ionization Mass Spectrometry;* Cole, R.B., Ed.; Wiley: New York, 1997; p. 17.
5. Cole, R.B. *J. Mass Spectrom.* **2000,** *35,* 763-772.
6. Rodgers, A. H.; Subramanian, S.; Morgan Jr., L. R. *J. Chromatogr., B* **1995**, *670*, 365-368.
7. Mussini, T.; Covington, A. K.; Longhi, P.; Rondinini, S. *International Union of Pure and Applied Chemistry*, **1985**, 865-876.
8. Mussini, T.; Covington, A. K.; Longhi, P.; Rondinini, S.; Zou, Z.Y. *Biochemica Acta,* **1983**, *11*, 1593-1598.

9. Vosburge, W. C.; Cooper, G. R. *J. Am. Chem. Soc.* **1941**, *63*, 437-442.
10. Stapelfeldt, H.; Skibsted, L. H. *J. Dairy Research* **1999,** *66,* 545-558.
11. Lee, C., Sung, Y.W., and Park, J.W. *J. Phys. Chem. B* **1999,** *103*, 893-898.
12. Salomon, K.; Burgi, D. S.; Helmer, J. C. *J. Chromatogr.* **1991,** *559,* 69-80.
13. VanOrman, B. B.; Liversidge, G. G.; McIntire, G. L.; Olefirowicz, T. M.; Ewing, A. G. *J. Microcol. Sep.* **1990,** *2,* 176-180.
14. Issaq, H. J.; Atamna, I. Z.; Muschik, G. M.; Janini, G. M. *Chromatographia* **1991,** *32,* 155-161.
15. Wright, P. B.; Lister, A. S.; Dorsey, J. G. *Anal.Chem.* **1997**, *69*, 3251-3259.
16. Fujiwara, S., and Honda, S. *Anal. Chem.,* **1987,** *59,* 487-490.
17. Gorse, J., Balchunas, A.T., Swaile, D.F., and Sepaniak, M.J. *J. High Resolut. Chromatogr. Chromatogr. Commun.,* **1988,** *11,* 554-559.
18. Bushey, M.M., and Jorgenson, J.W., *J. Microcol. Sep.,* **1989,** *1,* 125-130.
19. Liu, J., Cobb, K., and Novotny, M. *J. Chromatogr.,* **1988,** *468,* 55-65.
20. Srinivasan, K.; Bartlett, M. G. *Rapid Commun. Mass Spectrom.* **2000**, *14*, 624-632.
21. Kuhn, R.; Hoffstetter-Kuhn, S.; Capillary Electrophoresis: Principles and Practice; Springer-Verlag Berlin Heidelberg: Germany, 1993; Chapter 2.
22. Ahmed, A.; Ibrahim, H.; Pastore, F.; Lloyd, D. K. *Anal. Chem.* **1996**, *68*, 3270-3273.

CHAPTER III: DETERMINATION OF BOND DISSOCIATION ENERGIES USING ELECTROSPRAY TANDEM MASS SPECTROMETRY AND A NOVEL DERIVED EFFECTIVE REACTION PATH LENGTH APPROACH

3.1 Introduction

The measurement of the dissociation of gas-phase complexes by collision-induced dissociation (CID) tandem mass spectrometry has been a useful approach in the study of thermodynamic properties of complexes such as bond dissociation energies. Armentrout and Beauchamp[1] introduced an ion beam apparatus for the study of the bond dissociation energy (BDE) of a cobalt carbene ion, and Armentrout et al. have since refined the measurement of non-covalent, collision-induced threshold bond energies of metal-ligand complexes by mass spectrometry[2-9]. The array of uses of CID tandem mass spectrometry[10] for the measurement of thermodynamic properties of gas-phase complexes includes investigations of bond dissociation energies[11], gas-phase dissociative electron-transfer reactions[12], non-covalent interactions[10,13-15], bond dissociation energies using guided ion beam tandem mass spectrometry[2-9], critical energies for ion dissociation using a quadrupole ion trap[13], or a flowing afterglow-triple quadrupole[14,15], or an electrospray triple quadrupole[16,17], and gas-phase equilibria[18-20].

Electrospray[21-24] is an ionization method that is well known to produce intact gas-phase ions with minimal fragmentation during the ionization process. Thus, studies of gas-phase thermochemical properties of species originating from solution are quite accessible by electrospray mass spectrometry. MALDI is another “soft” ionization approach to gas-phase ionic complex analysis, but the complex’s character in the solution phase can be lost during crystallization with the matrix. However, Gidden et al.[25] derived experimental cross sections for a set of alkali metal ion cationized poly(ethylene terephthalate) (PET) oligimers using a MALDI ion source coupled to a hybrid mass spectrometer.

In this paper, we report on a mass spectrometry study of bond dissociation energies of alkali metal (Li^+) adducts, and halide (Cl^-) adducts, of monoacylglycerol, 1,2-diacylglycerol, and 1,3-diacylglycerol lipids. The energies required for the dissociation of one acylglyceride from lithium-bound dimers of monoacylglycerol, 1,2-diacylglycerol, and 1,3-diacylglycerol, were also studied. The specific use of lithium adducts for ionization and structural analysis has been reported for fast atom bombardment (FAB) of aryl 1,2-diols[26] and fatty acids[27], and ES determinations of triacylglycerides[28,29], and di- and tri-oligosaccharides[30-33]. Chloride ion has also been reported to form adducts of diacylglycerols in liquid chromatography-negative chemical ionization mass spectrometry[34,35], and its adducts have been used for structural elucidation employing ES-tandem mass spectrometry[36-39].

In this work, all bond dissociation energies were measured using a "triple quadrupole" (actually QhQ = quadrupole-hexapole-quadrupole) mass spectrometer using electrospray as the ionization method. A new approach to the measurement of the dissociation of an alkali metal ion, or a halide ion from ionic adducts of intermediate molecular weight lipids (316 Da to 596 Da) has been developed. An analogous model (differing only in input parameters used for regression) to predict bond dissociation energies for low molecular weight cationic adducts such as CH_3OHLi^+, $C_2H_5OHLi^+$, $ACNLi^+$, $CH_3OCH_3Li^+$, etc., is also presented. The results obtained from the mass spectrometry experiments were compared to both literature BDE values (when available), and to computer generated BDE's employing the Becke-style 3-Parameter Density Functional Theory (B3LYP, using the Lee-Yang-Parr correlation functional, at the 6-31G* level)[40]. The newly developed method does not require extensive calculations of degrees of freedom, vibrational states, etc., which can be cumbersome for very high molecular weight systems. It has been demonstrated to be applicable over a wide range of m/z values of the employed triple quadrupole, i.e. from the detection of the lithium ion at m/z 7, up to the 1-stearin-2-palmitin diacylglycerol lithium-bound dimer ion at m/z 1199.

3.2 Experimental

Mass spectra were obtained using a "triple quadrupole" (actually quadrupole-hexapole-quadrupole, QhQ) mass spectrometer (Quattro II, Micromass, Inc., Manchester, UK) equipped with an electrospray source operating at solution flow rates of 2-4 μL/min. Nitrogen was used as both nebulizing and drying gas. Cone voltages were 18 V for the low molecular weight lithium-solvent adducts, and 40 V for lithium adducts of the higher molecular weight lipids. The ES capillary voltage was set at 2.5 to 3.5 kV. Argon was used as collision gas during CID experiments at pressures of approximately 1.3×10^{-4} mBar (measured externally to the central hexapole collision cell) for single collision measurements. The hexapole offset energy values range from 0 eV up to 250 eV with a minimum increment of 1.0 eV. MassLynx software (Micromass) was used to acquire, process, and store mass spectral data.

3.3 Results and Discussion

3.3.1 Measurement of Collision Cell Path Length

In calculating thermochemical values such as the bond dissociation energy for a gas-phase ionic complex by CID tandem mass spectrometry, the collision cell path length, or the mean free path of reaction, are most often unknown. One approach to estimating this collision path length would be to interject guesses into data reduction equations to iteratively test which value results in a best fit. Chen et al[41] presented a new model for determining bond energies for holomyoglobin noncovalent gas-phase complexes where the collision cell path length is described as the average distance that ions travel before dissociating. In their method, estimated values for the path length were iteratively used until a realistic fit was obtained. A second approach would be to employ the actual measured dimensions of the gas cell, e.g., the central hexapole. This is essentially the method used by Ervin et al.[2], where the dimensions of their gas cell are well-defined, but they also take into account the pressure profile of the collision gas within the system to derive an effective cell length. The approach taken in our new method is to measure the dissociation of standards with known BDE values to obtain I_P/I_0 values which then can be related to the reaction path length according to the thin target limit equation[2]:

$$I_P/I_0 = I_P/(I_R + \sum I_P) = \sigma_P n \ell \qquad (1)$$

where I_P is the transmitted product ion signal intensity, I_R is the transmitted reactant ion signal intensity, I_0 is the incident ion signal intensity, σ_P is the product cross section (cm^2), n is the number gas density (cm^{-3}), and ℓ is the collision cell path length (cm). In this approach, it is assumed that the sum of the transmitted product peak intensities is equal to the incident reactant ion peak intensity; the latter in actuality, is not readily measurable. Therefore, a "derived effective reaction path length" is being obtained from the measurement of known standards. At the thin target limit, the effective path length represents the average distance that the complex travels before dissociation takes place (or the average distance of travel before one collision resulting in dissociation occurs). According to the thin target limit (eq 1), the slope of a plot of the $I_P/(I_R + \sum I_P)$ ratio, versus number gas density, is related to the collision cross section[2]. The number gas density, n, is calculated according to the ideal gas law[42]:

$$n = PL/RT = P/k_B \alpha T \qquad (2)$$

where P is the pressure in atm, k_B is the Boltzmann constant, α is a conversion factor of 9.869 $cm^3 atm/J$, and T is the temperature in kelvin. Figure 3.1 displays mass spectra obtained from lithium adducts of methanol, used as a standard for effective reaction path length determination, and it depicts the emergence of the dissociation of the lithium cation from the precursor adduct. For bond dissociation energy calculations, the supplied energy for the collision is converted from the laboratory frame of reference to the center-of-mass frame of reference according to $E_{COM} = E_{LAB}(m/(m + M))$, where E_{LAB} is the selected value of the offset for the central hexapole, m is the mass of the stationary target Ar atom, and M is the mass of the precursor ion. Figure 3.1a shows the measurement of the incident lithium adduct ion without the detection of the lithium cation at 0 eV offset value for the central hexapole. Figure 3.1b shows the emergence of the dissociated lithium cation, at m/z 7, from the precursor methanol/lithium adduct at an offset value = 0.50 eV (center-of-mass frame of reference, E_{COM}) for the central hexapole. This illustrates that the initial dissociation of the adduct can be measured, but the spectra indicate an earlier threshold energy value than what is expected from the known BDE of 1.596 eV[9]. Figure 3.1c is the spectrum acquired at a 1.01 eV E_{COM} offset for the central hexapole. The ratio of the intensities of the lithium cation peak to the precursor peak at 0.5 eV is 8.0×10^{-5}, while at 1.0 eV the ratio is 2.5×10^{-4}, demonstrating that the employed triple quadrupole possesses the required sensitivity to perform gas-phase thermochemical bond dissociation energy measurements.

Figure 3.2a is a graph of the $I_P/(I_R + \sum I_P)$ ratio versus number gas density for a dimethyl sulfoxide (DMSO) lithium adduct standard. The values in the graph were obtained by acquiring product ion mass spectra from CID of the DMSO lithium adduct at fixed collision energy (E_{LAB} = 10 eV) but increasing gas cell pressures; the latter equates to an increasing number gas density of argon. The “zero point” collision cell gas pressure corresponds to the pressure measured in

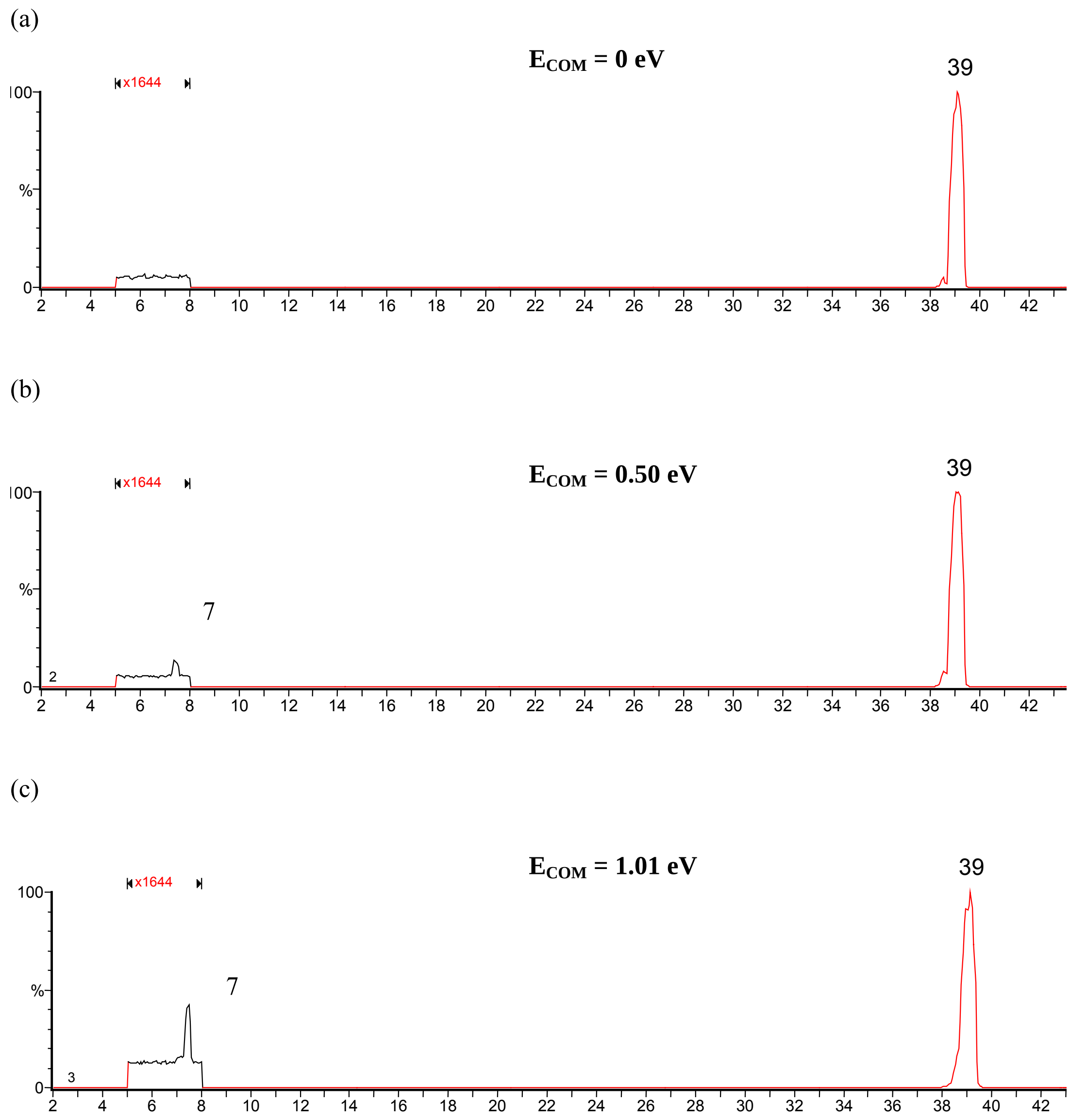

Figure 3.1. CID product ion mass spectra of the lithium adduct of methanol (m/z 39) illustrating the appearance of the dissociation of the lithium cation (m/z 7, BDE = 1.596 eV[12]). (a) 0 eV, no detection of lithium, (b) emergence of the dissociated lithium cation at 0.50 eV (E_{COM}), and (c) 1.01 eV (E_{COM}).

the analyzer in the absence of argon, i.e., 7 - 8 x 10^{-6} mbar (1.7 - 1.9 x 10^{11} cm^{-3}, expressed as number gas density), representing a very small probability for collisions with nitrogen or other ambient gas. The slope of the curve in Figure 3.2a, which is related to the product cross section according to the thin target limit (eq 1)[2] as slope = $\sigma_P \ell$, can be extracted from the plot and then used to calculate the cross sections of the DMSO lithium adducts, and estimate ℓ of the QhQ mass spectrometer. For the initial cross section calculations using the thin target limit ratio relationship σ_P = slope/ℓ, we assign ℓ = 1 cm. This assignment allows the simplifying approximation that σ_P = slope, but also necessitates a subsequent correction of the derived reaction path length, i.e., actual length ℓ = 1 cm + correction. Figure 3.2b is a plot of the $I_P/(I_R + \sum I_P)$ ratio versus E_{COM} for CID of the DMSO lithium adduct, at a fixed collision gas pressure of 1.3 x 10^{-4} mBar (number gas density of 3.14 x 10^{12} cm^{-3}). The $I_P/(I_R + \sum I_P)$ ratio is directly related to the cross section according to the thin target limit (eq 1). Therefore, it is assumed that at constant n and ℓ values, the change in the $I_P/(I_R + \sum I_P)$ ratio will be directly proportional to the change in the cross section. From this assumption arises the basic premise of our method, i.e., the magnitude in the change of the $I_P/(I_R + \sum I_P)$ ratio can be used to predict the subsequent decreasing cross sections, from the initial number gas density determined cross section, for decreasing energies in the center-of-mass frame of reference.

Figure 3.2c shows the derived cross sections for the DMSO lithium adduct. Figure 3.2c is generated by first evaluating the cross section from the number gas density plot of Figure 3.2a obtained at the highest collision energy (E_{LAB} = 10 eV) where the S/N of the product ion is maximized. Then, each subsequent energy cross section at progressively lower energies is calculated relative to this initial point, according to the magnitude of the change in the ratios given in Figure 3.2b. The reference BDE value for the DMSO lithium adduct is 2.36 eV[43].

Taking this literature BDE value, the best fit of Figure 3.2b gives an $I_P/(I_R + \sum I_P)$ ratio of 1.879 x 10^{-3}, at a number gas density of 3.14 x 10^{12}. The best fit of Figure 3.2c gives a cross section value of 2.878 x 10^{-16} cm^2, at 2.36 eV, and number gas density of 3.14 x 10^{12}. These three values, the number gas density of 3.14 x 10^{12}, the $I_P/(I_R + \sum I_P)$ ratio of 1.879 x 10^{-3}, and the cross section of 2.878 x 10^{-16} cm^2, can then be used to calculate an experimentally derived corrected effective reaction path length (initially set at 1 cm) using the thin target limit relationship, namely ℓ = 2.08 cm (see Appendix 1 for example calculations). This approach was also used with lithium adducts of MeOH, DMF, and ACN to calculate an average effective reaction path length of 1.95 ± 0.56 cm (using 7 individual determinations). This experimentally derived effective reaction path length value was then used in all subsequent cross section calculations and ensuing BDE evaluations.

3.3.2 Theoretical Calculation of BDE and Optimized Structures

There are now numerous bond dissociation energy values in the literature for many small compounds that are adducted to lithium ion (ranging anywhere from 4 up to 30 atoms), but not larger compounds such as the lipids which are described here (ranging from 40 to 119 atoms). With no literature values available, in order to determine whether reasonable bond energy values were obtained for the unknown lipids using the triple quadrupole mass spectrometer, theoretical bond energy values were calculated using Becke-style 3-Parameter Density Functional Theory computational methods (B3LYP, using the Lee-Yang-Parr correlation functional, at the 6-31G* level). The computer modeling experiment consists of minimizing the potential energy of a lithium-lipid adduct structure, and then sequentially altering the lithium ion distance to the lipid

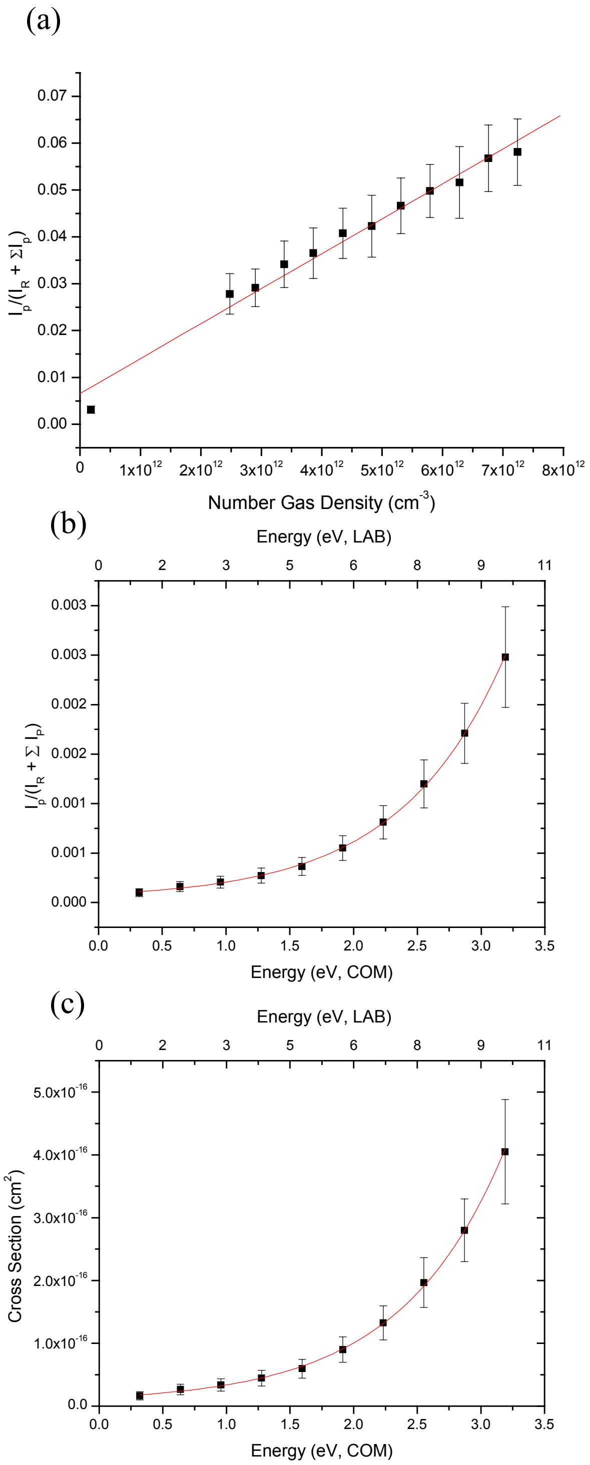

Figure 3.2. (a) Ratio of product ion abundances to incident ion abundances (the latter is approximated by ($I_R + \sum I_P$)), versus number gas density for the lithium adduct of DMSO at constant collision energy (E_{LAB} = 10 eV). The slope of the curve is related to the product cross section (σ_P) of the lithium-DMSO cationic complex according to the thin target limit as σ_P =

slope/ℓ, (b) plotted results of $I_P/(I_R + \sum I_P)$ ratio versus collision energy (E_{LAB}, top) (E_{COM}, bottom) for the dissociation of the DMSO-lithium adduct. The best fit gives an $I_P/(I_R + \sum I_P)$ ratio of 1.879×10^{-3}, at 2.36 eV[42], and a number gas density of 3.14×10^{12}, used in calculating a derived effective reaction path length, and (c) calculated cross sections for the DMSO-lithium cationic adduct employing the σ_P = slope/ℓ relationship from Figure 3.2a and the proportional changes of the $I_P/(I_R + \sum I_P)$ ratios with collision energy in Figure 3.2b. Using the 2.36 eV BDE value, the best fit of Fig. 3.2c gives a cross section value of 2.878×10^{-16} cm^2 and, by the thin target limit relationship, a path length of $\ell = 2.08$ cm.

(i.e., assigning incrementally larger distances to the nearest neighboring atom via increases in the "R" parameter of Gaussian 98[40]) while performing potential energy surface scans of the adduct complex at each step. The obtained potential energies are plotted versus distance, and the electrostatic bond dissociation energy can be calculated from the difference between the potential energy obtained at the minimum, and the potential energy at complete dissociation, i.e., where the charge on the lithium has reached +1 and does not change. Figure 3.3a illustrates an optimized structure, and a plot of the potential energy surface scans versus distance for the orientation is found for the lithium adduct of 1,3-dipentadecanoin, where the lithium cation has oriented itself between the two carbonyl oxygens, and the oxygen atom of the hydroxyl group. The distance between the lithium cation and the hydroxyl oxygen is 2.01 angstroms, and the distance between the lithium cation and the two carbonyl oxygens is 1.88 and 2.00 angstroms. For the lithium adduct of 1-stearin-2-palmitin diacylglycerol, the lithium cation was also found to orient itself between the two carbonyl oxygens of the 1- and 2-position fatty acyl chains and the oxygen of the hydroxyl group. The distance between the lithium cation and the hydroxyl oxygen is 1.97 angstroms, whereas the distance between the lithium cation and the two carbonyl oxygens is 1.88 and 2.04 angstroms.

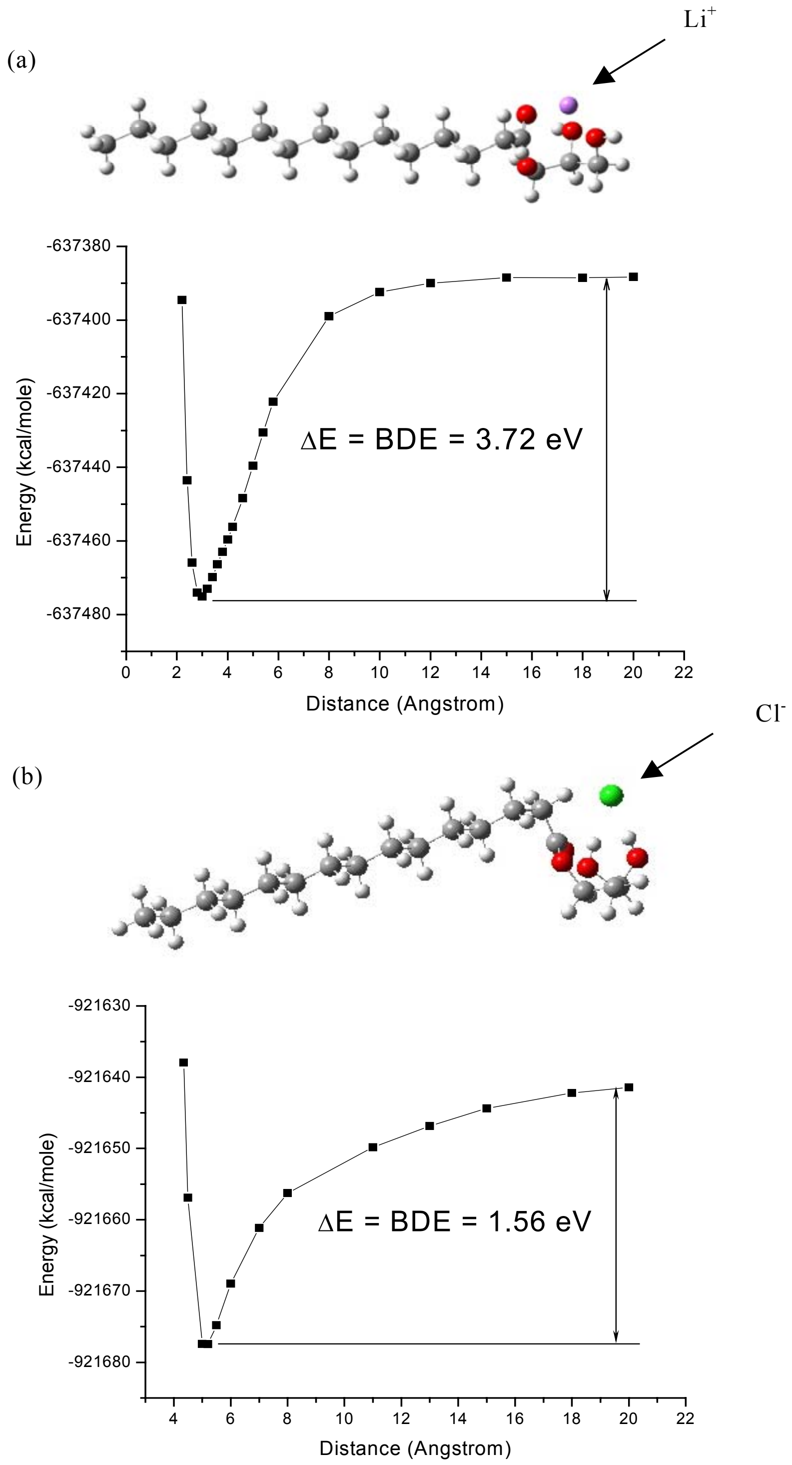

Figure 3.3. Optimized structures and computer modeling results for the theoretical determination of the electrostatic bond dissociation energies for: (a) The monopentadecanoin lithium adduct. The lithium cation is initially located between the carbonyl oxygen at a distance of 1.86 angstroms, and the 1-position hydroxyl oxygen at 1.96 angstroms. The distance to the 2-position hydroxyl oxygen is 1.92 angstroms. The bond dissociation energy value is extracted as the difference in the energy from the minimum of the potential well, to the electrostatic bond

distance where the charge has reached unity for the adducted ion. The BDE was calculated to be 3.72 eV. (b) The monopentadecanoin chloride adduct. The chloride anion is between the 1-position and 2-position hydoxyl hydrogens, each at a distance of 2.18 angstroms. The BDE was calculated to be 1.56 eV.

The same approach was used for calculating the bond dissociation energies for chloride adducts of the lipids: Figure 3.3b illustrates an optimized structure, and a plot of the potential energy surface scans versus bond distance for the chloride adduct of monopentadecanoin. The chloride anion is situated nearest to the 1-position and 2-position hydroxyl hydrogens at distances of 2.18 angstroms and 2.18 angstroms, respectively, as would be expected due to their higher acidities (more electropositive hydrogens) as compared to hydrocarbon hydrogen atoms. Orientation of the chloride ion in close proximity to the lone hydroxyl hydrogen is found for the optimized structures of the 1,2- and 1,3-diacylglycerols. For the 1,2-diacylglycerol-chloride adduct, the distance between the hydroxyl hydrogen and the chloride ion is 2.09 angstroms, while for the 1,3-diacylglycerol, the distance is 2.07 angstroms.

3.3.3 Mass Spectral Determination of Li^+ and Cl^- Lipid Adduct BDE's

The first electrostatic complex that was measured using the newly proposed derived effective path length approach was the cationic lithium adduct of monopentadecanoin. In order to determine the thresholds for the endothermic CID reaction:

$$M^{+}L \xrightarrow{\text{Ar (gas)}} M^{+} + L \tag{3}$$

where M is the metal cation, L is the lipid, and Ar is the stationary target gas, the free metal cation M^+ (m/z 7) and the precursor ion M^+L (m/z 323) signals are measured at increasing collision energies, as are all other products formed via CID. Figure 3.4 shows the emergence of the lithium cation (m/z 7) near the threshold energy for eq 3. Figure 3.4a is the CID product ion mass spectrum obtained at 2.75 eV (E_{COM}), where the lithium metal cation is present only at noise level (S/N = 2). In Figure 3.4b, a significant peak at m/z 7 has emerged for the lithium cation (S/N = 6) at 3.30 eV (E_{COM}) indicating that the threshold energy for eq 3 has been acheived. The bond dissociation energy value for the lithium-monopentadecanoin adduct calculated from the computer modeling results illustrated in Fig. 3.3a was 3.72 eV. This gives a threshold energy value that is just below the E_{COM} value of 3.85 eV that was used to obtain the CID product ion spectrum shown in Fig 3.4c.

The appearance of decomposition products at an energy lower than the threshold energy for dissociation as calculated by computer modeling can be the result of a combination of factors which contribute to error in the direct measurement of a threshold energy value for eq 3. The magnitude of uncertainty in potential energy calculations at the B3LYP 6-31G* level has been estimated to be 3.9 kcal•mol^{-1}, or 0.17 eV[44] (mean absolute deviation).

Uncertainty in mass spectrometrically estimating dissociation energies has been attributed to: (1) initial internal energy content which may lead to metastable decompositions (resulting in underestimation of BDE's), (2) non-neglible translational energy at 0 eV (E_{LAB}) collision energy (underestimation of BDE's)[15,16], (3) collisions outside of the reaction cell (e.g., in Q_1)[15,16] (underestimation of BDE's), (4) instrumental bias against observation of "slow kinetics" reactions (overestimation of BDE's)[45], and (5) deposition of energy in competitive vibrational excitation modes (overestimation of BDE's)[46]. Some competitive fragmentation reactions were observed in most of the product ion mass spectra, as illustrated in Figure 3.5. Figure 3.5a is the CID spectrum obtained for the decomposition of lithium adducts in the reaction threshold range at 3.85 eV (E_{COM}), illustrating a small contribution to the relative error in the measurement of the BDE if only the intensity of the lithium cation is used as $\sum I_p$ instead of using the actual sum of the products as $\sum I_P$ in calculating $I_0 = I_R + \sum I_P$. If the intensities of the "extraneous" products are much smaller than the precursor, then the product ion intensities that are not being monitored can be neglected when applying eq 1[2]. However, in this study it

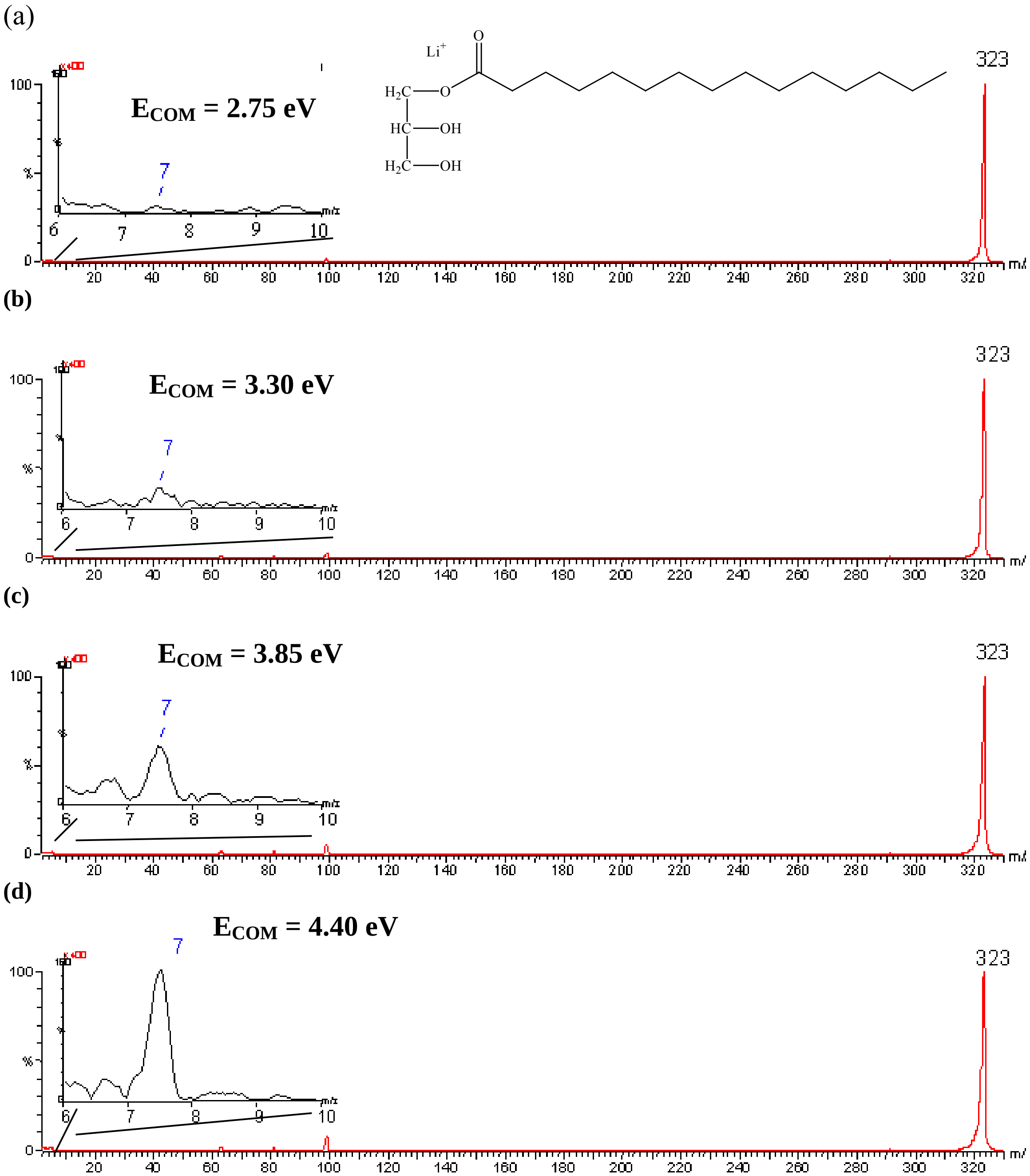

Figure 3.4. Product ion mass spectra illustrating the appearance of the lithium cation upon CID of the lithium-monopentadecanoin adduct near the threshold energy for dissociation. E_{COM} energies: (a) 2.75 eV, (b) 3.30 eV, (c) 3.85 eV, threshold area, and (d) 4.40 eV.

was observed that many of the lipids yielded other CID fragment ions, in addition to the loss of the lithium cation, at abundances that could not be considered much smaller than the precursor. Therefore, in evaluating cross sections for each precursor adduct displayed in Fig. 3.5, product ion abundances for all fragmentation pathways were summed along with the transmitted precursor abundance when applying eq 1.

Figure 3.5b is the product ion spectrum of the Li^+ adduct of another lipid, i.e., 1-stearin,2-palmitin diacylglycerol at 3.10 eV (E_{COM}). The spectrum shows a considerable number of lower abundance products formed during CID, in addition to the lithium cation. Figure 3.5c also shows product ions in addition to the lithium cation for the CID of a third lipid, 1,3-dipentadeacoin lipid, at 3.74 eV (E_{COM}). In both the chloride adduct studies and the dimer dissociation studies, competitive product fragment ions were not observed and posed no problem as contributors to error in estimating I_0. Furthermore, the use of electrospray as the ionization method helps to reduce error, as only a minimal amount of internal energy is imparted to the complex during ionization, owing to the soft nature of the ES process (no physically imparted desorption/ionization energy such as laser flux or heat in MALDI). In addition, cooling collisions in the source region, and relaxation of the complex through the desolvation process, help to dissipate the low amount of internal energy initially present.

According to the simplified version of Rice-Ramsperger-Kassel-Marcus (RRKM) theory[47], the rate of a unimolecular decomposition is approximated by:

$$k(E) = \nu(E - E_0/E)^{n-1} \qquad (4)$$

where n is the number of vibrational degrees of freedom, ν is the frequency factor, E is the kinetic energy, and E_0 is the threshold energy for reaction. Eq 4 is directly related to the

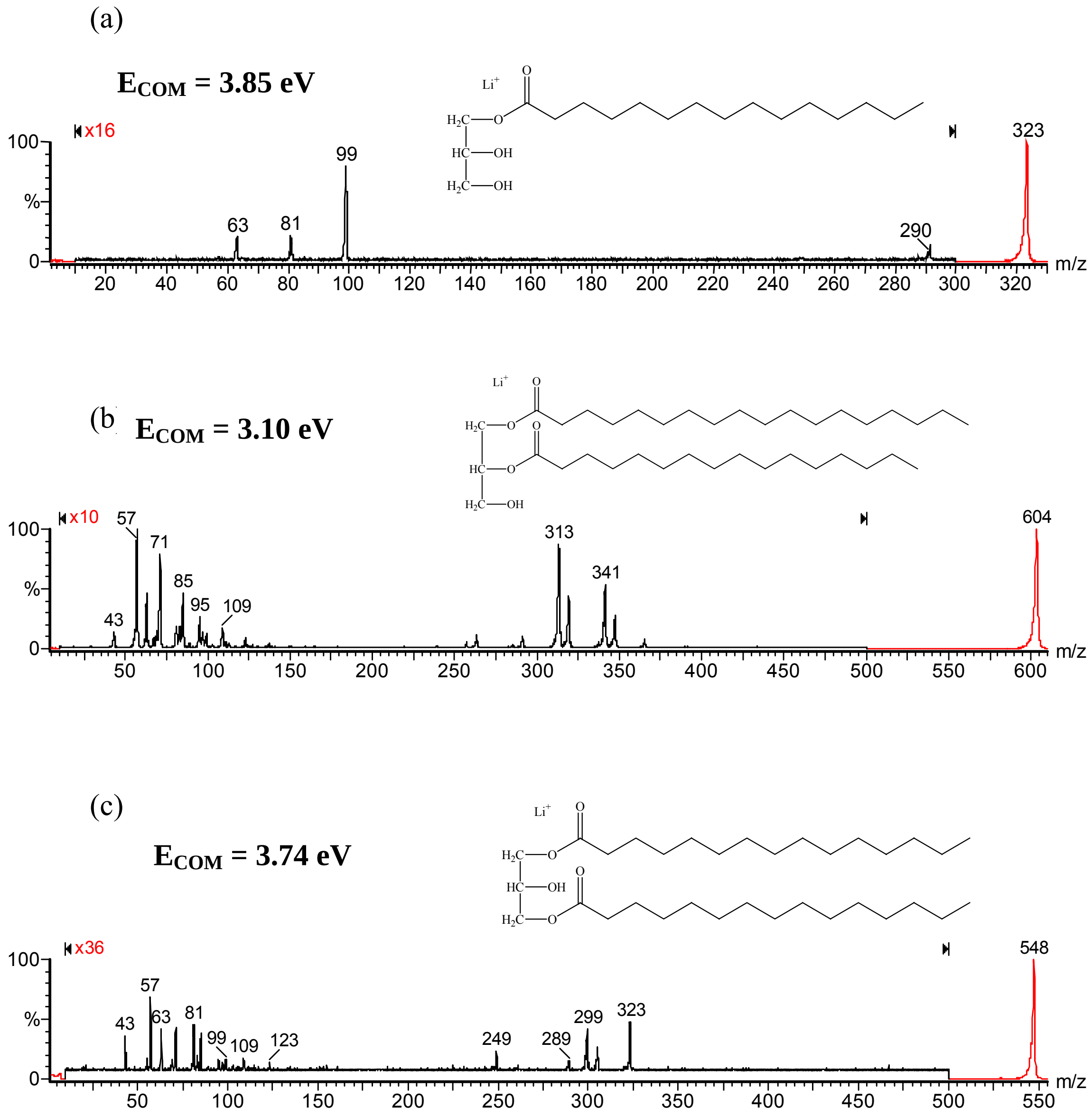

Figure 3.5. Competitive fragmentation reactions in CID of product ion mass spectra of lithium-lipid adducts illustrating a contribution to error in the measurement of BDE's. (a) Lithium adduct of monopentadecanoin in the reaction threshold range (3.85 eV E_{COM}). (b) Lithium adduct of 1-stearin,2-palmitin diacylglycerol at 3.10 eV (E_{COM}). (c) Lithium adduct of 1,3-dipentadeacoin at 3.74 eV (E_{COM}). All three show a considerable array of fragmentation products.

activated complex's populated energy states. The theoretically derived mathematical function used to obtain a best fit of the experimentally determined cross sections, according to the transient energy states of the decomposing ion at the time of the dissociating collision is[1,9]:

$$\sigma(E) = \sigma_0 \sum g_i (E + E_i - E_0)^n / E^m \qquad (5)$$

where E and E_0 remain as above, E_i represents the individual reactant states (electronic, rotational and vibrational) with populations g_i, σ_0 is a scaling factor, and n and m are adjustable parameters. According to the thin target limit relationship of the reaction cross sections (σ_p) to the measured intensities in eq 1, the cross sections for the determination of the threshold energy for eq 3 can be calculated for each of the lithium adducts in Figs. 3.5a, b, and c. Figure 3.6a shows the results of these cross section calculations at increasing collision energies, covering an activation energy range approximately three times that of the threshold energy region, for decompositions of the lithium adduct of monopentadecanoin. The cross sections (right axis) are related to the ratio of abundances of the product ions over all ions (left axis) through eq 1. Consistent with the mathematical forms of equations 4 and 5, curve fitting of the cross sections obtained from the mass spectrometric measurements of the BDE's for the lithium-monopentadecanoin electrostatic adduct, as well as all the other adducts measured, was empirically observed to fit an exponential growth equation of the following form:

$$\sigma_P(E) = \sigma_0 \exp(E_{COM}/\alpha) + y_0 \qquad (6)$$

where $\sigma_P(E)$ is the experimentally determined cross section in cm^2, $\sigma_0 + y_0$ is the y-intercept of the fit in cm^2 (for multivariate regression, y_0 is insignificant enough to be neglected, see *multivariate regression bond energy prediction* section below). This equation effectively relates the product cross section to the system energy (supplied by the central hexapole offset) in the center-of-mass frame of reference. The suitability of a *single* exponential equation is serendipitous in that the ensuing multivariate regression entails fewer independent variables (as compared to higher order equations), allowing relative ease in deriving the polynomial equation used to estimate BDE values. The solid line in Figure 3.6a shows the fit of the experimentally determined cross sections in the threshold region of the dissociation of the lithium-monopentadecanoin adduct, calculated using eq 6. Figure 3.6b shows the results of single exponential curve fitting of the cross section vs energy for the chloride adduct of monopentadecanoin. Analogous calculations were made for the other two lipids, i.e., the diacylglycerols 1-stearin,2-palmitin diacylglycerol, and 1,3-dipentadecanoin introduced in Figs. 3.5b and 3.5c, respectively. Figure 3.7a shows the cross sections for the lithium adduct of 1-stearin,2-palmitin diacylglycerol, and Figure 3.7b is a plot of the cross sections for the chloride adduct of 1-stearin,2-palmitin diacylglycerol, each versus collision energy. Figures 3.8a and 3.8b are plots of the cross sections versus collision energy for the lithium and chloride adducts, respectively, of 1,3-dipentadecanoin diacylglycerol. The curves shown in Figs. 3.6-3.8 will be used to apply the derived effective reaction path length method to deduce BDE values for each compound in the following section.

3.3.4 MULTIPLE REGRESSION MODEL FOR PREDICTING BDE's

3.3.4.1 High molecular weight BDE predictive model

The general multivariate growth curve model (GCM-Polynomial Regression)[48] was used to create a predictive model for bond dissociation energies involving the relatively high molecular weight lipid standards, using the cross section results obtained for the ES triple quadrupole mass spectrometer. Single exponential cross section vs energy curves, derived as

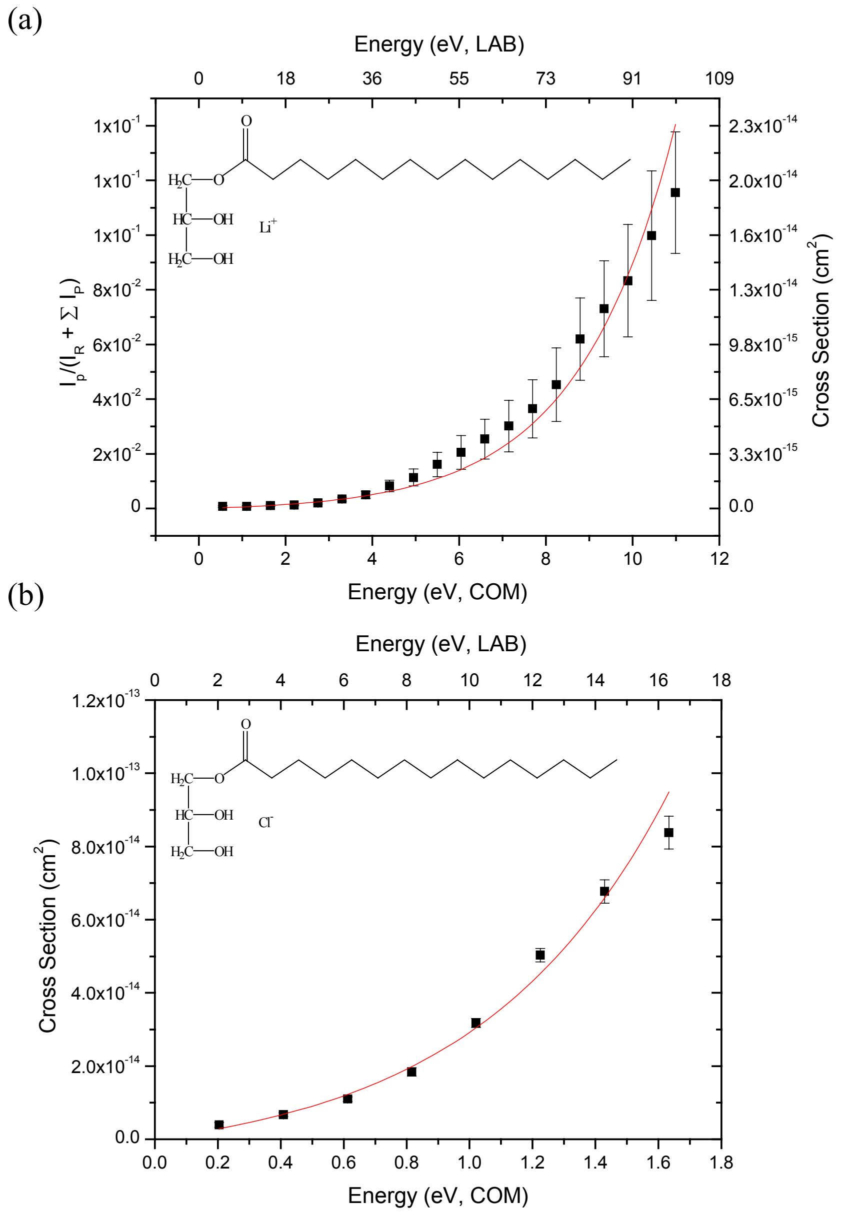

Figure 3.6. (a) Plot of the ratio of abundances of the dissociated lithium cation to the total product ions ($I_P/(I_R + \sum I_P)$, left y-axis) in an energy range that is approximately 3 times greater than the expected dissociation threshold energy of 3.72 eV predicted by computer modeling. The reaction cross sections for the lithium adduct of monopentadecanoin, illustrated on the right y-axis, are calculated from the experimentally obtained ratios according to eq 1. The solid line is the best-fit of the experimental data using eq 6. The bond dissociation energy for CID of the lithium cation was experimentally determined to be 3.69 ± 0.29 eV (E_{COM}). The theoretical value was calculated to be 3.72 eV. (b) Cross sections of the chloride adduct of monopentadecanoin. The bond dissociation energy was experimentally determined to be 1.65 ± 0.05 eV (E_{COM}) for CID of the chloride anion. The theoretical value was calculated to be 1.56 eV.

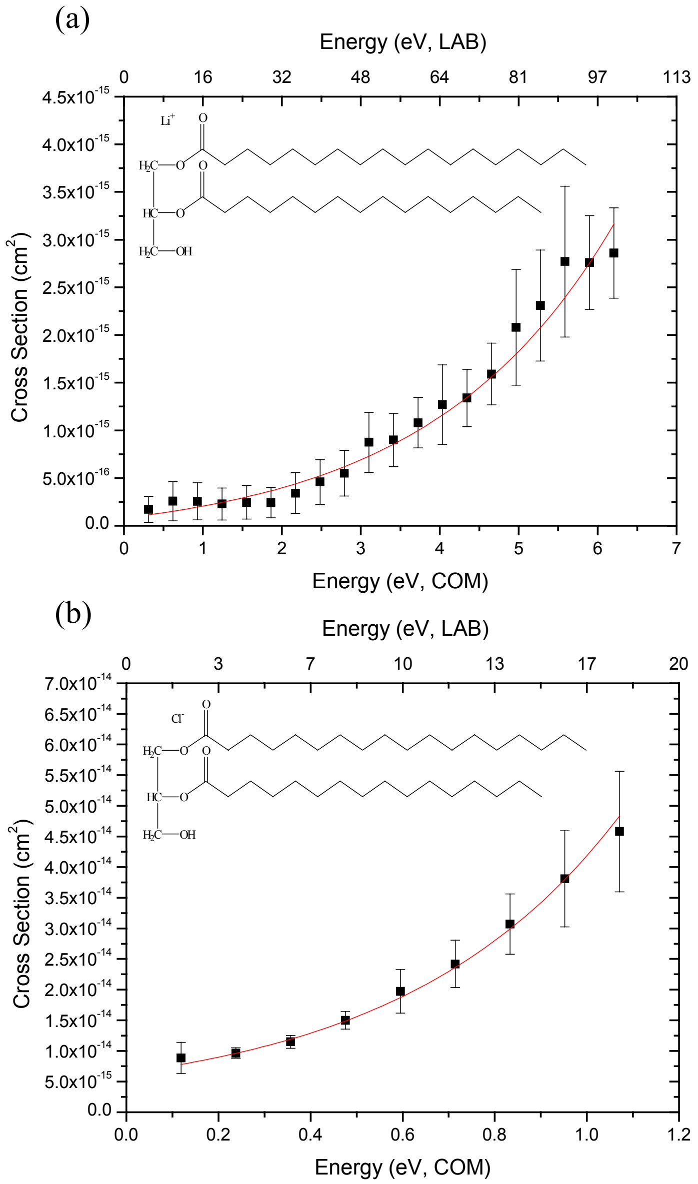

Figure 3.7. Cross section vs collision energy for: (a) the lithium adduct of 1-stearin,2-palmitin diacylglycerol, with a growth curve model predicted BDE of 3.59 ± 0.18 eV (theoretical predicted value: 3.98 eV), (b) the chloride adduct of 1-stearin,2-palmitin diacylglycerol, with a growth curve predicted BDE of 1.26 ± 0.03 eV (theoretical predicted value: 1.37 eV).

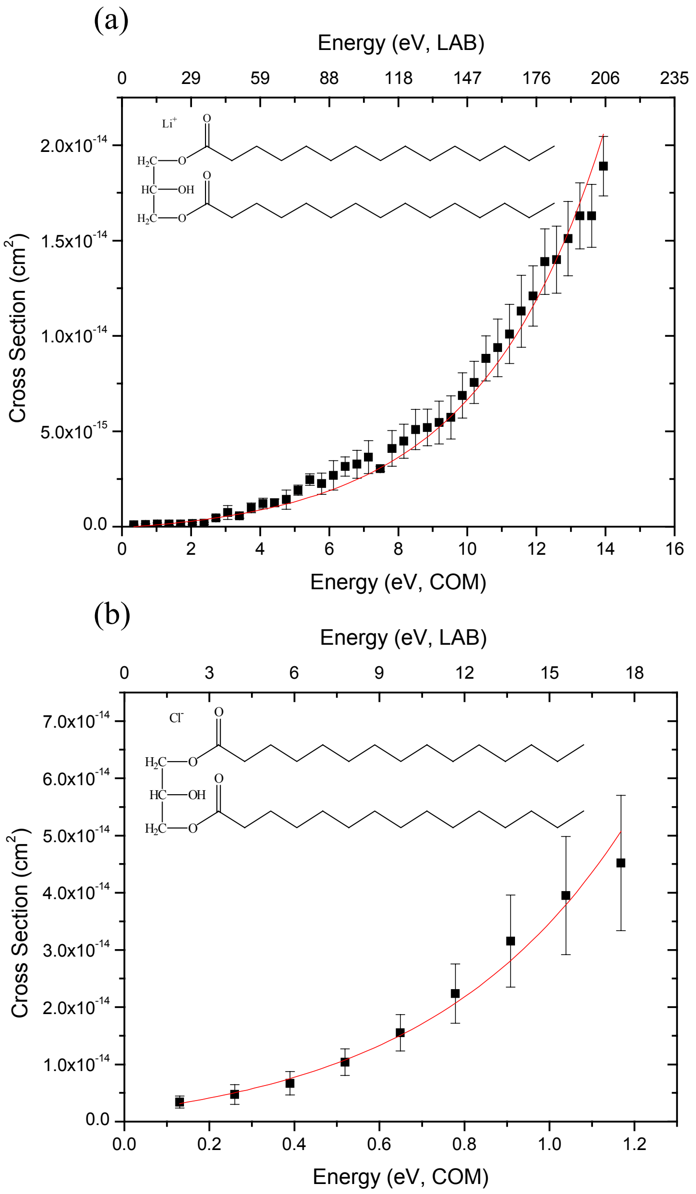

Figure 3.8. Cross section vs collision energy for: (a) the lithium adduct of 1,3-dipentadecanoin diacylglycerol, with a growth curve model predicted BDE of 3.78 ± 0.39 eV (theoretical predicted value: 3.52 eV), (b) the chloride adduct of 1,3-dipentadecanoin diacylglycerol, with a growth curve predicted BDE of 1.63 ± 0.23 eV (theoretical predicted value: 1.48 eV).

outlined in the previous section for each lithium and chloride adduct of the monopentadecanoin, dipentadecanoin, and 1-stearin,2-palmitin diacylglycerol standards, were used to create a multivariate curve polynomial expression that can be used to calculate BDE values for unknown complexes. To create the polynomial expression, the independent parameters of eq 6, σ_0 and α, are regressed with the dependent variable represented by the BDE values (obtained from DFT computational methods) for each experimentally evaluated complex that had generated a single exponential cross section vs energy curve. Analysis of the variance gave an adjusted regression factor of 0.928, and a probability factor of < 0.0001, demonstrating the statistical significance of the multivariate growth curve model. The model resulted in the following general second order polynomial descriptive equation that was subsequently used to predict the bond dissociation energies of the higher molecular weight (e.g., m/z 300 to 700) adducts:

$$\mathrm{BDE\ (eV)} = 0.78051 - 1.7180\mathrm{x}10^{13}\sigma_0 + 1.4627\alpha - 0.16327\alpha^2 \qquad (7)$$

To use this equation to predict a BDE for an unknown complex, it is first necessary to generate a single exponential cross section vs energy curve that will provide values for the σ_0 and α parameters. Table 3.1 is a compilation of the results obtained from the newly developed single exponential cross section vs energy method, juxtaposed against the theoretical computer modeling method, and where applicable, the "50% dissociation of dimers" method (see "*Mass Spectral Determination of Li^+ Lipid Dimer Adduct BDE's*" section below). Also included in the table are the theoretical charges and closest electrostatic bond distances of either the lithium ion, or the chloride ion, for the computationally optimized structures of the complexes. The cationic lithium adducts, the anionic chloride adducts, and the dimers are relatively large systems, spanning molecular weights from 323 Da to 603 Da, that contain substantial numbers of vibrational degrees of freedom. This is reflected in the magnitude of observed coefficients of variation (CV) for the studied systems such as 7.6% for the lithium adduct of monopentadecanoin, 10.5% for the lithium adduct of dipentadecanoin diacylglycerol, and 4.8% for the lithium adduct of 1-stearin,2-palmitin diacylglycerol. Overall, excellent agreement is observed between the theoretical BDE's obtained from computational molecular modeling, and those obtained by the multivariate growth curve fitting method using one second order polynomial (eq 7) to evaluate all three types of complexes (Table 3.1). The relative uncertainty of the experimentally determined bond dissociation energies using this method is approximated to be ± 7%, while absolute uncertainties are estimated to range between 10 and 20%. Rodgers et al.[8], reported cross section absolute uncertainties of ± 20%, and relative uncertainties of ± 5% for their guided ion beam mass spectrometer. The variation in their cross section measurements was attributed to errors in gas cell pressure measurements, and errors in estimating interaction region lengths. In the method reported here, gas cell pressure uncertainty still exists, but the calculation of an effective reaction path length is believed to reduce the magnitude of the path length error's contribution to uncertainty in BDE estimations.

3.3.4.2 Low molecular weight BDE predictive model

The general multivariate growth curve model (GCM-Polynomial Regression) was used to evaluate bond dissociation energies of adducts of relatively low molecular weight solvent standards, using the ES triple quadrupole mass spectrometer cross section results according to the procedure outlined above. It was found that the regression and probability factors were much improved when high molecular weight compounds were regressed separately from low molecular weight compounds. For this reason, a separate general second order polynomial

Adduct	Theoretical BDE (eV)	Measured BDE (eV)	Charge on Li$^+$ or Cl$^-$	Electrostatic bond Distance of Li$^+$ or Cl$^-$ (angstroms)
Li$^+$ monopentadecanoin	3.72	3.69 ± 0.29	+0.628	1.9
Cl$^-$ monopentadecanoin	1.56	1.65 ± 0.05	-0.777	2.2
Li$^+$ monopentadecanoin Dimer	NA[c]	1.43 ± 0.04 (exp)[a] or 1.31 ± 0.32 (50%)[b]	+0.527	NA[c]
Li$^+$ 1,3-dipentadecanoin	3.52	3.78 ± 0.39	+0.669	1.9
Cl$^-$ 1,3-dipentadecanoin	1.48	1.63 ± 0.23	-0.845	2.1
Li$^+$ 1,3-dipentadecanoin Dimer	NA[c]	1.43 ± 0.01 (exp)[a] or 0.90 ± 0.09 (50%)[b]	+0.595	NA[c]
Li$^+$ 1-stearin-2-palmitin glycerol	3.98	3.59 ± 0.18	+0.579	1.9
Cl$^-$ 1-stearin-2-palmitin glycerol	1.37	1.26 ± 0.03	-0.836	2.1
Li$^+$ 1-stearin-2-palmitin glycerol Dimer	NA[c]	1.38 ± 0.01 (exp)[a] or 1.16 ± 0.07 (50%)[b]	NA[c]	NA[c]

[a] Experimental BDE obtained from the newly developed single exponential cross section vs energy method.

[b] Experimental BDE obtained from 50% dissociation as illustrated in Figure 3.10.

[c] NA: Not analyzed, computational BDE not reported.

Table 3.1. Calculated (theoretical) BDE values, charges on Li$^+$ or Cl$^-$, and distances obtained using the Becke-style 3-Parameter Density Functional Theory. The measured BDE values were extracted from the plotted results of cross sections versus center-of-mass energies, obtained by tandem mass spectrometry.

descriptive equation was used to predict the bond dissociation energies of the low molecular weight (e.g., m/z 30-100) adducts:

$$\text{BDE (eV)} = -4.22589 - 9.83647\text{x}10^{15}*\sigma_0 + 14.3319*\alpha + 2.20399\text{x}10^{31}*\sigma_0^2 - 7.43328*\alpha^2 \quad (8)$$

Table 3.2 is a compilation of the results obtained from the newly developed single exponential cross section vs energy method using eq 8 to predict the BDE's. Overall, excellent agreement between the literature BDE's and the single exponential cross section vs energy method is observed for the low molecular weight complexes studied, as illustrated in Table 3.2.

Adduct	Reference BDE (eV)	Model Fit BDE (eV)
CH_3OHLi^+	1.596 (0.083)[9]	1.57 ± 0.08
$ACNLi^+$	1.468[43]	1.60 ± 0.15
$DMSOLi^+$	2.36[43]	2.44 ± 0.12
$DMFLi^+$	2.43[43]	2.20 ± 0.09
$C_2H_5OHLi^+$	1.70 (0.08)[9]	1.72 ± 0.06
$CH_3OCH_3Li^+$	1.71 (0.11)[9]	1.68 ± 0.18

Table 3.2. Comparison of the model fitted results for the low molecular weight lithium adduct standards versus the measured BDE calculated from growth curve multivariate regression models from the single exponential cross section vs energy method, obtained by ES triple quadrupole tandem mass spectrometry. Parentheses represent uncertainties in the BDE values.

3.3.5 Mass Spectral Determination of Li^+ Lipid Dimer Adduct BDE's

The primary method used for the CID tandem mass spectrometric determination of BDE values for dimers is to equate the point of 50% dissociation, measured as $ML/(ML + M_2L)$, to the center-of-mass collision energy[11,39]. All of the lipids that were used in the current study (i.e., the monoacylglycerol, the 1,2-diacylglycerol, and the 1,3-diacylglycerols), have been observed to form lithium-bound noncovalent dimers of the form $[M_2Li]^+$. Using the high molecular weight growth model developed for our triple quadrupole, the energy for the dissociation of the monopentadecanoin dimer was measured to be 1.43 ± 0.04 eV. Figure 3.9a shows the results of the mass spectrometric determination of the BDE for the lithium-bound monopentadecanoin dimer in the range of the threshold energy for dissociation. Figure 3.9b plots the experimentally determined cross sections versus collision energy for the dissociation of the 1,3-dipentadecanoin lithium bound dimer. The growth curve model yields a dissociation energy of 1.43 ± 0.01 eV for the 1,3-dipentadecanoin lithium-bound dimer. Figure 3.9c presents the results of the 1-stearin,2-palmitin diacylglycerol lithium-bound dimer dissociation with an estimated BDE value of 1.38 ± 0.01 eV.

Figure 3.10a is a plot of the ratio of the product ion abundance (from the dissociation of the monoacylglycerol dimer) over the total ion abundance (to approximate the precursor ion abundance), $MLi^+ / (MLi^+ + M_2Li^+)$. The BDE's for the different dimer systems were obtained by fitting 4th order polynomials to the $MLi^+ / (MLi^+ + M_2Li^+)$ ratio data versus collision energy, setting the fitted polynomial equal to 0.50, and then solving for the roots. Inspection of the roots always gave an obvious choice as to the BDE for the dimer system being studied. For 50% dissociation of the monopentadecanoin dimer an E_{COM} of 1.31 ± 0.32 eV was experimentally required (growth curve model predicted a BDE = 1.43 ± 0.04 eV). Figure 3.10b is a plot of the ratio of the product ion from the dissociation of one of the 1,3-diacylglycerol dimers over the parent ion intensity, $MLi^+ / (MLi^+ + M_2Li^+)$. For 50% dissociation, an E_{COM} of 0.90 ± 0.09 eV was needed (growth curve model predicted a BDE = 1.43 ± 0.01 eV). Figure 3.10c is the plotted results of the 1- stearin,2-palmitin diacylglycerol lithium bound dimer, with a 50% dissociation E_{COM} value of 1.16 ± 0.07 eV (growth curve model predicted a BDE = 1.38 ± 0.01 eV). The experimentally obtained energy values corresponding to 50% dissociation are fairly close to the growth curve model predicted BDE's (Table 3.1). The former may be slightly lower owing to specific issues leading to underestimation of BDE's as previously discussed.

3.4 CONCLUSIONS

An important aspect of accurately determining bond dissociation energies by CID mass spectrometry is the measurement of a gas-phase reaction cell path length. The newly developed "derived effective reaction path length" method described here does not require extensive calculations of degrees of freedom, vibrational states, etc., which can be quite cumbersome for very large molecular weight systems. Unlike previous approaches, the method bases the determination of the reaction path length on data obtained from the CID reactions of known standards. Moreover, it can be implemented on standard commercial tandem mass spectrometers such as the triple quadrupole. By deriving an effective reaction path length using known standards, an empirically "error corrected" collision cell length is made available for use in the ensuing cross section/BDE calculations, and the error associated with reaction path length assignment is decreased. This reduction in uncertainty combined with the fact that electrospray can effectively transfer a solution phase complex into the gas phase with minimal energy uptake and perturbation of the complex, make the study of adducts by the derived effective reaction path length approach attractive. We have further built upon the derived effective reaction

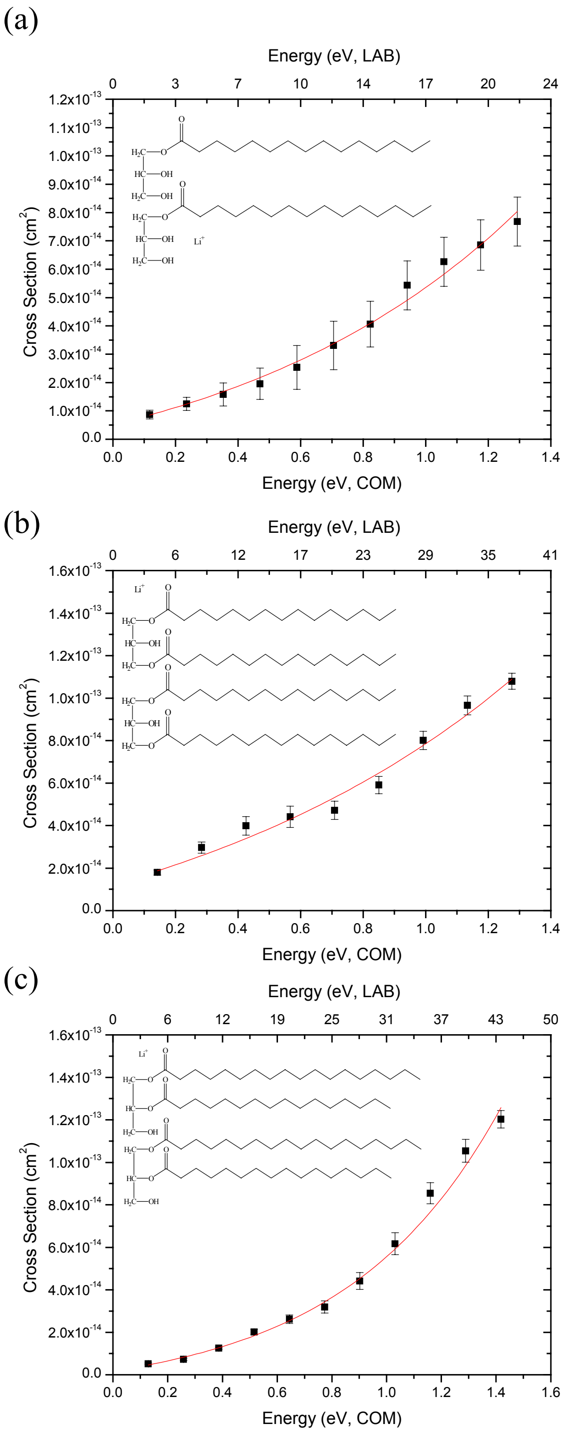

Figure 3.9. Cross section vs collision energy for: (a) the lithium-bound monopentadecanoin dimer. The BDE of 1.43 ± 0.04 eV (E_{COM}), for dimer dissociation was obtained from the exponential growth curve model, (b) the lithium-bound 1,3-dipentadecanoin dimer. The growth curve model yielded a dissociation energy of 1.43 ± 0.01 eV, (c) the lithium-bound 1-stearin,2-palmitin diacylglycerol dimer, yielding a BDE value of 1.38 ± 0.01 eV.

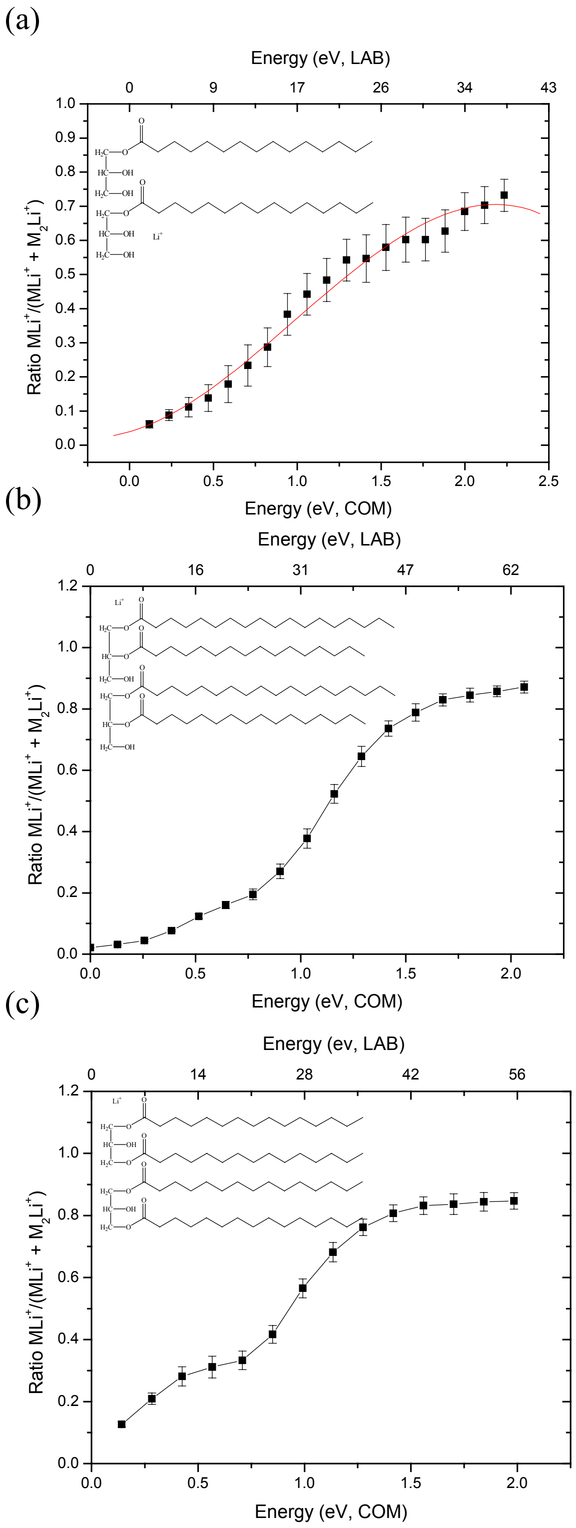

Figure 3.10. Ratio of MLi^+ to (MLi^+ + M_2Li^+) for the CID of lithium-bound dimers of: (a) monopentadecanoin. The BDE extracted from the point of 50% dissociation gives a value of 1.31 ± 0.32 eV E_{COM} (exponential growth curve model predicted 1.43 ± 0.04 eV). (b) 1,3-dipentadecanoin. At 50% dissociation, the BDE was measured to be 0.90 ± 0.09 eV (growth

curve model predicted 1.43 ± 0.01 eV). (c) 1-stearin,2-palmitin diacylglycerol with a 50% dissociation energy value of 1.16 ± 0.07 eV (growth curve model predicted 1.38 ± 0.01 eV).

path length and introduced a single exponential cross section vs energy method to enable the estimation of BDE's for relatively high molecular weight compounds. While the newly developed methodology has been rigorously tested on a triple quadrupole that uses a central hexapole collision cell, we see no reason that the method could not be applied to a Q-ToF, or any other instrumental configuration employing a floated collision cell under user control.

Density functional theory calculations of BDE's allowed a comparison with BDE's obtained using the derived effective reaction path length approach and subsequent curve fitting procedures; excellent agreement was observed for all of the lipid adducts and dimers studied. The monoacyl, 1,2- and 1,3-diacylglycerols, had very similar bond energies for the adducted lithium (3.5 eV to 4.0 eV), and adducted chloride (1.4 eV to 1.6 eV) ions. This study demonstrates that the derived effective reaction path length approach can be used for cationic and anionic adducted compounds, for dimers, and for larger molecular weight complex systems such as lipids.

3.5 References

1. Armentrout, P. B.; Beauchamp, J. L. *J. Chem. Phys.* **1981**, *74*, 2819-2826.
2. Ervin, K. M.; Armentrout, P. B. *J. Chem. Phys.* **1985**, *83*, 166-189.
3. Weber, M. E.; Elkind, J. L.; Armentrout, P. B. *J. Chem. Phys.* **1986**, *84*, 1521-1529.
4. Aristov, N.; Armentrout, P. B. *J. Chem. Phys.* **1986**, *90*, 5135-5140.
5. Hales, D. A.; Lian, L.; Armentrout, P. B. *Int. J. Mass Spectrom. Ion Processes* **1990**, *102*, 269-301.
6. Schultz, R. H.; Crellin, K. C.; Armentrout, P. B. *J. Am. Chem. Soc.* **1991**, *113*, 8590-8601.
7. Rodgers, M. T.; Ervin, K. M.; Armentrout, P. B. *J. Chem. Phys.* **1997**, 106, 4499-4508.
8. Rodgers, M. T.; Armentrout, P. B. *J. Chem. Phys.* **1998**, *109*, 1787-1800.
9. Rodgers, M. T.; Armentrout, P. B. *Mass Spec Rev* **2000**, *19*, 215-247.
10. Pramanik, B. N.; Bartner, P. L.; Mirza, U. A.; Liu, Y. H.; Ganguly, A. K. *J. Mass Spectrom.* **1998**, *33*, 911-920.
11. Shukla, A. K.; Futrell, J. H. *J. Mass Spectrom.* **2000**, *35*, 1069-1090.

12. Dougherty, R. C. *J Am Soc Mass Spectrom* **1997**, *8*, 510-518.
13. Daniel, J. M.; Friess, S. D.; Rajagopala, S.; Wendt, S.; Zenobi, R. *Int. J. Mass Spectrom.* **2002**, *216*, 1-27.
14. Graul, S. T.; Squires, R. R. *J. Am. Chem. Soc.* **1990**, *112*, 2517-2529.
15. Sunderlin, L. S.; Wang, D.; Squires, R. R. *J. Am. Chem. Soc.* **1993**, *115*, 12060-12070.
16. Anderson, S. G.; Blades, A. T.; Klassen, J.; Kebarle, P. *Int. J. Mass Spectrom Ion Processes* **1995**, *141*, 217-228.
17. Klassen, J. S.; Anderson, S. G.; Blades, A. T.; Kebarle, P. *J. Phys. Chem.* **1996**, *100*, 14218-14227.
18. Nielsen, S. B.; Masella, M.; Kebarle, P. *J. Phys. Chem. A* **1999**, *103*, 9891-9898.
19. Kebarle, P. *Int. J. Mass Spectrom.* **2000**, *200*, 313-330.
20. Peschke, M.; Blades, A. T.; Kebarle, P. *J. Am. Chem. Soc.* **2000**, *122*, 10440-10449.
21. Whitehouse, C. M.; Dreyer, R. N.; Yamashita, M.; Fenn, J. B. *Anal. Chem.* **1985**, *57*, 675-679.
22. Fenn, J. B. *J Am Soc Mass Spectrom* **1993**, *4*, 524-535.
23. Cole, R. B. *J. Mass Spectrom.* **2000**, *35*, 763-772.
24. Cech, N. B.; Enke, C. G. *Mass Spec Rev* **2001**, *20*, 362-387.
25. Gidden, J.; Wyttenbach, T.; Batka, J. J.; Weis, P.; Jackson, A. T.; Scrivens, J. H.; Bowers, M. T. *J Am Soc Mass Spectrom* **1999**, *10*, 883-895.
26. Leary, J. A.; Pederson, S. F. *J. Org. Chem.* **1989**,*54,* 5650-5651.
27. Adams, J.; Gross, M. L. *Anal. Chem,* **1987**, 59, 1576-1582.
28. Han, X.; Gross, R. W *Analytical Biochemistry* **2001**, *295*, 88-100.
29. Hsu, F. F.; Turk, J. *J Am Soc Mass Spectrom,* **1999**, *10*, 587-599.
30. Hofmeister, G. E.; Zhou, Z.; Leary, J. A. *J. Am. Chem. Soc.* **1991**, *113*, 5964-5970.
31. Staempfli, A.; Zhou, Z.; Leary, J. A. *J. Org. Chem.* **1992**, *57*, 3590-3594.
32. Zhou, Z.; Ogden, S.; Leary, J. A. *Journal of Organic Chemistry* **1990**, *55*, 5444-5446.
33. Striegel, A. M.; Timpa, J. D.; Piotrowiak, P.; Cole, R. B. *Int. J. Mass Spectrom. Ion Processes* **1997**,*162*, 45-53.
34. Marai, L.; Kuksis, A.; Myher, J. J.; Itabashi, Y. *Biol Mass Spectrom*, **1992**, *21*, 541-547.
35. Dougherty, R. C. *Anal. Chem.* **1981**, *53*, 625A-636A.
36. Cole, R. B.; Zhu, J. *Rapid Commun. Mass Spectrom.* **1999**, *13*, 607-611.
37. Zhu, J.; Cole, R. B. *J Am Soc Mass Spectrom,* **2000**, *11*, 932-941.
38. Zhu, J.; Cole, R. B. *J Am Soc Mass Spectrom,* **2001**, *12*, 1193-1204.
39. Cai, Y.; Cole, R. B. *Anal. Chem.*, **2002**, *74*, 985-991.
40. Gaussian 98, Revision A.3, M. J. Frisch, G. W. Trucks, H. B. Schlegel, G. E. Scuseria, M. A. Robb, J. R. Cheeseman, V. G. Zakrzewski, J. A. Montgomery, Jr., R. E. Stratmann, J. C. Burant, S. Dapprich, J. M. Millam, A. D. Daniels, K. N. Kudin, M. C. Strain, O. Farkas, J. Tomasi, V. Barone, M. Cossi, R. Cammi, B. Mennucci, C. Pomelli, C. Adamo, S. Clifford, J. Ochterski, G. A. Petersson, P. Y. Ayala, Q. Cui, K. Morokuma, D. K. Malick, A. D. Rabuck, K. Raghavachari, J. B. Foresman, J. Cioslowski, J. V. Ortiz, B. B. Stefanov, G. Liu, A. Liashenko, P. Piskorz, I. Komaromi, R. Gomperts, R. L. Martin, D. J. Fox, T. Keith, M. A. Al-Laham, C. Y. Peng, A. Nanayakkara, C. Gonzalez, M. Challacombe, P. M. W. Gill, B. Johnson, W. Chen, M. W. Wong, J. L. Andres, C. Gonzalez, M. Head-Gordon, E. S. Replogle, and J. A. Pople, Gaussian, Inc., Pittsburgh PA, 1998.
41. Chen, Y. L.; Campbell, J. M.; Collings, B. A.; Konermann, L.; Douglas, D. J. *Rapid Commun. Mass Spectrom.* **1998**, *12*, 1003-1010.

42. Noggle, J. H. *Physical Chemistry*, 3rd ed.; Harper Collins College Publishers: New York, 1996; p 28.
43. Taft, R.W.; Anvia, F.; Gal, J.F.; Walsh, S.; Capon, M.; Holmes, M.C.; Hosn, K.; Oloumi, G.; Vasanwala, R.; Yazdani, S. *Pure & Appl. Chem.***1990**, *62*, 17-23.
44. Foresman, J. B. *Exploring Chemistry with Electronic Structure Methods*, 2rd ed.; Gaussian, Inc.: Pittsburg, PA, 1996; p 157.
45. Chupka, W. A. *J. Chem. Phys.*, **1959**, *30*, 458-465.
46. Armentrout, P. B. *Top Curr Chem*, **2003**, *225*, 233-262.
47. McLafferty, F. W.; Turecek, F. *Interpretation of Mass Spectra*, 4th ed.; University Science Books: Sausalito, CA, 1993; p 126.
48. Srivastava, M. S. *Methods of Multivariate Statistics*, 1st ed.; John Wiley & Sons, Inc.: New York, 2002; p 365.

3.6 APPENDIX 1

Derived effective path length calculation

Using the three following values for the BDE determination of the lithium adduct of DMSO:

number gas density, $n = 3.14 \times 10^{12}\ \text{cm}^{-3}$

$I_P/(I_R + \sum I_P) = 1.879 \times 10^{-3}$

product cross section, $\sigma_P = 2.878 \times 10^{-16}\ \text{cm}^2$

The unit cell path length can be calculated using the following thin target limit relationship:

$$I_P/I_0 = I_P/(I_R + \sum I_P) = \sigma_P n\, \ell$$

rearranged into the form:

$$\ell = [I_P/(I_R + \sum I_P)]/\sigma_P n$$

$$\ell = (1.879 \times 10^{-3})/(\ 2.878 \times 10^{-16}\ \text{cm}^2)(\ 3.14 \times 10^{12}\ \text{cm}^{-3})$$

$$\ell = 2.08\ \text{cm}$$

CHAPTER IV: DETERMINATION OF APPARENT THRESHOLD ENERGIES OF LITHIATED ACYLGLYCEROLS USING TANDEM MASS SPECTROMETRY AND A NOVEL DERIVED EFFECTIVE REACTION PATH LENGTH APPROACH

4.1 Introduction

Electrospray [1-3] tandem mass spectrometry (ES-MS/MS) is a well established and powerful analytical tool for compound identification and structural elucidation [4-6]. Employing collision-induced dissociation (CID) [7] tandem mass spectrometry, a wide range of mass spectrometers have been used to study thermochemistry in the gas phase such as that of non-covalent receptor-ligand complexes by electrospray triple quadrupole [8-10], non-covalent bond dissociation energy studies by guided ion beam tandem mass spectrometry [11-19], critical energies for ion dissociation by quadrupole ion trap [21] or flowing afterglow-triple quadrupole [22, 23], reaction enthalpies and ion-ligand bond energies by electrospray triple quadrupole [24, 25], and binding energies from gas phase ion-equilibrium [26] studies by electrospray triple quadrupole [27-28]. For structural elucidation by triple quadrupole tandem mass spectrometry, the precursor ion of interest is isolated by the first quadrupole acting as a mass filter, subjected to collision induced dissociation in the rf-only second quadrupole (actually hexapole), and finally the product ions are scanned in the third quadrupole. Typically, collision energy and collision cell gas pressure are chosen to achieve 20 - 70% attenuation of the precursor ion abundance, and the products from the collision induced fragmentation are thereby formed under multiple collision conditions. However, in energy-resolved mass spectrometry studies [29-36] where the specific kinetics of the fragmentation pathways are of interest, single collision conditions (~10% attenuation of precursor) are employed in the triple quadrupole, and multiple spectra are obtained at increasing activation energies controlled by the energy offset of the central hexapole. During energy-resolved mass spectrometry studies, a wealth of information is being collected which can be used to qualitatively describe the unimolecular fragmentation pathways through the use of breakdown graphs, where the percentage of the total abundance for each product ion is plotted versus collision energy. One quantitative aspect of the breakdown graphs is the comparative abundances of the product ions at specific collision energies. A higher relative product ion abundance, expressed as the percentage of total ions measured, equates to a more favored reaction pathway at that energy as compared to other product ions under the same condition. The collection of spectra at incrementally increasing energy offset allows for the calculation and graphing of branching ratios [37], and product cross sections. The product cross sections of unimolecular reactions are directly related to the activation energies required for dissociation according to the Rice-Ramsperger-Kassel-Marcus (RRKM) theory [38] of unimolecular reactions which occur during fragmentation studies employing CID. Our previous work, taking advantage of the thin target limit relationship to collision cross sections [12], resulted in the development of a predictive model for bond dissociation energies of alkali metal or halide ion adducts [39], where only the simple dissociation of the alkali metal cation or halide anion was considered. In the current work, we have extended this new model by applying it to the description of *covalent* bond dissociation energies (apparent threshold energies, ΔE_0) involved in the unimolecular fragmentations of lithiated acylglycerols.

4.2 Experimental

4.2.1 Materials and Methods

Methanol and chloroform solvents were of HPLC/spectroscopy grade and were purchased from EM Science (Darmstadt, Germany). Monopentadecanoin and 1,3-dipentadecanoin were obtained from Nu-Chek Prep, Inc. (Elysian, MN), with stated purities of >

99%. 1-Stearin-2-palmitin diacylglycerol was purchased from Larodan Fine Chemicals AB (Malmo, Sweden), with stated purity of 99%. Lithium chloride was ACS grade in granular form from J. T. Baker Inc. (Phillipsburg, NJ). All standards were used as received without further purification.

4.2.2 Instrumentation

Mass spectra were obtained using a "triple quadrupole" (actually quadrupole-hexapole-quadrupole, QhQ) mass spectrometer (Micromass, Inc., Manchester, UK, model Quattro II) equipped with an electrospray source operating at typical sample solution flow rates of 2-4 μL/min. Nitrogen was used as both nebulizing and drying gas. Typical cone voltage was 40 V for CID of the lithium adducts of the acylglycerols. The ES capillary voltage was held at 2.5 to 3.5 kV. Argon was used as collision gas during CID experiments at collision gas pressures of approximately 1.3×10^{-4} mBar (measured externally to the central hexapole collision cell) to obtain the single collision conditions employed in all experiments. The hexapole offset energy values range from 0 eV up to 250 eV with a minimum increment of 1 eV (E_{LAB}). MassLynx software (Micromass) was used to acquire, process, and store mass spectral data.

4.2.3 Apparent threshold energy predictive model

A typical experiment consists of collecting a product ion spectrum at 0 eV (E_{LAB}), as set by the energy offset of the central hexapole, followed by sequentially collecting spectra at increasing offset values in 1 eV (E_{LAB}) increments. Most experiments employed collision energy values ranging from 0 eV up to 200 eV (E_{LAB}). The supplied energy for the collision is converted from the laboratory (LAB) frame of reference to the center-of-mass (COM) frame of reference according to $E_{COM} = E_{LAB}(m/(m + M))$, where E_{LAB} is the measured offset for the central hexapole, m is the mass of the stationary target Ar atom, and M is the mass of the analyte. Using the thin target limit relationship [12]:

$$I_P/I_0 = I_P/(I_R + \Sigma I_P) = \sigma_P n \ell \qquad (1)$$

where I_P is the transmitted product ion abundance, I_R is the transmitted reactant ion abundance, I_0 is the incident (precursor) ion abundance, σ_P is the product cross section (cm^2), n is the number gas density (cm^{-3}), and ℓ is the collision cell path length (cm), individual product cross sections can be obtained for each product ion at a specified collision energy. The product cross sections are plotted versus the collision energy, in the center-of-mass frame of reference, and the following exponential growth equation:

$$\sigma_P(E) = \sigma_0 \exp(E_{COM}/\alpha) + y_0 \qquad (2)$$

is fit to the data in the threshold activation energy range for product ion formation, between approximately 0.06 - 4 eV (E_{COM}). The parameters of the fitted curve are then used in the following general multivariate growth curve model (GCM-Polynomial Regression) [40] developed for the triple quadrupole in our laboratory [39]:

$$\text{BDE (eV)} = 0.78051 - 1.7180\text{x}10^{13}\sigma_0 + 1.4627\alpha - 0.16327\alpha^2 \qquad (3)$$

to calculate the apparent bond dissociation energy from unimolecular fragmentation for that particular product ion.

4.3 Results and Discussion

4.3.1 Apparent threshold energies for lithiated mono-pentadecanoin

The first monoacylglycerol that the derived effective reaction path length approach for the measurement of apparent threshold energies was applied to was the lithium adduct of monopentadecanoin. Figure 4.1a is a product ion spectrum of the collisionally activated monopentadecanoin lithium adduct, collected at 40 eV (E_{LAB}) under single collision conditions, showing the major fragments produced during unimolecular dissociation. There are four major product ions produced, and their assignments are presented in Figure 4.1b. The m/z 99 product ion is the result of the neutral loss of the C15 fatty acyl chain as a ketene from the precursor ion, and it is the most abundant ion in the spectrum. The m/z 81 and m/z 63 ions are produced from one water loss, and two water losses, respectively, from the m/z 99 product ion. The m/z 57 ion is the result of LiOH loss from the m/z 81 ion, as depicted in Figure 4.1b, with a potential minor contribution from the fragmentation pathway which produces the hydrocarbon series $C_nH_{2n+1}^+$ (n = 4). Over a wide range of collision energies, the "% Total Ion Abundance" of the four product ions follows the trend: m/z 99 > m/z 81 > m/z 63 > m/z 57, as is visually apparent in the breakdown graph presented in Figure 4.2. For these energy-resolved determinations, CID spectra acquired were under single collision conditions; therefore the % Total Ion Abundances for the product ion fragments are very low. The precursor % Total Ion Abundance was also plotted (but note the discontinuity in the y-axis) to further contrast the precursor vs product ion abundances during these experiments.

It is known from the theory of unimolecular ion decompositions [38] that the bond with the lowest critical energy for dissociation is not always the one to rupture at each respective internal energy state. This arises due to kinetic considerations in enthalpy driven reactions where the energy barrier required to cleave a given bond may be lowered due to simultaneous formation of new bonds during the fragmentation process, thus resulting in a more abundant product ion at a certain internal energy state. Moreover, fragment ions produced from a "loose

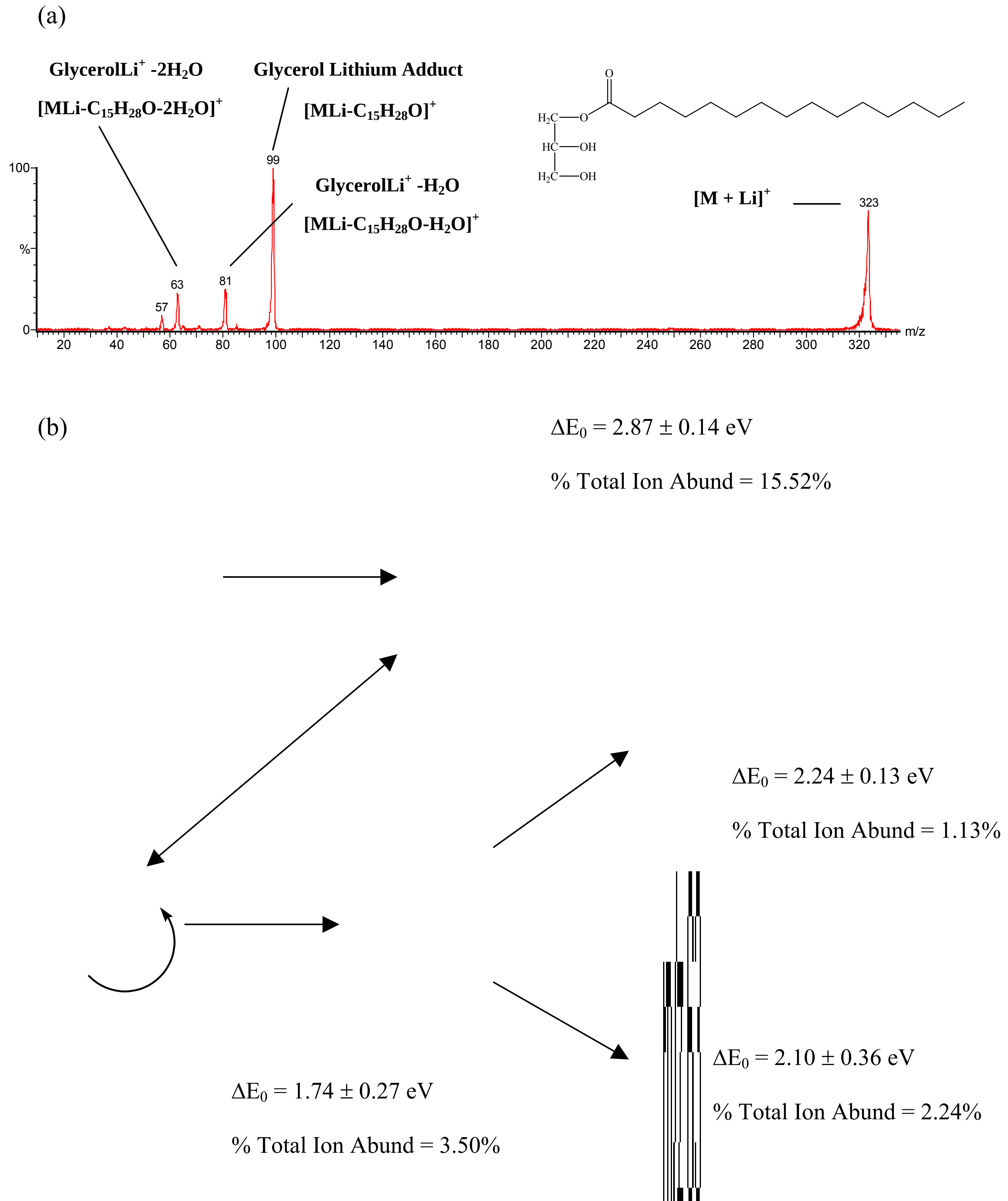

Figure 4.1. (a) Product ion spectrum of the collision activated monopentadecanoin lithium adduct, collected at 40 eV (Lab). Major fragments produced: (1) m/z 99 from the neutral loss of C15 fatty acyl chain as ketene, producing lithiated glycerol, (2) m/z 81 produced by water loss from m/z 99, (3) m/z 63 produced by two water losses from m/z 99, and (4) m/z 57 formed by loss of LiOH from m/z 81, and from part of the $C_nH_{2n+1}^+$ hydrocarbon series from the fatty acid acyl chain. (b) Fragmentation pathways, structures, apparent threshold energies, and % Total Ion Abundance for the four major product ions formed from CID of lithiated mono-pentadecanoin.

The m/z 99 ion is the result of the neutral loss of C15 fatty acyl chain as ketene from the precursor ion, and is the most abundant ion in the spectrum, at an apparent threshold energy of 2.87 ± 0.14 eV (E_{COM}). The m/z 81 and m/z 63 ions are produced from one water loss, then two water losses, respectively. The m/z 81 ion has the lowest threshold energy at 1.74 ± 0.27 eV (E_{COM}). The m/z 57 ion is formed primarily by LiOH loss from the m/z 81 ion.

complex" state are often observed at higher threshold energies than those formed from "tight complexes" because the later more often benefit from stabilization of the transition state owing to new bond formation. But decomposition reactions that proceed through "tight complexes" have unfavorable entropic factors, hence, they are disfavored in cases where substantial amounts of excess energy are present, and insufficient time is available for the tight complex to form.

Our predictive model for calculating apparent threshold energies for the fragmentation pathways from the energy-resolved mass spectral data gives a new quantitative aspect to describe the product ions produced from CID experiments. As can be deduced from Figure 4.1b, the % Total Ion Abundance calculated at a given collision energy (at saturation, i.e. 7 eV, E_{COM}) are not inversely related to the apparent threshold energies (ΔE_0). This indicates that some of the product ions are produced through secondary or competitive processes. If a closer look is taken at the apparent threshold energies, it can be noted that the production of the m/z 81 ion, ΔE_0 = 1.74 ± 0.27 eV (E_{COM}) is the most enthalpy favored process compared to the other three product ion pathways. This is followed by the m/z 63 ion at ΔE_0 = 2.10 ± 0.36 eV (E_{COM}), the m/z 57 ion at ΔE_0 = 2.24 ± 0.13 eV (E_{COM}), and finally the m/z 99 ion at ΔE_0 = 2.87 ± 0.14 eV (E_{COM}). Clearly from a % Total Ion Abundance of 15.52%, the m/z 99 product ion has a much greater rate of formation than the other three product ions at elevated collision energies, suggesting that the m/z 99 product ion is the most entropically favored fragmentation pathway.

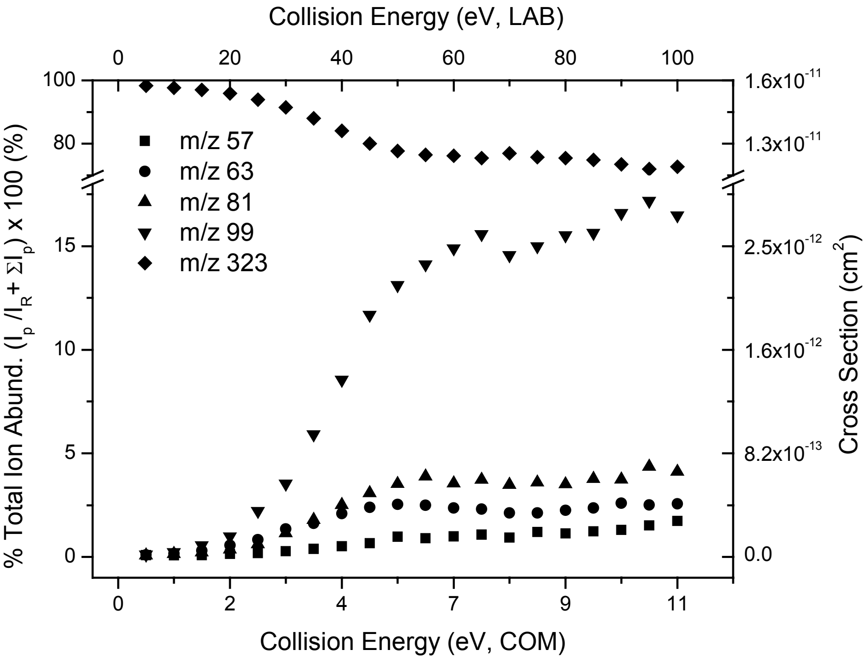

Figure 4.2. Energy-resolved breakdown graph for the dissociation of the lithiated mono-pentadecanoin diacylglycerol. The % Total Ion Abundances are very low due to collection under single collision conditions. The precursor % Total Ion Abundance is included in the plot to illustrate the small percentage losses during these experiments. % Total Ion Abundances appears to follow the trend of m/z 99 > m/z 81 > m/z 63 > m/z 57.

From the breakdown graph an additional interesting pathway description is observed. At lower collision energies, the m/z 63 product ion is slightly favored compared to the m/z 81 product ion, suggesting a very initial favored pathway (due to stearic arrangement?), but is quickly overcome by the m/z 81 product ion, which has a considerably lower apparent reaction enthalpy, overall.

4.3.2 Apparent threshold energies for lithiated 1-stearin,2-palmitin diacylglycerol

The lithium adduct of diacylglycerol 1-stearin,2-palmitin was the next to be studied using energy-resolved mass spectra. The product ion spectrum of the collision induced dissociation of 1,2-diacylglycerol is shown in Figure 4.3a, at a collision energy of 50 eV (E_{LAB}). The spectrum shows a number of lower molecular weight fragment ions from approximately m/z 43 to m/z 123, and higher molecular weight product ions ranging from m/z 257 to m/z 365. The latter higher molecular weight range contains 7 product ions, which are assigned in Figure 4.3b. All 7 of these higher mass product ions appear to have plausible fragmentation pathways that do not arise from consecutive dissociations. The proposed mechanisms each constitute a single dissociation involving one H-transfer in concert with cleavage to produce the array of product ions listed in Figure 4.3b.

In contrast to the product ions of the lithium adduct of mono-pentadecanoin presented, the product ions from 1-stearin,2-palmitin diacylglycerol dissociations appear in % Total Ion Abundances have that are inversely related to the apparent threshold energies. Table 4.1 is a listing of the apparent threshold energies versus % Total Ion Abundance, which more clearly shows the inverse relationship. For this set of fragmentation pathways, except for a slight anomaly for the last ion (m/z 365), a lower threshold energy equates to a higher % Total Ion Abundance.

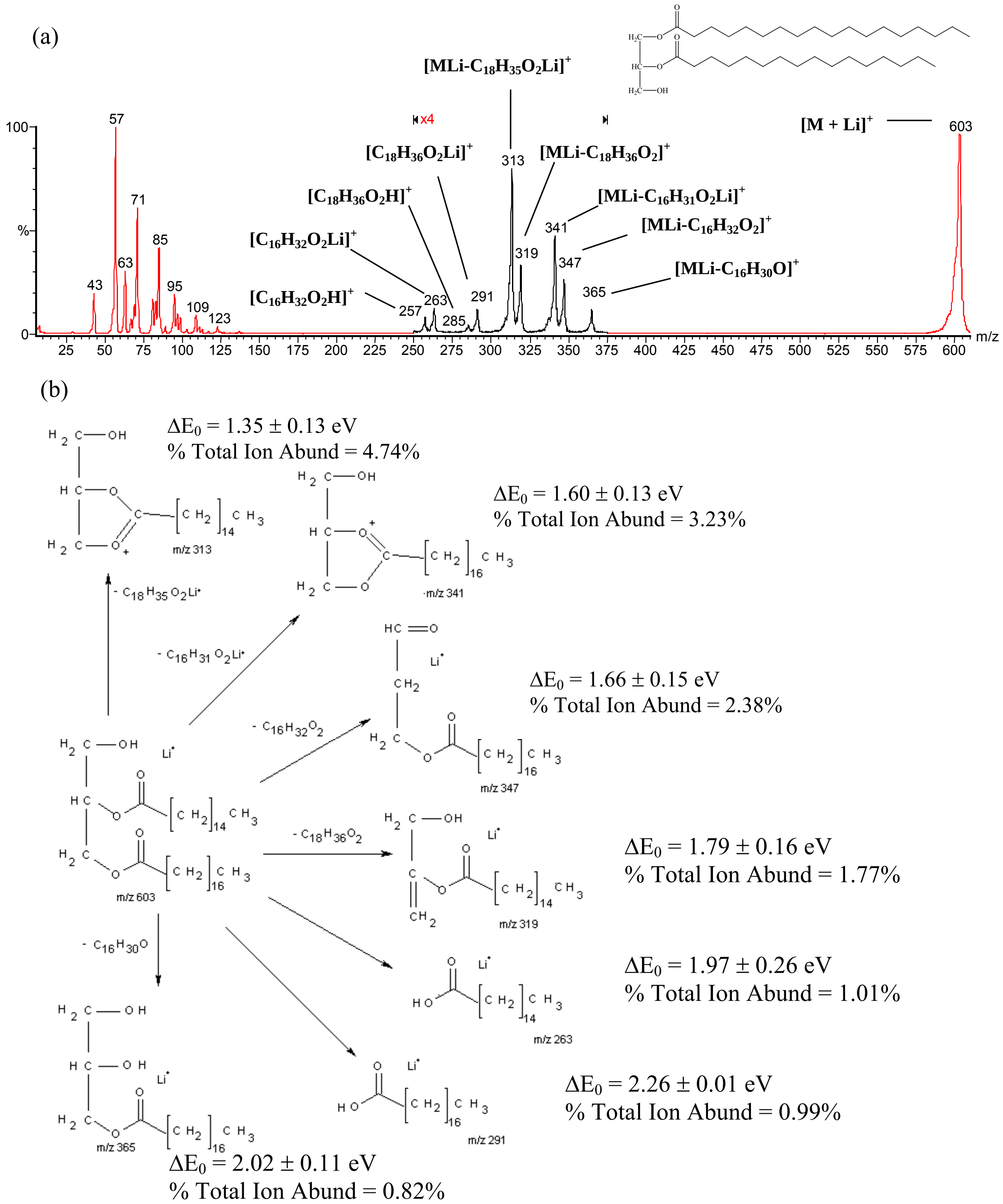

Figure 4.3. (a) Product ion spectrum of the collision induced dissociation of lithiated 1-stearin,2-palmitin diacylglycerol, at collision energy of 50 eV (Lab). Lower molecular weight fragment ions appear from approximately m/z 43 to m/z 123, primarily representing the hydrocarbon series $C_nH_{2n+1}^+$ from σ-bond fatty acyl chain cleavage. Higher molecular weight product ions ranging from m/z 257 to m/z 365 produced from single cleavage reactions of fatty acyl loss in several forms (fatty acyl chain as ketene, lithium fatty acetate, and fatty acid). (b) Fragmentation

pathways, structures, apparent threshold energies, and % Total Ion Abundance for the high molecular weight range product ions produced from the CID of 1-stearin,2-palmitin, ranging from m/z 257 to m/z 365. Paired products include the neutral loss of C18 and C16 lithium fatty acetate at m/z 313 and m/z 341, and neutral loss of C18 and C16 fatty acid at m/z 319 and m/z 347. M/z 365 is formed by the neutral loss of C16 fatty acyl chain as ketene. Fragmentation ranking of: loss of lithium fatty acetate > loss of fatty acid > loss of fatty acyl ketene.

Product ion (m/z)	% Total Ion Abundance (%)	Apparent Threshold Energy (ΔE_0, eV)	Cross Section (cm^2)
313	4.74	1.35 ± 0.13	7.74×10^{-13}
341	3.23	1.60 ± 0.13	5.28×10^{-13}
319	2.38	1.66 ± 0.15	3.90×10^{-13}
347	1.77	1.79 ± 0.16	2.90×10^{-13}
263	1.01	1.97 ± 0.26	1.65×10^{-13}
291	0.99	2.26 ± 0.01	1.62×10^{-13}
365	0.82	2.02 ± 0.11	1.34×10^{-13}

Table 4.1. % Total Ion Abundances, apparent threshold energies, and cross sections of high molecular weight product ions for the lithium adduct of 1-stearin,2-palmitin diacylglycerol.

Figure 4.4a is the breakdown graph of the higher molecular weight product ions, which also illustrates that each fragmentation pathway increases in product ion intensity, in a roughly similar pattern, with increasing collision energy, i.e., little curve crossing occurs. The fact that curves in Fig. 4.4a do not cross indicates that the relative importance of entropic vs enthalpic factors which govern the rates of decomposition for each process, does not change substantially as higher internal energy uptake is achieved. The m/z 313 product ion has the greatest abundance as seen in the breakdown graph, followed by the m/z 341 ion. As illustrated in Figure 4.3b, the structures of these two product ions are related in that both have lost a neutral lithium fatty acetate molecule. As has been observed previously in our laboratory [41], the loss of the 1-position substituent giving rise to the m/z 313 product ion is the favored pathway, a conclusion which the current studies also support. As noted above, the m/z 313 product ion has the lowest apparent threshold energy at 1.35 ± 0.13 eV (E_{COM}), followed by the m/z 341 product ion at 1.60 ± 0.13 eV (E_{COM}).

In summary then, for the losses involving the fatty acid substituents from this diacylglycerol, the pair of product ions with the highest abundances, and lowest apparent threshold energies, are from the neutral loss of the lithium fatty acetates at m/z 313 and m/z 341. The next most abundant pair, with somewhat higher apparent threshold energy product ions observed are from the neutral loss of the fatty acid substituent (acid form) at m/z 347 and and m/z 319. Third in this fatty acid loss series, with the lowest abundance, and highest apparent threshold energy, is the neutral loss of the fatty acyl chain as ketene at m/z 365, suggesting the following favored fragmentation pathway neutral loss ranking of: loss of lithium fatty acetate > loss of fatty acid > loss of fatty acyl chain as ketene.

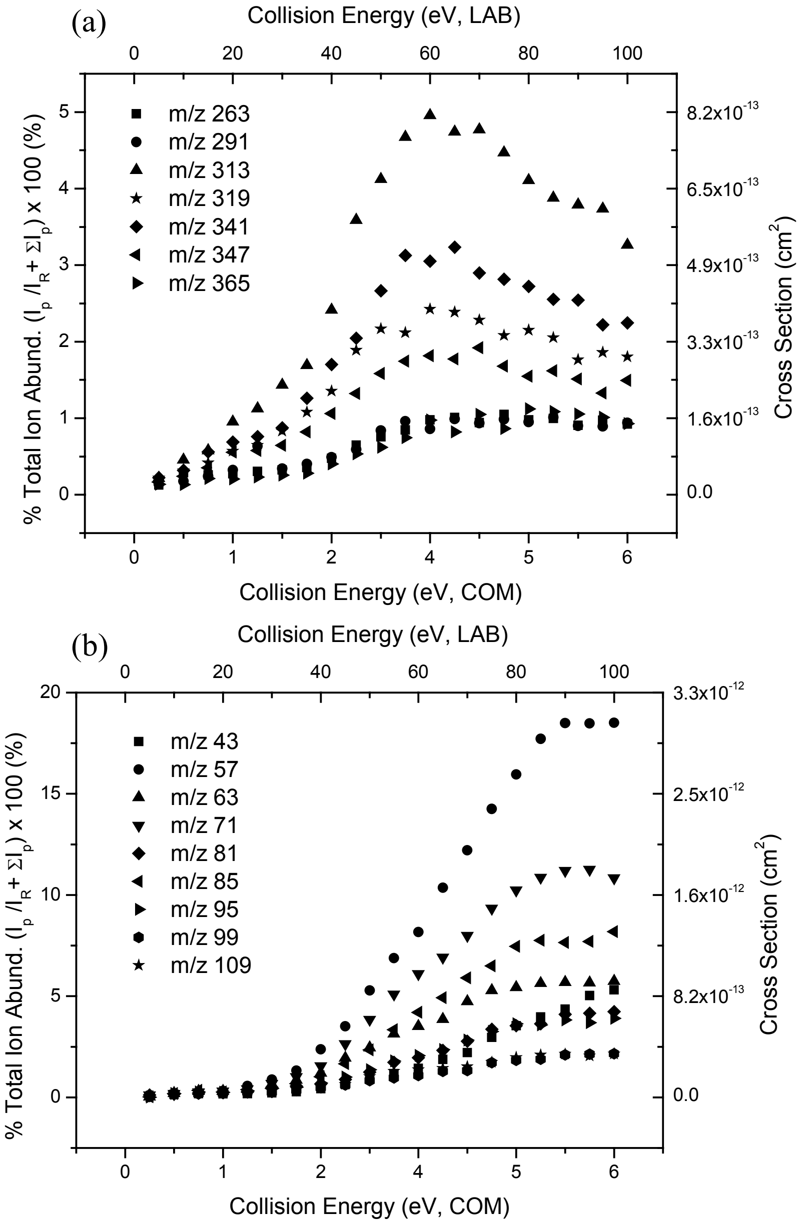

Figure 4.4. Breakdown graph of: (a) the higher molecular weight product ions from CID of 1-stearin,2-palmitin. Fragmentation pathways arise primarily from losses of fatty acid substituents in the form of fatty acyl chain as ketene, lithium fatty acetate, and fatty acid. All increase in product ion intensity in a similar pattern for increasing collision energy. (b) The lower molecular weight product ions from CID of 1-stearin,2-palmitin. Peak series m/z 43, m/z 57, m/z 71, m/z 85, m/z 99 result from alkyl chain fragmentation through σ-bond cleavage of the fatty acid hydrocarbon chains producing the series $C_nH_{2n+1}^+$.

The breakdown graph of the lower molecular weight product ions is illustrated in Figure 4.4b; the corresponding apparent threshold energies are listed in Table 4.2. Often, low molecular weight product ions in the m/z 43 to 127 region are the result of alkyl chain fragmentation through σ-bond cleavage of the fatty acid hydrocarbon chain producing the series $C_nH_{2n+1}^+$. In the product ion spectrum in Figure 3a, the hydrocarbon series from σ-bond cleavages of the fatty acid alkyl chain consists of m/z 43, m/z 57, m/z 71, m/z 85, and m/z 99. The m/z 57 product ion has the highest % Total Ion Abundance at 15.96%, and the lowest apparent threshold energy at 1.35 ± 0.26 eV (E_{COM}). Analogous to the fragmentation of the mono-pentadecanoin acylglycerol in Figure 4.1b, the m/z 57 product ion may also be formed through a multi-step process requiring first, losses of both fatty acyl chains to form m/z 99, then loss of water, followed finally by loss of LiOH. Thus, two processes may be responsible for formation of the m/z 57 product ion resulting in the observance of a greater abundance, and lower apparent threshold energy. Also included in the low molecular weight series are the m/z 81 and m/z 63 product ions from the losses of one, and then two waters, respectively, from the lithiated glycerol backbone, in a manner analogous to the pathways illustrated in Figure 4.1b.

4.3.3 Reaction enthalpies for lithiated 1,3-dipentadecanoin

Figure 4.5a is a product ion spectrum for the collision induced dissociation of lithiated 1,3-dipentadecanoin, acquired at 60 eV (E_{LAB}). Similar to the 1-stearin,2-palmitin diacylglycerol CID spectrum, the 1,3-dipentadecanoin produces low molecular weight product ions ranging from m/z 29 to m/z 99 by the same processes that were

	Mono-pentadecanoin		1-stearin,2-palmitin diacylglycerol		1,3-dipentadecanoin	
Product ion (m/z)	Abund. (%)	ΔE_0 (eV)	Abund. (%)	ΔE_0 (eV)	Abund. (%)	ΔE_0 (eV)
43	-----	-----	3.54	1.78 ± 0.03	2.36	1.87 ± 0.30
57	1.13	2.24 ± 0.13	15.96	1.35 ± 0.26	8.16	1.69 ± 0.10
63	2.24	2.10 ± 0.36	5.43	1.71 ± 0.03	3.30	1.68 ± 0.19
71	-----	-----	10.24	1.55 ± 0.09	5.08	1.53 ± 0.07
81	3.50	1.74 ± 0.27	3.54	1.87 ± 0.18	5.07	1.51 ± 0.26
85	-----	-----	7.46	1.70 ± 0.05	3.34	1.70 ± 0.15
95	-----	-----	3.63	1.88 ± 0.05	1.48	1.65 ± 0.35
99	15.52	2.87 ± 0.14	1.84	2.07 ± 0.35	2.16	1.62 ± 0.15

Table 4.2. % Total Ion Abundance and apparent threshold energy for the lithium adduct of mono-pentadecanoin acylglycerol, 1-stearin,2-palmitin diacylglycerol, and 1,3-dipentadecanoin.

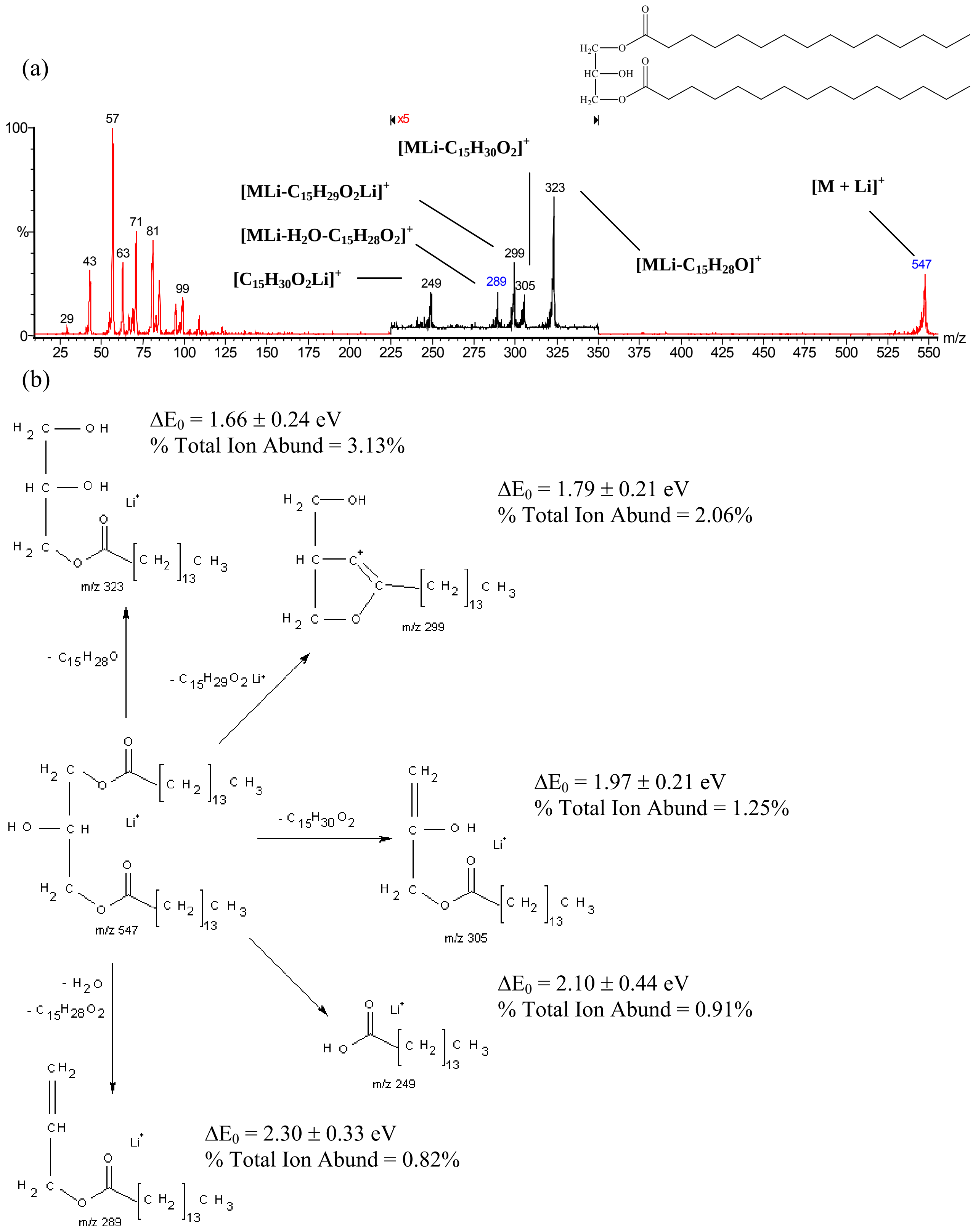

Figure 4.5. (a) Product ion spectrum of the collision induced dissociation of lithiated 1,3-dipentadecanoin, collected at 60 eV (E_{LAB}). Low molecular weight product ions ranging from

m/z 29 to m/z 99 expressed by the hydrocarbon series $C_nH_{2n+1}^+$ produced from σ-bond fatty acyl chain cleavage. Higher molecular weight range of m/z 249 to m/z 323 produced from single cleavage reactions of fatty acyl loss in several forms (fatty acyl chain as ketene, lithium fatty acetate, and fatty acid). (b) Fragmentation pathways, structures, apparent threshold energies, and % Total Ion Abundance for the high molecular weight range product ions produced from the CID of 1,3-dipentadecanoin, ranging from m/z 249 to m/z 323. Neutral loss of fatty acyl chain as ketene at m/z 323 contains the highest abundance, and lowest threshold energy. This is followed by neutral loss of lithium fatty acetate at m/z 299, then neutral loss of the fatty acid at m/z 305. Fragmentation ranking of: loss of fatty acyl ketene > loss of lithium fatty acetate > loss of fatty acid. The m/z 289 product ion is produced from the consecutive neutral losses of H_2O followed by C15:1 alpha-beta unsaturated fatty acid.

discussed above. In the higher molecular weight range of m/z 249 to m/z 323, 5 principle product ions are observed. Similar to 1,2-diacylglycerol described above, these product ions also are formed primarily through single cleavages of a fatty acid substituent with concomitant H-transfer resulting in the losses of various neutrals, such as loss of the fatty acyl chain as a ketene, loss of lithium fatty acetate, and loss of fatty acid (acid form). Figure 4.5b depicts assignments for the product ions along with their respective % Total Ion Abundances and apparent threshold energies. Similar to the 1-stearin,2-palmitin diacylglycerol example there is an inverse relationship observed between % Total Ion Abundance and apparent threshold energy, as listed in Table 4.3. Among the competitive decomposition processes, the product ion with the highest abundance, and lowest threshold results from the neutral loss of the fatty acyl chain as a ketene at m/z 323. The next highest abundance, slightly higher threshold energy product ion observed is from the neutral loss of lithium fatty acetate at m/z 299. Third in this fatty acid loss series, with the next highest abundance, and even higher reaction threshold, is the neutral loss of the fatty acid substituent at m/z 305, suggesting the following ranking favored of fragmentation pathways: neutral loss of fatty acyl chain as ketene > neutral loss of lithium fatty acetate > neutral loss of fatty acid. The m/z 289 product ion is produced from the consecutive neutral losses of H_2O followed by C15:1 alpha-beta unsaturated fatty acid (this order was established by precursor scan inspection of m/z 289 [41]), thus resulting in the lowest % Total Ion Abundance, and highest apparent threshold energy up to this point. Figure 4.6a is the breakdown plot for formation of the higher molecular weight product ions which graphically illustrates the observed % Total Ion Abundances vs collision energy.

Product ion (m/z)	% Total Ion Abundance (%)	Apparent Threshold Energy (ΔE_0, eV)	Cross Section (cm^2)
323	3.13	1.66 ± 0.24	5.11×10^{-13}
299	2.06	1.79 ± 0.21	3.37×10^{-13}
305	1.25	1.97 ± 0.21	2.05×10^{-13}
249	0.91	2.10 ± 0.44	1.49×10^{-13}
289	0.82	2.30 ± 0.33	1.34×10^{-13}

Table 4.3. % Total Ion Abundances, apparent threshold energy, and cross sections of high molecular weight product ions for the lithium adduct of 1,3-dipentadecanoin

The low molecular weight product ions range from m/z 43 to m/z 99, produced primarily from a mixture of the $C_nH_{2n+1}^+$ hydrocarbon series (m/z 43, m/z 57, m/z 71, m/z 85, and m/z 99), and product ions arising from the glycerol backbone (m/z 63, m/z 81, and m/z 99). Table 4.2 shows the % Total Ion Abundance and apparent threshold energies for the 1,3-dipentadecanoin diacylglycerol, as compared with the mono-pentadecanoin acylglycerol, and the 1-stearin,2-

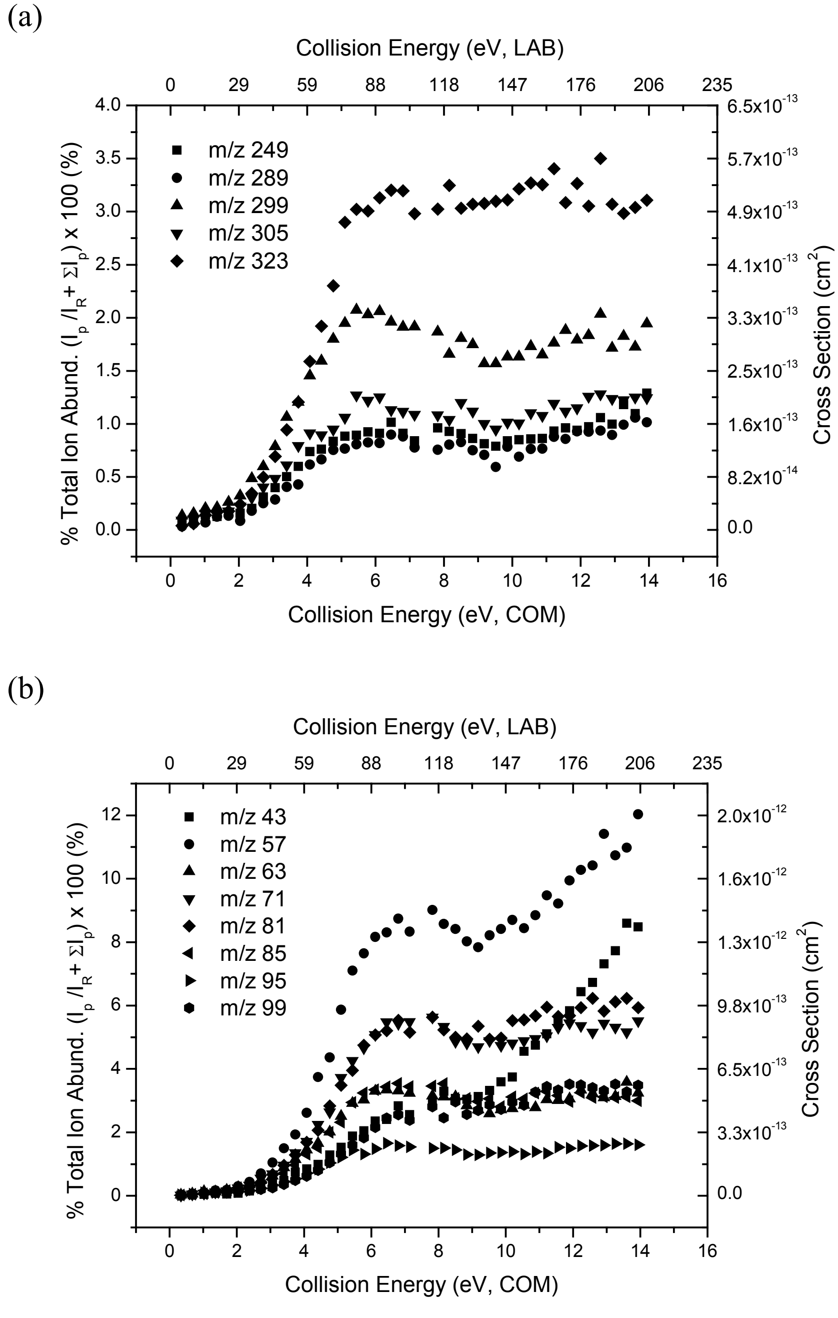

Figure 4.6. Breakdown graphs for: (a) high molecular weight product ions produced from CID of 1,3-dipentadecanoin, and (b) low molecular weight product ions produced from CID of 1,3-dipentadecanoin. M/z 57 product ion is the favored fragmentation pathway due to joint production by glycerol backbone water loss, and fatty acyl chain hydrocarbon cleavage. M/z 43 product ion rapidly increases, as the collision energy is increased, produced from σ-bond cleavage of the fatty acyl hydrocarbon chain and the glycerol backbone $[C_2H_3O]^+$, appearing to be a favored pathway at increasing collision energies.

the other product ions, as the collision energy is increased. The m/z 43 product ion is produced through two processes: σ-bond cleavage of the fatty acyl hydrocarbon chain, and a two carbon species from the glycerol backbone $[C_2H_3O]^+$.

4.3.4 Computational Reaction Enthalpies versus Predicted Apparent Threshold Energies

Computational methods for surface potential energies were obtained by Gaussian 98 [42] to create a benchmark to evaluate the derived effective reaction path length approach for predicting the apparent threshold energies of covalent dissociations arising from CID of the acylglycerols. For all of the monopentadecanoin CID products listed in Fig. 4.1b, surface potential energies were calculated along with those of the respective neutral molecules formed concomitantly. For the pathway producing the m/z 99 lithiated glycerol product and the neutral fatty acyl chain as ketene, the computational reaction enthalpy (ΔH^0_{rxn}) was determined to be 2.19 eV. The magnitude of uncertainty in potential energy calculations at the B3LYP 6-31G* level has been estimated to be 3.9 $kcal{\cdot}mol^{-1}$, or 0.17 eV [42] (mean absolute deviation). The apparent threshold energy (ΔE_0) was experimentally determined to be 2.87 ± 0.14 eV. This is illustrated in Figure 4.7a where the ground state surface potential energy of the precursor m/z 323 monopeantadecanoin lithium adduct has been set to a value of 0 eV. The three product ions m/z 81, 63, and 57 (m/z 57 not shown), are observed to have lower ΔE_0 values than the m/z 99 product ion (Fig. 4.1b). For the three product ions m/z 81, 63, and 57 an inverse relationship between the % Total Ion Abundance and the apparent threshold energy ΔE_0 is observed. However, these three product ions are produced by consecutive decompositions after the first step of loss of the fatty acyl chain as a ketene yielding the m/z 99 ion which initially requires a ΔE_0 of 2.87 ± 0.14 eV.

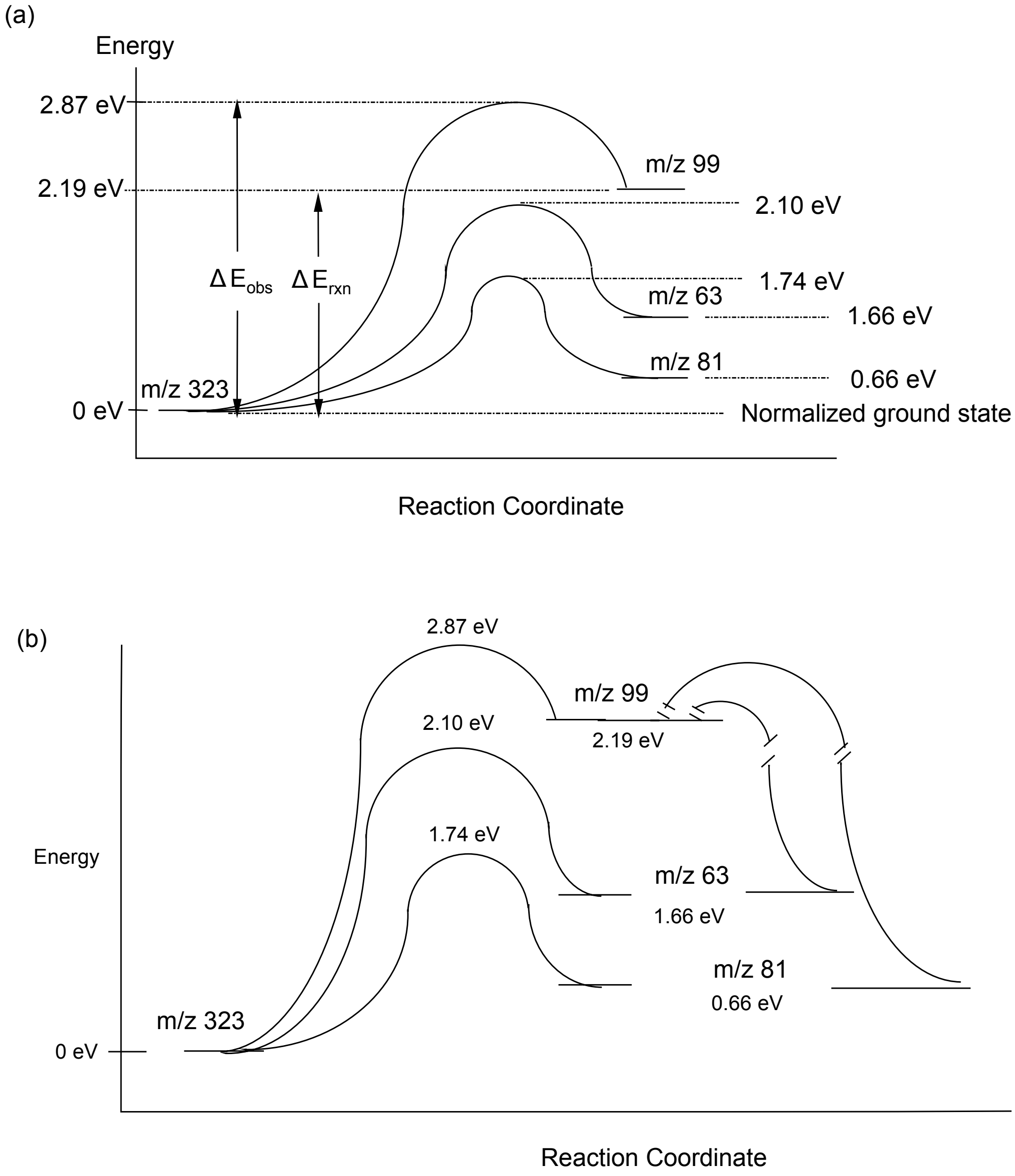

Figure 4.7. Energy diagrams for: (a) production of the m/z 63, 81, and 99 product ions from the monopentadecanoin lithium adduct, (b) production of the m/z 63, 81, and 99 product ions from the monopentadecanoin lithium adduct including the high energy pathways.

The pathway for the production of the m/z 99 product involves a single hydrogen transfer. If a consecutive loss is assumed for the production of the m/z 81 ion, two hydrogen transfers are involved suggesting a higher energy barrier. For the production of the m/z 81 ion:

$$\text{M/z 323} \xrightarrow{\text{CID}} \text{m/z 81 + ketene + H}_2\text{0} \qquad (4)$$

the ΔH^0_{rxn} was determined to be 0.66 eV (by the Gaussian 98 method), and the ΔE_0 was determined to be 1.74 ± 0.27 eV (by the derived effective reaction path length approach). The production of the m/z 81 ion may be passing through the initial ketene loss mechanism which produces the m/z 99 product ion, thus requiring an activation energy of 2.87 ± 0.14 eV. Or, alternatively the m/z 81 product ion may be produced through a separate pathway requiring the 1.74 ± 0.27 eV predicted by the derived effective reaction path length approach. Figure 4.8 illustrates a proposed mechanism for the production of the m/z 81 product ion from the m/z 323 precursor ion. In order to ascertain the production of the m/z 81 ion, the product ions m/z 99, 81, 63, and 57 that are also produced in the CID of the 1,2- and the 1,3-diacylglycerols can also give information concerning the fragmentation pathways involved. As can be seen in Table 4.2, the experimentally derived ΔE_0 for the m/z 99, 81, 63, and 57 of the 1,2- and the 1,3-diacylglycerols are all lower than 2.2 eV (most are much lower around 1.6 to 1.7 eV). Ratio plots of m/z 81, 63, and 57 to m/z 99 are shown in Figure 4.9 for the three acylglycerols. As illustrated in the plots, the mechanisms for the production of the m/z 81, 63, and 57 product ions are different for the monoacylglycerol (Fig. 4.9a) as compared to the 1,2- (Fig. 4.9b) and the 1,3-diacylglycerols (Fig. 4.9c). For the 1,2- and the 1,3-diacylglycerols, the m/z 81, 63, and 57 product ions increase in production as the internal energy uptake of the system increases, whereas for the

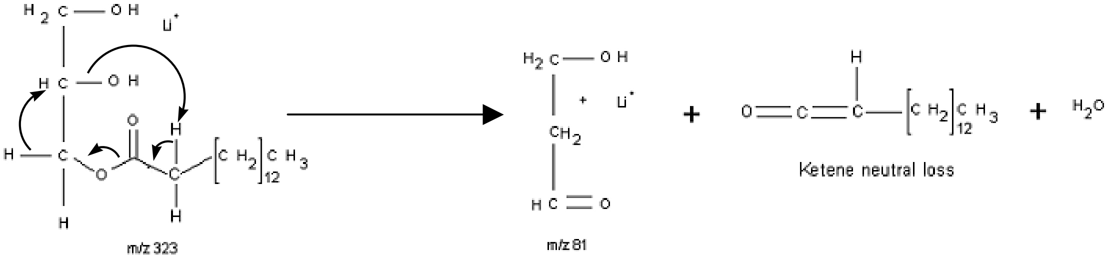

Figure 4.8. Proposed pathway for the direct production of the m/z 81 product ion from the m/z 323 precursor ion.

monoacylglycerol, the m/z 81, 63, and 57 product ions decrease in production as the internal energy uptake of the system increases. This suggests that the m/z 81, 63, and 57 product ions for the monoacylglycerol have pathways of formation that are competitive with the m/z 99 product ion at lower internal energies, and could have lower activation energies than the m/z 99 product ion as is reflected in the lower ΔE_0 values predicted by the derived effective reaction path length approach. An energy diagram describing the three pathways for the production of the m/z 99, 81, and 63 ions from the m/z 323 precursor is illustrated in Figure 4.7a. The energy diagram represents low energy pathways that do not require initial production of m/z 99. However, the apparent threshold energies that are being calculated represent the weighted average of all pathways that result in these product ions. Near the threshold region this is most likely to correspond to a single or predominant pathway to for a given m/z ion. The 1,3-dipentadecanoin lithium adduct was also modeled by Gaussian 98 for potential energy surfaces for the prediction of ΔH^0_{rxn} values for the production of the m/z 323 product ion through the neutral loss of a fatty acyl chain as a ketene. For the production of the m/z 323 product ion the ΔH^0_{rxn} was determined to be -0.42 eV (indicating an exothermic process), and the ΔE_0 was determined to be 1.66 ± 0.24 eV. The lower ΔE_0 for the initial ketene loss from the 1,3-dipentadecanoin compared to the ketene loss from the monopentadecanoin (1.66 ± 0.24 versus 2.87 ± 0.14 eV) is reflected in the lower energy state of the m/z 323 monopentadecanoin's ΔH^0_{rxn} of –0.42 eV. Though the mechanism for the dominant fatty acid substituent loss from the 1,2-diacylglycerol (loss of lithium fatty acetate forming m/z 313, ΔE_0 of 1.35 ± 0.13 eV) is different from that from the 1,3-diacylglycerol, i.e. loss of fatty acyl chain as ketene forming m/z 323, ΔE_0 of 2.87 ± 0.14 eV, (see Table 4.1 and Figure 4.3b) indicates an even lower stability of the 1,2-diacylglycerol as compared to the 1,3-diacylglycerol (and the monoacylglycerol). As illustrated in Fig. 4.7a, at low energies the production of the m/z 81 and m/z 63 ions appear to be from channels that circumvent m/z 99, and their apparent threshold energies are lower. However, at higher collision energies the predominant pathway for the production of the m/z 81 and m/z 63 product ions appears to occur by consecutive decompositions of the m/z 99 product ion as is illustrated in Figure 4.7b. The breaks in the higher energy pathways illustrate that the second threshold for the production of the m/z 81 and 63 product ions is unknown, and the current methodology cannot predict these.

4.4 Conclusions

The newly developed derived effective reaction path length approach for predicting BDE's with the triple quadrupole in our lab has demonstrated an effective use in fragmentation pathway studies as an enhancement to traditional energy-resolved mass spectrometry studies. By combining the calculated apparent threshold energies with the % Total Ion Abundance breakdown graphs, a more extensive quantitative description of fragmentation pathways is

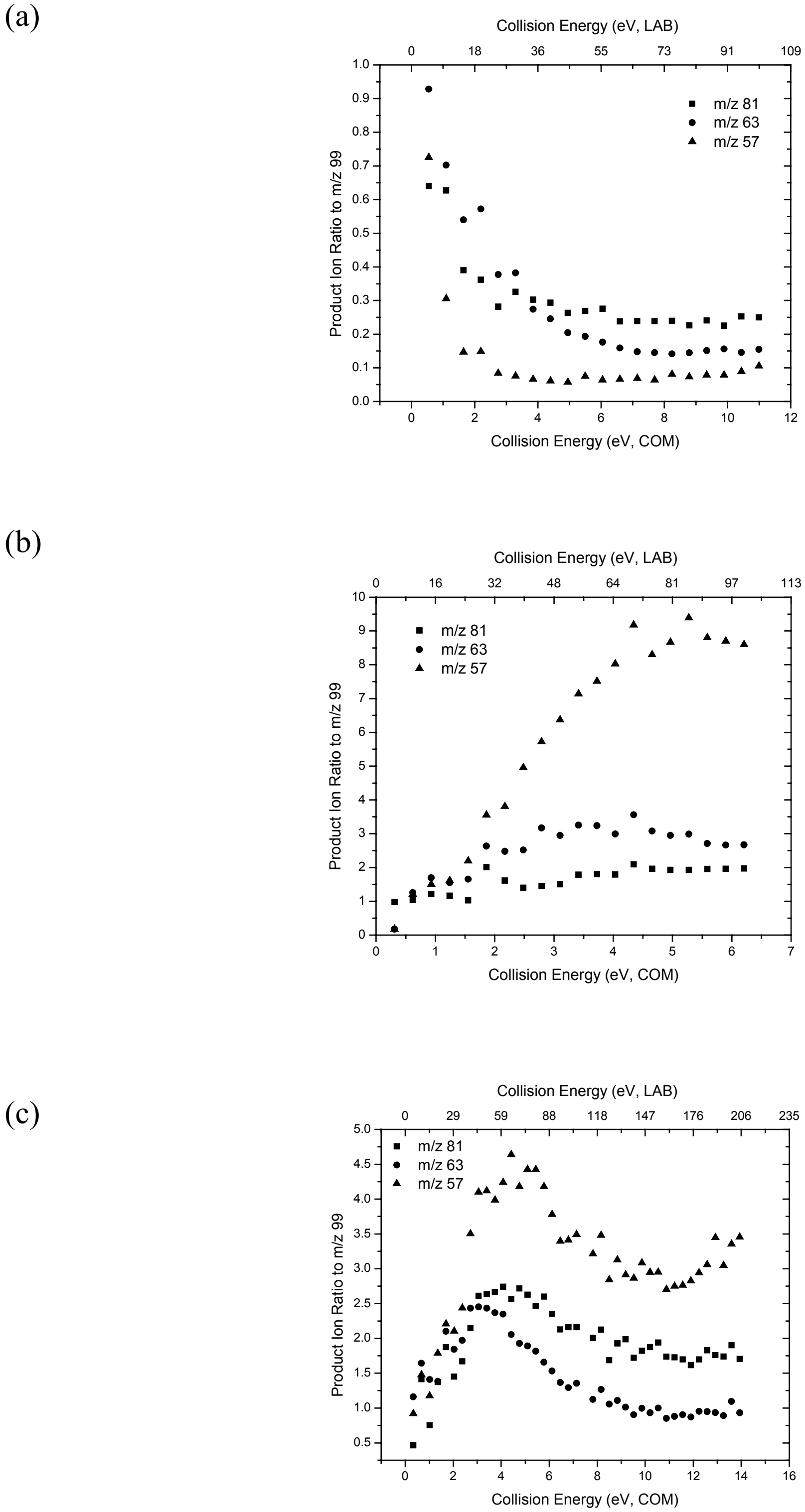

Figure 4.9. Ratio plots of m/z 57, 63, and 81 to m/z 99 for: (a) monopentadecanoin lithium adduct, (b) 1-stearin,2-palmitin diacylglycerol lithium adduct, and (c) 1,3-dipentadecanoin lithium adduct.

possible. The use of the derived effective reaction path length approach to calculate apparent threshold energies for the unimolecular fragmentation reactions of lithiated acylglycerols, by triple quadrupole, enabled unique interpretation of the product ion results. The observance of an inverse relationship between % Total Ion Abundance versus apparent threshold energies for the dissociation of the fatty acid substituents of the 1,2- and the 1,3-diacylglycerols suggests simple cleavage mechanisms that are competitive on the basis of activation energy. Also revealed by the calculated apparent threshold energies are the dissociation rankings of the form of the neutral loss of the fatty acyl substituent for the 1,2- and the 1,3-diacylglycerol. For the 1-stearin,2-palmitin diacylglycerol, the following favored fragmentation pathway was observed: loss of lithium fatty acetate > loss of fatty acid > loss of fatty acyl chain as ketene, and for the 1,3-dipentadecanoin diacylglycerol, the following favored fragmentation pathway was observed: loss of fatty acyl chain as ketene > loss of lithium fatty acetate > loss of fatty acid. Coupling the interpretative results for the mono-pentadecanoin fragmentation pathways and product ions, the high abundance, low apparent threshold energy observed for the production of the low molecular weight m/z 57 ion in the CID of the 1,2- and the 1,3-diacylglycerols was explained through two production mechanisms. In general, the derived effective reaction path length approach for apparent threshold energy determinations is relatively fast, straightforward, and easy to use, and has demonstrated itself to be applicable to both non-covalent, and covalent bond dissociation studies, making it versatile and general in gas-phase thermochemistry applications.

4.5 References

1. Whitehouse, C. M.; Dryer, R. N.; Yamashita, M.; Fenn, J. B. Electrospray interface for liquid chromatographs and mass spectrometers. *Anal. Chem.* **1985**, *57*, 675-679.
2. Kebarle, P.; Ho, Y. In *Electrospray Ionization Mass Spectrometry,* Cole, R. B.; Ed.; Wiley: New York, 1997; p 17.

3. Cole, R. B. Some tenets pertaining to electrospray ionization mass spectrometry. *J. Mass Spectrom.* **2000**, *35*, 763-772.
4. Cao, P.; Stults, J. T. Mapping the phosphorylation sites of proteins using on-line immobilized metal affinity chromatography/capillary electrophoresis/electrospray ionization multiple stage tandem mass spectrometry. *Rapid Commun. Mass Spectrom.* **2000**, *14*, 1600-1606.
5. Ho, Y. P.; Huang, P. C.; Deng, K. H. Metal ion complexes in the structural analysis of phospholipids by electrospray ionization tandem mass spectrometry. *Rapid Commun. Mass Spectrom.* **2003**, *17*, 114-121.
6. Kocher, T.; Allmaier, G.; Wilm, M. Nanoelectrospray-based detection and sequencing of substoichiometric amounts of phosphopeptides in complex mixtures. *J. Mass Spectrom.* **2003**, *38,* 131-137.
7. Shukla, A. K.; Futrell, J. H. Tandem mass spectrometry: dissociation of ions by collisional activation. *J. Mass Spectrom.* **2000,** *35*, 1069-1090.
8. Katta, V.; Chait, B. T. Observation of the Heme-Globin complex in native myoglobin by electrospray-ionization mass spectrometry. *J. Am. Chem. Soc.* **1991,** *113*, 8534-8535.
9. Ganem, B.; Li, Y. T.; Henion, J. D. Detection of noncovalent receptor-ligand complexes by mass spectrometry. *J. Am. Chem. Soc.* **1991**, *113*, 6294-6296.
10. Ganem, B.; Li, Y. T. Henion, J. D. Observation of noncovalent enzyme-substrate and enzyme-product complexes by ion-spray mass spectrometry. *J. Am. Chem. Soc.* **1991**, *113*, 7818-7819.
11. Armentrout, P. B.; Beauchamp, J. L. Cobalt carbene ion: reactions of Co^{+} with C_2H_4, cyclo-C_3H_6, and cyclo-C_2H_4O. *J. Chem. Phys.* **1981**, *74*, 2819-2826.
12. Ervin, K. M.; Armentrout, P. B. Translational energy dependence of $Ar^{+} + XY = ArX^{+} + Y$ ($XY=H_2,D_2,HD$) from thermal to 30 eV c.m. *J. Chem. Phys.* **1985**, *83*, 166-189.
13. Weber, M. E.; Elkind, J. L.; Armentrout, P. B. Kinetic energy dependence of $Al^{+} \rightarrow O_2$ $AlO^{+} + O$. *J. Chem. Phys.* **1986**, *84,* 1521-1529.
14. Aristov, N.; Armentrout, P. B. Collision-induced dissociation of vanadium monoxide ion. *J. Chem. Phys.* **1986**, *90*, 5135-5140.
15. Hales, D. A.; Lian, L.; Armentrout, P. B. Collision-induced dissociation of Nb^{+}_{n} (n=2-11): bond energies and dissociation pathways. *Int. J. Mass Spectrom. Ion Processes* **1990**, *102*, 269-301.
16. Schultz, R. H.; Crellin, K. C.; Armentrout, P. B. Sequential bond energies of $Fe(CO)_x^{+}$ (x=1-5): systematic effects on collision-induced dissociation measurements. *J. Am. Chem. Soc.* **1991**, *113*, 8590-8601.
17. Rodgers, M. T.; Ervin, K. M.; Armentrout, P. B. Statistical modeling of collision-induced dissociation thresholds. *J. Chem. Phys.* **1997**, *106*, 4499-4508.
18. Rodgers, M. T.; Armentrout, P. B. Statistical modeling of competitive threshold collision-induced dissociation. *J. Chem. Phys.* **1998**, *109*, 1787-1800.
19. Rodgers, M. T.; Armentrout, P. B. Noncovalent metal-ligand bond energies as studied by threshold collision-induced dissociation. *Mass Spec Rev* **2000**, *19*, 215-247.
20. Daniel, J. M.; Friess, S. D.; Rajagopala, S.; Wendt, S.; Zenobi, R. Quantitative determination of noncovalent binding interactions using soft ionization mass spectrometry. *Int. J. Mass Spectrom.* **2002**, *216*, 1-27.
21. Colorado, A.; Brodbelt, J. An Empirical Approach to Estimation of Critical Energies by Using a Quadrupole Ion Trap, *J Am Soc Mass Spectrom* **1996**, *7*, 1116-1125.

22. Graul, S. T.; Squires, R. R. Gas-Phase Acidities Derived from Threshold Energies for Activated Reactions, *J. Am. Chem. Soc.* **1990**, *112*, 2517-2529.
23. Sunderlin, L. S.; Wang, D.; Squires, R. R. Bond Strengths in First-Row-Metal Carbonyl Anions, *J. Am. Chem. Soc.* **1993**, *115*, 12060-12070.
24. Anderson, S. G.; Blades, A. T.; Klassen, J.; Kebarle, P. Determination of ion-ligand bond energies and ion fragmentation energies of electrospray-produced ions by collision-induced dissociation threshold measurements, *Int. J. Mass Spectrom Ion Processes* **1995**, *141*, 217-228.
25. Klassen, J. S.; Anderson, S. G.; Blades, A. T.; Kebarle, P. Reaction enthalpies for M+L = M+ + L, where M+ = Na+ and K+ and L = acetamide, N-methylacetamide, N,N-dimethylacetamide, glycine, and glyvylglycine, from determinations of the collision-induced dissociation thresholds, *J. Phys. Chem.* **1996**, *100*, 14218-14227.
26. Kebarle, P. Gas phase ion thermochemistry based on ion-equilibria. From the ionosphere to the reactive centers of enzymes, *Int. J. Mass Spectrom.* **2000**, *200*, 313-330.
27. Nielsen, S. B.; Masella, M.; Kebarle, P. Competitive gas-phase solvation of alkali metal ions by water and methanol, *J. Phys. Chem. A* **1999**, *103*, 9891-9898.
28. Peschke, M.; Blades, A. T.; Kebarle, P. Binding energies for doubly-charged ions M2+ = Mg2+, Ca2+ and Zn2+ for n = 1 to 7 from gas phase equilibria determinations and theoretical calculations *J. Am. Chem. Soc.*, **2000**, *122*, 10440-10449.
29. Reid, C. J. Breakdown diagrams for low-mass cation from angle-resolved mass spectrometric measurements, *Organic Mass Spectrometry* **1991**, *26*, 402-409.
30. Martinez, R. I.; Ganguli, B. Kinetics and mechanism of the collision-activated dissociation of the acetone cation, *J Am Soc Mass Spectrom* **1992**, *3*, 427-444.
31. Rogalewicz, F.; Hoppilliard, Y.; Ohanessian, G. Fragmentation mechanisms of α-amino acids protonated under electrospray ionization: a collisional activation and ab initio theoretical study, *Int. J. Mass Spectrom.* **2000**, *195/196*, 565-590.
32. Vazquez, S.; Truscott, R. J. W.; O'Hair, R. A. J.; Weimann, A.; Sheil, M. M. A study of kynurenine fragmentation using electrospray tandem mass spectrometry, *J Am Soc Mass Spectrom* **2001**, *12*, 786-794.
33. Butcher, C. P. G.; Dyson, P. J.; Johnson, B. F. G.; Langridge-Smith, P. R. R.; McIndoe, J. S.; Whyte, C. On the use of breakdown graphs combined with energy-dependent mass spectrometry to provide a complete picture of fragmentation processess, *Rapid Commun. Mass Spectrom.* **2002**, *16*, 1595-1598.
34. Harrison, A. G. Energy-resolved mass spectrometry: a comparison of quadrupole cell and cone-voltage collision-induced dissociation, *Rapid Commun. Mass Spectrom.* **1999**, *13*, 1663-1670.
35. Harrison, A. G.; Csizmadia, I. G.; Tang, T. H.; Tu, Y. P. Reaction competition in the fragmentation of protonated dipeptides, *J. Mass Spectrom.* **2000**, *35*, 683-688.
36. Chass, G. A.; Marai, C. N. J.; Harrison, A. G.; Csizmadia, I. G. Fragmentation reactions of a2 ions derived from deprotonated dipeptides – a synergy between experiment and theory, *J. Phys. Chem. A* **2002**, *106*, 9695-9704.
37. Martinez, R. I.; Instrument-independent MS/MS database for xqq instruments: a kinetics-based measurement protocol *J Res. Natl. Inst. Std. Technol. (U.S.)* **1989**, *94*, 281- 304.
38. McLafferty, F. W.; Turecek, F. *Interpretation of Mass Spectra*, 4th ed.; University Science Books: CA, 1993; p 115.

39. Ham, B. M.; Cole, R. B. Determination of Bond Dissociation Energies Using Electrospray Tandem Mass Spectrometry and a Novel Derived Effective Reaction Path Length Approach (manuscript accepted by Analytical Chemistry).
40. Srivastava, M. S. *Methods of Multivariate Statistics*, 1st ed.; John Wiley & Sons, Inc.: New York, 2002; p 365.
41. Ham, B. M.; Jacob, J. T.; Keese, M. M.; Cole, R. B. Identification, quantification and comparison of major non-polar lipids in normal and dry eye tear lipidomes by electrospray tandem mass spectrometry. *J. Mass Spectrom.* **2004**, *39*, 1321-1336.
42. Gaussian 98, Revision A.3, M. J. Frisch, G. W. Trucks, H. B. Schlegel, G. E. Scuseria, M. A. Robb, J. R. Cheeseman, V. G. Zakrzewski, J. A. Montgomery, Jr., R. E. Stratmann, J. C. Burant, S. Dapprich, J. M. Millam, A. D. Daniels, K. N. Kudin, M. C. Strain, O. Farkas, J. Tomasi, V. Barone, M. Cossi, R. Cammi, B. Mennucci, C. Pomelli, C. Adamo, S. Clifford, J. Ochterski, G. A. Petersson, P. Y. Ayala, Q. Cui, K. Morokuma, D. K. Malick, A. D. Rabuck, K. Raghavachari, J. B. Foresman, J. Cioslowski, J. V. Ortiz, B. B. Stefanov, G. Liu, A. Liashenko, P. Piskorz, I. Komaromi, R. Gomperts, R. L. Martin, D. J. Fox, T. Keith, M. A. Al-Laham, C. Y. Peng, A. Nanayakkara, C. Gonzalez, M. Challacombe, P. M. W. Gill, B. Johnson, W. Chen, M. W. Wong, J. L. Andres, C. Gonzalez, M. Head-Gordon, E. S. Replogle, and J. A. Pople, Gaussian, Inc., Pittsburgh PA, 1998.

CHAPTER V: IDENTIFICATION, QUANTITATION AND COMPARISON OF MAJOR NON-POLAR LIPIDS IN NORMAL AND DRY EYE TEAR LIPIDOMES BY ES-MS-MS

5.1 Introduction

Millions of humans are afflicted with *keratoconjunctivitis sicca* (KCS, also known as "dry eye"), which can be associated with aging, disease, smoke, surgery, or any form of irritation of the eye. The National Eye Institute's (NEI) definition of dry eye states that KCS is a disorder of the ocular tear film layer usually caused by a tear deficiency, or excessive evaporation of the aqueous layer, resulting in damage to the ocular surface and symptoms of discomfort(1). Some forms of dry eye may be physiologically related, perhaps from the breakdown of the eye tear layer, or to hormones, as demonstrated in a hormone replacement study by Schaumberg, et.al.(1). In two separate demographic studies, it has been estimated that 11% of Europeans (Copenhagen criteria), between the ages of 30 and 60 years suffer from dry eye symptoms(2), and that 14.6% of Americans over the age of 65 years (approximately 4.3 million people) also suffer from dry eye symptoms(3). Although their symptoms are similar, the underlying causes are often unknown and no practical method for evaluating the composition of tears from such patients exists. Therapeutical approaches for the treatment of dry eye include application of artificial tear drops for wetting and lubrication(4,5), corticosteroids (anti-inflammatory agents), anti-biotics and immunosuppresants such as cyclosporin(6). The widely used dry eye drops consist of various solutions containing electrolytes, organic additives, etc., but are primarily composed of water (97-99%)(4).

The structure of the ocular tear film is generally divided into three layers: the innermost corneal layer, an intermediate aqueous-mucin layer(7,8), and an outermost lipid layer(9). One of the functions of the outer lipid layer is to retard the evaporation of the inner aqueous layer. The lipids are supplied to the tear film through the meibomian gland. The chemical composition of the human meibomian gland liquid secretions is a complex mixture of cholesterol and wax esters, triglycerides, free fatty acids, diesters, free cholesterol, hydrocarbons, and polar lipids(10-14), with water composing 98-98.5%(4). Some forms of dry eye may be related to the breakdown of the eye tear layer.

Electrospray(15-17) tandem mass spectrometry (ES-MS/MS) is a powerful analytical tool for compound identification(18-20). In this paper, we use this method to develop a standard lipid component profile of normal tears and identify specific component differences in the tears from a dry eye model. Through the development of this technology to provide specific information concerning the lipid profile of a healthy person's tear, it may be possible to identify a defective lipid profile, something which has been suggested to be a major contributor to the dry eye syndrome(21). The mass spectrometric analysis of acylglycerides, which are comprised of mono-, di-, and triglycerides, has been reported using various approaches such as derivative gas chromatography-electron ionization mass spectrometry GC-EI-MS(22-24), positive chemical ionization(22), negative chemical ionization(25-27) (NCI) of chloride adducts, ES-MS/MS(28,29) including ES-MS/MS of ammonium adducts(30,31), MALDI-TOF(32,33), fast atom bombardment (FAB)(34), atmospheric pressure chemical ionization (APCI) mass spectrometry(30,35), and APCI liquid chromatography/mass spectrometry(36-38) (LC/MS). Quantifying triglycerides using ratios of diacylglyceride fragment ions vs parent ions and fragmentation schemes has been reported for single-stage APCI-MS experiments(39-42). Saturated acylglycerides do not readily form protonated molecules, even in acidified solutions, so alkali metal salt (Na^+), and ammonium acetate (NH_4^+), have been used as additives in chloroform:methanol for both ES, and APCI

LC/MS. It has also been reported(36) that APCI LC/MS is not sensitive enough to detect even moderately low amounts (about 2.5 mg/mL) of monoacylglycerides under standard solutions.

In our mass spectrometry work involving the identification of lipid fractions in tear samples, Li^+ was chosen as the alkali metal for adduct formation for both the non-polar lipids such as the acylglycerides and wax esters that, to our knowledge, have not appeared in the literature, and for the more polar phosphorylated lipids, which have previously been reported(43). The specific use of lithium adducts has been reported for FAB-MS-MS, and ES-MS studies of oligosaccharides(44,45), for the ES ionization and structural determination of triacylglycerides(29,46), for ionization of aryl 1,2-diols by fast atom bombardment(34), and for FAB ionization and structural identification of fatty acids(47). In this paper, we present a detailed description of the major fragments produced from ES-MS/MS studies employing collisionally induced dissociation (CID) of lithium adducts of monoacylglycerides, and 1,2- and 1,3-diacylglycerides, which can produce informative product ion spectra for the identification of complex biological extracts.

5.2 Experimental

5.2.1 Instrumentation

Mass spectra were obtained using a triple quadrupole mass spectrometer (Micromass, Inc., Manchester, UK, model Quattro II) equipped with an electrospray interface operating at typical flow rates of 2-4 µL/min. Nitrogen was used as both nebulizing and drying gas. Argon was used as collision gas during collision induced dissociation (CID) experiments, at collision cell pressures of approximately 3.0×10^{-4} mBar (measured external to the cell). The typical "cone" voltage setting was 40 V, and the ES capillary voltage was held at 2.5 to 3.5 kV. For quantification of the lipids, internal standards having similar structures to the lipids (monopentadecanoin, dipentadecanoin, triheptadecanoin, and palmityl behenate) were employed to minimize differences in ionization efficiencies(53). MassLynx software (Micromass) was used to acquire, process, and store mass spectral data.

5.2.2 Rabbit Dry Eye Model

The rabbit dry eye model was created in female New Zealand white rabbits by two sequential surgical procedures. First, the main lacrimal gland was removed from the experimental eye; the contralateral eye was used as the control. Approximately 2 weeks later, the accessory lacrimal gland and nictitating membrane were removed from the experimental eye. Tear breakup time (TBUT, measured by slit lamp with a Tearscope^{tm}) was measured daily. When the TBUT of the surgical eye was half or less that of the control eye, the surgical eye was considered to be 'dry'. Baseline tears (representing tears produced under non-irritating conditions) were collected daily from the normal and surgically induced dry eyes using 5 µL silanated microcapillary pipettes.[48–50] The usual volume obtained from a normal eye was 3 µL each, whereas only 1 µL was typically obtained from a dry eye. The tear samples were immediately placed in Eppendorf tubes and preserved by storage at –70 °C. The non-polar lipid fractions were extracted from tear samples with a simple chloroform solvent modification procedure[51,52] and reconstituted in 9 : 1 methanol–chloroform solutions containing 2 mM LiCl.[43]

5.2.3 A Note on Stereochemistry of Acylglycerides

All vicinal diacylglycerides in this report have unknown stereochemistries at the chiral carbon. Differentiation between 1,2-diglycerides and 2,3-diglycerides is not possible, and for convenience these are all designated as 1,2-diglycerides in the text. Similarly, 3-position monoglycerides are not distinguishable from 1- position monoglycerides, and the 1-position is used to describe both. Moreover, 1,3-diglycerides cannot be distinguished from their enantomers and the 1-position is arbitrarily assigned to the largest alkyl chain.

5.3 Results and Discussion

It was observed that, in the positive mode, mass spectral signal intensities of the lithiated adduct species (upon addition of 2 mM LiCl) were more reproducible than those of the corresponding protonated lipid molecules, or mass analysis of the deprotonated lipid species in the negative mode. Upon decomposition, the lithium adducts were also observed to form product ions that were characteristic of the lipid being analyzed, as will be described below.

Comparison of ES-MS spectra for normal human tear and normal rabbit tear, obtained in our laboratory, have shown close similarities where the total chloroform extractables from normal rabbit tears match quite closely those from human tears. This suggests that the rabbit tears are quite close in composition to human tears, which would allow extrapolation of findings from one species to the other. Secondly, it was noted that there was not a readily observable difference in major components when comparing normal tears with dry eye tear total chloroform extractables, though changes in the fatty acid fragments of the non-polar, and polar lipids have been reported by Sullivan, et. al.(54-57) for people suffering from dry eye due to an androgen deficiency caused by Sjogren’s syndrome, menopause, and aging.

5.3.1 MS of Lipid Standards

5.3.1.1 Product Ion Spectra

Figure 5.1a is the product ion spectrum of the lithiated adduct of triheptadecanoin. The characteristic informative peaks include the C17:0 acylium ion at m/z 253 $[C_{17}H_{33}O]^+$, the lithium adduct of heptadecanoic acid at m/z 277 $[C_{17}H_{34}O_2Li]^+$, the neutral loss of heptadecanoic acid, then the neutral loss of a C17:1 alpha-beta unsaturated fatty acid, to give the m/z 317 product ion $[MLi - C_{17}H_{34}O_2 - C_{17}H_{32}O_2]^+$, the parent ion minus lithiated heptadecanoate at m/z 579 $[MLi – C_{17}H_{33}O_2Li]^+$, and the parent ion minus the neutral loss of heptadecanoic acid at m/z 585 $[MLi – C_{17}H_{34}O_2]^+$. The m/z 579 product ion from the neutral loss of a catonized fatty acetate, from triglycerides, is observed in ES tandem mass spectrometry studies with ammonium adducts(36), but the product ions of m/z 317 and m/z 585, which both involve the neutral loss of a fatty acid, have not. Hsu et al.(46) also reported the neutral loss of fatty acids from lithiated triglycerides using a triple quadrupole with an electrospray interface. The spectrum also contains hydrocarbon fragment ions at m/z 43, m/z 57, m/z 71, and m/z 85 which are derived from σ-bond cleavage of the fatty acid hydrocarbon chains. Also included in the lower mass region is the product ion at m/z 99 which is the lithium adduct of the glycerol backbone, and an ion at m/z 81 derived from water loss from this glycerol backbone.

The product ion spectrum of 1,3-dipentadecanoin, Figure 5.1b, also contains the hydrocarbon fragment ions, and a peak at m/z 63 for two water losses from the glycerol backbone, in addition to m/z 99 and m/z 81 from glycerol. In the m/z 200 to m/z 350 region there are two major fragment peaks which characterize this diglyceride, i.e., lithiated pentadecanoic acid at m/z 249 $[C_{15}H_{30}O_2Li]^+$, and the m/z 323 fragment ion that has undergone

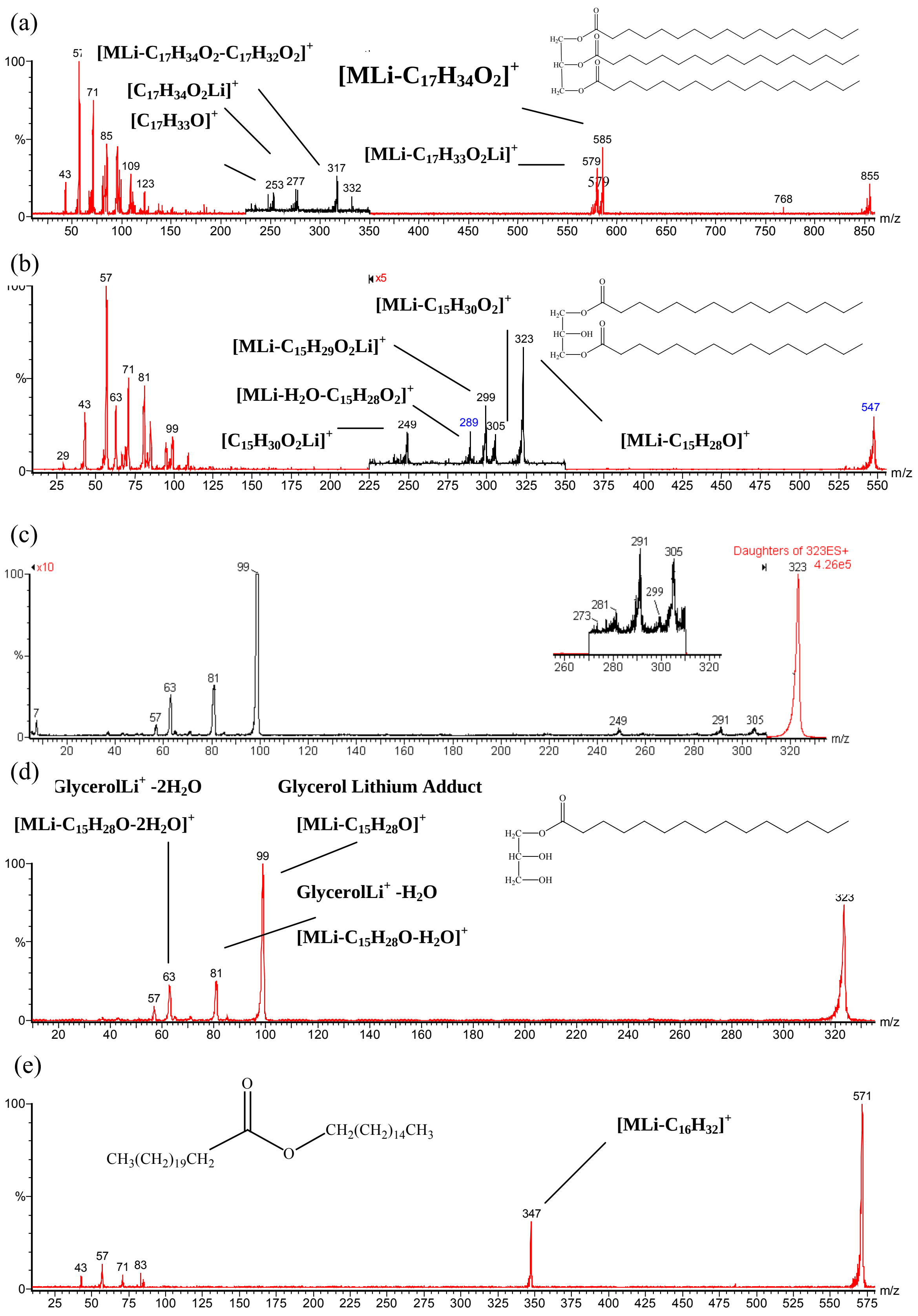
(a)
$[MLi-C_{17}H_{34}O_2-C_{17}H_{32}O_2]^+$
$[C_{17}H_{34}O_2Li]^+$
$[C_{17}H_{33}O]^+$
$[MLi-C_{17}H_{34}O_2]^+$
$[MLi-C_{17}H_{33}O_2Li]^+$
57
71
85
43
109
123
253
277
317
332
585
579
579
768
855
100
%
0
m/z
50
100
150
200
250
300
350
400
450
500
550
600
650
700
750
800
850
(b)
x5
57
71
81
43
63
99
29
249
289
299
305
323
547
$[MLi-C_{15}H_{30}O_2]^+$
$[MLi-C_{15}H_{29}O_2Li]^+$
$[MLi-H_2O-C_{15}H_{28}O_2]^+$
$[C_{15}H_{30}O_2Li]^+$
$[MLi-C_{15}H_{28}O]^+$
25
50
75
100
125
150
175
200
225
250
275
300
325
350
375
400
425
450
475
500
525
550
m/z
(c)
x10
99
63
81
57
7
249
291
305
Daughters of 323ES+
4.26e5
323
291
305
299
281
273
260
280
300
320
20
40
60
80
100
120
140
160
180
200
220
240
260
280
300
320
m/z
(d)
$GlycerolLi^+ -2H_2O$
Glycerol Lithium Adduct
$[MLi-C_{15}H_{28}O-2H_2O]^+$
$[MLi-C_{15}H_{28}O]^+$
$GlycerolLi^+ -H_2O$
$[MLi-C_{15}H_{28}O-H_2O]^+$
99
63
81
57
323
20
40
60
80
100
120
140
160
180
200
220
240
260
280
300
320
m/z
(e)
O
$CH_2(CH_2)_{14}CH_3$
$CH_3(CH_2)_{19}CH_2$
O
$[MLi-C_{16}H_{32}]^+$
571
347
43
57
71
83
25
50
75
100
125
150
175
200
225
250
275
300
325
350
375
400
425
450
475
500
525
550
575
m/z

Figure 5.1. Positive mode ES-MS/MS product ion spectra of the lithium adducts of the internal acylglyceride standards used for identification and quantification of extracted lipids $[MLi]^+$, with peak assignments of major informative fragment ions for: (a) triheptadecanoin m/z 855, (b) 1,3-dipentadecanoin m/z 547, (c) "up-front" CID-MS-MS experiment using precursor (m/z 323) fragment ions formed from "up-front" dissociation of the 1,3-dipentadecanoin standard (m/z 547) $[M + Li]^+$. The product ion peak at m/z 299 (inset) indicates the minor pathway of a step-wise initial "in-source" loss of ketene, followed by LiOH, in addition to production of m/z 299 from the loss of the lithium fatty acetate from m/z 547. Positive mode ES-MS/MS product ion spectra of: (d) monopentadecanoin m/z 323, and (e) palmityl behenate m/z 571.

neutral loss of C15:0 fatty acyl chain as a ketene $[MLi – C_{15}H_{28}O]^+$. Also observed are peaks at m/z 289 from the consecutive neutral losses of H_2O followed by C15:1 alpha-beta unsaturated fatty acid $[MLi – H_2O – C_{15}H_{28}O_2]^+$. The order of this consecutive process was ascertained by a precursor scan of m/z 289 that showed peaks at m/z 547 for the lithiated parent ion, and m/z 529 representing loss of H_2O from the m/z 547 parent. Notably the peak that would correspond to initial $C_{15}H_{28}O_2$ loss at m/z 307 was not observed, thus indicating a two-step process with H_2O loss being the first step. Fig. 5.1b also shows peaks at m/z 299 formed from the neutral loss of C15:0 lithium fatty acetate $[MLi - C_{15}H_{29}O_2Li]^+$, and at m/z 305 for the neutral loss of C15:0 fatty acid $[MLi – C_{15}H_{30}O_2]^+$. The loss of NH_4OH, then ketene, has been observed and reported by APCI LC/MS(36), which would be analogous to the pathway leading to m/z 299 if the process occurs in two steps, involving initial loss of C:15 fatty ketene, followed by loss of LiOH; alternatively it could be formed through neutral loss of C15:0 lithium fatty acetate. To distinguish which fragment pathway was responsible for the m/z 299 product ion, an experiment was performed where the loss of the C:15 fatty ketene from the m/z 547 precursor was produced in the source using high cone voltage (i.e. "in-source" or "up-front" collision induced dissociation, CID). M/z 323 was then isolated with the first quadrupole, subjected to CID in the central hexapole, and the product ions scanned by the third quadrupole for the loss of LiOH at m/z 299. Figure 5.1c illustrates the results of the experiment where a small peak was observed at m/z 299 indicating that this fragmentation pathway can occur, i.e., the loss of a fatty ketene followed by loss of LiOH, but it is much less favored than the direct neutral loss of the C:15 lithium fatty acetate from the m/z 547 precursor. Finally, to the best of our knowledge, the second product ion observed at m/z 323 (Fig. 5.1b) through the loss of ketene, resulting in a lithium adduct of monoacylglycerol has not been reported.

Figure 5.1d is the product ion spectrum from the collision induced dissociation of lithiated monopentadecanoin. Three peaks characteristic of the fragmentation of lithiated monoglycerides are observed in the lower molecular weight region. The major ion at m/z 99 is the glycerol backbone derived from the neutral loss of the C15:0 fatty ketene from the parent ion $[MLi - C_{15}H_{28}O]^+$. The next two ion peaks at m/z 81 and m/z 63 are the subsequent loss of one, and then two H_2O molecules from the glycerol backbone as was observed for the tri- and diglycerides. Figure 5.1e is the product ion spectrum of the lithium adduct of palmityl behenate, a representative fatty acid/fatty alcohol wax ester. In the low mass region, only the hydrocarbon fragments are observed at m/z 43, m/z 57, m/z 71, m/z 83 (one unsaturation), and m/z 85. In the m/z 350 region there is one predominant peak appearing at m/z 347. This represents the neutral loss of the carbon chain of the fatty alcohol $[MLi - C_{16}H_{32}]^+$, leaving the lithium adduct of the fatty acid portion of the wax ester at m/z 347 $[C_{22}H_{44}O_2Li]^+$.

5.3.1.2 Lipid Fragmentation Pathways

Figures 5.2, 5.3, and 5.4 are diagrams illustrating the major fragment ions produced from CID of the lithium adducts of the acylglycerides triheptadecanoin, 1,3-dipentadecanoin, and monopentadecanoin, respectively. Mu, et. al.(36), and Holcapek, et. al.(37), each have reported different types of fragmentation pathways for the CID of CI-generated diglycerides employing ammonium adducts(36), or protonated, diglycerides with 3 or more double bonds(37). To determine whether a different product ion spectrum would be obtained for the two types of substitution (1,2- versus 1,3-), and whether a distinction could be made between the two substituents on a 1,2-diglyceride, a 1-stearin-2-palmitin diglyceride standard was analyzed by tandem mass spectrometry as the lithium adduct. Recall that in the product ion spectrum of the 1,3-dipentadecanoin standard (Figure 5.1b), the predominant ion was the m/z 323 peak from the loss of C15:0 fatty acyl chain as a ketene from the parent ion $[MLi - C_{15}H_{28}O]^+$, followed by the peak at m/z 299 for the neutral loss of C15:0 lithium fatty acetate $[MLi - C_{15}H_{29}O_2Li]^+$. In Fig. 5.5a, the product ion spectrum of the lithium adduct of the 1,2-diglyceride, the predominant product ions are m/z 313 and m/z 341. The m/z 313 product ion is derived from the loss of C18:0 lithium fatty acetate, which is in the 1- position, $[MLi - C_{18}H_{35}O_2Li]^+$. The second major product ion at m/z 341 is derived from the loss of C16:0 lithium fatty acetate, which is in the 2-position, $[MLi - C_{16}H_{31}O_2Li]^+$. The greater intensity of the m/z 313 peak versus m/z 341 indicates that lithium fatty acetate loss occurs with greater facility from the 1-position relative to the analogous loss from the 2-position. Thus, when two non-identical fatty acyl substituents are present on a 1,2- diglyceride, the higher intensity monoacyl fragment has lost the substituent that was formerly at the 1-position. This behavior is identical to the type of selective loss of the fatty acid from the 1-position being greater than the analogous loss from the 2-position observed with the phosphorylated lipids(43). To verify the positional selectivity of this lithium fatty acetate loss, the lithium adduct of 1-palmitin-2-stearin diglyceride was subjected to CID under similar conditions. The product ion spectrum showed that the predominant neutral loss was that of C16:0 lithium fatty acetate, from the 1-position. This behavior indicates that the principal factor in determining the preferred neutral loss of a lithium fatty acetate is the position (i.e, 1-position is favored over the 2-position), rather than chain length. The spectrum (Fig. 5.5a) also contains a low intensity peak at m/z 365 for the loss of the 2-position C16:0 fatty acyl chain as a ketene [MLi - $C_{16}H_{30}O$]$^+$, and a very minor peak at m/z 337 for the loss of the 1-position C18:0 fatty

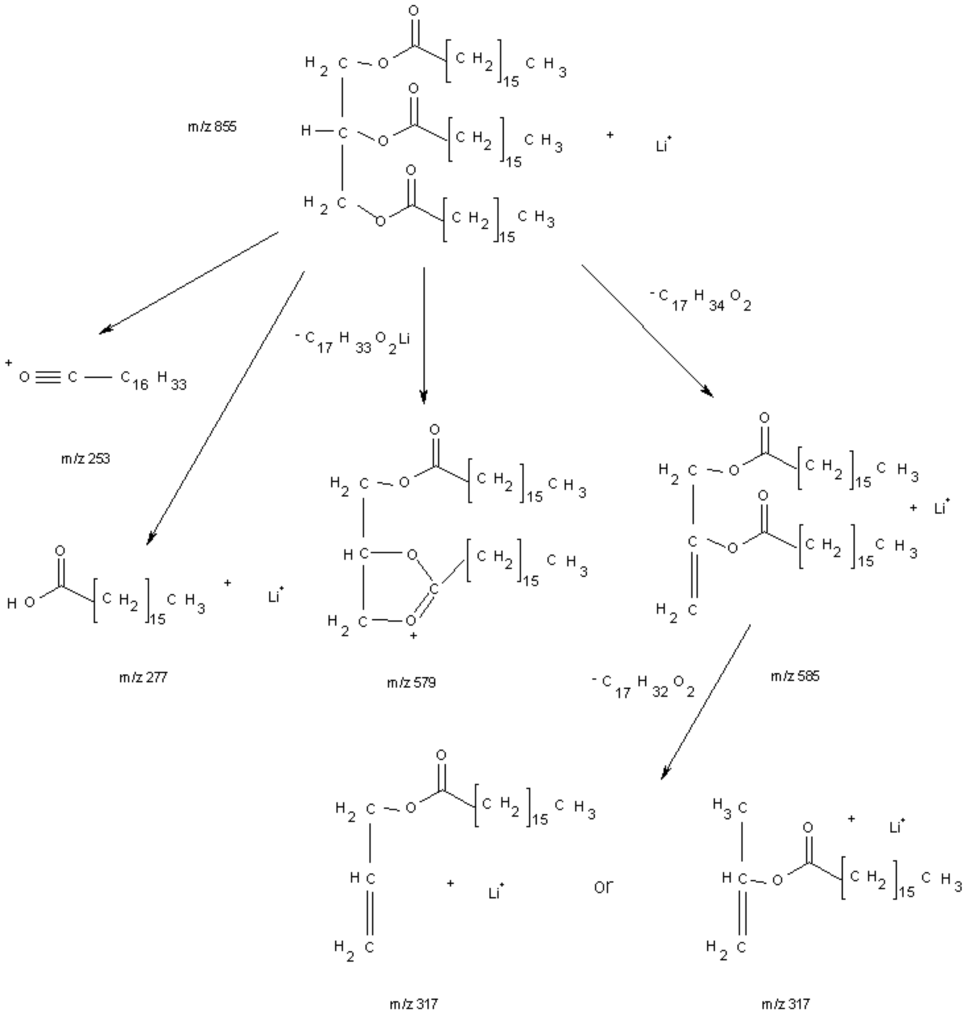

Figure 5.2. Major fragment ions produced from the collisionally induced dissociation of triheptadecanoin m/z 855 [MLi]$^+$: the C17:0 acylium ion at m/z 253 [$C_{17}H_{33}O$]$^+$, the lithium adduct of heptadecanoic acid at m/z 277 [$C_{17}H_{34}O_2Li$]$^+$, the neutral loss of heptadecanoic acid, then the neutral loss of a C17:1 alpha-beta unsaturated fatty acid, to give the m/z 317 product ion [MLi - $C_{17}H_{34}O_2$ - $C_{17}H_{32}O_2$]$^+$, the parent ion minus lithiated heptadecanoate at m/z 579 [MLi –

$C_{17}H_{33}O_2Li]^+$, and the parent ion minus the neutral loss of heptadecanoic acid at m/z 585 [MLi – $C_{17}H_{34}O_2]^+$.

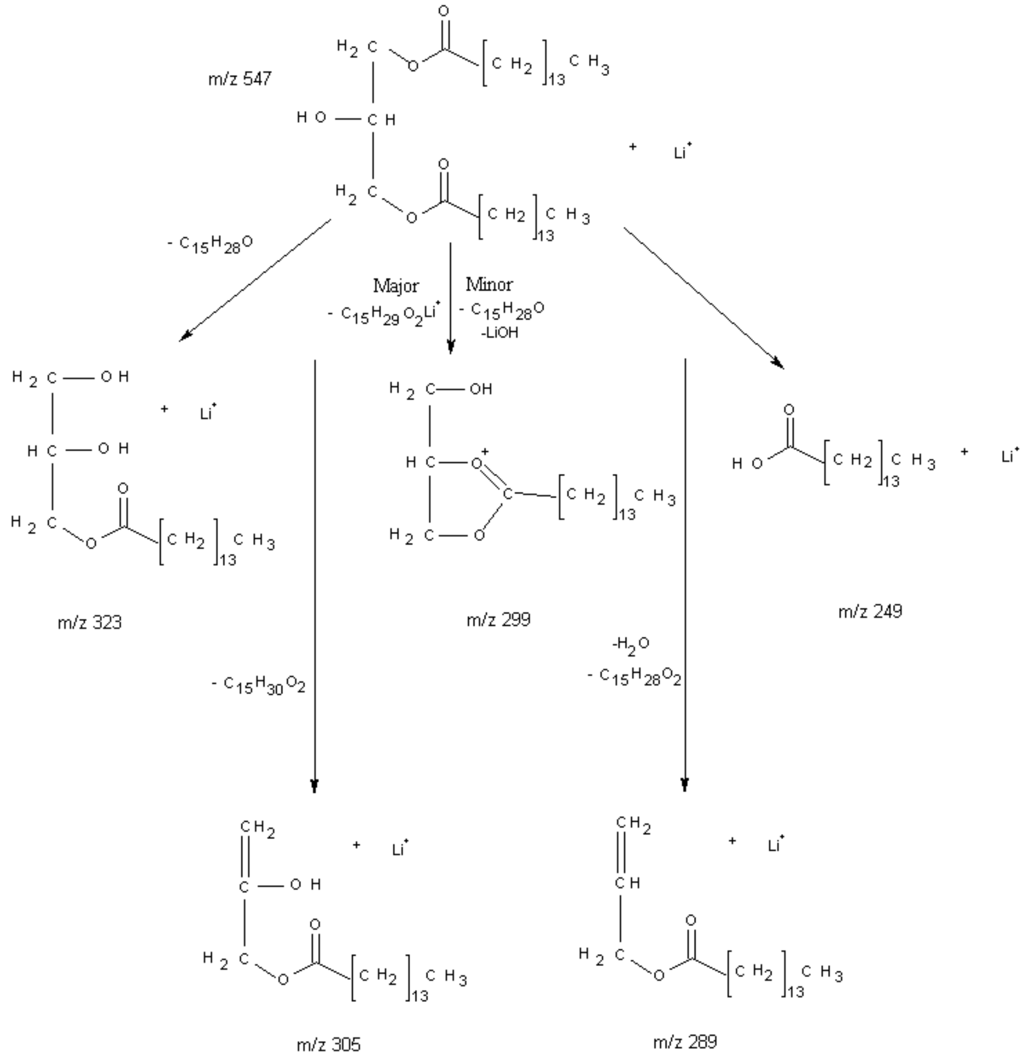

Figure 5.3. Major fragment ions produced from the collisionally induced dissociation of 1,3-dipentadecanoin m/z 547 $[MLi]^+$: the parent ion peak minus the neutral loss of C15:0 fatty acyl chain as ketene at m/z 323 $[MLi – C_{15}H_{28}O]^+$, the neutral loss of C15:0 lithium fatty acetate at m/z 299 $[MLi – C_{15}H_{29}O_2Li]^+$ (major path), or the loss of C15:0 fatty acyl chain as ketene from the parent ion followed by LiOH at m/z 299 $[MLi - C_{15}H_{28}O - LiOH]^+$ (minor path), the neutral loss of C15:0 fatty acid at m/z 305 $[MLi - C_{15}H_{30}O_2]^+$, the consecutive losses of H_2O followed by C15:1 alpha-beta unsaturated fatty acid at m/z 289 $[MLi - H_2O - C_{15}H_{28}O_2]^+$, and the lithiated fatty acid ion, pentadecanoic acid, at m/z 249 $[C_{15}H_{30}O_2Li]^+$.

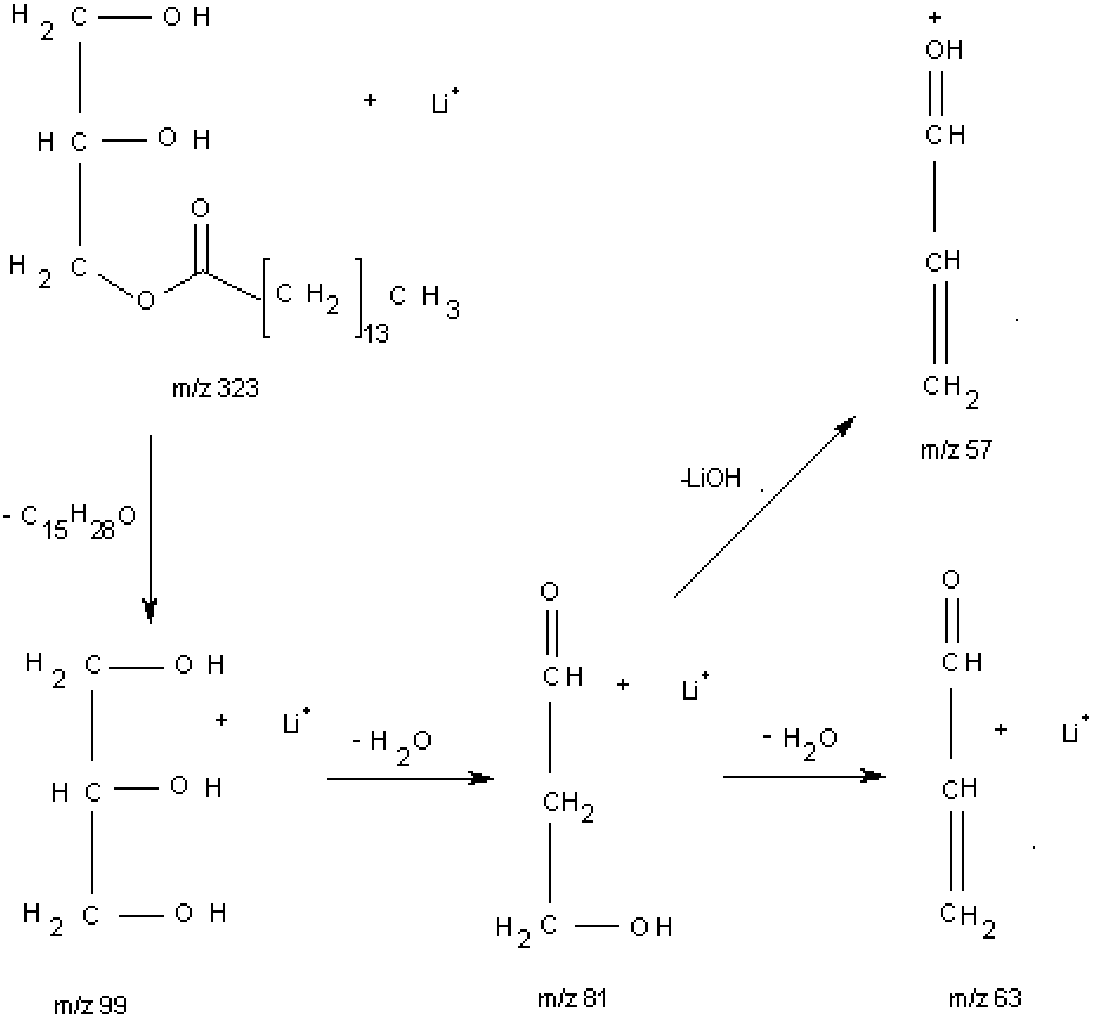

Figure 5.4. Major fragment ions produced from the collisionally induced dissociation of monopentadecanoin m/z 323 $[MLi]^+$: the major ion at m/z 99 is the glycerol backbone derived from the neutral loss of the C15:0 fatty acyl chain as a ketene from the parent ion $[MLi - C_{15}H_{28}O]^+$, and the m/z 81 and m/z 63 are the subsequent losses of one, and then two H_2O molecules from the lithiated glycerol backbone.

acyl chain as a ketene [MLi - $C_{18}H_{34}O$]$^+$. This behavior contrasts with that of a 1,3- diglyceride in that the latter shows significant ketene loss from the 1-, or 3-position as being responsible for the predominant product ions, whereas neutral losses of lithium fatty acetates are only minor. As a further control, the asymmetric 1,3-diglyceride 1-palmitin-3-stearin was analyzed under similar CID conditions. The resultant product ion spectrum confirmed that neutral losses of the fatty acyl chains as ketenes are the favored product ion pathways for 1,3-diglycerides, and peaks representing losses of each of the two fatty acid substituents were observed. Notably, for the asymmetric 1,3-diglyceride, loss of the longer C18:0 fatty acyl chain as a ketene was the slightly favored product ion as compared to the loss of the shorter C16:0 fatty acyl chain as a ketene, suggesting that for the asymmetric 1,3-diglyceride, a longer chain length can subtly increase the propensity for ketene loss. Also identified in the Fig. 5.5a spectrum are peaks for the neutral loss of C16:0 fatty acid at m/z 347 [MLi - $C_{16}H_{32}O_2$]$^+$, the neutral loss of the C18:0 fatty acid at m/z 319 [MLi - $C_{18}H_{36}O_2$]$^+$, and the lithium adducts of stearic acid at m/z 291 [$C_{18}H_{36}O_2Li$]$^+$, and palmitic acid at m/z 263 [$C_{16}H_{32}O_2Li$]$^+$.

Figure 5.5b is a diagram illustrating the major fragment ions produced from the collision induced dissociation of the lithium adduct of the 1-stearin-2-palmitin diglyceride standard. Figure 5.6 illustrates four proposed fragmentation pathways for the collisionally induced dissociation of the lithium adduct of 1-stearin-2-palmitin diglyceride. The top two processes (Fig. 5.6a and 5.6b) illustrate the major pathways producing product ions through the neutral loss of a lithium fatty acetate. The bottom two processes (Fig. 5.6c and 5.6d) are minor pathways each producing product ions through the neutral loss of a fatty ketene, followed by the loss of LiOH. Both processes result in the same m/z product ion with 5-membered ring formation to

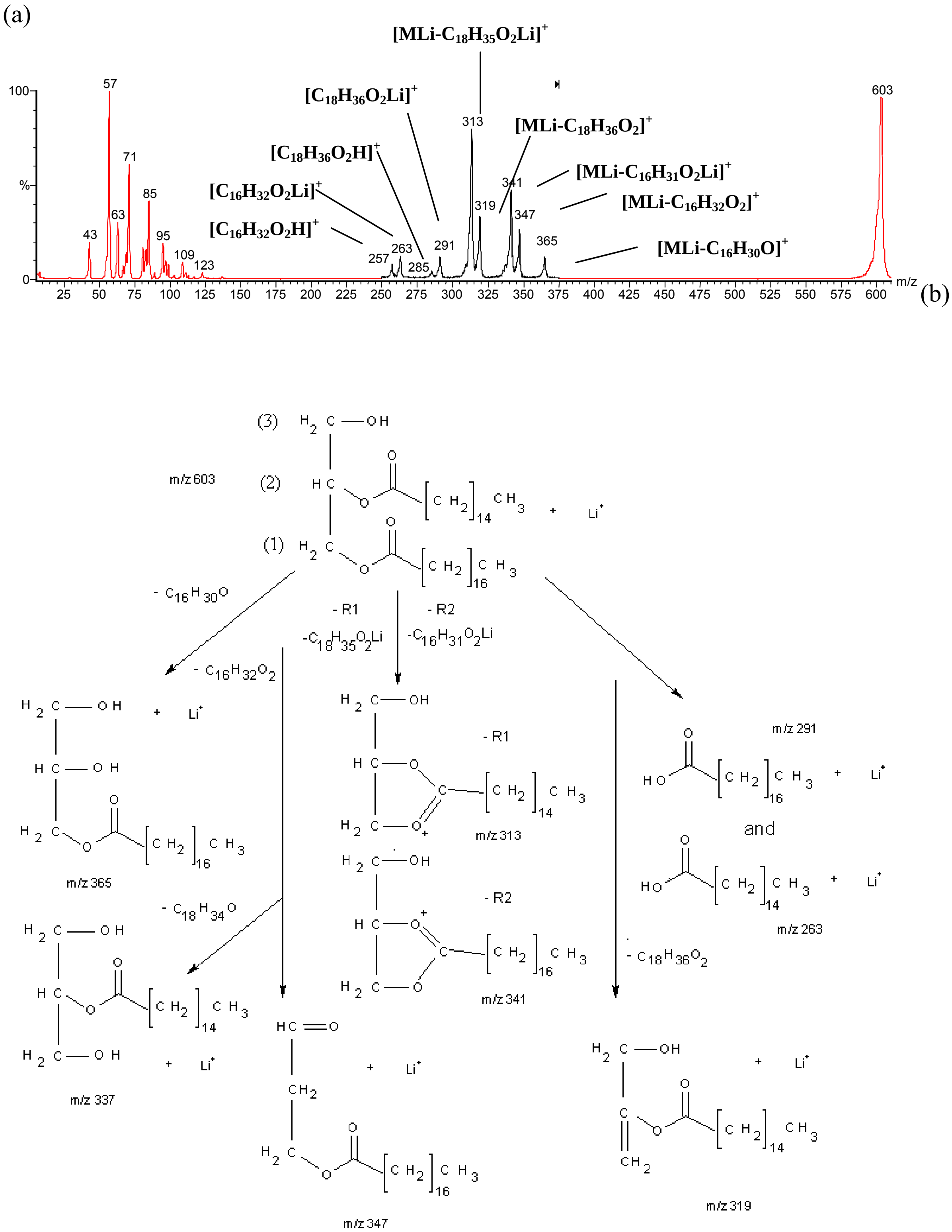

Figure 5.5. (a) Product ion spectrum of 1-stearin-2-palmitin standard at m/z 603. The greater intensity of the m/z 313 vs. m/z 341 allows the identification of the 1- position of the 1,2-diglyceride. (b) Major fragment ions produced from the collisionally induced dissociation of 1-stearin-2-palmitin diacylglycerol m/z 603 $[MLi]^+$: the m/z 313 ion from the neutral loss of C18:0

lithium fatty acetate (1- position), [MLi – $C_{18}H_{35}O_2Li$]$^+$, the ion at m/z 341 from the neutral loss of C16:0 lithium fatty acetate (2- position), [MLi – $C_{16}H_{31}O_2Li$]$^+$, the m/z 365 ion from the loss of the C16:0 fatty acyl chain as ketene [MLi - $C_{16}H_{30}O$]$^+$, the neutral loss of C16:0 fatty acid at m/z 347 [MLi - $C_{16}H_{32}O_2$]$^+$, the neutral loss of the C18:0 fatty acid at m/z 319 [MLi - $C_{18}H_{36}O_2$]$^+$, the lithium adducts of stearic acid at m/z 291 [$C_{18}H_{36}O_2Li$]$^+$, the lithium adduct of palmitic acid at m/z 263 [$C_{16}H_{32}O_2Li$]$^+$, and protonated stearic and palmitic acids at m/z 285 [$C_{18}H_{36}O_2H$]$^+$, and m/z 257 [$C_{16}H_{32}O_2H$]$^+$, respectively.

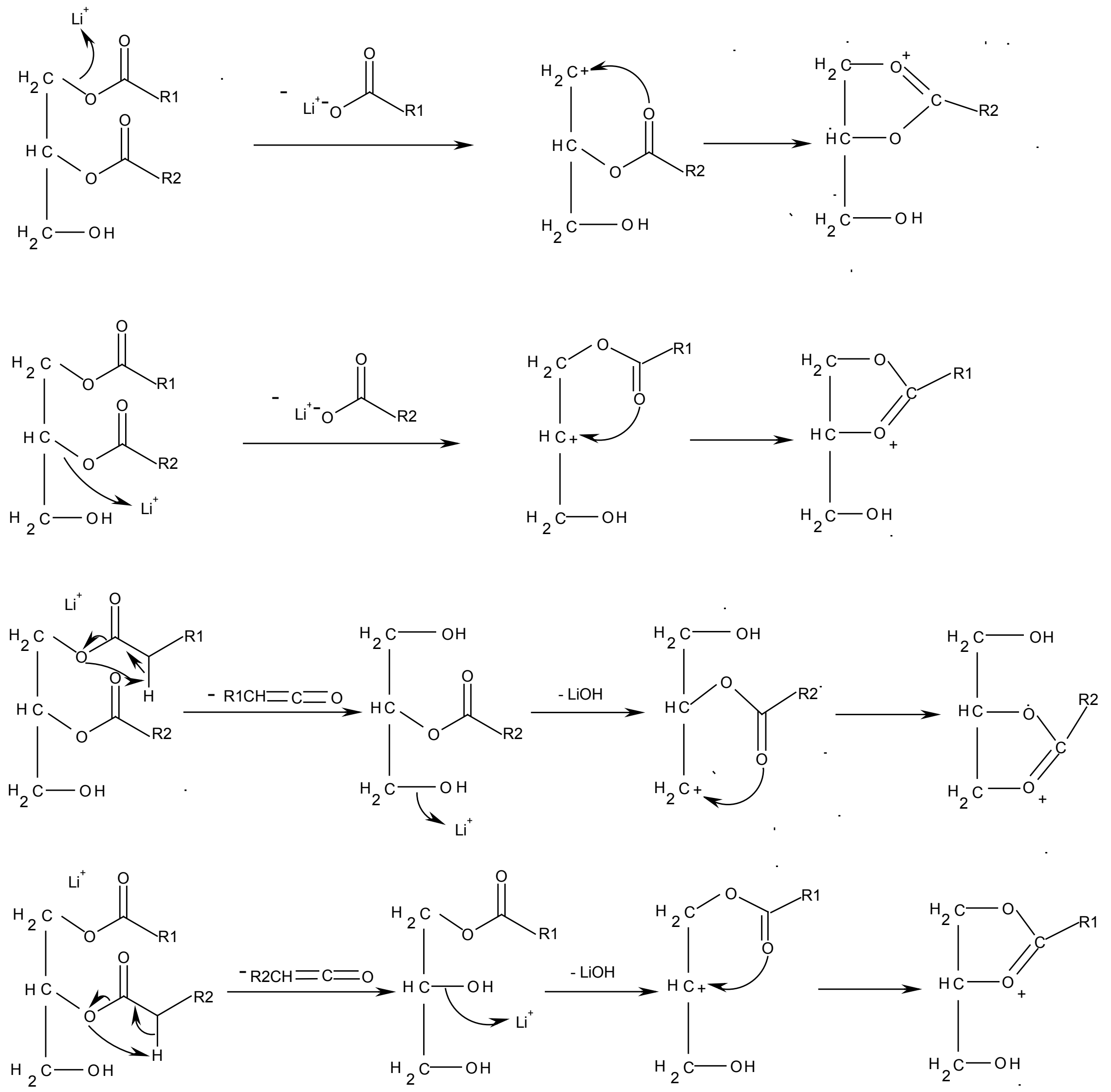

Figure 5.6. Proposed fragmentation pathways for the collisionally induced dissociation of the lithium adduct of 1-stearin-2-palmitin diglyceride involving the fatty acid substituent and loss of

LiOH. In the major fragment pathway process (top set (a) and (b)), there is the neutral loss of lithium fatty acetate (1- position or 2- position) forming the product ion. In the minor fragment pathway (bottom set (c) and (d)), the initial step is the loss of the ketene of either the 1- position or the 2- position fatty acid substituent, followed by the loss of LiOH forming the product ion.

make the most stable structure. The 1,3-diacylglycerides would have analogous pathways for the two-step neutral loss of a fatty acyl chain as a ketene, followed by the loss of LiOH. However, the neutral loss of a lithium fatty acetate for the 1,3- would be slightly more complicated, involving a hydroxyl shift to form the final stable 5-membered ring product ion (e.g., see m/z 299 in Fig. 5.3).

5.3.1.3 Distinguishing Asymmetric 1,2-diglycerides, and 1,2- from 1,3-diglycerides

Figure 5.7 presents a general scheme that can be used in the identification of diglycerides under low-energy (e.g., up to 100 eV E_{LAB}) collision conditions. The top part of panel (a) illustrates the usage of product ion intensities for determining substituent location within an asymmetric 1,2-diglyceride. First of all, a characteristic of the 1,2-diglycerides vs. the 1,3- is that the predominant product ions are those formed via losses of lithium fatty acetates. Furthermore, it has been observed that the R1 substituent in the 1-position of the 1,2-diglyceride shows a greater loss of the neutral lithium fatty acetate compared to the R2 substituent in the 2-position, when both are initially present. The product ion pathways leading to losses of R1 and R2 fatty acyl ketenes (Fig 5.7a, bottom half) are minor decomposition routes. In contrast to this behavior, as shown in the top half of Fig. 5.7b, for decompositions of lithiated 1,3-diglycerides the neutral losses of both the R1 and the R3 substituents as fatty acyl ketenes are observed to be the major product ions formed. Finally, the bottom part of panel (b) illustrates that the 1,3-

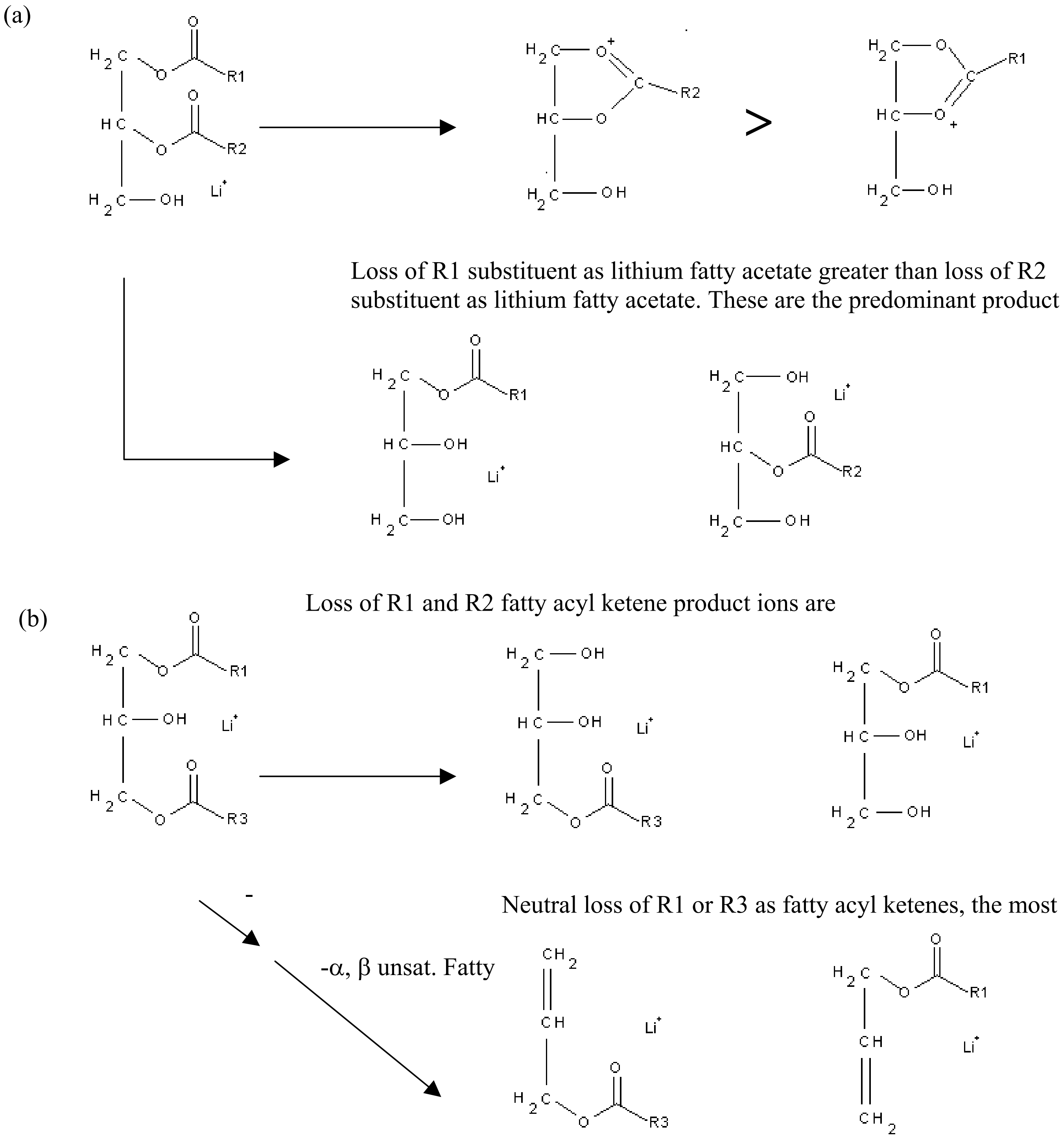

Loss of R1 substituent as lithium fatty acetate greater than loss of R2 substituent as lithium fatty acetate. These are the predominant product

Loss of R1 and R2 fatty acyl ketene product ions are

Neutral loss of R1 or R3 as fatty acyl ketenes, the most

Figure 5.7. General scheme for distinguishing asymmetric 1,2-diglycerides, and 1,2-diglycerides from 1,3-diglycerides based upon MS/MS decompositions of lithium adducts. (a) Illustrates the usage of product ion abundances for determining substituent location within an

asymmetric 1,2-diglyceride. Loss of R1 substituent as lithium fatty acetate is greater than the R2 loss. Indicative of 1,2-diglycerides is that neutral losses of lithium fatty acetates are the predominant product ions. Bottom half of panel (a) shows that losses of fatty acyl ketenes are minor product ions. Top half of panel (b) illustrates that the neutral losses of the R1 or the R3 substituent as fatty acyl ketenes are observed for the 1,3-diglyceride isomer, and these are the major product ions. Bottom part of panel (b) illustrates that the 1,3-diglyceride has a fragmentation pathway which results in the neutral loss of H_2O with subsequent loss of an alpha-beta unsaturated fatty acid. This fragmentation pathway is not observed for the 1,2-diglycerides.

diglyceride has a fragment pathway which results in a consecutive neutral loss of H_2O followed by neutral loss of an alpha-beta unsaturated fatty acid (this order was established by inspection of precursor scans of the ions shown at the bottom of Fig. 5.7b). The latter fragmentation pathway is not observed in the 1,2-diglycerides.

5.3.2 MS of Rabbit Tear Lipids

Figure 5.8 contains the mass spectra of normal eye rabbit tears, panel (a), and dry eye model rabbit tears, panel (b), extracted lipid lithium adducts. The spectra also contain lithium adduct peaks of four internal standards that were used to quantify the extracted lipids which are identified in Figure 5.8 by “IS”. Three major envelopes are observed consisting of monoglycerides, diglycerides, and triglycerides.

5.3.2.1 Identification of Monoglycerides

The m/z 300 to m/z 500 region contains three major peaks at m/z 337, m/z 365, and m/z 421. The first two have been identified as monoglycerides with empirical formulas of $C_nH_{2n}O_4Li^+$, having the single substituent of C16:0 for the m/z 337 peak, identified as

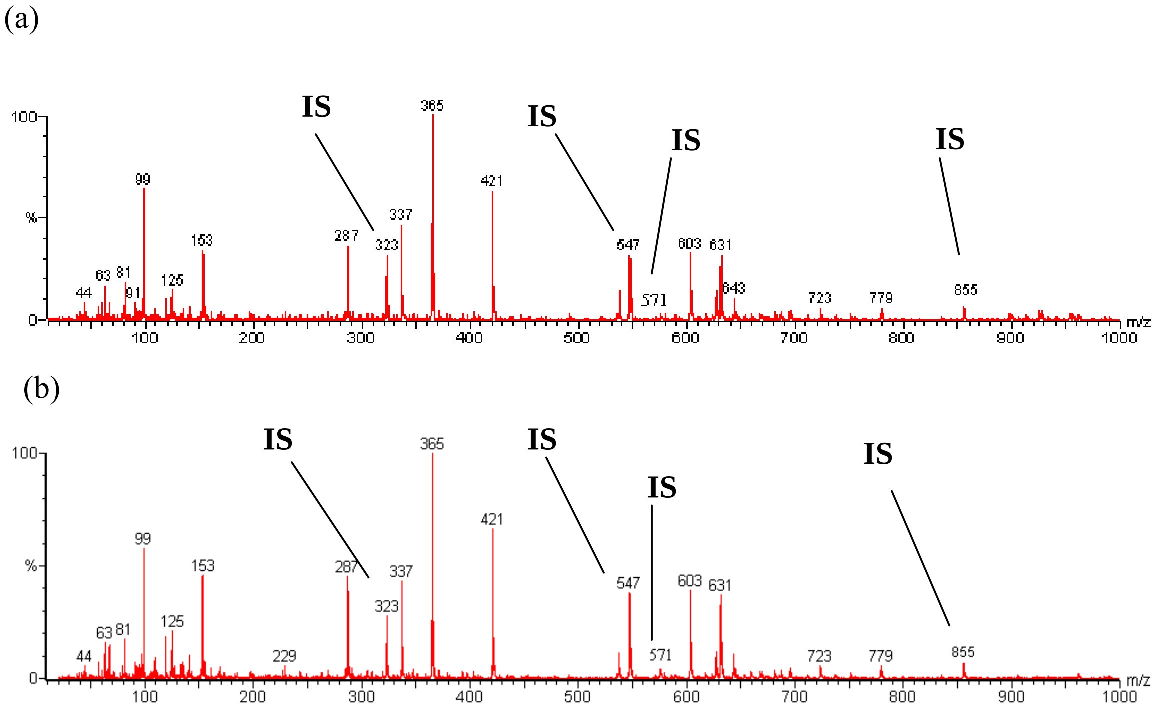

Figure 5.8. Typical single stage MS positive mode ES scans of the lithium adducts of extracted compounds, including the spiked internal standards (IS) of: (a) normal rabbit tear extract, and (b) dry eye rabbit model tear extract. The internal standards include: $3.65\text{x}10^{-5}$ mg/µL monopentadecanoin at m/z 323, $4.35\text{x}10^{-5}$ mg/µL dipentadecanoin at m/z 547, $4.8\text{x}10^{-5}$ mg/µL palmityl behenate at m/z 571, and $5.2\text{x}10^{-5}$ mg/µL triheptadecanoin at m/z 855.

monopalmitin glyceride, and C18:0 for the m/z 365 peak, identified as monostearin glyceride (the m/z 421 has been identified as a lithium adduct of an isoprene acetal). Figure 5.9a is the product ion spectrum of the m/z 365 compound in the normal rabbit tear extract. Analogous to the product ion spectrum of monopentadecanoin, the spectrum contains the glycerol backbone lithium adduct at m/z 99 derived from the neutral loss of C18:0 stearyl fatty ketene from the parent ion $[\text{MLi} - C_{18}H_{34}O]^+$, and ions at m/z 81 and m/z 63 derived from the further loss of one, and then two water molecules from the glycerol backbone.

5.3.2.2 Identification of Diglycerides

The m/z 500 to m/z 800 region of the spectra contains three major peaks at m/z 575, m/z 603, and m/z 631. The m/z 575, m/z 603, and m/z 631 peaks have been identified as diglycerides with empirical formulas of $C_nH_{2n-2}O_5Li^+$, where n = 35, 37, and 39, respectively.

5.3.2.2.1 m/z 575

The m/z 575 compound, as a diglyceride, has two possible fatty acid configurations. The product ion spectrum of m/z 575, Fig. 5.9b, allows assignment of at least two isomeric components having fatty acid compositions of dipalmitoyl, and stearin + myristin. For the dipalmitoyl glyceride, the spectrum contains informative peaks at m/z 337 for the loss of C16:0 fatty acyl chain as a ketene from the parent ion $[MLi – C_{16}H_{30}O]^+$, at m/z 263 for the lithium adduct of palmitic acid $[C_{16}H_{32}O_2Li]^+$, at m/z 319 for the neutral loss of C16:0 fatty acid $[MLi - C_{16}H_{32}O_2]^+$, at m/z 313 for the neutral loss of C16:0 lithium fatty acetate $[MLi – C_{16}H_{31}O_2Li]^+$, and at m/z 303 for the neutral loss of H_2O followed by consecutive loss of C16:1 alpha-beta unsaturated fatty acid $[MLi\text{-}H_2O\text{-}C_{16}H_{30}O_2]^+$. According to the identification scheme illustrated in Fig. 5.7, the observation of the m/z 303 peak confirms the presence of the 1,3-dipalmitoyl isomer, however, a minor presence of the 1,2-dipalmitoyl isomer cannot be ruled out (conversely, the absence of m/z 303 could be used to rule out the 1,3- isomer). Secondly, the identification scheme illustrated in Fig. 5.7 suggests that the greater intensity of the m/z 337 product ion (from the C16:0 fatty acyl ketene loss), as compared to the m/z 313 product ion (from C16:0 lithium fatty acetate loss), indicates a 1,3-dipalmitoyl isomer. Concerning the stearin, myristin diacylglyceride, the spectrum contains peaks that allow identification of both fatty acid substituents, including: a product ion peak at m/z 235 for C14:0 lithiated fatty acid $[C_{14}H_{28}O_2Li]^+$, at m/z 347 for the neutral loss of C14:0 fatty acid $[MLi – C_{14}H_{28}O_2]^+$, and at m/z 291 for both C18:0 lithiated fatty acid $[C_{18}H_{36}O_2Li]^+$ and for the neutral loss of C18:0 fatty acid $[MLi – C_{18}H_{36}O_2]^+$ (also m/z 291). Peaks at m/z 309 for the loss of C18:0 fatty acyl chain as ketene $[MLi – C_{18}H_{34}O]^+$, and at m/z 365 for the loss of C14:0 fatty acyl chain as ketene $[MLi – C_{14}H_{26}O]^+$, are observed in similar intensities, and more predominant than those of the corresponding lithium fatty acetate losses, which is illustrative of the 1,3-isomer. However, the spectrum does contain peaks corresponding to these lithium fatty acetate losses at m/z 285 ($[MLi – C_{18}H_{35}O_2Li]^+$), and at m/z 341 ($[MLi -C_{14}H_{27}O_2Li]^+$). Because the latter peaks are found in higher abundances than one would expect from a case where only the 1,3-diglyceride was present, it is likely that the 1,2-isomer exists as a minor component. The intensity of the m/z 341 ion for the neutral loss of the C14:0 lithium fatty acetate is slightly greater than the m/z 285 ion for the neutral loss of the C18:0 lithium fatty acetate suggesting that the 1,2-isomer consists largely of 1-myristin,2-stearin. Finally, a peak at m/z 275 is observed for the neutral loss of H_2O followed by consecutive loss of C18:1 alpha-beta unsaturated fatty acid $[MLi-H_2O-C_{18}H_{34}O_2]^+$, also indicative of the 1,3-isomer. Thus, the parent ion contains one C14:0 fatty acid in the 3-position, while the C18:0 fatty acid is in the 1-position allowing the assignment of 1-stearin,3-myristin diglyceride. The spectrum also contains the low molecular weight hydrocarbon ions m/z 43, m/z 57, m/z 71, and m/z 85, plus the m/z 99, m/z 81, and m/z 63 ions from the lithiated glycerol backbone. The m/z 575 precursor ion was thus identified as a mixture of lithiated 1,3-dipalmitin (major component), and of 1,3-stearin-myristin and 1-myristin,2-stearin (minor components) diglyceride isomers.

5.3.2.2.2 m/z 603

Similar characterization is found with the m/z 603 parent ion (Figure 5.9 panel (c)). A major product ion appears at m/z 365 produced from the neutral loss of a C16:0 fatty acyl chain as a ketene from the parent $[MLi - C_{16}H_{30}O]^+$. A peak with slightly greater intensity is observed at m/z 337 from the 1-position loss of the C18:0 fatty acyl chain as a ketene $[MLi - C_{18}H_{34}O]^+$. According to the identification scheme in Figure 5.7, the observance of the loss of these two different fatty acid ketenes as the predominant product ions provides evidence that this diglyceride is present as the 1,3- isomer. Moreover, the intensities of the peaks at m/z 263 for the lithiated fatty acid ion hexadecanoic $[C_{16}H_{32}O_2Li]^+$ and m/z 291 from the lithiated fatty acid ion octadecanoic $[C_{18}H_{36}O_2Li]^+$ are also similar in intensity, which further indicates that the compound is composed primarily of the 1,3-isomer. Characteristic peaks for the 1,3-isomer are also observed at m/z 303 for the consecutive neutral losses of H_2O, followed by loss of C18:1 alpha-beta unsaturated fatty acid $[MLi\text{-}H_2O\text{-}C_{18}H_{34}O_2]^+$, and at m/z 331 for the neutral losses of H_2O and C16:1 alpha-beta unsaturated fatty acid $[MLi\text{-}H_2O\text{-}C_{16}H_{30}O_2]^+$. Also observed are lower intensity (minor) peaks at m/z 313 from the neutral loss of C18:0 lithium fatty acetate $[MLi - C_{18}H_{35}O_2Li]^+$, and at m/z 341 from the neutral loss C16:0 lithium fatty acetate $[MLi - C_{16}H_{31}O_2Li]^+$. Also present in lower intensities are peaks at m/z 319 for the neutral loss of octadecanoic acid $[MLi - C_{18}H_{36}O_2]^+$, and at m/z 347 for the neutral loss of hexadecanoic acid $[MLi - C_{16}H_{32}O_2]^+$. The hydrocarbon ions at m/z 43, 57, 71, and 85 are present, as are the glycerol backbone ions at m/z 99, 81 and 63. The product ion at m/z 585 is due to the loss of water from the parent ion $[MLi - H_2O]^+$. The above evidence indicates that the m/z 603 parent ion primarily consists of the 1-stearin,3-palmitin isomer.

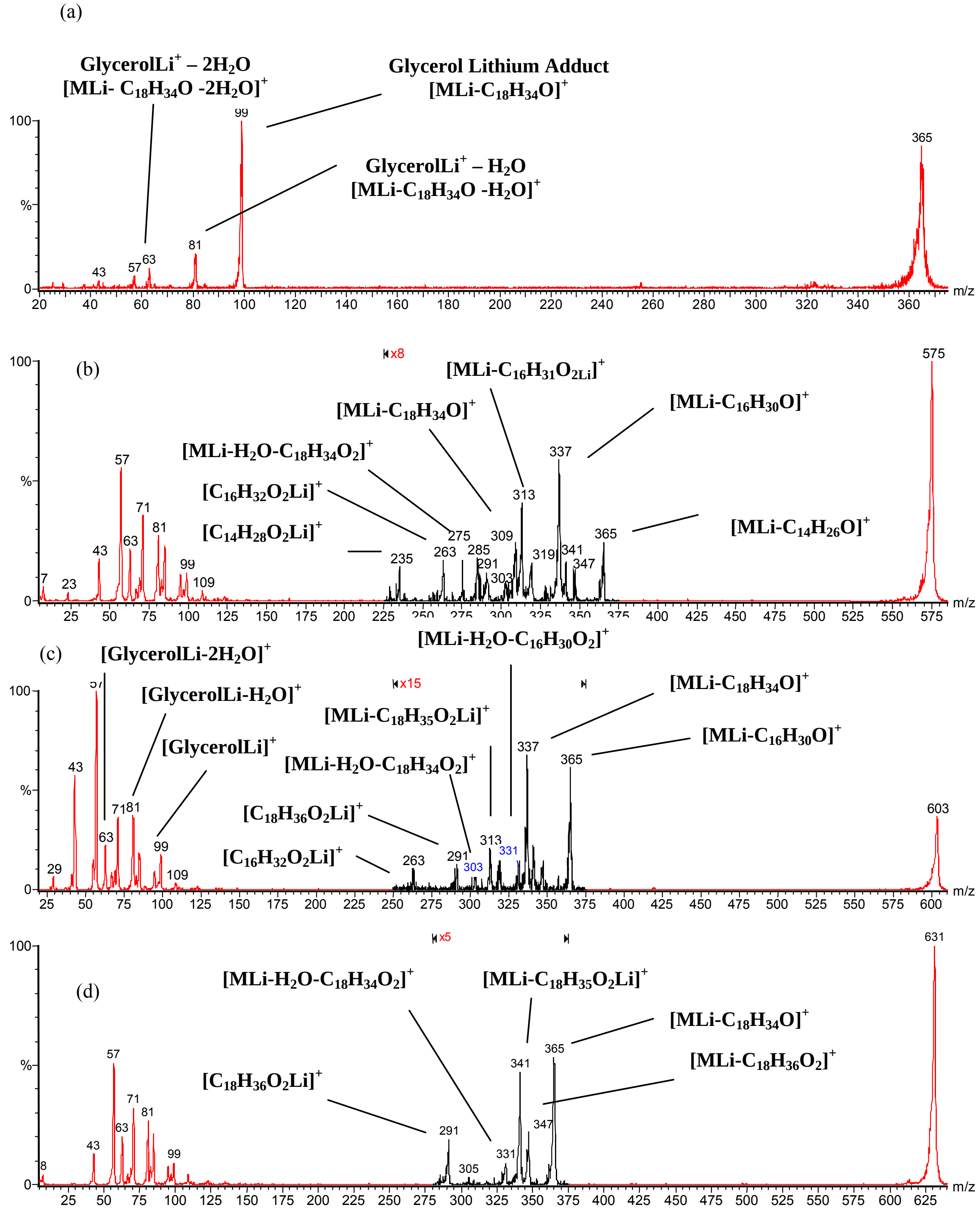

Figure 5.9. Positive mode ES tandem mass spectra illustrating informative fragment ions used for identification of: (a) the m/z 365 lipid lithium adduct, identified as monostearyl glyceride, (b) the m/z 575 lipid lithium adduct, identified as 1,3-dipalmitin diglyceride being the major component, with a minor 1-stearin,3-myristin constituent, and a minor 1-myristin,2-stearin constituent, (c) the m/z 603 lithium adduct identified as 1-stearyl,3-palmityl diglyceride, and (d) the m/z 631 lithium adduct identified as 1,3-distearin acylglyceride.

5.3.2.2.3 m/z 631

Finally, for the spectrum of the m/z 631 compound in Figure 5.9d a product ion at m/z 365 is observed for the neutral loss of C18:0 fatty acyl chain as a ketene $[MLi - C_{18}H_{34}O]^+$, and the ion at m/z 331 from the consecutive neutral losses of H_2O and C18:1 alpha-beta unsaturated fatty acid $[MLi\text{-}H_2O\text{-}C_{18}H_{34}O_2]^+$ that is indicative of a 1,3-diglyceride, is also observed. The spectrum also contains the lithium adduct of stearic acid at m/z 291 $[C_{18}H_{36}O_2Li]^+$, and peaks at m/z 341 for the neutral loss of C18:0 lithium fatty acetate $[MLi\text{-}C_{18}H_{35}O_2Li]^+$, as well as at m/z 347, representing the neutral loss of the C18:0 fatty acid $[MLi\text{-}C_{18}H_{36}O_2]^+$. The spectrum is also characterized by the low molecular weight product ions from carbon-carbon bond dissociation, and the product ions for the glycerol backbone, and subsequent one and two water losses. The structure is thus assigned as the 1,3-distearin diglyceride, but the presence of a minor amount of the 1,2- isomer cannot be ruled out.

5.3.2.3 Identification of Triglycerides

The m/z 800 to m/z 1100 range consists of triesters of the empirical formula $C_nH_{2n-4}O_6Li^+$. Figure 5.10a shows an expanded mass axis illustrating the m/z 850 to m/z 970 region. As can be seen by the relative peak intensity of the internal standard triheptadecanoin (m/z 855), the triesters are present in relatively low concentrations. Peaks in this area, such as the m/z 863, the m/z 877, the m/z 905, m/z 961, etc., were analyzed by MS/MS and were found to be singly charged Li^+-bound mixed dimers primarily comprised of species from the 500 to 800 Da region noncovalently bound with species in the 300 to 500 Da region. The product ion spectrum of the m/z 897 peak, Figure 5.10b contains ions that are consistent with the characterization of triglycerides, such as the m/z 267 peak for the C18:0 acylium ion $[C_{18}H_{35}O]^+$, the lithium adduct of octadecanoic acid at m/z 291 $[C_{18}H_{36}O_2Li]^+$, the parent ion minus lithiated arachidinoate at m/z 579 $[MLi – C_{20}H_{39}O_2Li]^+$, the parent ion minus the neutral loss of arachidinoic acid at m/z 585 $[MLi – C_{20}H_{40}O_2]^+$, the parent ion minus lithiated octadecanoate at m/z 607 $[MLi - C_{18}H_{35}O_2Li]^+$, and the parent ion minus neutral loss of octadecanoic acid at m/z 613 $[MLi - C_{18}H_{36}O_2Li]^+$. A low intensity peak is observed at m/z 641 from the loss of palmitic acid $[MLi – C_{16}H_{32}O_2]^+$. The absence of more of the ions of the fatty acids is probably due to the low concentration levels being measured. The spectrum also contains lower molecular weight ions from the fragmentation of the fatty acids through carbon-carbon bond cleavage. The peak at m/z 897 is thus assigned as the lithium adduct of a mixture of two triglyceride isomers with the predominant one being trioctadecanoin, and the minor being 1-arachidin,2-stearin,3-palmitin.

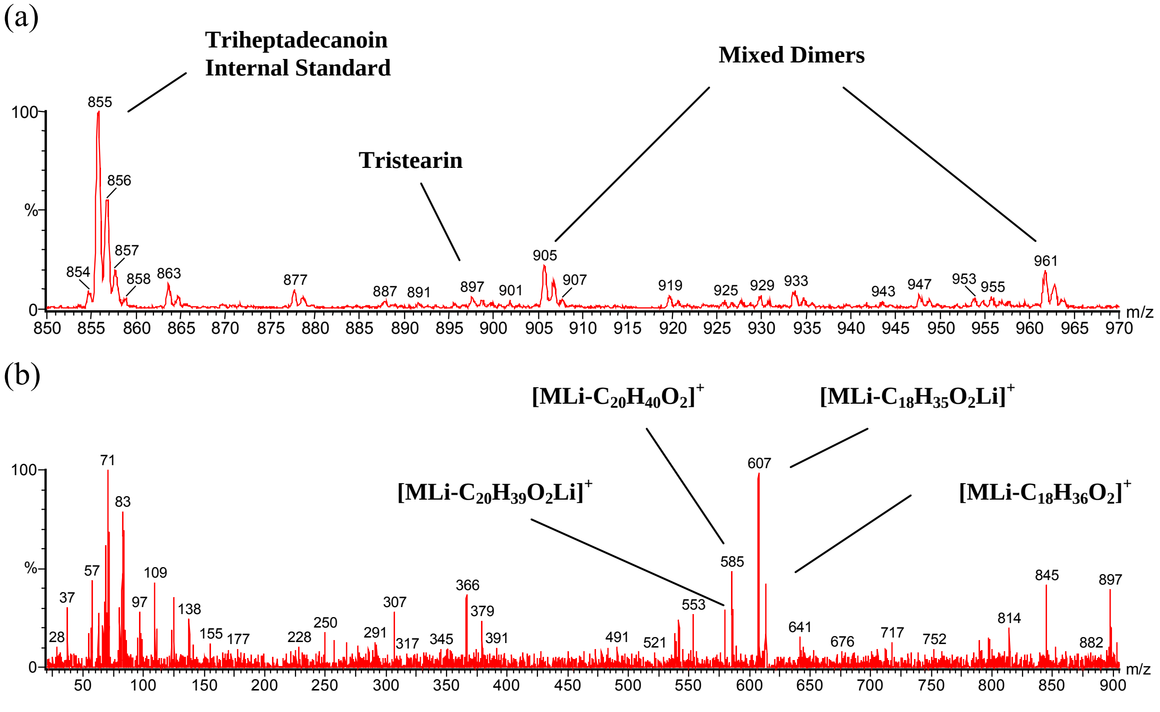

Figure 5.10 (a) Expanded mass axis of the triester spectral region (m/z 850 to m/z 970) of normal tear extract lithium adducts illustrating the occurrence of mixed dimers, and low concentrations of triacylglycerols present in the extract. (b) Product ion spectrum with peak

assignments of informative product ions of the m/z 897 precursor identified as an isomeric mixture of tristearin and 1-arachidin,2-stearin,3-palmitin.

5.3.2.4 Wax Ester Analysis

Also included in the extract is a peak at m/z 571 from the spiking addition of palmityl behenate, a fatty acid/fatty alcohol wax ester standard (see Figure 5.1e for structure). The wax ester was found to have a low ionization efficiency compared to the other components in the tear extract. This was expected, as the ionization efficiency for lipids with ammonium acetate showed greater response as the polarity of the lipid increased(28) (increase in number of alcohol groups, one for diglyceride, two for monoglyceride, etc.), while the product ions were only of the protonated species from the initial loss of NH_3. This trend was also observed with an equimolar mixture of lipid standards, where the monoglycerides exhibited the greatest response, followed by the diglycerides, with the triglycerides showing the weakest response, though the product ions were mostly lithiated, with some appearing as fragment ions (e.g., acylium). Some of the experiments yielded good responses for the palmityl behenate wax ester standard, and peaks in the region expected for wax esters (m/z 500 to m/z 700) were analyzed by tandem mass spectrometry, but these peaks were not found to correspond to wax esters. The major components of the non-polar tear lipids have been reported in the past literature as wax esters(10-14), such as the C27 alcohol/C15 fatty acid wax ester which would have a lithiated mass at m/z 625. None of the simple, fatty alcohol/fatty acid wax esters(58) were observed in any of the extracts reported in this study. Previous work in our lab (unpublished results) showed that the optimum response for lithiated *phosphorylated* lipids was at approximately 10 mM LiCl. A new ionization-internal standard solution was used which contained 10 mM LiCl, instead of the 2 mM LiCl solution which had been used in all previous experiments. While the individual wax ester standard gave an excellent response when run with 10 mM LiCl, poor responses were still achieved when it was present with other lipids in a mixture, suggesting that the low response for the wax ester standard was due to suppression from the acylglycerides. However, a search for the simple fatty alcohol/fatty acid wax esters, such as the C27 alcohol/C15 fatty acid wax ester (lithium adduct mass at m/z 625), resulted in the conclusion that the wax esters are probably not detectable by this method, as they are likely present below the method's limit of detection for wax esters (i.e., 1.4×10^{-5} mg/μL, S/N = 3) established for the spiked palmityl behenate internal standard. This means that under the method's conditions for ES of the lithium adducts, the wax and cholesterol esters are not being observed. Other separation methods performed in our lab such as TLC indicated that the wax and cholesterol esters are indeed present, but the current ES-MS method suppresses their response.

5.3.2.5 Quantification of the Tear Lipids

To estimate the concentration of the lipids in the extract, standards were chosen which were predicted to have ionization efficiencies very similar to those of the extracted lipids. For the m/z 20 to m/z 500 region, monopentadecanoin was used with a lithium adduct mass of m/z 323, for the m/z 500 to m/z 800 region, dipentadecanoin was used with a lithium adduct mass of m/z 547, for the m/z 800 to m/z 1100 region, triheptadecanoin was used with a lithium adduct mass of m/z 855; for the wax esters, palmityl behenate was used with a lithium adduct mass of m/z 571. Figure 5.8a is the spectrum of the lithium adducts of normal tear lipid extract where the locations of the internal standards are marked with "IS". The concentrations of the four internal standards were chosen to be in the same approximate range as the extracted lipids, namely

3.65×10^{-5} mg/μL monopentadecanoin, 4.35×10^{-5} mg/μL dipentadecanoin, 5.2×10^{-5} mg/μL triheptadecanoin, and 4.8×10^{-5} mg/μL palmityl behenate, all in 50:50 chloroform/methanol with 2 mM LiCl. To quantify the terpenoids, the response factor of the diacylglyceride dipentadecanoin was used due to the expected similarity in ionization efficiency (one alcohol group) for the two.

Table 5.1 shows a comparison of quantitative results of the normal and dry eye tear lipid extracts. The total lipid extract value for the normal eye is 7.3 ± 0.7 μg μl^{-1}, while the dry eye total lipid extract average result was determined to be 14.0 ± 2.1 μg μl^{-1}. This indicates that the total lipid content in dry eye tears is much greater, approximately double, as compared to what is observed in normal eye tears. This might be explained by the fact that the dry eye may have less aqueous content in the tear layer compared to normal eyes, resulting in a higher concentration of lipids per microliter of tears. In particular, the glyceryl isoprene acetals appear to have increased in concentration the most (approximately three-fold relative to the normal eye). The relatively large standard errors of the means (see Table 5.1) indicate variation in lipid composition from sample to sample. The general overall pattern for the two lipid extracts is similar when comparing each compound's percentage of the total extract.

Compound Identification	Li^+ Adduct (m/z)	Normal Eye[a] (mg/μL)	Dry Eye[b] (mg/μL)	Percent Increase (%)
Free glycerol	99	$9.6x10^{-4} \pm 2.3x10^{-4}$	$1.5x10^{-3} \pm 2.7x10^{-4}$	56
Glyceryl-isoprene acetal	153	$6.8x10^{-4} \pm 2.7x10^{-4}$	$1.7x10^{-3} \pm 8.5x10^{-4}$	150
Glyceryl-isoprene acetal	287	$7.5x10^{-4} \pm 2.9x10^{-4}$	$1.8x10^{-3} \pm 9.2x10^{-4}$	140
Monopalmitin	337	$7.4x10^{-4} \pm 1.6x10^{-4}$	$1.1x10^{-3} \pm 2.0x10^{-4}$	49
Monostearin	365	$1.6x10^{-3} \pm 3.4x10^{-4}$	$2.5x10^{-3} \pm 2.5x10^{-4}$	56
Glyceryl-isoprene acetal	421	$1.2x10^{-3} \pm 3.7x10^{-4}$	$2.9x10^{-3} \pm 1.6x10^{-3}$	142
1,3-dipalmitin (major) 1-stearin,3-myristin (minor) 1-myristin,2-stearin (minor)	575	$1.4x10^{-4} \pm 3.1x10^{-5}$	$2.1x10^{-4} \pm 2.3x10^{-5}$	50
1-stearin,3-palmitin (major)	603	$5.2x10^{-4} \pm 9.5x10^{-5}$	$7.3x10^{-4} \pm 2.7x10^{-5}$	40
1,3-distearin (major)	631	$5.1x10^{-4} \pm 9.0x10^{-5}$	$7.2x10^{-4} \pm 1.3x10^{-5}$	41
Tristearin (major) [c] 1-arachidin,2-stearin, 3-palmitin (minor)	897	$1.3x10^{-4} \pm 5.5x10^{-5}$	$1.8x10^{-4} \pm 9.9x10^{-5}$	38
TOTAL		$7.3x10^{-3} \pm 7.1x10^{-4}$	$1.4x10^{-2} \pm 2.1x10^{-3}$	92

[a] Averages and standard errors of the mean reported for normal eye results were derived from four different sets of composite rabbit tear samples, where each composite set was analyzed separately. Tear composite volumes were 12 μL, 12 μL, 7 μL, and 7 μL.

[b] Dry eye results are the average and standard error of the mean of two different composite sets which were analyzed individually. Tear composite volumes were 6 μL, and 7 μL.

[c] Reported value for the triglyceride tristearin is substantially above the method's limit of detection for triglycerides (i.e., 5.8 x 10^{-6} mg/μL).

Table 5.1. Comparison of Quantitative Results of Normal and Dry Eye Tear Lipid Extracts.

5.4 Conclusions

Tandem mass spectrometry experiments on the major components of the total chloroform extracts identified that these compounds were more polar than the simple "fatty acid esterified to a fatty alcohol" type of wax ester, which is what has been previously reported to make up the majority of the non-polar lipids. Empirical formulas were derived which can be used to calculate the number of oxygens, and double bonds, for the species in three mass regions which primarily indicate lipids. The first region (m/z 20 to m/z 500) consists of free glycerol, three glyceryl-terpene acetals, and monoacylglycerols with empirical formulas of $C_nH_{2n}O_4Li^+$. The m/z 500 to m/z 800 region consists of diacylglycerols with empirical formulas of $C_nH_{2n-2}O_5Li^+$, and the m/z 800 to m/z 1100 region is comprised of triacylglycerols with empirical formulas of $C_nH_{2n-4}O_6Li^+$.

The work reported here using lithium adducts, combined with electrospray tandem mass spectrometry (ES-MS-MS), for the analysis of complicated biological extracts has shown a marked improvement over past approaches of TLC, HPLC-MS, derivative GC-MS, etc., that have been used to characterize the tear film lipids. New, informative product ion spectra are presented for lithiated monoacyl, 1,2- and 1,3-diacyl, and triacylglyceride standards. Newly proposed structures and fragment pathways for the major product ions are presented for the 1,2- and 1,3-diglycerides, and for the monoglyceride. The mass spectra of the lithium adducts of the acylglycerides contain detailed and informative product ions that were successfully used to identify the acylglycerides, and the terpenoid type compounds that were observed to be present in the tear extracts. Through the use of ES-MS/MS, the normal and dry eye rabbit tear extracted lipids were found to be primarily comprised of acylglycerides that exhibited high responses in ES, whereas the wax and cholesterol esters were not detected, presumably due to ionization suppression. Also, with this approach, separation such as HPLC, TLC, SPE, etc., was not essential due to separation by mass. Finally, all extracted compounds that are subsequently ionized and measured by the mass spectrometer can be quantified, and analyzed by tandem mass spectrometry to identify their molecular structures.

5.5 REFERENCES

1. Schaumberg DA, Buring JE, Sullivan DA, Dana MR. Hormone replacement therapy and dry eye syndrome. *JAMA*. 2001; **286**: 2114.
2. Bjerrum KB. Keratoconjunctivitis sicca and primary Sjogren's syndrome in a Danish population aged 30-60 years. *Acta Ophthalmologica Scandinavica*. 1997; **75**: 281.
3. Schein OD, Munoz B, Tielsch JM, Bandeen-Roche K, West S. Prevalence of dry eye among the elderly. *American Journal of Ophthalmology*. 1997; **124**: 723.
4. Murube J, Paterson A, Murube E. Classification of artificial tears. I: Composition and properties. *Adv. Exp. Med. Biol.* 1998; **438**: 693.
5. Rieger G. Lipid-containing eye drops: a step closer to natural tears. *Ophthalmologica*. 1990; **201**: 206.
6. Hillenkamp J, Reinhard T, Ross RS, Bohringer D, Cartsburg O, Roggendorf M, De Clercq E, Godehardt E, Sundmacher R. Topical treatment of acute adenoviral keratoconjunctivitis with 0.2% cidofovir and 1% cyclosporine: a controlled clinical pilot study. *Arch Ophthalmol.* 2001; **119**: 1487.
7. Moore JC, Tiffany JM. Human ocular mucus. Chemical studies. *Exp. Eye Res*. 1981; **33***:* 203.
8. Carrington SD, Hicks SJ, Corfield AP, Kaswan RL, Packer N, Bolis S, Morris CA. Structural analysis of secreted ocular mucins in canine dry eye. *Adv. Exp. Med. Biol.* 1998; **438**: 253.
9. McCulley JP, Shine WE. The lipd layer: the outer surface of the ocular surface tear film. *Bioscience Reports*. 2001; **21**: 407.
10. Nicolaides N, Santos EC. The di- and triesters of the lipids of steer and human meibomian glands. *LIPIDS*. 1985; **20**: 454.
11. Miyazaki M, Man WC, Ntambi JM. Targeted disruption of stearoyl-CoA desaturase1 gene in mice causes atrophy of sebaceous and meibomian glands and depletion of wax esters in the eyelid. *Nutrient-Gene Expression*. 2001; 2260.
12. McCulley JP, Shine WE. A compositional based model for the tear film lipid layer. *Tr. Am. Opth. Soc.* 1997; **95**: 79.
13. Mathers WD, Lane JA.Meibomian gland lipids, evaporation, and tear film stability. *Adv. Exp. Med. Biol.* 1998; **438**: 349.
14. Nicolades N, Kaitaranta JK, Rawdah TN, Macy JI, Boswell III FM, Smith RE. Meibomian gland studies: comparison of steer and human lipids. *Invest. Ophthalmol. Vis. Sci.* 1981; **20**: 522.
15. Whitehouse CM, Dryer RN, Yamashita M, Fenn JB. Electrospray interface for liquid chromatographs and mass spectrometers. *Anal. Chem.* 1985; **57**: 675.
16. Kebarle P, Ho Y. In *Electrospray Ionization Mass Spectrometry,* Cole RB, (ed). Wiley: New York 1997; 17.
17. Cole RB. Some tenets pertaining to electrospray ionization mass spectrometry. *J. Mass Spectrom*. 2000; **35**: 763.
18. Cao P, Stults JT. Mapping the phosphorylation sites of proteins using on-line immobilized metal affinity chromatography/capillary electrophoresis/electrospray ionization multiple stage tandem mass spectrometry. *Rapid Commun. Mass Spectrom*. 2000; **14**: 1600.
19. Ho YP, Huang PC, Deng KH. Metal ion complexes in the structural analysis of phospholipids by electrospray ionization tandem mass spectrometry. *Rapid Commun. Mass Spectrom*. 2003; **17**: 114.

20. Kocher T, Allmaier G, Wilm M. Nanoelectrospray-based detection and sequencing of substoichiometric amounts of phosphopeptides in complex mixtures. *J. Mass Spectrom.* 2003; **38***:* 131.
21. Shimazaki J, Sakata M, Tsubota K. Ocular surface changes and discomfort in patients with meibomian gland dysfunction. *Arch. Ophthalmol.* 1995; **113**: 1266.
22. Murphy, RC. Triacylglycerols, diacylglycerols and monoacylglycerols (Chapter 6). In: *Mass Spectrometry of Lipids*. Plenum Press: New York 1993; 189.
23. Liu QT, Kinderlerer JL. Preparative thin-layer chromatographic separation and subsequent gas chromatographic-mass spectrometric analysis of monoacylglycerols derived from butter oil by fungal degradation. *J. Chromatogr. A.* 1999; **855***:* 617.
24. Harvey DJ, Tiffany JM. Identification of meibomian gland lipids by gas chromatography-mass spectrometry: application to the meibomian lipids of the mouse. *Journal of Chromatography*. 1984; **301**: 173.
25. Kuksis A, Marai L, Myher JJ. Reversed-phase liquid chromatography-mass spectrometry of complex mixtures of natural triacylglycerols with chloride-attachment negative chemical ionization. *Journal of Chromatography*. 1991; **588**: 73.
26. Marai L, Kukis A, Myher JJ, Itabashi Y. Liquid chromatography chloride attachment negative chemical ionization mass spectrometry of diacylglycerol dinitrophenylurethanes. *Biological Mass Spectrometry*. 1992; **21**: 541.
27. Cole RB, Zhu J. Chloride anion attachment in negative ion electrospray ionization mass spectrometry. *Rapid Commun. Mass Spectrom.* 1999; **13**: 607.
28. Duffin KL, Henion JD. Electrospray and tandem mass spectrometric characterization of acylglycerol mixtures that are dissolved in nonpolar solvents. *Anal. Chem.* 1991; **63**: 1781.
29. Han X, Gross RW. Quantitative analysis and molecular species fingerprinting of triacylglyceride molecular species directly from lipid extracts of biological samples by electrospray ionization tandem mass spectrometry. *Analytical Biochemistry*. 2001; **295**: 88.
30. Byrdwell, WC, Neff, WE Dual parallel electrospray ionization and atmospheric pressure chemical ionization mass spectrometry (MS), MS/MS and MS/MS/MS for the analysis of triacylglycerols and triacylglycerol oxidation products. *Rapid Commun. Mass Spectrom.* 2002; **16**: 300.
31. Marzilli, LA, Fay, LB, Dionisi, F, Vouros, P. Structural characterization of triacylglycerols using electrospray ionization-MS^n Ion Trap MS. *J. Am. Chem. Oil Soc.*, 2003: **80**: 195.
32. Waltermann M, Luftmann H, Baumeister D, Kalscheuer R, Steinbuchel A. Rhodococcus opacus strain PD630 as a new source of high-value single-cell oil? Isolation and characterization of triacylglycerols and other storage lipids. *Microbiology*; 2000: **146**, 1143.
33. Schiller J, Arnhold J, Benard S, Muller M, Reichl S, Arnold K. Lipid analysis by matrix-assisted laser desorption and ionization mass spectrometry: a methodological approach. *Analytical Biochemistry*. 1999; **267**: 46.
34. Leary JA, Pederson SF. A reliable method for fast atom bombardment mass spectrometric analysis of α-aryl 1,2-diols. Formation of lithium-diol adducts. *J. Org. Chem.* 1989; **54**: 5650.
35. Byrdwell, WC Atmospheric pressure chemical ionization mass spectrometry for analysis of lipids. *Lipids* 2001; **36**:327
36. Mu H, Sillen H, Hoy CE. Identification of diacylglycerols and triacylglycerols in a structured lipid sample by atmospheric pressure chemical ionization liquid chromatography/mass spectrometry. *J. Am. Oil Chem. Soc.* 2000: **77**: 1049.

37. Holcapek M, Jandera P, Fischer J. Analysis of acylglycerols and methyl esters of fatty acids in vegetable oils and in biodiesel. *Critical Reviews in Analytical Chemistry*. 2001; **31**: 53.
38. Mottram HR, Woodbury SE, Evershed RP. Identification of triacylglycerol positional isomers present in vegetable oils by high performance liquid chromatography/atmospheric pressure chemical ionization mass spectrometry. *Rapid Commun. Mass Spectrom.* 1997; **11**: 1240.
39. Holcapek M, Jandera P, Fischer J, Prokes B. Analytical monitoring of the production of biodiesel by high-performance liquid chromatography with various detection methods. *J. Chromatogr. A* 1999; **858**, 13.
40. Holcapek M, Jandera P, Zderadicka P, Hruba L. Characterization of triacylglycerol and diacylglycerol composition of plant oils using high-performance liquid chromatography – atmospheric pressure chemical ionization mass spectrometry. *J. Chromatogr. A* 2003; **1010**, 195.
41. Jakab A, Jablonkai I, Forgacs E. Quantification of the ratio of positional isomer dilinoleoyl-oleoyl glcerols in vegetable oils. *Rapid Commun. Mass Spectrom.* 2003; **17**: 2295.
42. Fauconnot L, Hau J, Aeschlimann JM, Fay, LB, Dionisi F. Quantitative analysis of triacylglycerol regioisomers in fats and oils using reversed-phase high-performance liquid chromatography and atmospheric pressure chemical ionization mass spectrometry. *Rapid Commun. Mass Spectrom.* 2004; **18**: 218.
43. Hsu FF, Bohrer A, Turk J. Formation of lithiated adducts of glycerophoscholine lipids facilitates their identification by electrospray ionization tandem mass spectrometry. *J Am Soc Mass Spectrom*. 1998; **9***:* 516.
44. Zhou Z, Ogden S, Leary JA. Linkage position determination in oligosaccharides: ms/ms study of lithium-cationized carbohydrates. *Journal of Organic Chemistry*. 1990; **55**: 5444.
45. Striegel AM, Timpa JD, Piotrowiak P, Cole RB. *International Journal of Mass Spectrometry and Ion Processes*. Multiple neutral alkali halide attachments onto oligosaccharides in electrospray ionization mass spectrometry. 1997; **162**: 45.
46. Hsu FF, Turk J. Structural characterization of triacylglycerols as lithiated adducts by electrospray ionization mass spectrometry using low-energy collisionally activated dissociation on a triple stage quadrupole instrument. *J Am Soc Mass Spectrom.*1999; **10**: 587.
47. Adams J, Gross ML. Tandem mass spectrometry for collisionally activation of alkali-metal-cationized fatty acids: a method for determining double bond location. *Anal. Chem*. 1987; **59**: 1576.
48. Wollensak G, Mur E, Mayr A, Baier G, Gottinger W, Stoffler G. Effective methods for the investigation of human tear film proteins and lipids. *Graefe's Archive for Clinical and Experimental Ophthalmology*. 1990; **228**: 78.
49. Augustin AJ, Spitznas M, Kaviani N, Meller D, Koch FHJ, Grus F, Gobbels MJ. Oxidative reactions in the tear fluid of patients suffering from dry eyes. *Graefe's Arch Clin Exp Ophthalmol*. 1995; **233**: 694.
50. Choy CK, Cho P, Chung WY, Benzie IF: Water-soluble antioxidants in human tears: effect of the collection method. *Invest. Ophthalmol. Vis. Sci.* 2001; **42**: 3130.
51. Folch J, Lees M, Stanley GHS. A simple method for the isolation and purification of total lipides from animal tissues. *J. Biol. Chem.* 1957; **226**: 497.
52. Bligh EG, Dyer WJ. A rapid method of total lipid extraction and purification. *Can. J. Biochem. Physiol.* 1959; **37**: 911.

53. Brugger B, Erben G, Sandhoff R, Wieland FT, Lehmann WD. Quantitative analysis of biological membrane lipids at the low picomole level by nano-electrospray ionization tandem mass spectrometry. *Proc. Natl. Acad. Sci. USA.* 1997; **94**: 2339.
54. Sullivan BD, Evans JE, Cermak JM, Krenzer KL, Dana MR, Sullivan DA. Complete androgen insensitivity syndrome. *Arch Ophthalmol*. 2001; **120***:* 1689.
55. Sullivan BD, Evans JE, Krenzer KL, Dana MR, Sullivan DA. Impact of antiandrogen treatment on the fatty acid profile of neutral lipids in human meibomian gland secretions. *Clinical Endocrinology & Metabolism*. 2000; **85**: 4866.
56. Sullivan BD, Cermak JM, Sullivan RM, Papas AS, Evans JE, Dana MR, Sullivan DA. Correlations between nutrient intake and the polar lipid profiles of meibomian gland secretions in women with Sjogren's syndrom. *Adv. Exp. Med. Biol.* 2002; **506 (PtA)**: 441.
57. Sullivan BD, Evans JE, Dana MR, Sullivan DA. Impact of androgen deficiency on the lipid profiles in human meibomian gland secretions. *Adv. Exp. Med. Biol.* 2002; **506 (PtA)**: 449.
58. Patel S, Nelson DR, Gibbs AG. Chemical and physical analysis of wax ester properties. *Journal of Insect Science*. 2001; **1.4**: 1.

CHAPTER VI : MALDI-TOF MS OF PHOSPHORYLATED LIPIDS IN BIOLOGICAL FLUIDS USING IMMOBILIZED METAL AFFINITY CHROMATOGRAPHY AND A SOLID IONIC CRYSTAL MATRIX

6.1 INTRODUCTION

Lipids are important biomolecules that are found in all living species. These include non-polar lipids such as the acylglycerols, and the more polar phosphorylated lipids. Of the non-polar lipids, triacylglycerols are thought to be a storage form of carbon in the cells[1], while diacylglycerols are of special importance for their role as physiological activators of protein kinase C (PKC)[2,3]. Of the polar lipids, those containing phosphoryl head groups, such as the phosphatidylcholines (PC), the phosphatidylethanolamines (PE), and the phosphatidylserines (PS) (see Fig. 1 for structures), constitute the bilayer components of biological membranes, determine the physical properties of these membranes, and directly participate in membrane protein regulation and function. Other types of phosphorylated lipids are the sphingomyelins and the glycosphingolipids which have been reported to be involved in different biological processes such as growth and morphogenesis of cells[4]. Thus, analysis of this special class of biomolecules has been of great interest to medical researchers, biologists, and chemists.

Recent analyses of phospholipids have employed HPLC[5], MEKC[5,6], CE-ES-MS[7], ES-MS-MS[8-15], and to a lesser extent MALDI-FTICR[16], and MALDI-TOF[17-21]. The mass spectrometric analyses of nonvolatile lipids has been reviewed by Murphy, et al.[22], and it is pointed out that the advent of soft ionization techniques such as ES-MS and MALDI-MS, has obviated the need for derivatization of lipids. Biological samples are complex mixtures of a wide variety of compounds that can have a negative influence on the ability to identify and quantify lipids by mass spectrometry; effects include signal suppression, and interferences from isomeric and isobaric compounds.

In this paper, a MALDI-TOF MS study of the phosphorylated lipids of normal human eye tear is reported using a novel solid ionic crystal MALDI matrix comprised of para-nitroaniline and butyric acid. MALDI-TOF has become an important tool for the characterization of complex biological extracts due to its high sensitivity, high resolution, and limited fragmentation of the compounds of interest. Front-end isolation of the phosphorylated lipids was achieved using immobilized metal affinity chromatography (IMAC). The chemical composition of the human meibomian gland liquid secretions (tear) has previously been characterized by HPLC[23], P-NMR[24], TLC[25], and fatty acid fragment profiles have been generated by HPLC-MS[26]. The newly developed methods reported in this paper enable the detection of very low-level phosphorylated lipids in tear samples, and have the potential for use for phosphorylated lipid determinations in other complex biological samples.

6.2 EXPERIMENTAL SECTION

6.2.1 Extraction of non-Polar and Polar Lipids

The non-polar and polar lipid fractions were extracted from tear samples with a simple modified chloroform-water partitioning procedure[27,28]. The aqueous phase contained the tear proteins, while the chloroform phase held the lipids.

6.2.2 Synthesis of Solid Ionic Crystal MALDI Matrix

Scheme 6.1 is a reaction scheme showing the synthesis of the solid ionic crystal matrix for MALDI. 250 mg of 4-nitroaniline and 333 μL of butyric acid were added to 9.05 mL of methanol with vortex mixing. After one minute, solvent was removed by rotovap. Upon removal of the methanol, yellow, slightly oily, pungent crystals were formed. The MALDI matrix used for further studies consisted of 20 mg of the solid ionic crystal 4-nitroaniline/butyric acid dissolved in 1 mL of ethanol.

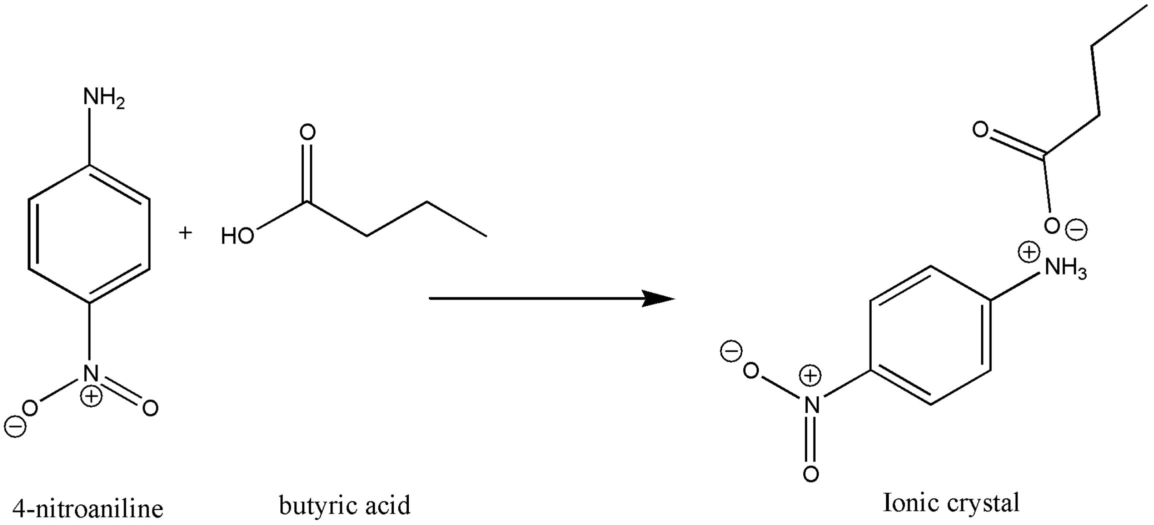

Scheme 6.1. Synthesis of MALDI ionic crystal matrix.

6.2.3 MALDI-TOF MS Analysis

MALDI-TOF mass spectra were acquired using an Applied Biosystems Voyager Elite r-ToF with Delayed Extraction (Applied Biosystems, Inc., Framingham, MA). An applied extraction voltage of 20 kV was typically employed. Delayed extraction mode was used for all acquisitions with a 175 ns delay time setting. The laser was operated just above the threshold energy required to obtain desorption/ionization. Each phospholipid mass spectrum constitutes an average of 150 to 200 traces. For sample plate spotting, 3 μL of phospholipid solution was mixed with 3 μL of matrix and then deposited onto the MALDI plate and allowed to air dry.

All spectra were calibrated using a two-point calibration employing protonated lyso PC, at *m/z* 496.34, and protonated DMPC at *m/z* 678.51. Phospholipids in the biological samples are identified according to their MALDI-TOF MS spectral molecular weights derived from either protonated molecules, sodiated molecules, and/or PSD product ions.

6.3 RESULTS AND DISCUSSION

6.3.1 Characterization and Optimization of the Ionic Crystal MALDI matrix

Experiments were performed in order to characterize and optimize the MALDI matrix for the mass spectral analysis of the phosphorylated lipids extracted from tear samples. In general, prompt fragmentation involving cleavage at the head group of phosphorylated lipids is a common problem when analyzing biological lipid extracts by MALDI. Difficulties pertaining to the ability to obtain quantitative[29] and spatial[30] information also arise when using solid MALDI matrixes. Inhomogeneous deposits of the analyte within the matrix and non-uniformities in the matrix layer cause variations in responses due to so-called "hot" or "sweet" spots versus the areas that produce lower-level signals. In general, a rather complex relationship exists between the MALDI spectral signal intensity and the amount of the measured analyte present in the spot.[31] A recent study by Rujoi et al.[32], reported the use of para-nitroaniline as a matrix for the study of the neutral phospholipids phosphatidylcholine and sphingomyelin in lens tissue, where the obtained $[M + H]^+$, $[M + Na]^+$, and $[M + K]^+$ signals appeared in greater sensitivities as compared to the 2,5-dihydroxybenzoic acid (DHB) matrix often used for phosphorylated lipids. Recently reported by Mank et al.[29] is the use of ionic liquid matrixes which have improved shot-to-shot reproducibility of signal intensities over traditional solid matrixes. This should enable more accurate quantitative analysis by MALDI. Also reported is a reduction in fragmentation

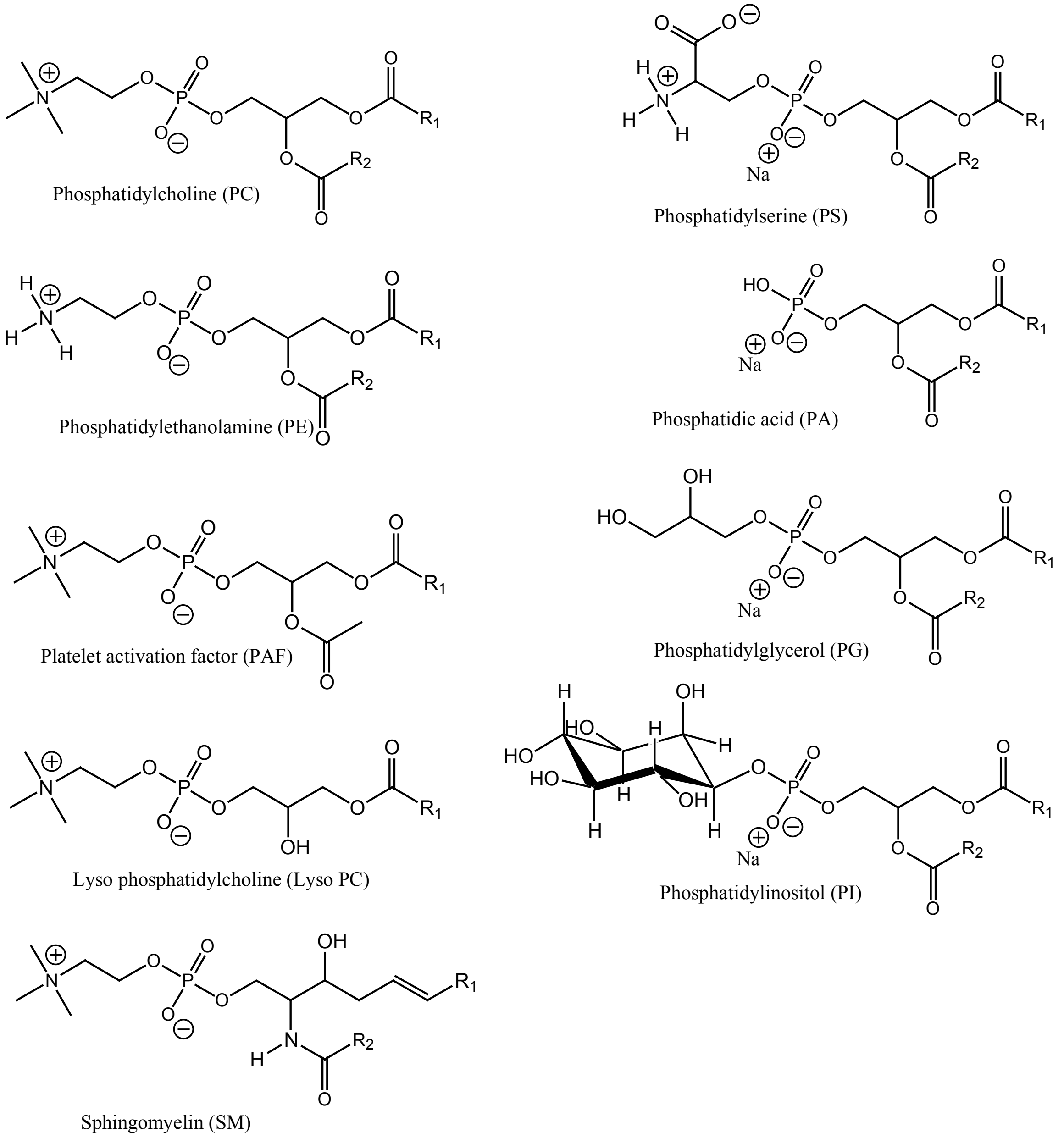

Phosphatidylcholine (PC)

Phosphatidylserine (PS)

Phosphatidylethanolamine (PE)

Phosphatidic acid (PA)

Platelet activation factor (PAF)

Phosphatidylglycerol (PG)

Lyso phosphatidylcholine (Lyso PC)

Phosphatidylinositol (PI)

Sphingomyelin (SM)

Figure 6.1. Structures of the main phosphorylated lipids included in this study. The left side lists the neutral, polar, zwitterionic phosphorylated lipids. The right side lists the anionic phosphorylated lipids as their neutral sodium adducts.

induced by the MALDI ionization technique when using the ionic liquid matrixes. Three examples of ionic liquid matrixes used by Mank et al.[29] are illustrated in Figure 6.2: (a) 2,5-dihydroxybenzoic acid butylamine, (b) alpha-cyano-4-hydroxycinnamic acid butylamine, and (c) 3,5-dimethoxy-4-hydroxycinnamic acid triethylamine. The ionic liquid matrixes are formed through combining the appropriate viscous liquid amines with the crystal MALDI matrix, after having dissolved both in methanol. The methanol and free amine are subsequently removed, thus producing the ionic pair which is then mixed with a small amount of ethanol to reduce the viscosity of the liquid matrix.

In the present study, para-nitroaniline was reacted with butyric acid as shown in Scheme 6.1. This mixture contrasts with those in Fig. 6.2 in that an ionic liquid was not produced. Rather, upon analyte mixing and drying, a solid ionic crystal is formed that acts as a powerful gas-phase proton donor and enhances phosphorylated lipid response. Because the final matrix preparation is crystalline, it shows deposition (spotting) behavior similar to other widely used solid MALDI matrixes such as sinapinic acid, DHB, or α-CHCA. Furthermore, difficult applications, such as depositing the matrix upon tissue or other surfaces for MALDI analyses revealing two-dimensional spatial distributions, will be more likely to succeed when a solid ionic crystal matrix is used in preference to an ionic liquid matrix. Finally, acidification of the analyte environment should not be severe with the solid ionic crystal matrix (where butyric acid is largely ion-paired with a p-nitroaniline), in contrast to the acidic MALDI matrixes DHB or α-CHCA.

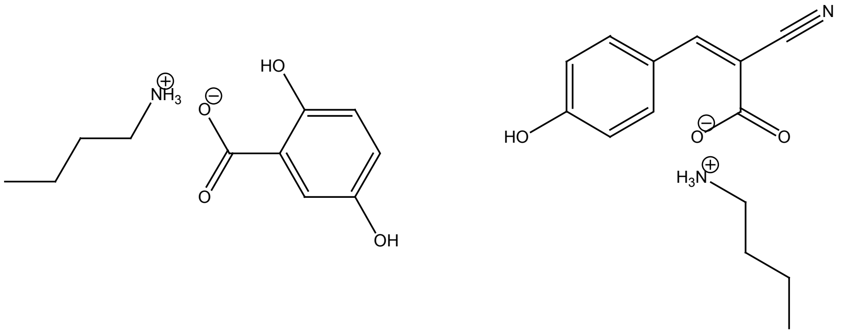

2,5-dihydroxybenzoic acid butylamine

alpha-cyano-4-hydroxycinnamic acid butylamine

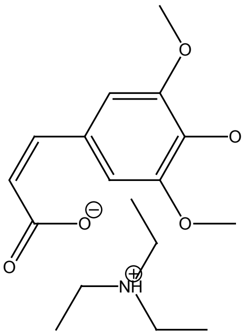

3,5-dimethoxy-4-hydroxycinnamic acid
triethylamine

Figure 6.2. Ionic liquid matrixes used for improved shot-to-shot reproducibility, and a reduction in fragmentation induced by MALDI. (a) 2,5-dihydroxybenzoic acid butylamine, (b) alpha-cyano-4-hydroxycinnamic acid butylamine, and (c) 3,5-dimethoxy-4-hydroxycinnamic acid triethylamine.

6.3.2 Zwitterionic Phospholipid MALDI Matrix Comparison.

For the optimization of the MALDI matrix for phosphorylated lipid analyses, six matrix preparations were evaluated in a comparison of the PNA-butyric acid matrix (with and without TFA) to 4 standard matrix preparations. The six matrixes consisted of (1) 20 mg/mL DHB dissolved in 1:1 MeOH:$CHCl_3$, (2) 10 mg/mL DHB + 10 mg/mL α-CHCA + 0.1% TFA dissolved in 2:1 $CHCl_3$:MeOH, (3) 20 mg/mL PNA dissolved in EtOH, (4) 20 mg/mL PNA + 0.1% TFA dissolved in EtOH, (5) 20 mg/mL PNA-butyric acid ionic crystals dissolved in EtOH, and (6) 20 mg/mL PNA-butyric acid ionic crystals + 0.1% TFA dissolved in EtOH. TFA was included in certain preparations to either aid in analyte protonation, or to enhance the dissolution of the lipids in the matrix[17].

Table 6.1 shows the zwitterionic phosphorylated lipids' major molecular ions observed in the MALDI spectra for the six different matrixes; Figure 6.1 illustrates the structures of the phosphorylated lipids used in this study. The left side of Figure 6.1 lists the neutral, polar zwitterionic phosphorylated lipids. The right side of Figure 6.1 shows the anionic phosphorylated lipids as their neutral sodium salts. In Table 6.1, the most striking feature found was that the PNA-butyric acid matrix and the PNA-butyric acid plus TFA matrix both produce the protonated form of PE as the predominant molecular ion. This is illustrated in Figure 6.3 which compares the MALDI spectra of PE using the six separate matrixes obtained at a laser fluence just above the threshold energy for appearance. For the DHB matrix, Fig. 6.3a, the major molecular ion peak is the sodium adduct $[PE+Na]^+$ at m/z 714, while the protonated molecule $[PE+H]^+$ at m/z 692 is of considerably lower abundance in the spectrum. Also observed in the spectrum are major ions produced through neutral head group losses at m/z 537 $[PE+H-C_3H_{10}NO_4P]^+$, at m/z

Lipid	DHB	50/50 αCHCA/DHB 0.1% TFA	PNA	PNA 0.1% TFA	PNA + Butyric Acid	PNA + Butyric Acid 0.1% TFA
PE	$[PE+Na]^+$ $[PE-HG]^+$	$[PE+Na]^+$ $[PE-HG]^+$	Very Low Signal	$[PE+H]^+$ $[PE-HG]^+$	$[PE+H]^+$	$[PE+H]^+$ $[PE-HG]^+$
Lyso PC	$[PC+H]^+$ $[PC+Na]^+$	$[PC+H]^+$	$[PC+H]^+$	$[PC+H]^+$	$[PC+H]^+$	$[PC+H]^+$
SM	$[SM+H]^+$ $[SM+Na]^+$	$[SM+H]^+$	$[SM+H]^+$	$[SM+H]^+$	$[SM+H]^+$	$[SM+H]^+$
PC	$[PC+H]^+$	$[PC+H]^+$	$[PC+H]^+$	$[PC+H]^+$	$[PC+H]^+$	$[PC+H]^+$
PAF	$[PAF+H]^+$	$[PAF+H]^+$	$[PAF+H]^+$	$[PAF+H]^+$	$[PAF+H]^+$	$[PAF+H]^+$

Table 6.1. Comparative Study of the Zwitterionic Phosphorylated Lipids' Major Spectral Molecular Ions Observed for the Six Different MALDI Matrixes.

551 $[PE+H-C_2H_8NO_4P]^+$, and at m/z 565 which is probably produced through post source decay (the peak is wide and the isotopes are not resolved). The 1:1 DHB:α-CHCA plus TFA matrix, Fig. 6.3b, produces the sodium adduct as the major MI, but there is significant head group loss leading to m/z 551. The protonated molecule, $[PE+H]^+$, is only a very minor peak at m/z 692. The PNA matrix, Fig. 6.3c, did not produce any appreciable positive mode molecular ions at

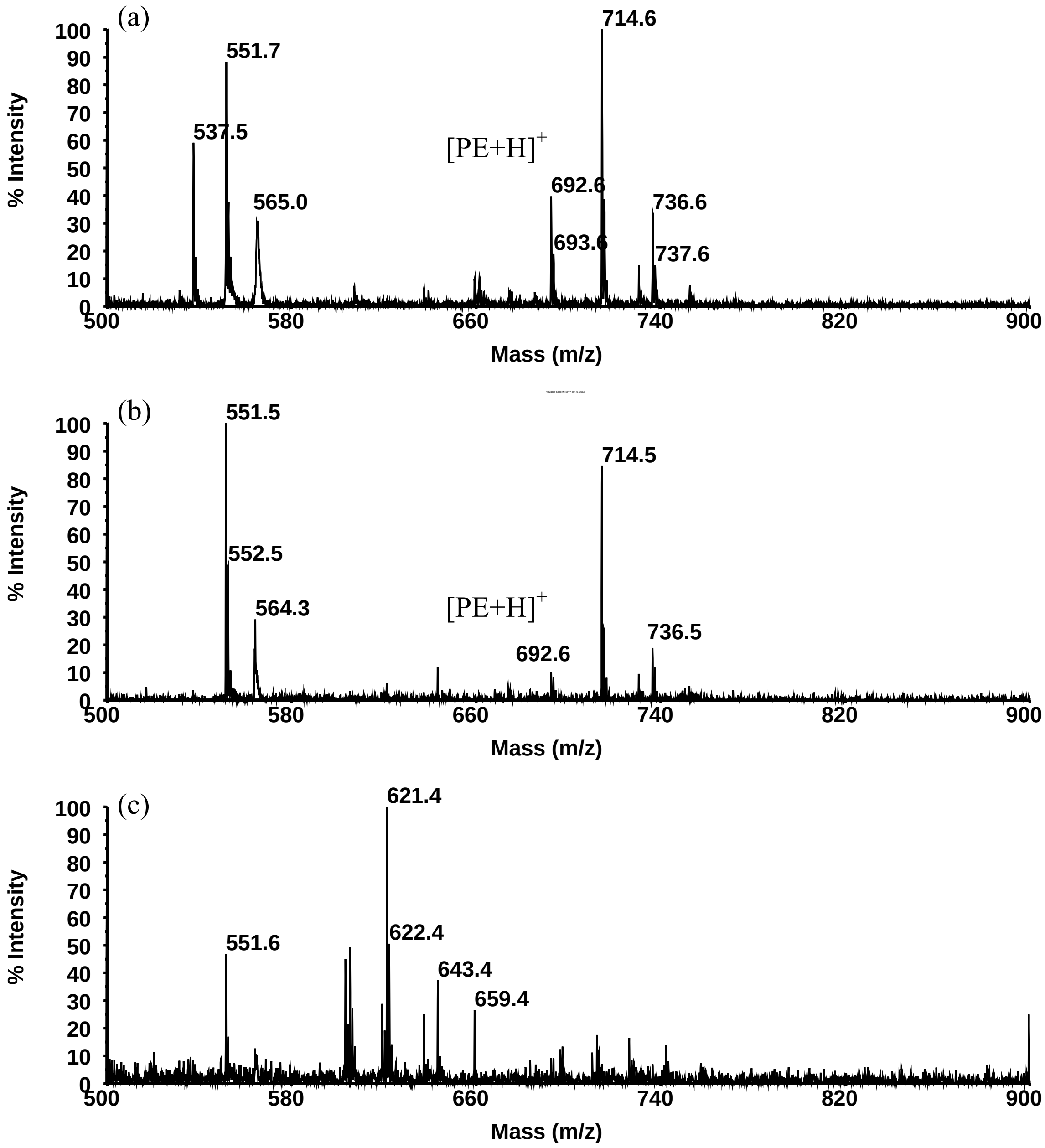
(a)
% Intensity
100
90
80
70
60
50
40
30
20
10
0
537.5
551.7
565.0
[PE+H]$^+$
692.6
693.6
714.6
736.6
737.6
500
580
660
740
820
900
Mass (m/z)
(b)
% Intensity
551.5
552.5
564.3
[PE+H]$^+$
692.6
714.5
736.5
Mass (m/z)
(c)
% Intensity
551.6
621.4
622.4
643.4
659.4
Mass (m/z)

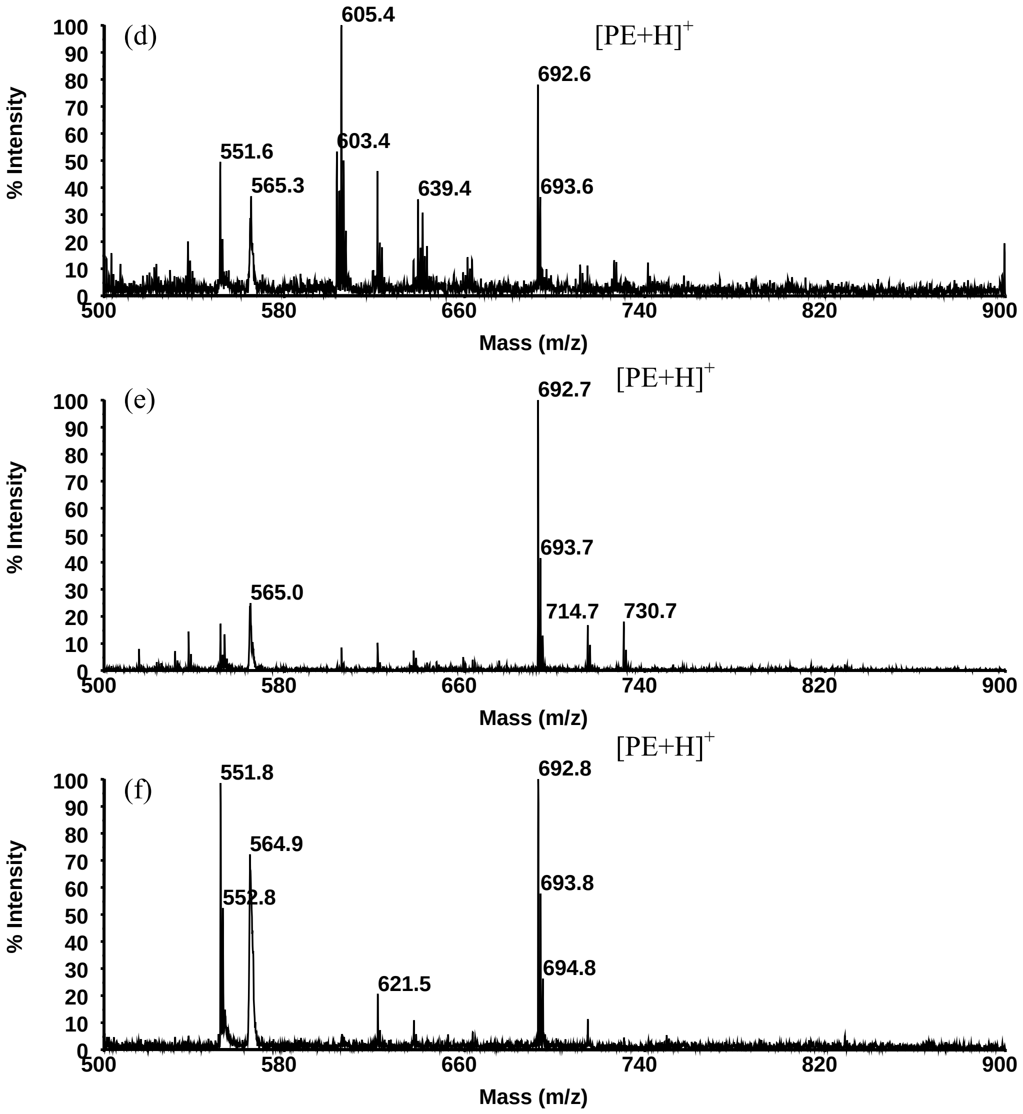

Figure 6.3. Comparison of the six MALDI matrixes for the analysis of phosphatidylethanolamine in positive ion mode. (a) DHB matrix showing predominant sodium adduct peak [PE+Na]$^+$ at m/z 714, and minor [PE+H]$^+$ at m/z 692. (b) α-CHCA/DHB plus TFA matrix with sodium adduct at m/z 714, but significant head group loss at m/z 551 observed, and a minor [PE+H]$^+$ peak at m/z 692. (c) PNA matrix shows no appreciable signals for sodium adducts or protonated molecules. (d) PNA plus TFA producing [PE+H]$^+$ at m/z 692, but major peaks for neutral losses of head group components at m/z 551, and m/z 605 are also observed. (e) PNA-butyric acid solid ionic crystal matrix producing predominantly the [PE+H]$^+$ ion at m/z 692 with only very minor amounts of the sodium adduct at m/z 714, and few fragment ions. (f) PNA-butyric acid plus TFA matrix producing the [PE+H]$^+$ ion at m/z 692 as a major spectral peak, but also significant headgroup loss ions at m/z 551 and m/z 565.

the expected m/z values of sodium or proton adducts. The PNA plus TFA matrix, Fig. 6.3d, did produce the protonated molecule $[PE+H]^+$ at m/z 692, but also major peaks for neutral losses of head group components at m/z 551, and m/z 605. In general, the inclusion of TFA was observed to promote fragmentation in the form of the loss of neutral head group components. The newly synthesized solid ionic crystal PNA-butyric acid matrix (Fig. 6.3e) and the PNA-butyric acid plus TFA matrix (Fig. 6.3f) were observed to produce protonated molecules as the major spectral peaks, with only very minor amounts of sodium adducts. However, the presence of TFA was again observed to induce significant fragmentation of the protonated molecule in the form of head group (neutral) loss at m/z 551 (Fig. 6.3f).

The observance of the protonated molecule, MH^+, as the major species in the mass spectrum helps to simplify spectral interpretation and can help enhance the fragmentation efficiency in tandem mass spectrometry experiments[33]. As illustrated in Table 6.1, the phosphatidylcholine head group containing lipids such as lyso PC, PC, PAF, and sphingomyelin all yield protonated molecules as the predominant molecular ion for the six matrixes studied. However, the solid ionic crystal PNA-butyric acid matrix allows formation of the strongest $[lipid+H]^+$ peak, and is the least conducive to head group loss.

Figure 6.4a is a MALDI-TOF spectrum of the para-nitroaniline/butyric acid matrix preparation illustrating the low molecular weight portion of the m/z range. The predominant spectral PNA-related ions include: m/z 108 $[PNA+H-HNO]^+$ and m/z 109

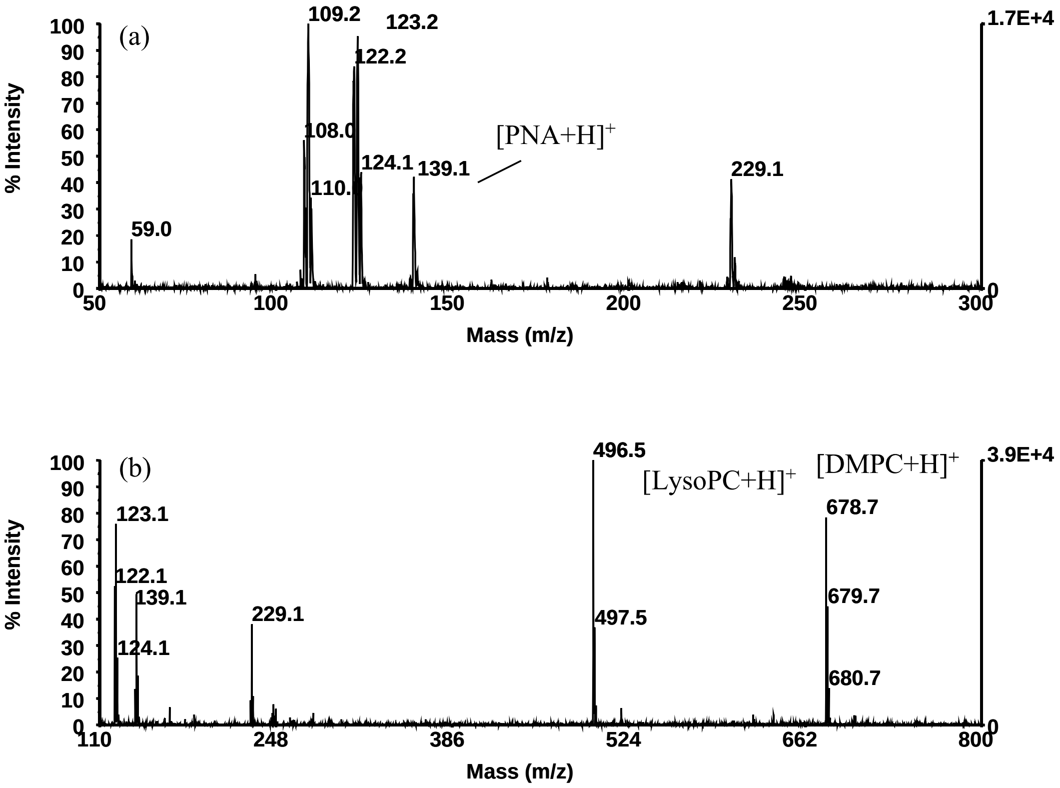

Figure 6.4. (a) MALDI-TOF mass spectrum of the para-nitroaniline/butyric acid matrix preparation illustrating the low mass region of the mass spectrum and showing background peaks originating from the matrix. (b) MALDI-TOF mass spectrum of a two-component mixture of lyso PC and DMPC standards showing protonated lyso PC at m/z 496, and protonated DMPC at m/z 678, using the PNA-butyric acid matrix.

$[PNA+H-NO]^+$ (both requiring rearrangement), m/z 122 $[PNA+H-NH_3]^+$, m/z 139 $[PNA+H]^+$, and m/z 229 $[2PNA+H-H_2NO_2]^+$ (actually produced through a reaction between two PNA molecules). Figure 6.4b is a MALDI-TOF spectrum of a two-component standard using the PNA-butyric acid matrix which includes the low molecular weight range of the spectrum. The standard consists of lyso PC and DMPC. As can be seen in Fig. 6.4b there is no interference of the matrix peaks with the lipid analytes. An approximate limit of detection was determined to be 1×10^{-6} M DMPC (~300 pg on sample target) using the novel solid ionic crystal as the MALDI matrix.

6.3.3 Anionic Phospholipid MALDI Matrix Comparison

Table 6.2 shows the anionic phosphorylated lipids' major molecular ions observed in MALDI mass spectra for the six different matrixes (see right side of Fig. 6.1 for structures). Row 1 of Table 6.2 shows the results for MALDI-TOF MS analysis of six matrixes with the lipid standard phosphatidylglycerol (PG) which is anionic and often present as a sodium salt. The DHB:α-CHCA plus TFA matrix was found to produce the $[PG+2Na-H]^+$ molecular ion as the predominant peak, while the other five were observed to produce the sodium adduct $[PG+Na]^+$ as the predominant molecular ion. For the PNA plus TFA matrix, the addition of TFA was found to promote prompt head group loss from both $[PG+2Na-H]^+$ and $[PG+Na]^+$. Figure 6.5a is the MALDI-TOF spectrum of PG using the PNA-butyric acid matrix showing the sodium adduct $[PG+Na]^+$ at m/z 771, and $[PG+2Na-H]^+$ at m/z 793. The phosphatidylserine lipid was also observed to suffer high degrees of head group loss with the addition of TFA as shown in Table 6.2, row 2. For the DHB:α-CHCA plus TFA matrix, PS exhibited facile prompt head group loss, and $[PS+Na]^+$ at m/z 784 was observed to be a very minor spectral ion. Head group loss for PS leading to m/z 577 $[PS-C_3H_7NO_6PNa]^+$ as a major spectral ion was observed for the PNA plus TFA matrix and for the PNA-butyric acid plus TFA matrix. Figure 6.5b is the MALDI-TOF spectrum of PS using the PNA-butyric acid matrix showing $[PS+Na]^+$ at m/z 784, and

Lipid	DHB	50/50 αCHCA/DHB 0.1% TFA	PNA	PNA 0.1% TFA	PNA + Butyric Acid	PNA + Butyric Acid 0.1% TFA
PG	[PG+Na]$^+$ [PG+2Na-H]$^+$ [PG-HG]	[PG+2Na-H]$^+$	[PG+Na]$^+$ [PG+2Na-H]$^+$	[PG+Na]$^+$ [PG+2Na-H]$^+$ [PG-HG]$^+$	[PG+Na]$^+$ [PG+2Na-H]$^+$	[PG+Na]$^+$
PS	[PS+Na]$^+$ [PS+2Na-H]$^+$	[PS-HG]$^+$	[PS+Na]$^+$	[PS+Na]$^+$ [PS-HG]$^+$	[PS+Na]$^+$	[PS-HG]$^+$
PA	[PA+Na]$^+$ [PA+2Na-H]$^+$	[PA+2Na-H]$^+$	Very Low Signal	[PA+2Na-H]$^+$ [PA+Na]$^+$	[PA+Na]$^+$ [PA+2Na-H]$^+$	Very Low Signal
PI	[PI+Na]$^+$ [PI+2Na-H]$^+$	[PI+2Na-H]$^+$ [PI+Na]$^+$	[PI+Na]$^+$ [PI+2Na-H]$^+$	[PI+Na]$^+$ [PI+2Na-H]$^+$	[PI+Na]$^+$ [PI+2Na-H]$^+$	[PI+Na]$^+$ [PI+2Na-H]$^+$

Table 6.2. Comparative Study of the Anionic Phosphorylated Lipids' Major Spectral Molecular Ions Observed for the Six Different MALDI Matrixes (for abbreviations, see text. HG = head group).

[PS+2Na-H]$^+$ at m/z 806. Notably, the phosphatidic acid (PA) lipid standard, Table 6.2, row 3, did not respond well when mixed with either the PNA matrix or the PNA-butyric acid plus TFA matrix. For PA in the PNA-butyric acid matrix (Fig. 6.5c), the predominant ion peak was observed to be the [PA+Na]$^+$ ion at m/z 697 which is in contrast to the DHB:α-CHCA plus TFA matrix and the PNA plus TFA matrix where the predominant ion is [PA+2Na-H]$^+$ (m/z 719). With the novel solid ionic crystal matrix (PNA-butyric acid), PG and PA are found predominantly as the sodium adducts [Phospholipid+Na]$^+$, and not as [Phospholipid+2Na-H]$^+$. This suggests that the butyric acid additive in the PNA matrix is acting as a protonating agent during MALDI analysis, displacing one of the sodium ions. This behavior is similar to that observed for PE (Table 6.1, row 1) where the predominant molecular ion is [PE+H]$^+$ (Fig. 6.3e), whereas the sodium adduct $[PE+Na]^+$ is observed as the predominant molecular ion with the DHB matrix (Fig. 6.3a) and the DHB:α-CHCA plus TFA matrix (Fig. 6.3b).

Other non-polar lipids that do not contain phosphate in the head group were also tested with the new matrix. These consisted of cholesteryl stearate, monopentadecanoin, 1-palmitin-2-stearin diacylglycerol, 1-palmitoyl-3-stearoyl diacylglycerol, triheptadecanoin, and the wax ester palmityl behenate. Observed in the MALDI-TOF spectra (not shown) for all of these non-polar lipids were sodium adducts as the predominant molecular ion peak, with minor potassium adducts.

As compared to traditional MALDI matrixes such as DHB for the study of phosphorylated lipids, one may summarize that the PNA-butyric acid solid ionic crystal offers: (1) reliable appearance of only the protonated molecules of lipids containing phosphatidylcholine head groups such as lyso PC, PC, and PAF; (2) reliable appearance of only the sodium adduct species for anionic phospholipids such as PG, PA, and PS; and (3) the ability to simultaneously detect all of the phosphorylated lipids represented in Figure 6.2 (including PE) in the positive mode of MALDI-MS. These three points can greatly simplify determinations of phosphorylated lipids present in complex biological samples and extracts.

6.3.4 PSD Fragmentation Study of Phosphatidylserine

Post source decay (PSD) analysis was performed on the phosphorylated lipid standards to study the decompositions of $[\text{Phospholipid}+H]^+$ for the neutral, polar zwitterionic phospholipids, and both the $[\text{Phospholipid}+Na]^+$ and $[\text{Phospholipid}+2Na-H]^+$ peaks for the anionic phospholipids. Figure 6.6a is the PSD spectrum of the sodium adduct of phosphatidylserine $[PS+Na]^+$ at m/z 784.

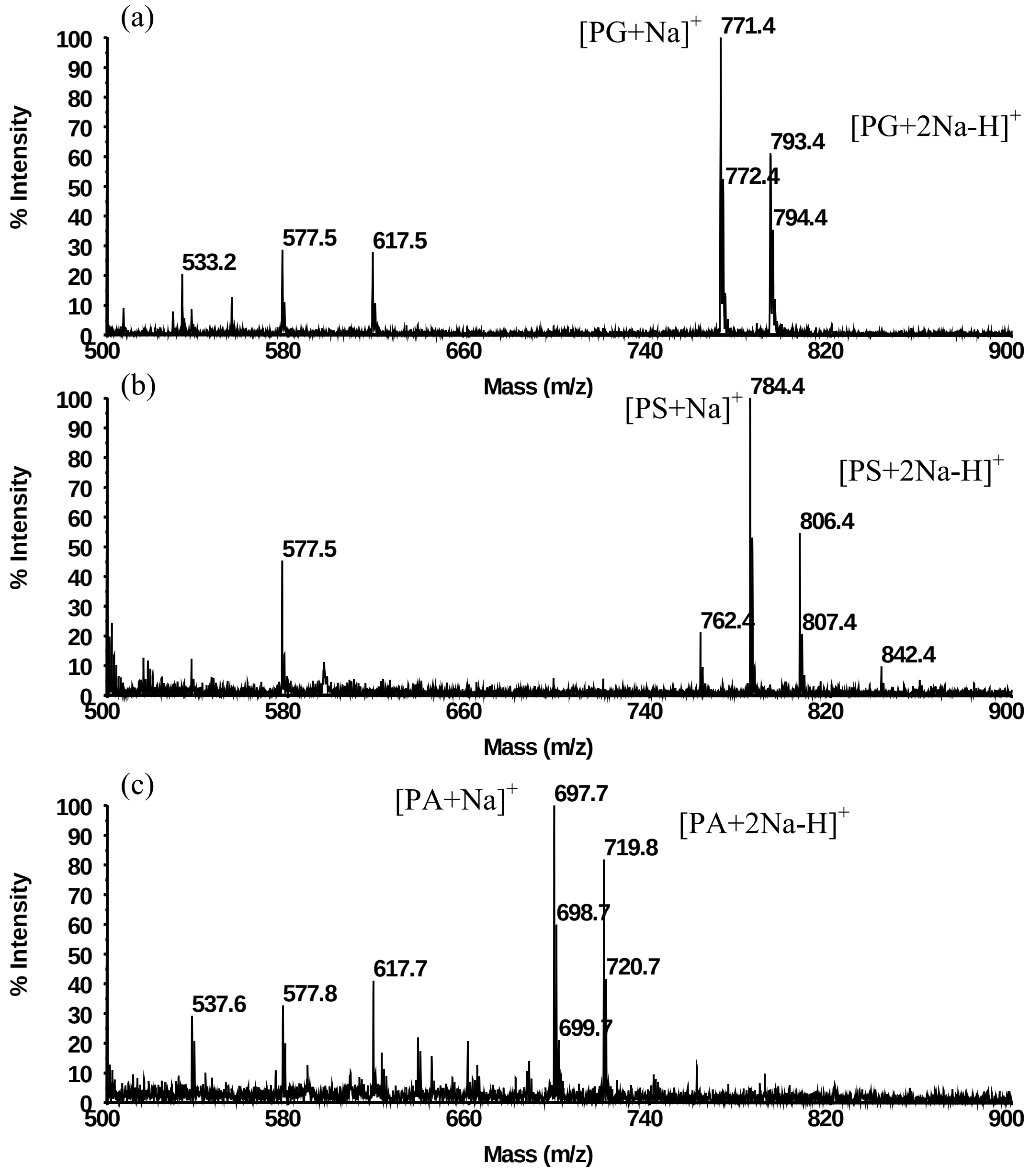

Figure 6.5. (a) MALDI-TOF mass spectra acquired using the PNA-butyric acid matrix: (a) PG showing [PG+Na]$^+$ at m/z 771, and [PG+2Na-H]$^+$ at m/z 793, (b) PS displaying [PS+Na]$^+$ at m/z 784, and [PS+2Na-H]$^+$ at m/z 806, and (c) PA showing [PA+Na]$^+$ at m/z 697, and [PA+2Na-H]$^+$ at m/z 719.

Figure 6.6b is the PSD spectrum of $[PS+2Na-H]^+$ at m/z 806. As can be seen in the two figures, the two molecular ions of PS have the same fragmentation pathways producing loss of head group fragments, but the favored pathways appear to be quite different. The phosphatidylserine lipid undergoes three forms of head group neutral loss under PSD conditions. The three product ion structures representing m/z 697, m/z 599, and m/z 577 are illustrated in Fig. 6.6a. As has been previously reported by Al-Saad et al[19], m/z 577 represents a six-membered ring product ion where the sodium was lost with the head group. The m/z 599 product ion is assigned as the sodium adduct of an alkene. The fragmentation pathway leading to the m/z 577 product ion is clearly favored over the m/z 599 product ion (Fig. 6.6a). The m/z 577 product ion involves the neutral loss of the sodium in the head group, while the production of the m/z 599 product ion results in the sodium staying adducted to the acylglycerol portion of the lipid. This indicates that for each molecular ion that contains two sodium atoms, one of the sodium ions is clearly associated with the negatively charged oxygen in the phosphoryl group. Secondly, the predominant m/z 208 product ion in Fig. 6.6a, which is comprised of the neutral head group sodium adduct, is similar to the fragmentation pathway forming m/z 577, except that a proton is transferred to the head group, so charge is retained on the latter. This further indicates that the predominant form of the precursor is the singly-sodiated molecule where the sodium is adducted to the phosphoryl head group, and not the acylglycerol portion of the lipid. For $[PS+2Na-H]^+$ the only predominant product ion is m/z 719 (Fig. 6.6b), which is formed through the neutral loss of $C_3H_5O_2N$ (87 Da). This indicates, as observed by Al-Saad et al.[19], that $[PS+2Na-H]^+$ is more stable than $[PS+Na]^+$. In fact, this is well known because charge on Na^+ is less mobile than on H^+ [33]. Figure 6.6b also contains structures of the different neutral molecules involved in head group losses.

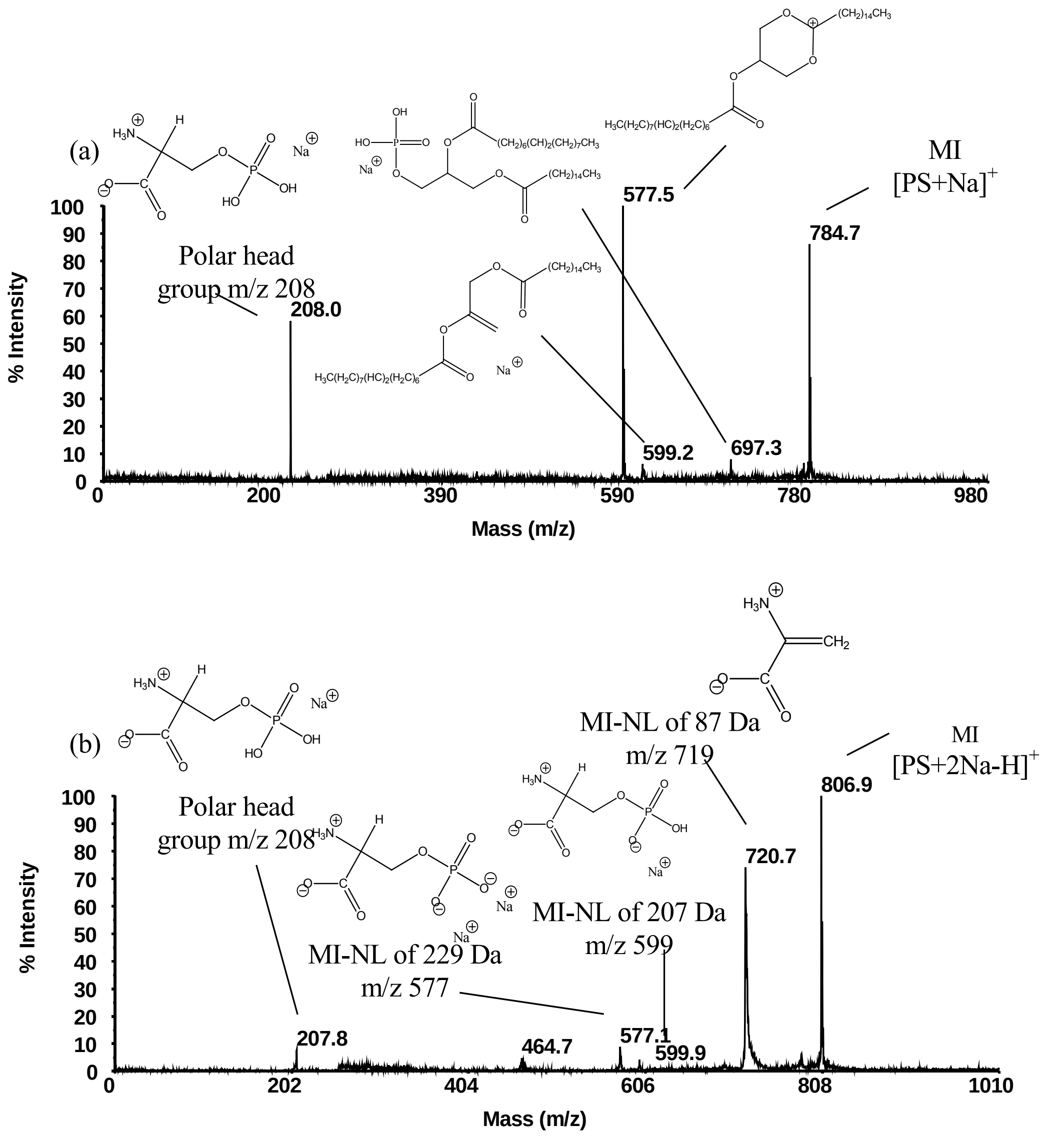

Figure 6.6. PSD spectra of: (a) phosphatidylserine $[PS+NA]^+$ precursor ion at m/z 784, and (b) phosphatidylserine $[PS+2Na-H]^+$ precursor ion at m/z 806.

6.3.5 PSD Fragmentation Study of Phosphatidic Acid

Head group loss pathways similar to those observed for phosphatidylserine were also observed in the PSD spectrum of phosphatidic acid, as illustrated in Figure 6.7a. In the spectrum there is the six-membered ring formation for the neutral loss of the sodium-containing head group at m/z 577 $[M+Na-PO_4H_2Na]^+$, and the alkene product ion formed through neutral head group loss at m/z 599 $[M+Na-PO_4H_3]^+$. Also observed in Fig. 6.7a are product ion peaks arising from neutral loss of the C16:0 fatty acid substituent at m/z 441 $[M+Na-C_{16}H_{32}O_2]^+$, neutral loss of C18:0 sodium fatty acetate at m/z 391 $[M+Na-C_{18}H_{35}O_2Na]^+$, and a sodium adduct of the phosphoric acid head group at m/z 121 $[H_3PO_4Na]^+$. Figure 6.7b is the PSD spectrum of $[PA+2Na-H]^+$. The two predominant peaks are formed through neutral loss of the fatty acid substituents, and can be used for identification purposes when coupled with the PSD spectrum of $[PA+Na]^+$ which gives head group information.

6.3.6 PSD Fragmentation Study of Lyso PC and DMPC

Figure 6.8a is the PSD spectrum of protonated lyso 1-palmitoyl choline (lyso-PC) at m/z 496. The predominant product ion in the spectrum is the expected peak representing the protonated phosphatidylcholine head group at m/z 184. However, there are three other peaks of interest in the spectrum.

The m/z 313 peak is derived from the neutral loss of the phosphatidylcholine head group from the m/z 496 precursor $[M+H-C_5H_{14}NO_4P]^+$, and the m/z 258 peak from the neutral loss of a fatty acyl chain as a ketene $[M+H-C_{16}H_{30}O]^+$. The observance of these two peaks can aid in the identification of the lyso phosphatidylcholine lipid. The third peak at m/z 104 is the head group

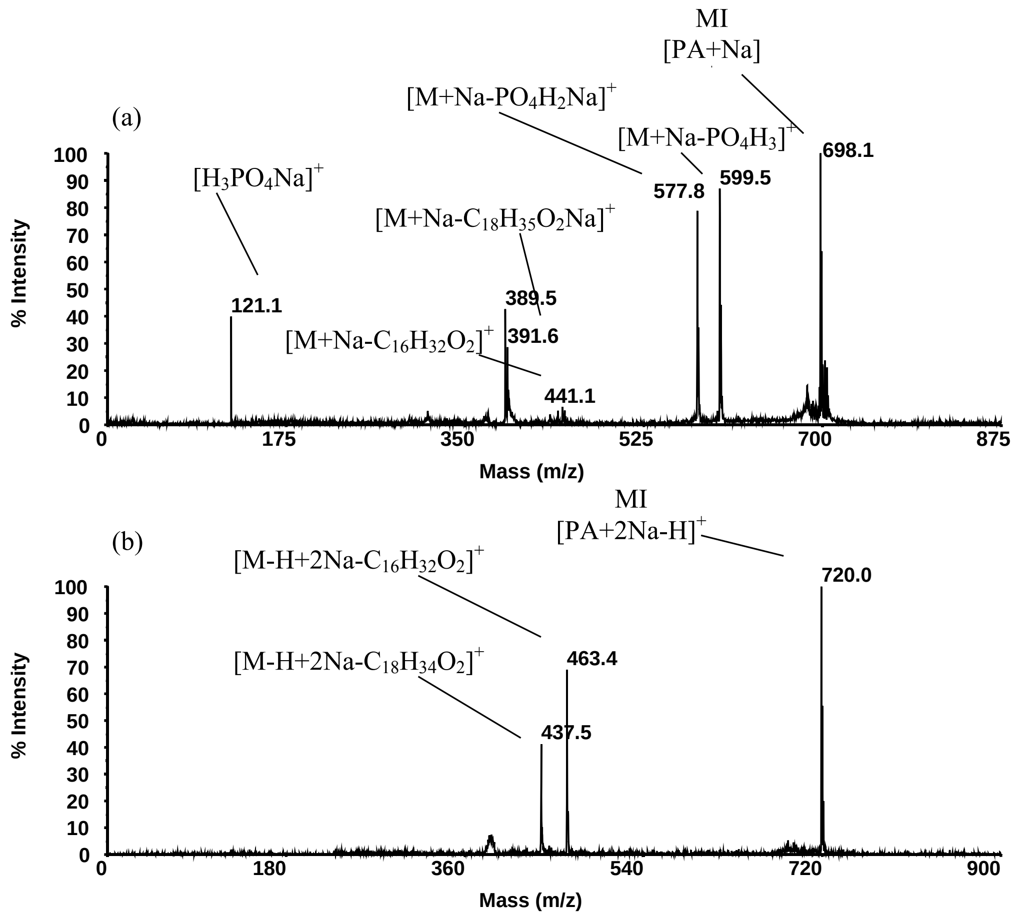

Figure 6.7. PSD spectra of: (a) phosphatidic acid $[PA+NA]^+$ precursor ion at m/z 697, (b) phosphatidic acid $[PA+2Na-H]^+$ precursor ion at m/z 719.

fragment ion $C_5H_{14}NO^+$, whose structure is illustrated in Fig. 6.8a. Figure 6.8b is the PSD spectrum of protonated dimyristyl phosphatidylcholine (DMPC) at m/z 678. In this spectrum there is also the m/z 184 product ion for the charged phosphatidylcholine head group that has previously been reported by Al-Saad, et al.[34], and a m/z 495 product ion derived from neutral loss of the PC head group $[M+H-C_{14}H_{14}NO_4P]^+$. For fatty acid substituent identification, there is the product ion at m/z 450 derived from the neutral loss of the C14:0 fatty acid $[M+H-C_{14}H_{28}O_2]^+$, and a product ion at m/z 468 from the neutral loss of a C14:0 fatty acyl chain as a ketene $[M+H-C_{14}H_{26}O]^+$. At m/z 86 in the spectrum there is a PC head group product ion whose structure is illustrated in Fig. 6.8b.

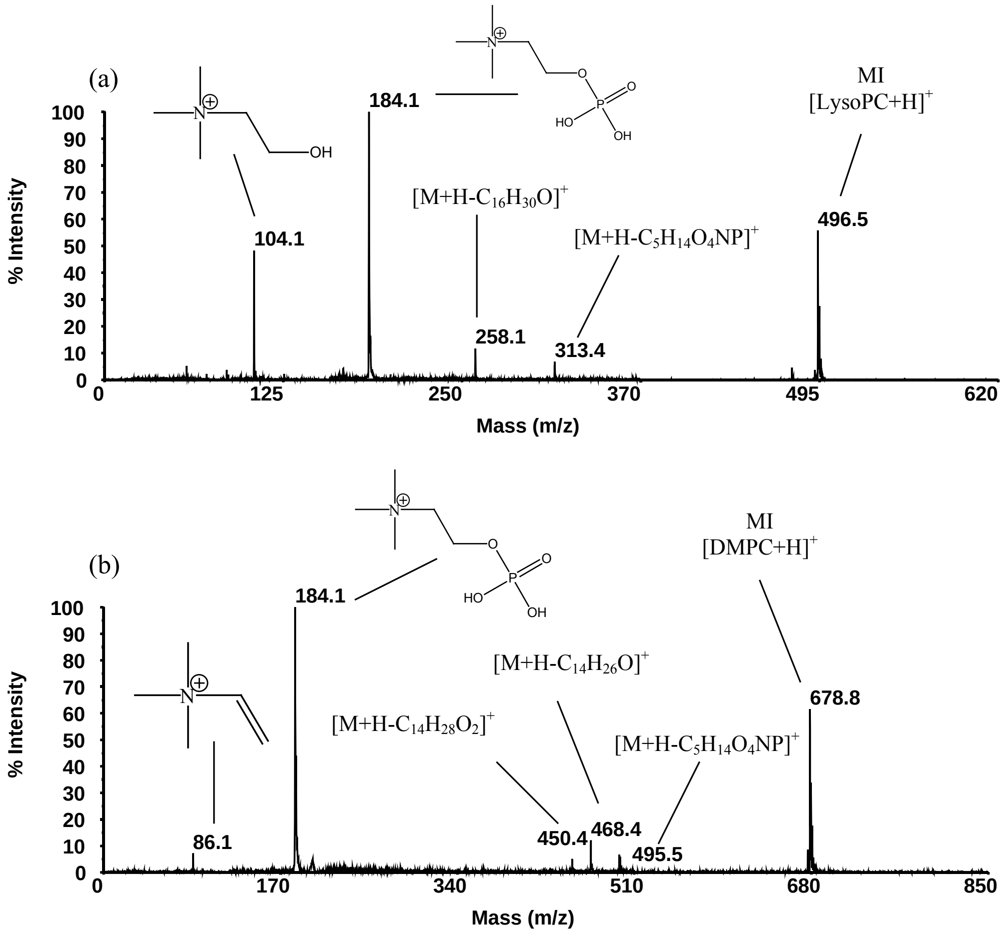

Figure 6.8. PSD spectra of: (a) lyso 1-palmitoyl choline (lyso-PC) $[LysoPC+H]^+$ precursor ion at m/z 496, and (b) dimyristyl phosphatidylcholine (DMPC) $[DMPC+H]^+$ precursor ion at m/z 678.

6.3.7 PSD Fragmentation Study of Phosphatidylglycerol

Figure 6.9a is the PSD spectrum of the sodium adduct of 1-palmitoyl-2-oleoyl-*sn*-glycero-3-[phospho-*rac*-(1-glycerol)] (sodium salt) (POPG) at m/z 771. In the spectrum, there are three predominant product ion peaks which involve the phospho-glycerol head group. At m/z 599, there is a minor peak for the neutral loss of the phospho-glycerol head group, and at m/z 577 there is the more predominant product ion peak for neutral loss of the phospho-glycerol head group (with sodium). The intensity of the m/z 577 peak being greater than the m/z 599 peak suggests that the departure of the neutral head group (with sodium) is the more favored fragmentation pathway, as was also observed in the PSD of PS (Fig. 6.6a). The most predominant product ion peak in the spectrum is the m/z 195 peak, i.e. the sodium adduct of the phospho-glycerol head group whose structure is illustrated in Fig. 6.9a. A minor peak is also observed at m/z 415 representing a two-step loss of a head group fragment (neutral loss of 74 Da, see Fig. 6.9b m/z 719 structure) in conjunction with neutral loss of the C18:1 fatty acid substituent $[M+Na-C_3H_6O_2-C_{18}H_{34}O_2]^+$, giving some structural information for the phosphorylated lipid. Fig. 6.9b is the PSD spectrum of $[PG+2Na-H]^+$ at m/z 793. This spectrum contains information concerning both the phospho-glycerol head group, and the two fatty acid substituents. M/z 719, m/z 217, and m/z 199 all involve the phospho-glycerol head group, and the associated structures are represented in the spectrum. The two fatty acid substituents are identified in the spectrum through two separate fragmentation pathways. There is a product ion formed as a result of neutral loss of the C18:1 fatty acid at m/z 511 $[M-H+2Na-C_{18}H_{34}O_2]^+$, and a product ion formed upon neutral loss of the C16:0 fatty acid at m/z 537 $[M-H+2Na-C_{16}H_{32}O_2]^+$. There are also two product ion peaks at m/z 437, and m/z 463, representing the combined neutral

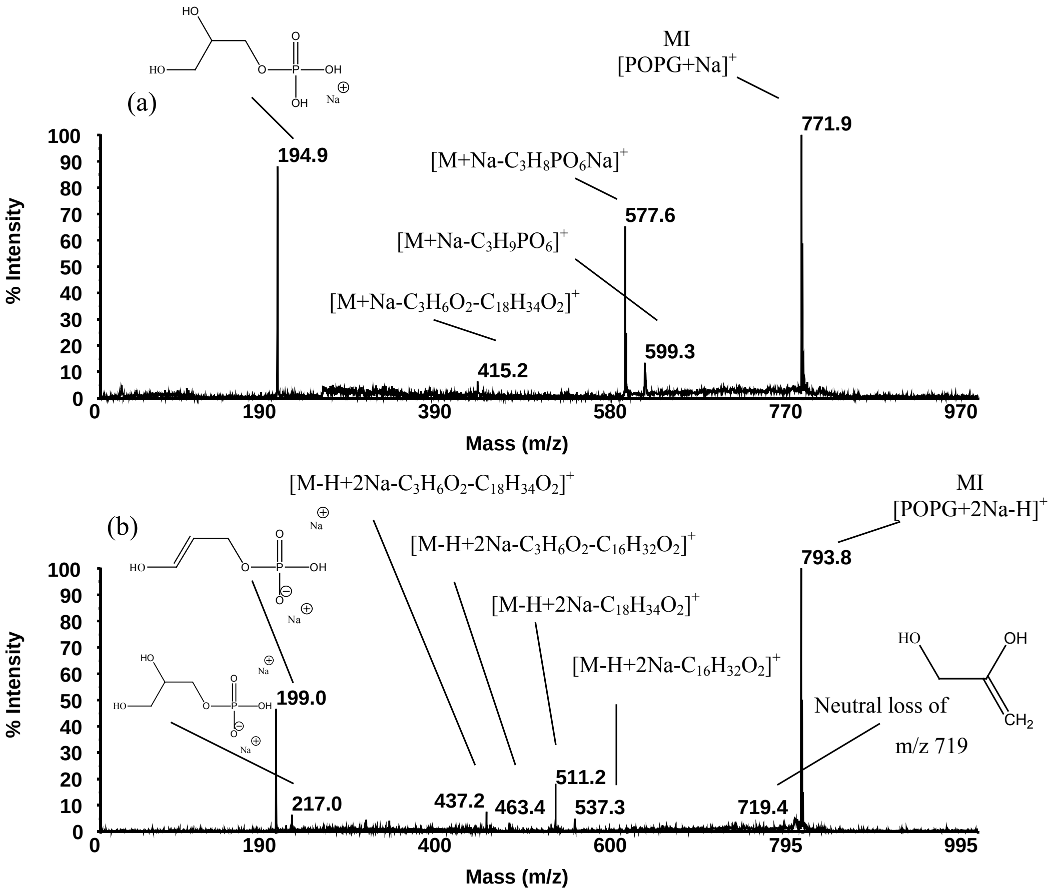

Figure 6.9. PSD spectra of: (a) 1-palmitoyl-2-oleoyl-*sn*-glycero-3-[phospho-*rac*-(1-glycerol)] (POPG) $[POPG+Na]^+$ precursor ion at m/z 771, and (b) $[POPG+2Na-H]^+$ precursor ion at m/z 793.

losses of a head group fragment and a fatty acid for the C18:1 and the C16:0 fatty acid substituents, respectively.

6.3.8 IMAC Cleanup and Preconcentration of Phosphorylated Lipids

A modified Millipore phosphopeptide enrichment method using ZipTip$_{MC}$ (Millipore Inc., Bedford, MA) pipette tips containing an immobilized metal ion affinity chromatography (IMAC) media (iminodiacetic acid, IDA resin) was used to enrich the phosphorylated lipids. The suggested method from the manufacturer was followed except for two key solutions: the binding solution was changed from 0.1% acetic acid (aqueous) to 0.1% acetic acid in 1:1 methanol:acetonitrile, and the elution solution was changed from 0.3 N ammonium hydroxide (aqueous) to 0.3 N ammonium hydroxide in 1:1 methanol:acetonitrile. The immobilized metal ion affinity chromatography (IMAC) media was found to be soluble in chloroform, therefore, care must be taken to remove all chloroform from the extracted lipids before application of the ZipTip$_{MC}$.

Figure 6.10 is a MALDI-TOF MS spectrum illustrating the recovery of a 4-component lipid standard mixture comprised of lyso phosphatidylcholine at m/z 496, dimyristyl phosphatidylcholine at m/z 678, dipalmitoyl phosphatidylethanolamine at m/z 692, and sphingomyelin at m/z 731, each detected in protonated form using the modified IMAC ZipTip$_{MC}$ method. The modified IMAC ZipTip$_{MC}$ method presented in this study has thus been demonstrated to be applicable to the isolation and cleanup of phosphorylated lipids in addition to the manufacturer's intended use for the isolation and cleanup of phosphorylated peptides.

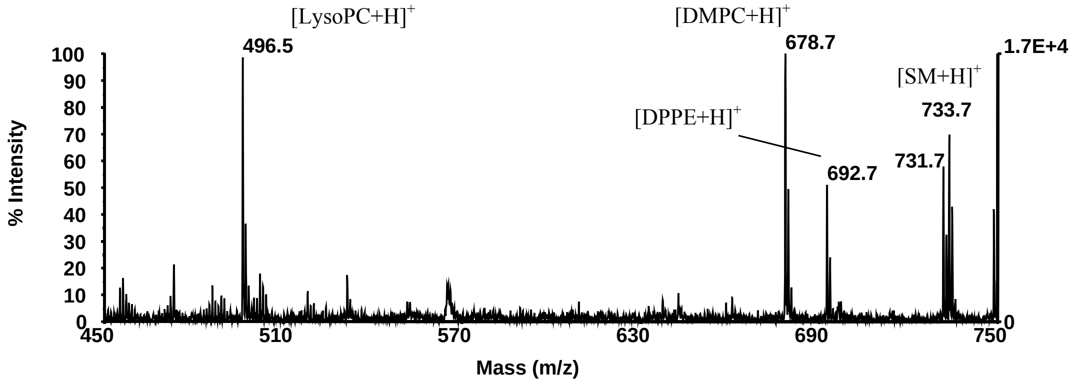

Figure 6.10. Recovery of a four-component phosphorylated lipid standard mixture using the IMAC ZipTip$_{MC}$. Protonated lyso phosphatidylcholine at m/z 496, protonated dimyristyl phosphatidylcholine at m/z 678, protonated dipalmitoyl phosphatidylethanolamine at m/z 692, and protonated sphingomyelin at m/z 731.

6.3.9 MALDI-TOF MS Analysis of Human Tear Film Lipid Layer

A normal eye tear sample was extracted, using the modified extraction procedure above, forming a chloroform phase containing lipids, and an aqueous phase containing proteins. The chloroform phase was evaporated, and the phosphorylated lipids were isolated using the IMAC ZipTip$_{MC}$ method. Figure 6.11a is a MALDI-TOF spectrum of the tear total chloroform extractables collected without the use of the IMAC ZipTip$_{MC}$ cleanup method. Figure 6.11b is the same extract with the use of the IMAC ZipTip$_{MC}$ cleanup prior to spectral collection. In Fig. 6.11a, the major peaks observed have been previously identified in our laboratory[35] as sodium adducts of monopalmitin acylglycerol at m/z 353 (not shown), monostearin acylglycerol at m/z 381 (not shown), a glyceryl-isoprene acetal at m/z 437, 1,3-dipalmitin diacylglycerol at m/z 591, 1-stearin,3-palmitin diacylglycerol at m/z 619, and 1,3-distearin diacylglycerol at m/z 647. As has been observed previously in our laboratory with electrospray, the phosphorylated lipids

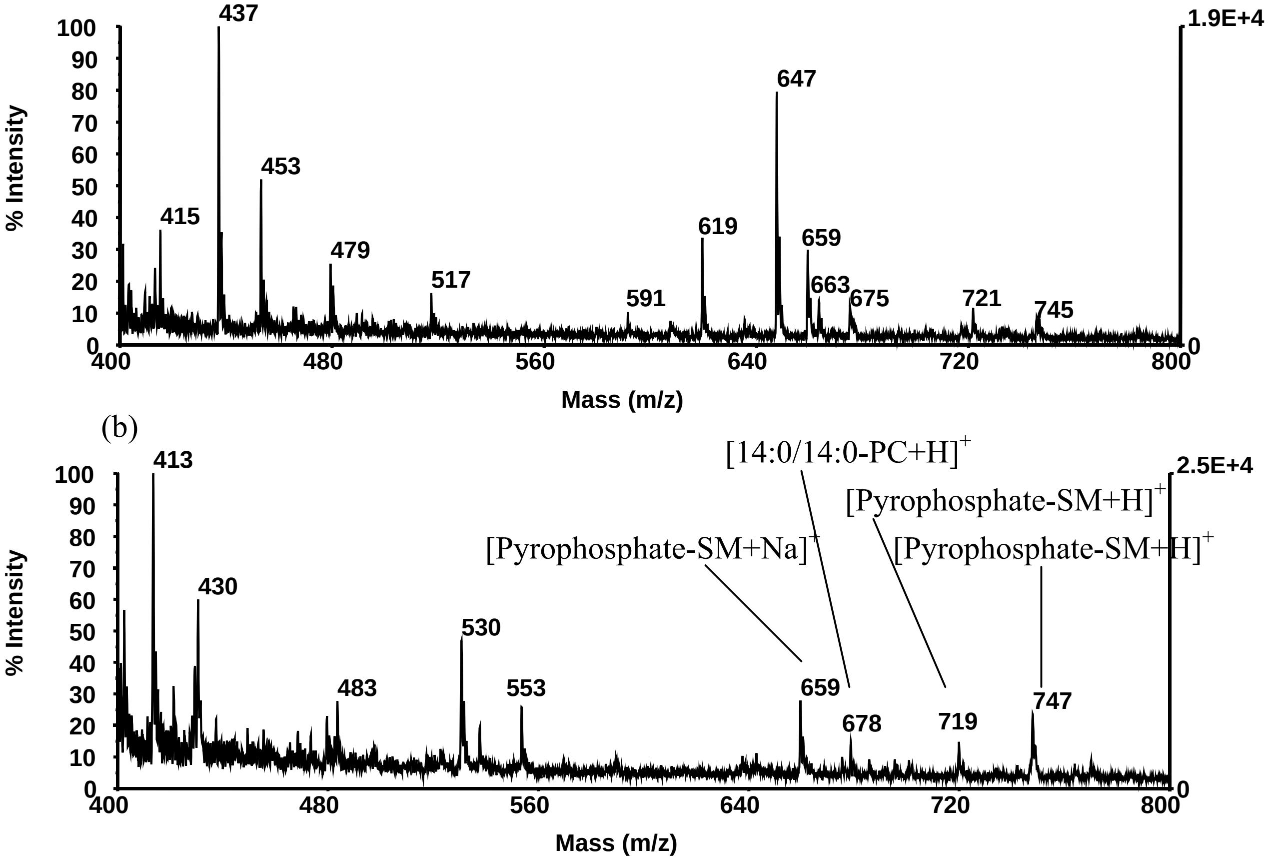

Figure 6.11. MALDI-TOF mass spectra of the tear total chloroform extractables collected: (a) without the use of the IMAC ZipTip$_{MC}$ cleanup method, and (b) with the use of the IMAC ZipTip$_{MC}$ cleanup prior to spectral acquisition.

are present in tear extracts in very low concentrations compared to the acylglycerols, and can experience a substantial amount, or even complete, signal suppression in positive mode electrospray. Figure 6.11a illustrates that signal suppression of the phosphorylated lipids in the tear extract, due to the acylglycerols also present, is again occurring with the use of MALDI. By applying the IMAC ZipTip$_{MC}$ isolation and cleanup procedure to the phosphorylated lipids, removal of the acylglycerols has been achieved and the phosphorylated lipids are now observable in Fig. 6.11b. In the ZipTip$_{MC}$ extract cleanup spectrum of Fig. 6.11b, m/z 659 is postulated to be the sodium adduct of a pyrophosphate sphingomyelin with a molecular formula of $C_{24}H_{50}N_2O_{13}P_2Na$, m/z 678 is protonated 1,2- (rac) dimyristoyl phosphocholine, and m/z 719 and 747 are also postulated to be protonated pyrophosphate sphingomyelins with molecular formulas of $C_{31}H_{65}N_2O_{12}P_2$, and $C_{33}H_{69}N_2O_{12}P_2$, respectively. There are also even numbered ions at m/z 430 and 530 indicating an odd number of nitrogens in those unidentified compounds.

6.4 CONCLUSIONS

Biological extracts, such as the tear film lipid layer presented in this study, are typically complex, multi-component mixtures. Separation schemes are usually employed to isolate the compounds of interest to simplify the mass spectra, and to lower the limits of detection. The novel solid ionic crystal MALDI matrix reported in this paper combines lipid detection enhancement through the use of para-nitroaniline as the matrix's ultraviolet light absorber with the powerful protonating additive butyric acid. Mass spectrum complexity is reduced and interpretation is simplified due to the phosphorylated lipids of interest existing primarily as $[M+H]^+$ ions for the neutral, polar zwitterionic phosphatidylcholine head group containing species lyso PC, PC, SM, and PAF. Further simplification is obtained because one need only monitor the mass spectrum for sodium adducts of the anionic phosphorylated lipids such as PG, PA, and PS. Finally, all of the phosphorylated lipids represented in this study can be measured simultaneously in the positive mode, including PE. It has also been demonstrated that the new ionic crystal matrix gives PSD spectra that can be used for head group identification, and fatty acid substituent characterization for both the nitrogen-containing phosphorylated lipids and those devoid of nitrogen.

A new extraction, isolation, and cleanup procedure has also been reported for the phosphorylated lipids using immobilized metal ion affinity chromatography (IMAC) media ZipTip$_{MC}$. It was shown that the ZipTip$_{MC}$ procedure is highly specific for recovery of the phosphorylated lipids. The ZipTip$_{MC}$ procedure has been successfully applied to a complex biological tear film lipid layer extract by removing the signal suppressing acylglycerols, thus allowing the determination of very low levels of phosphorylated lipids.

6.5 REFERENCES

1. Ohlrogge, J.; Browse, J. *Plant Cell* **1995***, 7*, 957-970.
2. Hodgkin, M. N.; Pettitt, T. R.; Martin, A.; Wakelam, M. J. O. *Biochem. Soc. Trans.* **1996**, *24*, 991-994.
3. Pettitt, T. R.; Martin, A.; Horton, T.; Liassis, C.; Lord, J. M.; Wakelam, M. J. O. *J. Biol. Chem.* **1997**, *272*, 17354-17359.
4. Gu, M.; Kerwin, J. L.; Watts, J. D.; Aebersold, R. *Anal. Biochem.* **1997**, *244*, 347-356.
5. Szucs, R.; Verleysen, K.; Duchateau, G. S.M.J.E.; Sandra, P.; Vandeginste, B.G.M. *J. Chromatogr. A* **1996**, *738*, 25-29.
6. Verleysen, K.; Sandra, P. *J. High Resol. Chromatogr.* **1997**, *20*, 337-339.
7. Raith, K.; Wolf, R.; Wagner, J.; Neubert, R. H.H. *J. Chromatogr. A* **1998**, *802*, 185-188.
8. Han, X.; Gross, R. W. *J. Am. Chem. Soc.* **1996**, *118*, 451-457.
9. Hoischen, C.; Ihn, W.; Gura, K.; Gumpert, J. *J. Bacteriol.* **1997**, *179*, 3437-3442.
10. Hsu, F.F.; Bohrer, A.; Turk, J. *J. Am. Soc. Mass Spectrom.* **1998**, *9*, 516-526.
11. Khaselev, N.; Murphy, R. C. *J. Am. Soc. Mass Spectrom.* **2000**, *11*, 283-291.
12. Hsu, F. F.; Turk, J. *J. Mass Spectrom.* **2000**, *35*, 596-606.
13. Liebisch, G.; Drobnik, W.; Lieser, B.; Schmitz, G. *Clin. Chem.* **2002**, *48*, 2217-2224.
14. Ho, Y. P.; Huang, P. C.; Deng, K. H. *Rapid Commun. Mass Spectrom.* **2003**, *17*, 114-121.
15. Hsu, F. F.; Turk, J. *J. Am. Soc. Mass Spectrom.* **2004**, *15*, 1-11.

16. Marto, J. A.; White, F. M.; Seidomridge, S.; Marshall, A. G. *Anal. Chem.* **1995**, *67*, 3979-3984.
17. Schiller, J.; Arnhold, J.; Benard, S.; Muller, M.; Reichl, S.; Arnold, K. *Anal. Biochem.* **1999**, *267*, 46-56.
18. Ishida, Y.; Nakanishi, O.; Hirao, S.; Tsuge, S.; Urabe, J.; Sekino, T.; Nakanishi, M.; Kimoto, T.; Ohtani, H. *Anal. Chem.* **2003**, *75*, 4514-4518.
19. Al-Saad, K. A.; Zabrouskov, V.; Siems, W. F.; Knowles, N. R.; Hannan, R. M.; Hill Jr., H. H. *Rapid Commun. Mass Spectrom.* **2003**, *17*, 87-96.
20. Rujoi, M.; Estrada, R.; Yappert, M. C. *Anal. Chem.* **2004**, *76*, 1657-1663.
21. Woods, A. S.; Ugarov, M.; Egan, T.; Koomen, J.; Gillig, K. J.; Fuhrer, K.; Gonin, M.; Schultz, J. A. *Anal. Chem.* **2004**, *76*, 2187-2195.
22. Murphy, R. C.; Fiedler, J.; Hevko, J. *Chem. Rev.* **2001**, *101*, 479-526.
23. Ohyama, T.; Matsubara, C.; Takamura, K. *Analyst*, **1996**, *121*, 1943-1947.
24. Greiner, J.V.; Glonek, T.; Korb, D. R.; Booth, R.; Leahy, C. D. *Ophthalmic Res*, **1996**, *28*, 44-49.
25. Wollensak, G.; Mur, E.; Mayr, A.; Baier, G.; Gottinger, W.; Stoffler, G. *Graefe's Arch Clin Exp Ophthalmol* **1990**, *228*, 78-82.
26. Sullivan, B.D.; Evans, J.E.; Krenzer, K.L.; Dana, M.R.; Sullivan, D.A. *JCEM,* **2000,** *85,* 4866-4875.
27. Folch, J.; Lees, M.; Stanley, G. H. S. *J. Biol. Chem.* **1957**, *226*, 497-509.
28. Bligh, E. G.; Dyer, W. J. *Can. J. Biochem. Physiol.* **1959**, *37*, 911-917.
29. Mank, M.; Stahl, B.; Boehm, G. *Anal. Chem.* **2004,** *76,* 2938-2950.
30. Luxembourg, S. L.; McDonnell, L. A.; Duursma, M. C.; Guo, X.; Heeren, R. M. A. *Anal. Chem.* **2003,** *75,* 2333-2341.
31. Aebersold, R.; Mann, M. *Nature* **2003**, *422*, 198-207.
32. Rujoi, M.; Estrada, R.; Yappert, M. C. *Anal. Chem.* **2004,** *76,* 1657-1663.
33. Cole, R. B.; Tabet, J.; Blais, J. *Int. J. Mass Spectrom. Ion Processes* **1990**, *98*, 269-283.
34. Al-Saad, K. A.; Siems, W. F.; Hill, H. H.; Zabrouskov, V.; Knowles, N. R. *J Am Soc Mass Spectrom* **2003**, *14*, 373-382.
35. Ham, B. M.; Jacob, J. T.; Keese, M. M.; Cole, R. B. *J. Mass Spectrom.* **2004**, *39*, 1321-1336.

CHAPTER VII: IDENTIFICATION AND COMPARISON OF THE POLAR PHOSPHORYLATED LIPIDS IN NORMAL AND DRY EYE RABBIT TEARS BY MALDI-TOF MASS SPECTROMETRY

7.1 Introduction

The ocular tear fluid is a dynamic and complex mixture of water, salts, mucins, and diverse biomolecules including proteins, enzymes, and lipids, whose components interact with one another to maintain the health and clarity of the cornea and ocular surface. The tear film acts as a lubricant during blinking, and protects the cells of the ocular surface from damaging debris and pathogens. Additionally, the tears transport oxygen and nutrients to the cells of the cornea and conjunctiva. Irregularities in the tear film can cause a number of ocular problems, including dry eye. The National Eye Institute defines dry eye syndrome as "a disorder of the tear film due to tear deficiency or excessive evaporation that causes damage to the interpalpebral ocular surface and is associated with symptoms of discomfort."[1] Approximately 10 to 14 million people in the United States alone have some form of dry eye.

The development of dry eye syndrome is associated with a number of physiological and environmental conditions, including aging,[2] hormonal imbalance,[3] disease,[4] surgery,[5,6] smoke, wind, heat, and/or low humidity.[1,7,8] However, the ability to classify dry eye patients within specific etiological categories, except for those caused by a specific disease state~~s~~ such as Sjögren's syndrome,[4] is difficult because the exact effect of the various causative conditions on the compositional structure of the tear film is unknown.

The normal tear fluid, which is approximately 7 μL in volume in both rabbits and humans, continuously bathes the corneal and conjunctival surface of the eye. The structure of the tear fluid is generally divided into three layers: the innermost epithelial-glycocalyx layer, an intermediate aqueous-mucin layer,[9,10] and an outermost lipid layer.[11] The components of the tear film are supplied by a number of ocular tissues. The innermost glycocalyx layer is secreted by the stratified squamous cells of the conjunctiva and cornea. Its primary functions are to protect the ocular surface cells from bacterial binding and smooth out any small surface irregularities. The aqueous-mucin layer, composed of mucins, proteins, and electrolytes, is secreted by the main and accessory lacrimal glands and the conjunctival goblet cells. The various proteins found in the aqueous layer perform a myriad of functions vital to maintaining the health of the ocular surface, regulating surface cell function, and maintaining the tear film structure.[12] The outer lipid layer is secreted by the meibomian glands, which are located in the eyelids; its main function is to retard the evaporation of the aqueous layer.[13,14] Because the cells of the ocular surface function within a narrow range of pH, osmolarity, and ionic compositions, it is vital that the tears maintain the appropriate concentrations of constituents in each of the three layers. Alterations of the composition of the tear film can result in development of dry eye syndrome and, ultimately, deleterious effects on vision.

The instability of the outer lipid layer of the tear film, due to changes in the polar lipid concentration, has been identified as a potential factor in the development of dry eye syndrome.[15,16] Previous investigations into molecular changes in tear film structure have been hampered by the need to pool tears to make up a sample quantity large enough to allow detection by analytical methods such as one- or two-dimensional electrophoresis.[17,18,19] Another problem is the requirement that the tear components be derivatized before they are subjected to gas chromatography (GC), mass spectrometry (MS), or both.[20,21] The chemical composition of the human meibomian gland liquid secretions has been characterized by high pressure liquid chromatography (HPLC),[22] pico-nuclear magnetic resonance (p-NMR),[23] and thin-layer chromatography (TLC),[24] and fatty acid fragment profiles have been obtained by HPLC-MS.[25]

During the past several years, the analysis of phospholipids in general has been reported by HPLC[26] and micellar electrokinetic chromatography (MEKC),[26,27] capillary electrophoresis-electrospray-mass spectrometry (CE-ES-MS),[28] electrospray tandem mass spectrometry (ES-MS/MS),[29-36] and to a lesser extent matrix-assisted laser desorption/ionization-Fourier-transform ion cyclotron resonance (MALDI-FTICR)[37] and MALDI-time-of-flight (TOF) MS.[38-42] Indeed However, with the advent of soft ionization techniques such as ES-MS and MALDI-MS, the derivatization of volatile lipids is no longer essential.[43] In this paper, we report a MALDI-TOF MS study of the phosphorylated lipids of normal and dry eye tears using an immobilized metal ion affinity chromatography (IMAC) ZipTip$_{\mathrm{MC}}$ (Millipore, Bedford, MA) clean-up method coupled with a newly synthesized solid ionic crystal MALDI matrix to detect nanogram to picogram quantities of phosphorylated lipids in small volume tear samples. Comparison of the types and relative quantities of the polar phospholipids in normal and dry eye rabbit tears should provide insight into the effect of polar lipid changes on the stability of the tear film.

7.2 Experimental

7.2.1 Animals

Six female New Zealand white rabbits (7-8 lbs body weight) purchased from Harlan (Indianapolis, IN) were used. All animal studies were conducted in accordance with the ARVO Statement on the Use of Animals in Ophthalmic and Vision Research.

7.2.2 Rabbit Tear Samples

The rabbit dry eye model was created in female New Zealand white rabbits by two sequential surgical procedures. First, the main lacrimal gland was removed from the experimental eye; the contralateral eye was used as the normal control. Approximately 2 weeks later, the accessory lacrimal gland and nictitating membrane were removed from the experimental eye. Tear breakup time (TBUT) was measured daily by slit lamp with a Tearscope (Keeler Instruments, Broomall, PA). When the TBUT of the surgical eye was half or less that of the control eye, the surgical eye was considered to be dry. Baseline tears (representing tears produced under non-irritating conditions) were collected daily from the normal and surgically induced dry eyes using 5-μL silanized microcapillary pipettes.[24] The tear samples were immediately placed in Eppendorf tubes and stored at –70ºC.

7.2.3 Chemicals

Lyso 1-palmitoyl choline, dimyristoyl phosphatidylcholine, 1,2-dipalmitoyl-sn-glycero-3-phosphoethanolamine, 1-palmitoyl-2-hydroxy-sn-glycero-3-phosphocholine, and sphingomyelin were purchased as standards (Avanti Polar Lipids, Alabaster, AL). Methanol and chloroform solvents of HPLC/spectroscopy grade were purchased from EM Science (Darmstadt, Germany). All other chemicals were of analytical-reagent grade. All standards and chemicals were used as received without further purification. Distilled and deionized (dd) water (18 MΩ, Milli-Q Water Purification System; Millipore Inc., Bedford, MA) was used throughout standard and sample preparations.

7.2.4 Extraction of Non-Polar and Polar Lipids

The non-polar and polar lipid fractions were extracted from tear samples with a simple two-phase (chloroform, water) extraction technique; the resulting aqueous phase contained the tear proteins and the chloroform phase contained the lipids.[44,45] Briefly, 1 week of tears collected from one eye was diluted to 300 μL with dd water. The aqueous tear solution was then extracted three times with 500 μL of chloroform. The chloroform extracts were combined and evaporated to near dryness. At least three weeks of samples per eye were analyzed using the Zip-Tip MALDI-TOF method described below.

To extract the phosphorylated lipids from the lacrimal glands, the gland was blended with 100 mL of chloroform. The extract was filtered and the volume of the solution was reduced to approximately 20 mL using low heat and a gentle stream of nitrogen. Aliquots were diluted 1:10 with matrix solution (see MALDI-TOF MS below) and spotted directly onto the MALDI target for analysis. At least three aliquots per sample type were analyzed by MALDI-TOF.

7.2.5 Zip-Tip Cleanup and Pre-concentration of Polar Lipids

A modified phosphopeptide enrichment method, previously developed in this laboratory (Ham et al., accepted for publication), using ZipTip$_{\text{MC}}$ pipette tips containing an IMAC medium (iminodiacetic acid, IDA resin) was used to concentrate the phosphorylated lipids. The suggested method from the manufacturer (Millipore) was followed except for two key solutions: the binding solution was changed from 0.1% acetic acid to 0.1% acetic acid in 1:1 methanol:acetonitrile, and the elution solution was changed from 0.3 N ammonium hydroxide to 0.3 N ammonium hydroxide in 1:1 methanol:acetonitrile. The IMAC medium was found to be soluble in chloroform; therefore, care was taken to remove all chloroform from the extracted lipids before application of the ZipTip$_{\text{MC}}$. The lipids were reconstituted in 5 :l of the Zip-Tip binding solution, aspirated through the Zip-tip matrix for binding, washed, and eluted with 3:l of elution solution.

7.2.6 MALDI-TOF MS

MALDI-TOF mass spectra were acquired using an Applied Biosystems Voyager Elite MALDI-rTOF mass spectrometer with delayed extraction (Applied Biosystems, Inc., Framingham, MA). A UV light, 337 nm emission wavelength, nitrogen laser was used for irradiation. A typical spectrum was collected at an extraction voltage of 20 kV. Delayed extraction mode was used for all acquisitions with a 175 ns delay. The laser power was adjusted to a level just above the threshold for signal appearance to minimize head group loss. Each phospholipid mass spectrum was collected by averaging data from 250 laser shots. For sample plate spotting, 3 μL of ZipTip$_{MC}$- eluted phospholipids was mixed with 3 μL of matrix and then deposited onto the MALDI plate and allowed to air dry. The MALDI matrix used in all studies consisted of a recently developed solid ionic crystal matrix of 20 mg of paranitroaniline (PNA) and butyric acid in a 1:2 molar ratio dissolved in ethanol (Ham et al., accepted for publication).

All spectra were collected using a two-point calibration of protonated lysophosphatidylcholine at a mass/charge ratio (*m/z)* of 496.34, and protonated dimyristoyl phosphatidylcholine (DMPC) at *m/z* 678.51. Phospholipids in the biological samples were assigned according to their molecular weights derived from either the monoisotopic protonated molecules, monoisotopic sodium adducts, and/or post source decay (PSD) product ions in MALDI-TOF mass spectra.

7.3 Results and Discussion

7.3.1 Rabbit Eyes and Tear Samples

All of the rabbit eyes remained healthy throughout the study period; the corneas and conjunctivas of both the normal and dry eyes were healthy and showed no epithelial staining.

The experimental dry eyes had TBUTs approximately one-third those of the corresponding contralateral control eyes. The usual tear volume obtained from a single normal eye was 3 μL, whereas only 1 μL was typically obtained from a dry eye.

7.3.2 MALDI-TOF MS Analysis of Tear Phospholipids

By inducing dry eye in only one eye of each rabbit, we were able to compare lipid expression in dry eye and normal tear samples from the same animal, thereby reducing or eliminating the effect of physiological variation from rabbit to rabbit. Samples of normal and dry eye tears were extracted with chloroform following the modified extraction method outlined above. The lipid-containing chloroform phase was recovered and evaporated, and the phosphorylated lipids were isolated using the IMAC ZipTip$_{MC}$ method; proteins were largely left behind in the aqueous phase. All presented mass spectra were acquired after extraction and ZipTip$_{MC}$ cleanup.

Figure 7.1 a and b are representative of normal and dry eye tear mass spectra obtained by our method. In general, the normal eye tear spectra showed six major peaks (m/z 494, 522, 550, 577, 610, 638) and seven minor peaks (m/z 637, 642, 659, 678, 695, 866, 936). The dry eye tear spectra showed 10 major (m/z 494, 522, 550, 577, 605, 621, 637, 659, 610, 642) and four minor (m/z 678, 695, 828, 886) peaks assignable within their mass spectra. Five of the major peaks (m/z 494, 522, 550, 577, 610) and two of the minor peaks (m/z 678, 695) were the same for both

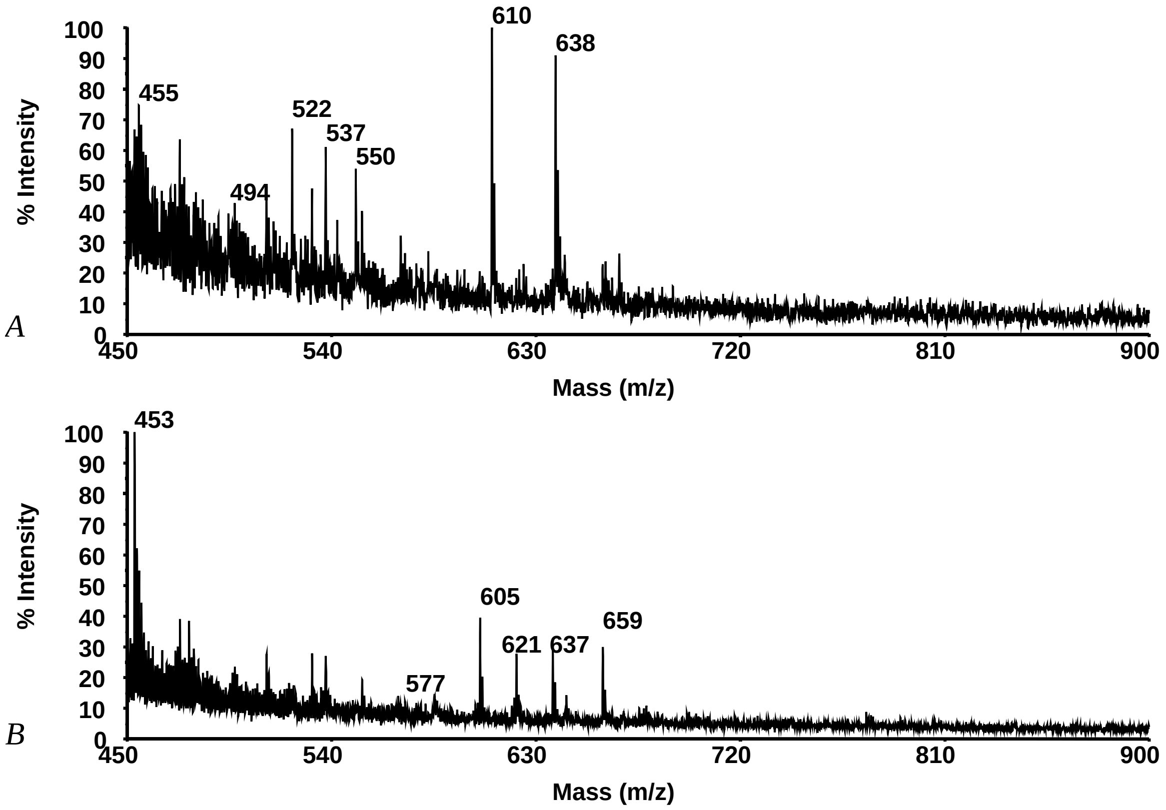

Figure 7.1. Representative MALDI-TOF spectra of (**A**) normal eye tear and (**B**) dry eye tear phosphorylated lipids. Important series include (1) C14:1-2:0 PAF (*m/z* 494), C16:1-2:0 PAF (*m/z* 522), and C18:1-2:0 PAF (*m/z* 550) in the normal tears, and (2) *m/z* 577, 605, 621, 637, and 659 in the dry eye tears. The second series consists of SMs, which may play a role in the dry eye response.

types of tears. The m/z 494, 522, and 550 species in the tear mass spectra did not have reliable post source decay (PSD) spectra for their specific identification. However, it is reasonable that they are phosphorylated and contain one nitrogen. For the m/z 494 species, possible assignments, based upon molecular weight alone, could be (1) a C14:1-2:0 PAF with molecular formula of $C_{24}H_{48}NO_7P$ or (2) a C16:1 Lyso-PC with a molecular formula of $C_{24}H_{48}NO_7P$. The m/z 522 and 550 species appear to be related to the m/z 494 species by the successive addition of two carbon atoms of chain length ($-CH_2CH_2-$). Figure 7.2 illustrates assigned structures of some of the main phosphorylated lipids observed in the tear extracts.

Next, as illustrated in Figure 7.3(a), we found a series of peaks which included m/z 577, 605, 621, 637, and 659. The five compounds exhibited affinities to the IMAC $\text{ZipTip}_{\text{MC}}$ resin, indicating they are phosphorylated lipids, and the odd numbered m/z values pointed to an even number of nitrogen atoms (e.g., 2) in each of the compounds. Additionally, the PSD spectra of the m/z 577, 605, and 621 species indicated an m/z 184 head group. These three findings support the hypothesis that the five compounds are related to sphingomyelin (SM). A similar series of m/z 605, 621, 637, 643 and 659 species has also been observed in a C18:1 sphingomyelin standard as impurity, Figure 7.3(b). From the sphingomyelin standard, PSD was also performed on the m/z 605 species, Figure 7.4. The spectral informative peaks include the phosphatidylcholine head group at m/z 184, a pyrophosphate phosphatidylcholine head group at m/z 280, neutral loss of the long chain substituent at m/z 335 $[M+H-C_{17}H_{34}O_2]^+$, and loss of the epoxide oxygen at m/z 589 $[M+H-O]^+$. From the derived molecular weights and PSD spectra, tentative assignments of these compounds, based upon sphingomyelin structures, can be made (Figure 7.5). The m/z 605, 621, and 637 species are proposed to be related structures where the

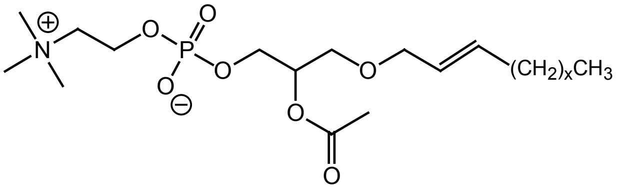

Platelet-activating factor
(x = 10, 12, 14)

for x = 10, 12 or 14, mol. wt. = 493, 521, or 549 Da

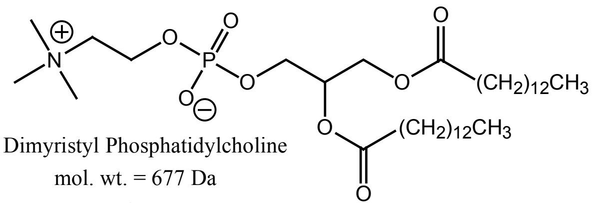

Dimyristyl Phosphatidylcholine
mol. wt. = 677 Da

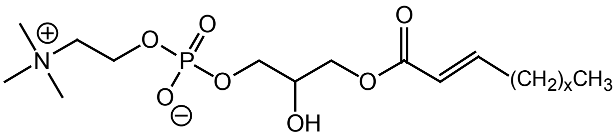

Lyso Phosphatidylcholine
(x = 12, 14, 16)

for x = 12, 14 or 18, mol. wt. = 493, 521, or 549 Da

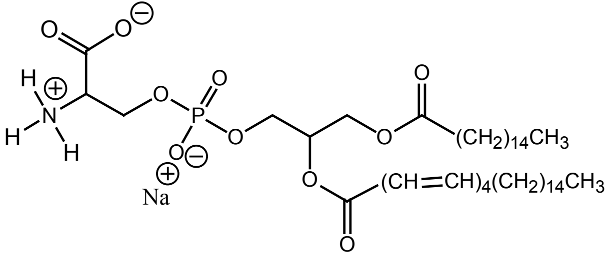

Phosphatidylserine
mol. wt. = 805 Da

Figure 7.2. Assigned structures of the major phosphorylated lipids observed in the tear extracts.

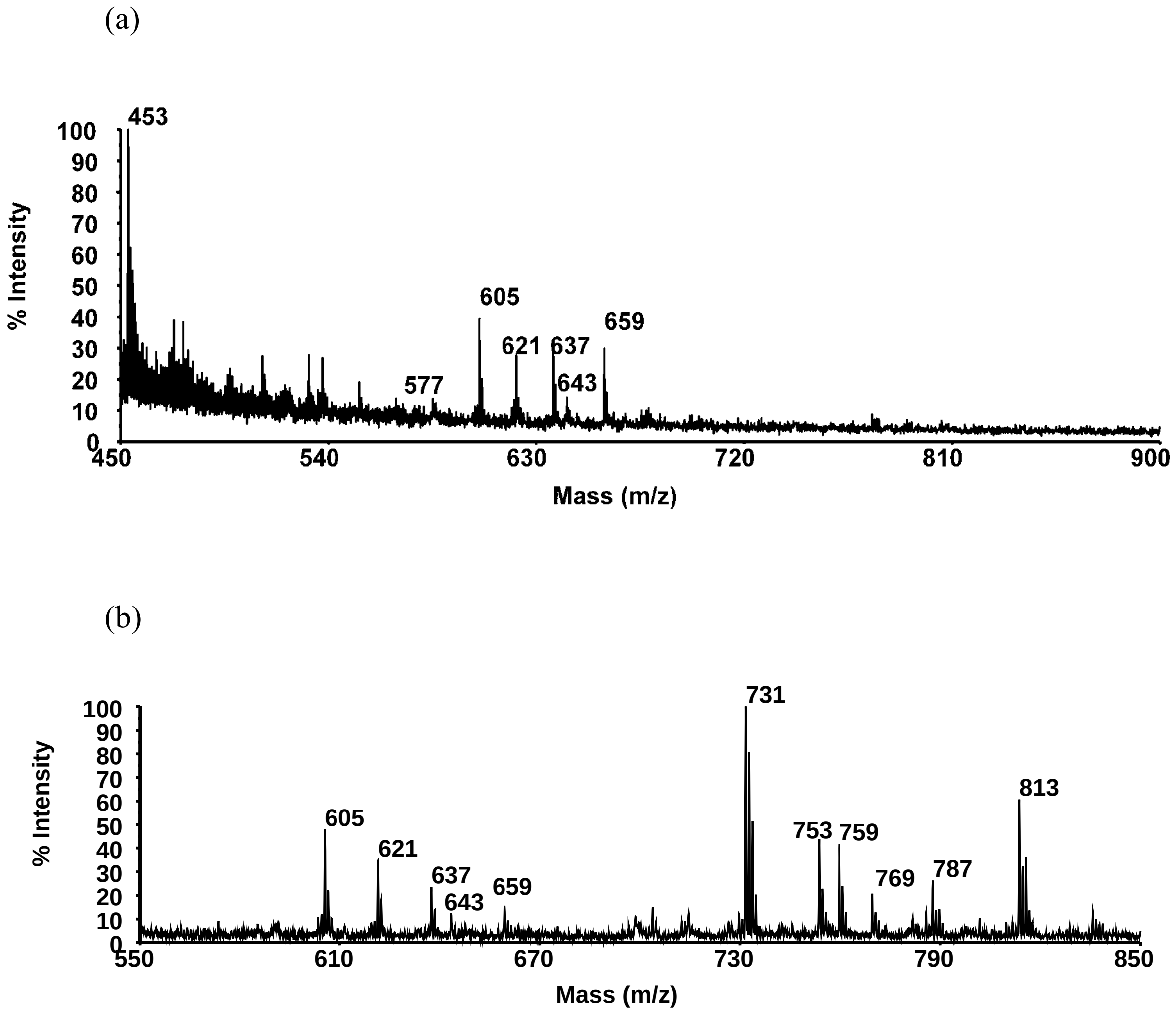

Figure 7.3. MALDI-TOF mass spectra of (a) dry eye tear extract lipids. (b) sphingomyelin standard.

m/z 605 is a protonated oxidized pyrophosphate sphingomyelin related compound with a molecular formula of $C_{24}H_{50}N_2O_{11}P_2$ likely resulting from epoxidation of the unsaturation on the long chain substituent. The m/z 621 species represents a further oxidized form of the same molecule resulting in peroxide formation with a molecular formula of $C_{24}H_{50}N_2O_{12}P_2$. The m/z 637 species is a further oxidized form of m/z 605 likely resulting from formation of an epoxide of the m/z 621 species, with a molecular formula of $C_{24}H_{50}N_2O_{13}P_2$. Finally, the m/z 659 species is the sodium adduct of the m/z 637 species with a molecular formula of $C_{24}H_{50}N_2O_{13}P_2Na$.

For the m/z 610 and 638 species found within the tear spectra, PSD spectra were obtained that indicate a relationship between the two (Figure 7.6). However, despite having a molecular weight equal to an oxidized form of phosphatidylcholine, the species are unassigned since no m/z 184 peak was evident. The m/z 642 species differs from the m/z 610 species by 32 Daltons, suggesting an oxidized state of m/z 610. The M/z 678 species has been identified as C14:0-14:0 PC based off of its molecular weight and the PSD spectrum which illustrates the m/z 184 product ion indicative of a phosphatidylcholine head group containing species (see Figure 7.7a). The PSD spectrum of the m/z 828 species indicates that it may be a phosphatidyl serine due to a diagnostic peak at m/z 741 (see Figure 7.7b). The m/z 695, 866, 886, and 936 species are currently unidentified.

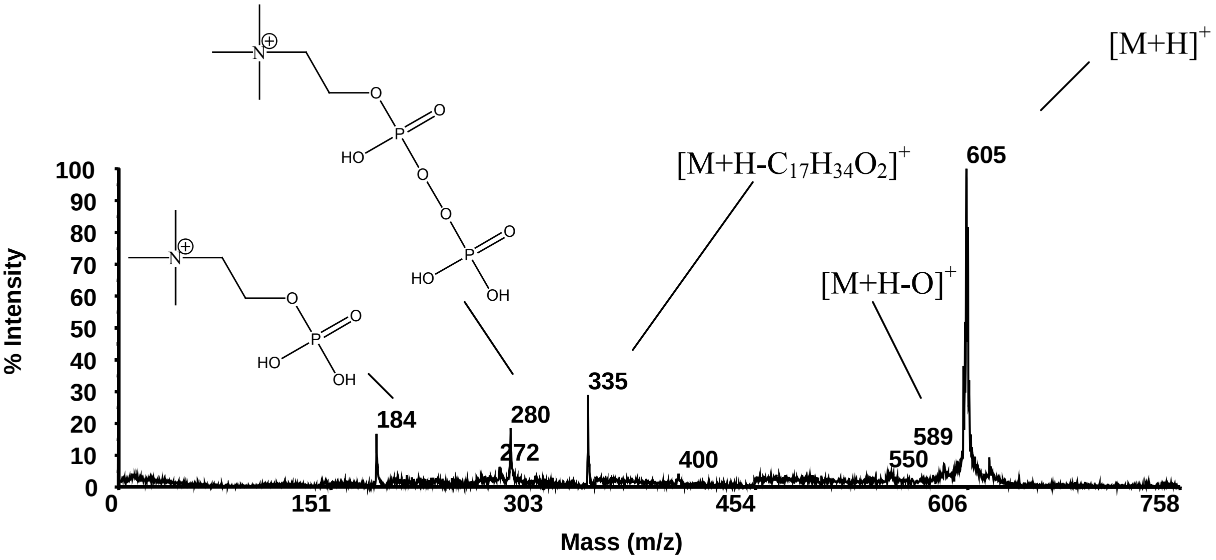

Figure 7.4. Post source decay (PSD) of m/z 605 species in the Sphingomyelin standard.

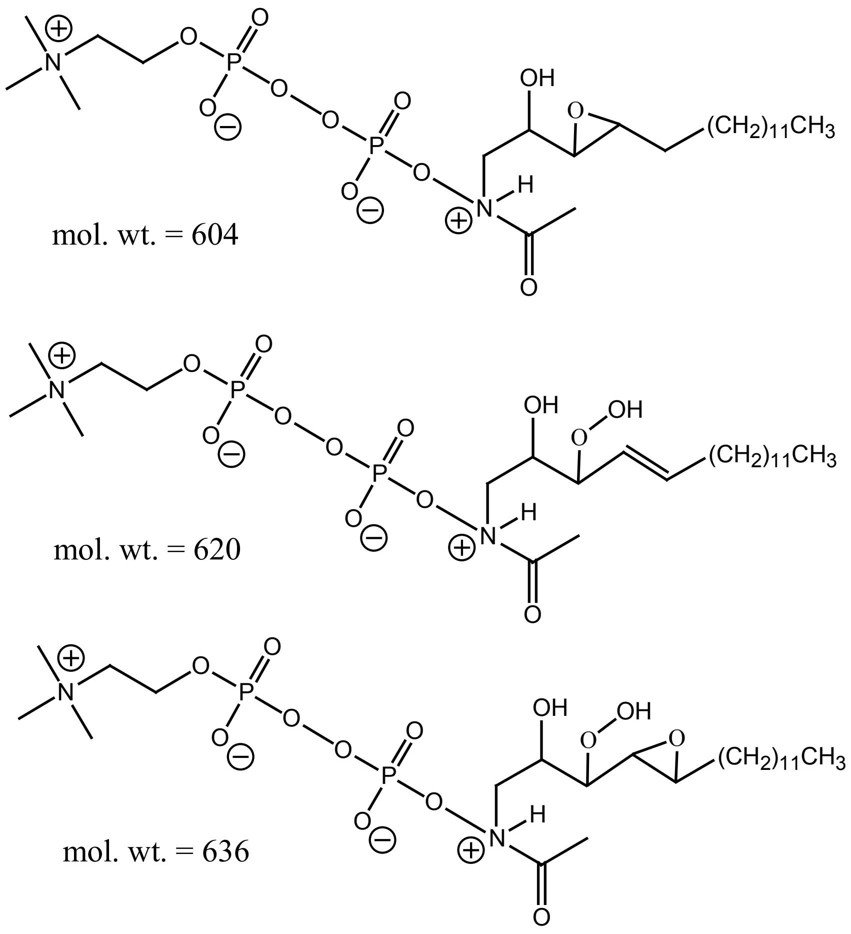

Figure 7.5. Proposed structures of pyrophosphate sphingomyelin.

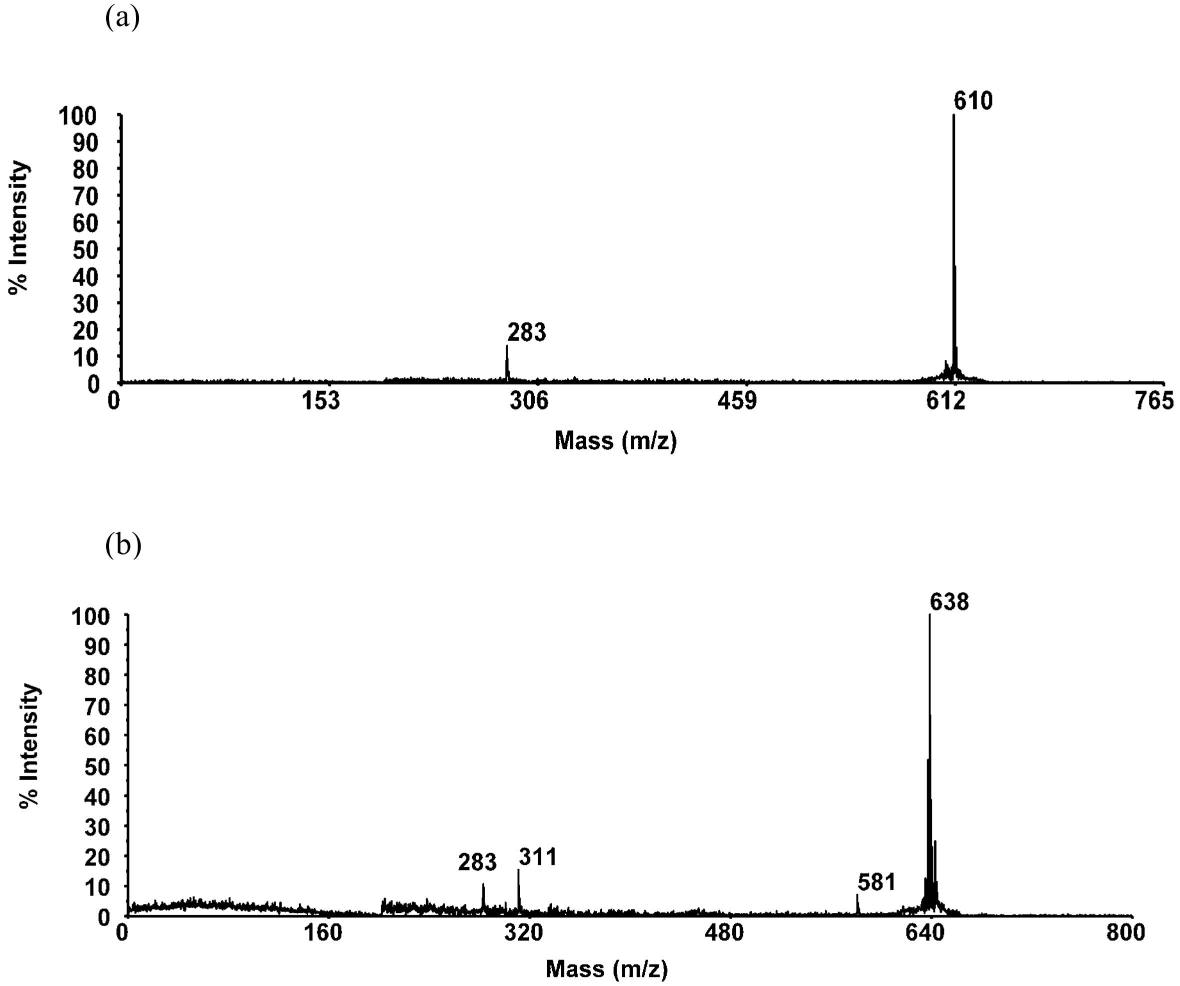

Figure 7.6. PSD spectrum of species found within the MALDI-TOF MS of tears. (a) PSD spectrum of m/z 610 species. (b) PSD spectrum of m/z 638 species.

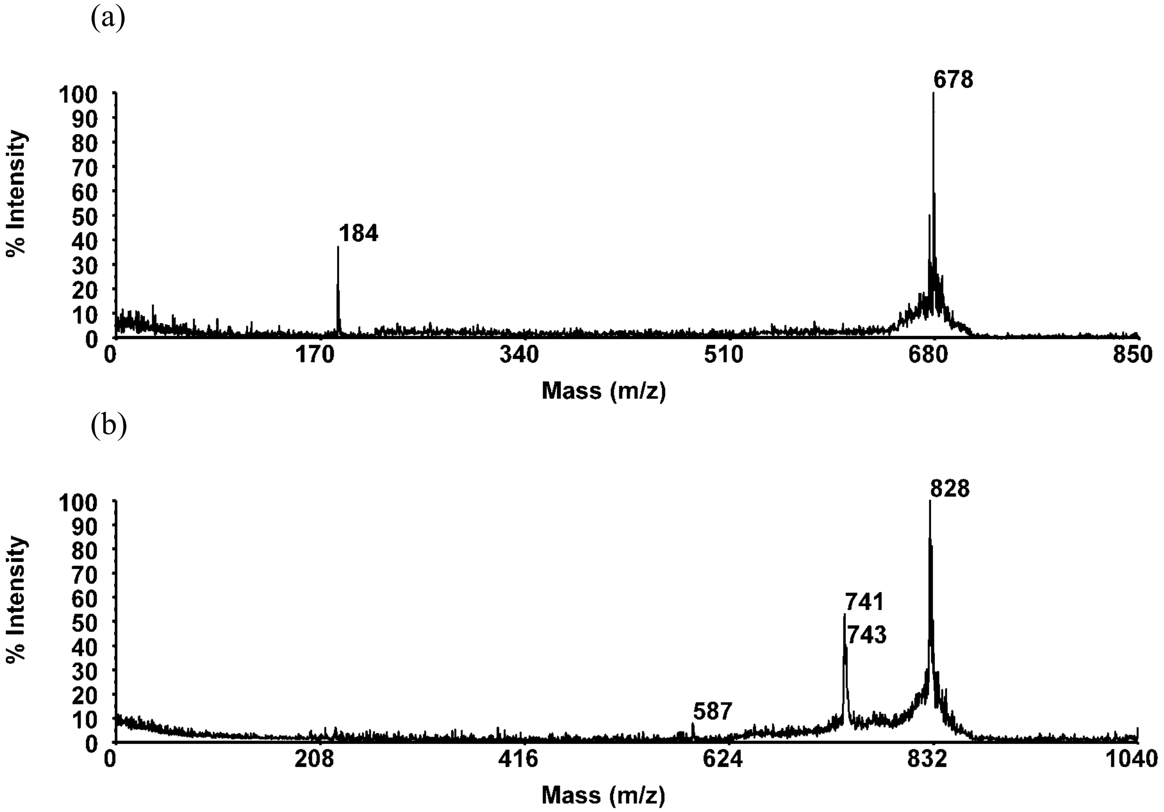

Figure 7.7. PSD spectrum of species found within the MALDI-TOF mass spectra of tears. (a) PSD spectrum of m/z 678 species. (b) PSD spectrum of m/z 828 species.

Table 7.1 lists the phosphorylated lipid species observed in the tear extracts and their relative abundances in normal versus dry eye tears. The major peak assignments corresponded to types of platelet activating factor (PAF) and pyrophosphate sphingomyelin (SM)-related compounds with minor peaks corresponding to phosphatidylcholine (PC) and phosphatidylserine (PS).-

Major differences in the normal and dry eye tear mass spectra were found in the peaks corresponding to SM and PS molecules. Two major SM peaks not found in the normal tears were present in the dry eye tears and two minor SM peaks found in the normal tears were major peaks in the dry eye tears. A minor peak~~s~~ corresponding to PS was identifiable in the dry eye tears but was not seen in the normal tears. Additionally, a minor peak in the normal eye tears possibly corresponding to an oxidized form the PC molecule was seen as a major peak in dry eye tears, and two of the minor, unidentifiable peaks in the normal eye tears were not present in the mass spectra of dry eye tears.

7.3.3 MALDI-TOF MS Analysis of Extracted Lacrimal Glands

Figure 7.8 is a representative MALDI-TOF MS spectrum of the extracted lipids from the main lacrimal glands of the rabbits. The predominant set of phosphorylated lipids, which is located in the region between *m/z* 700 and *m/z* 850, consists mainly of PCs, with some PEs. Table 7.2 lists the major peaks observed in the lacrimal gland extracts and their assignments. In addition to PC and PE molecules, peaks corresponding to PAF (*m/z* 496) and SM (*m/z* 577) were found. No peaks corresponding to PS were identified.

Lipid in Tear Extract	**Molecular Ion (MI)**	**Normal Eye***	**Dry Eye***
C14:1-2:0 PAF $C_{24}H_{48}NO_7P$ (?)	$[M+H]^+$, *m/z* 494	major	major
M/z 522	$[M+H]^+$	major	major
M/z 550	$[M+H]^+$	major	major
Pyrophosphate SM $C_{22}H_{46}N_2O_{11}P_2$	$[M+H]^+$, *m/z* 577	major	major
Pyrophosphate SM $C_{24}H_{50}N_2O_{11}P_2$	$[M+H]^+$, *m/z* 605		major
Pyrophosphate SM $C_{24}H_{50}N_2O_{12}P_2$	$[M+H]^+$, *m/z* 621		major
Pyrophosphate SM $C_{24}H_{50}N_2O_{13}P_2$	$[M+H]^+$, *m/z* 637	minor	major
Pyrophosphate SM $C_{24}H_{50}N_2O_{13}P_2Na$	$[M+Na]^+$, *m/z* 659	minor	major
M/z 610	$[M+H]^+$	major	major
M/z 638	$[M+H]^+$	major	
M/z 642	$[M+H]^+$	minor	major
C14:0-14:0 PC (DMPC)	$[M+H]^+$, *m/z* 678	minor	minor
M/z 695	$[M+H]^+$	minor	minor
16:0-20:4 PS $C_{42}H_{73}NO_{10}PNa$	$[M+2Na-H]^+$, *m/z* 828		minor
M/z 866	$[M+H]^+$	minor	
M/z 886	$[M+2Na-H]^+$		minor
M/z 936	$[M+H]^+$	minor	

*The assignment of a major or minor presence is qualitative and is derived from the relative intensity abundance of the peak in the mass spectra.

TABLE 7.1. Phospholipids Peaks in MALDI-TOF Mass Spectra of Normal and Dry Eye Rabbit Tears.

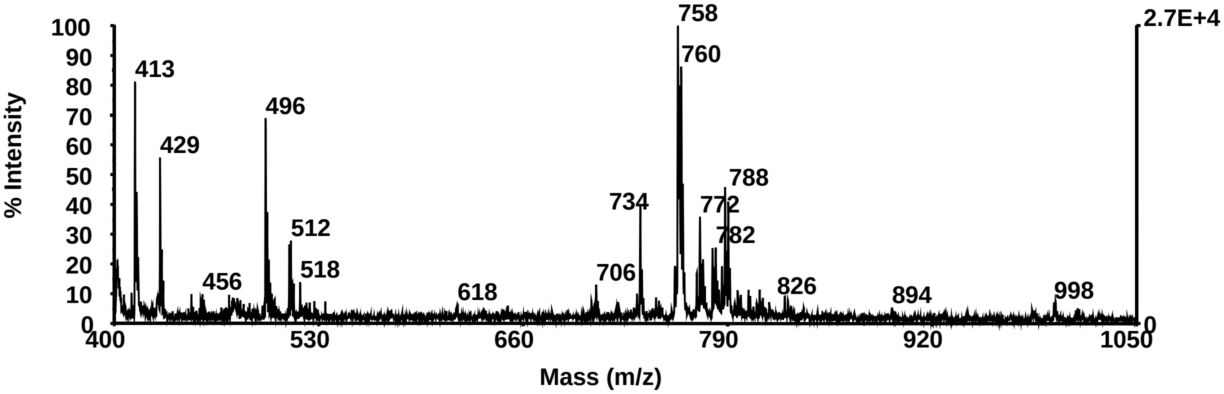

Figure 7.8. MALDI-TOF spectrum of lacrimal gland phosphorylated lipids.

Spectral Peak	**Compound Assignment**	**Spectral Peak**	**Compound Assignment**
M/z 413	2-N species with PC head-group, possibly SM related	*M/z* 756	16:0-18:3 PC or 16:1-18:2 PC
M/z 429	2-N species (*m/z* 413 oxidized) PC head-group, SM related	*M/z* 758	16:0-18:2 PC
M/z 496	C14:0-2:0 PAF	*M/z* 760	16:0-18:1 PC
M/z 511	Unidentified	*M/z* 762	16:0-18:0 PC
M/z 512	1-N species with PC head-group	*M/z* 770	18:0-20:3 PE
M/z 518	1-N species with PC head-group	*M/z* 772	18:0-20:2 PE
M/z 577		*M/z* 774	18:0-20:1 PE
M/z 610	16:0-5:1 oxidized PC $C_{29}H_{56}NO_{10}P$	*M/z* 780	16:1-20:4 PC
M/z 642	16:0-5:1 oxidized PC $C_{29}H_{56}NO_{12}P$	*M/z* 782	16:0-20:4 PC
M/z 706	14:0-16:0 PC	*M/z* 786	18:0-18:2 PC
M/z 720	16:0-18:0 PE	*M/z* 788	18:0-18:1 PC
M/z 734	14:0-18:0 PC		
M/z 744	18:0-18:2 PE	*M/z* 810	18:0-20:4 PC
M/z 746	18:0-18:1 PE		

TABLE 7.2. Assignment of MALDI-TOF Mass Spectra Peaks from Rabbit Main Lacrimal Gland

Current tear film models suggest that a chemically stable, lamellar layer of polar phospholipids lies anterior to the aqueous fluid and binds the non-polar meibomian oil to the aqueous layer. The presence of this polar phospholipid interface is thought to be critical to the spreading of the non-polar lipid film over the aqueous layer. Shine and McCulley[16] found that specific changes in the content of the polar phospholipid interface correlate directly to the presence of dry eye in patients with chronic blepharitis.

The majority of the phospholipids are supplied to the tear film through the meibomian glands, which are located in the eyelid. The chemical composition of the human meibomian gland secretions is a complex mixture of cholesterol and wax esters, triacylglycerols, free fatty acids, diesters, free cholesterol, hydrocarbons, and polar lipids.[20,46-49] The polar lipids found in the meibomian gland secretion contain 70% phospholipids and 30% sphingolipids, and the phospholipid portion consists of 38% PC, 18% PE, 7% SM, and 39% unknowns.[20] Polar lipids make up approximately 6-16% of the compounds found in the liquid phase of the tear film.[20,22,49] Based on these data, the percentages of phosphorylated lipids in the lipid phase of the tear film would be 1.6-4% PC, 0.8-2% PE, and < 1% SM. Analysis of the rabbit meibomian gland cells and secretions has shown the polar lipid content to be similar to that of humans, with PC, PE, SM, and PS making up the majority of the phospholipids.[23,50]

Although the meibomian gland supplies the majority of the lipids to the tear film, the lacrimal gland also provides some lipids, as well as the majority of tear proteins. An early study performed by Stuchell et al. (Stuchell RN, et al. IOVS 1984;25:ARVO Abstract, p. 320, #2) reported that the lipid composition of lacrimal gland secretions consisted of 55.0% glycolipids, 44.1% other neutral lipids, and 0.9% phospholipids. However, the types of phospholipids were not reported. In our study, we found that rabbit lacrimal glands had significant amounts of the same polar phospholipids found in the human tear fluid, although the degree to which these phospholipids are excreted into the tears is unknown.

In addition to the meibomian and main and accessory lacrimal glands, the rabbit has a harderian gland that has been shown to contribute to the tear film components. The harderian gland lies in the nasal region of the orbit with its secretions flowing through ducts within the nictitating membrane. Analysis of the harderian gland has shown that tear proteins and lipids are produced within the gland, although the degree to which these molecules are actively secreted is unknown.[21,51,52] In our dry eye model, both the main and accessory lacrimal glands were removed and the ducts from the harderian gland were severed and cauterized. Only the meibomian glands remained intact to supply lipids to the tear film.

The total chloroform extract of the tear layer constitutes a complex mixture of biological compounds that includes non-polar and polar lipids and some lipoproteins. The polar lipid components make up a very small fraction of the total extract, rendering their analyses difficult by mass spectrometry alone. Combining the use of the IMAC ZipTip$_{MC}$ with the optimized solid ionic crystal MALDI matrix para-nitroaniline/butyric acid allowed the identification and comparison of the lipoprotein and phosphorylated lipid components of normal versus dry eye rabbit tears.

Some similarities in the polar phospholipids were found in the normal and dry eye rabbit tears. For example, three compositions of PAF, a tear lipoprotein component known to be involved in the human lipid-mediated inflammatory response and such specific ocular conditions as allergic conjunctivitis[53] and contact lens induced acute red eye (CLARE),[54] were expressed to a similar degree in both the normal and dry eye rabbit tears. The three types of PAF lipids differed from one another in terms of two carbon atoms of chain length ($–CH_2CH_2–$). The similar degree of expression of the three PAFs indicates that the inflammatory response was not activated in our dry eye model.

Additionally, however, some significant differences in the polar phospholipids were found in the normal and dry eye rabbit tears using our novel analytical method. The types and concentrations of SM molecules were significantly increased in the dry eye tears compared with the normal tears. The normal rabbit tears showed the presence of three types of SM, with one major type present in significantly higher concentrations than the other two. The dry eye tears showed the same three SMs as the normal tears and two additional SMs, all in significantly high concentrations. Sphingomyelins are zwitterionic phospholipids which have been suggested to play a significant role in maintaining the interfacial layer between the aqueous and oil layers of the tear film. The polar head groups of zwitterionic and neutral phospholipids are known to align themselves head-to-tail, creating an interfacial layer between meibomian oil non-polar lipids and aqueous tears that is chemically stable and resistant to mechanical rupture.[11,50] A decrease in the percentage of SMs in the tear film was correlated with the presence of dry eye in patients with chronic blepharitis, although the different SM species within the tear film were not identified.[16] The presence of different SM species in the dry eye tears may indicate a compensation mechanism provided by the meibomian glands to stabilize the tear film in the absence of lacrimal and harderian gland secretions.

Previous work has shown that PE is present in human tears and may play a significant role as a zwitterionic phospholipid in the maintenance of tear stability.[16] PE was not found in either the normal or dry eye rabbit tears examined. However, PS, a precursor in PE synthesis in mammalian cells, was found in significant quantities in the dry eye tears. PS is an anionic phospholipid and, as such, aids in the spreading of the meibomian oil film within the lipid interfacial layer through the mutual repulsion of negative charges.

Our analytical method not only allowed the assignment of the types of polar phospholipids present in the tear film, but also allowed assignment of specific molecular compositions within the phospholipid groups. Comparative analysis of polar phospholipids in rabbit tears from normal and dry eyes points to the importance of SM and PS in stabilizing the tear film in the rabbit dry eye model.

7.4 Conclusions

The combination of ZipTip$_{MC}$ chromatography and the solid ionic crystal matrix for MALDI enabled the detection and assignment of phosphorylated lipids in the tears. Specific differences between polar phospholipid levels in normal and dry eye tears were observable with this methodology. The appearance of various SM and PS species only in the dry eye tears may provide markers for this disease state in the future.

7.5 References

1. Lemp MA. Report of the National Eye Institute/Industry workshop on clinical trials in dry eyes. *CLAO J.* 1995;21:221–232.
2. Schein OD, Tielsch JM, Munoz B, Bandeen-Roche K, West S. Relation between signs and symptoms of dry eye in the elderly. A population-based perspective. *Ophthalmology.* 1997;104:1395–1401.
3. Schaumberg DA, Buring JE, Sullivan DA, Dana MR. Hormone replacement therapy and dry eye syndrome. *JAMA.* 2001; 286:2114–2119.
4. Schaumberg DA, Sullivan DA, Buring JE, Dana MR. Prevalence of dry eye syndrome among US women. *Am J Ophthalmol.* 2003;136:318–326.
5. Lee JB, Ryu CH, Kim J-H, Kim EK, Kim HB. Comparison of tear secretion and tear film instability after photorefractive keratectomy and laser in situ keratomileusis. *J Cataract Refract Surg*. 2000;26:1326–1331.
6. De Paiva CS, Pflugfelder SC. Corneal epitheliopathy of dry eye induces hyperesthesia to mechanical air jet stimulation. *Am J Ophthalmol.* 2004;137:109–115.
7. Dursun D, Wang M, Monroy D, Li D-Q, Lokeshwar BL, Stern ME, et al. A mouse model of keratoconjunctivitis sicca. *Invest Ophthalmol Vis Sci.* 2002;43:632–638.
8. Ousler GW 3rd, Abelson MB, Nally LA, Welch D, Casavant JS. Evaluation of the time to “natural compensation" in normal and dry eye subject populations during exposure to a controlled adverse environment. *Adv Exp Med Biol.* 2002;506(Pt B):1057–1063.
9. Moore JC, Tiffany JM. Human ocular mucus. Chemical studies. *Exp Eye Res*. 1981;33:203–212.
10. Carrington SD, Hicks SJ, Corfield AP, Kaswan RL, Packer N, Bolis S, et al. Structural analysis of secreted ocular mucins in canine dry eyes. *Adv Exp Med Biol.* 1998;438:253–263.
11. McCulley JP, Shine WE. The lipid layer: the outer surface of the ocular surface tear film. *Biosci Rep*. 2001;21:407–418.
12. Hodges RR, Dartt DA. Regulatory pathways in lacrimal gland epithelium. *Int Rev Cytol.* 2003;231:129–196.
13. Mathers W. Evaporation from the ocular surface. *Exp Eye Res*. 2004;78:389–394.
14. Bron AJ, Tiffany JM, Gouveia SM, Yokoi N, Voon LW. Functional aspects of the tear film lipid layer. *Exp Eye Res*. 2004;78:347–360.
15. Mathers WD. Ocular evaporation in meibomian gland dysfunction and dry eye. *Ophthalmology.* 1993;100:347–351.
16. Shine WE, McCulley JP. Keratoconjunctivitis sicca associated with meibomian secretion polar lipid abnormality. *Arch Ophthalmol.* 1998;116:849–852.
17. Hemsley S, Cole N, Canfield P, Willcox MDP. Protein microanalysis of animal tears. *Res Vet Sci.* 2000;68:207–209.
18. Herber S, Grus F, Sabuncuo P, Augustin AJ. Two-dimensional analysis of tear protein patterns of diabetic patients. *Electrophoresis.* 2001;22:1838–1844.
19. Dartt DA, Matkin C, Gray K. Comparison of proteins in lacrimal gland fluid secreted in response to different stimuli. *Invest Ophthalmol Vis Sci.* 1988;29:991–995.
20. McCulley JP, Shine W. A compositional based model for the tear film lipid layer. *Trans Am Ophthalmol Soc.* 1997;95:79–88.
21. Millar TJ, Pearson M. The effects of dietary and pharmacological manipulation on lipid production in the meibomian and harderian glands of the rabbit. *Adv Exp Med Biol.* 2002;506(Pt A):431–440.

22. Ohyama T, Matsubara C, Takamura K. Sensitive densitometry for the determination of platelet-activating factor and other phospholipids in human tears. *Analyst* 1996;21:1943–1947.
23. Greiner JV, Glonek T, Korb DR, Booth R, Leahy CD. Phospholipids in meibomian gland secretion. *Ophthalmic Res.* 1996;28:44–49.
24. Wollensak G, Mur E, Mayr A, Baier G, Gottinger W, Stoffler G. Effective methods for the investigation of human tear film proteins and lipids. *Graefe's Arch Clin Exp Ophthalmol.* 1990;228:78–82.
25. Sullivan BD, Evans JE, Krenzer KL, Reza Dana M, Sullivan DA. Impact of antiandrogen treatment on the fatty acid profile of neutral lipids in human meibomian gland secretions. *J Clin Endocrinol Metab.* 2000;85:4866–4873.
26. Szucs R, Verleysen K, Duchateau GSMJE, Sandra P, Vandeginste BGM. Analysis of phospholipids in lecithins comparison between micellar electrokinetic chromatography and high-performance liquid chromatography. *J Chromatogr A.* 1996;738:25–29.
27. Verleysen K, Sandra P. Analysis of phospholipids in lecithins. Separation according to hydrophobicity by lowering the temperature. *J High Resolution Chromatogr.* 1997;20:337–339.
28. Raith K, Wolf R, Wagner J, Neubert RHH. Separation of phospholipids by nonaqueous capillary electrophoresis with electrospray ionisation mass spectrometry. *J Chromatogr A.* 1998;802:185–188.
29. Han X, Gross RW. Structural determination of lysophospholipid regioisomers by electrospray ionization tandem mass spectrometry. *J Am Chem Soc.* 1996;118:451–457.
30. Hoischen C, Ihn W, Gura K, Gumpert J. Structural characterization of molecular phospholipid species in cytoplasmic membranes of the cell wall-less *Streptomyces hygroscopicus* L form by use of electrospray ionization coupled with collision-induced dissociation mass spectrometry. *J Bacteriol.* 1997;179:3437–3442.
31. Hsu FF, Bohrer A, Turk J. Formation of lithiated adducts of glycerophosphocholine lipids facilitates their identification by electrospray ionization tandem mass spectrometry. *J Am Soc Mass Spectrom.* 1998;9:516–526.
32. Khaselev N, Murphy RC. Electrospray ionization mass spectrometry of lysoglycerophosphocholine lipid subclasses. *J Am Soc Mass Spectrom.* 2000;11:283–291.
33. Hsu FF, Turk J. Characterization of phosphatidylethanolamine as a lithiated adduct by triple quadrupole tandem mass spectrometry with electrospray ionization. *J Mass Spectrom.* 2000;35:596–606.
34. Liebisch G, Drobnik W, Lieser B, Schmitz G. High-throughput quantitation of lysophosphatidylcholine by electrospray ionization tandem mass spectrometry. *Clin Chem.* 2002;48:2217–2224.
35. Ho YP, Huang PC, Deng KH. Metal ion complexes in the structural analysis of phospholipids by electrospray ionization tandem mass spectrometry. *Rapid Commun Mass Spectrom.* 2003;17:114–121.
36. Hsu FF, Turk J, Shi Y, Groisman EA. Characterization of acylphosphatidylglycerols from *Salmonella typhimurium* by tandem mass spectrometry with electrospray ionization. *J Am Soc Mass Spectrom.* 2004;15:1–11.
37. Marto JA, White FM, Seldomridge S, Marshall AG. Structural characterization of phospholipids by matrix-assisted laser desorption/ionization Fourier transform ion cyclotron resonance mass spectrometry. *Anal Chem.* 1995;67:3979–3984.
38. Schiller J, Arnhold J, Benard S, Muller M, Reichl S, Arnold K. Lipid analysis by matrix-assisted laser desorption and ionization mass spectrometry. A methodological approach. *Anal Biochem.*

1999;267:46–56.

39. Ishida Y, Nakanishi O, Hirao S, Tsuge S, Urabe J, Sekino T, et al. Direct analysis of lipids in single zooplankter individuals by matrix-assisted laser desorption/ionization mass spectrometry. *Anal Chem.* 2003;75:4514–4518.
40. Al-Saad KA, Zabrouskov V, Siems WF, Knowles NR, Hannan RM, Hill HH Jr. Matrix-assisted laser desorption/ionization time-of-flight mass spectrometry of lipids: ionization and prompt fragmentation patterns. *Rapid Commun Mass Spectrom.* 2003;17:87–96.
41. Rujoi M, Estrada R, Yappert MC. In situ MALDI-TOF MS regional analysis of neutral phospholipids in lens tissue. *Anal Chem.* 2004;76:1657–1663.
42. Woods AS, Ugarov M, Egan T, Koomen J, Gillig KJ, Fuhrer K, Gonin M, Schultz JA. Lipid/peptide/nucleotide separation with MALDI-ion mobility-TOF MS. *Anal Chem.* 2004;76:2187–2195.
43. Murphy RC, Fiedler J, Hevko J. Analysis of nonvolatile lipids by mass spectrometry. *Chem Rev.* 2001;101:479–526.
44. Folch J, Lees M, Sloane Stanley GH. A simple method for the isolation and purification of total lipids from animal tissues. *J Biol Chem.* 1957;226:497–509.
45. Bligh EG, Dyer WJ. A rapid method of total lipid extraction and purification. *Can J Biochem Physiol.* 1959;37:911–917.
46. Nicolaides N, Santos EC. The di- and triesters of the lipids of steer and human meibomian glands. *Lipids.* 1985;20:454–467.
47. Miyazaki M, Man WC, Ntambi JM. Targeted disruption of stearoyl-CoA desaturase1 gene in mice causes atrophy of sebaceous and meibomian glands and depletion of wax esters in the eyelid. *J Nutr.* 2001;131:2260–2268.
48. Mathers WD, Lane JA. Meibomian gland lipids, evaporation, and tear film stability. *Adv Exp Med Biol.* 1998;438:349–360.
49. Nicolaides N, Kaitaranta JK, Rawdah TN, Macy JI, Boswell FM 3rd, Smith RE. Meibomian gland studies: comparison of steer and human lipids. *Invest Ophthalmol Vis Sci.* 1981;20:522–536.
50. Greiner JV, Glonek T, Korb DR, Leahy CD. Meibomian gland phospholipids. *Curr Eye Res.* 1996;15:371–375.
51. Dartt D, Knox I, Palau A, Bothelho SY. Proteins in fluids from individual orbital glands and in tears. *Invest Ophthalmol Vis Sci.* 1980;19:1342–1347.
52. Seyama Y, Kasama T, Yasugi E, Park SH, Kano K. Lipids in harderian glands and their significance. In: Webb SM, Hoffman RA, Puig-Domingo ML, Reier RJ, eds. *Harderian Glands: Porphyrin, Metabolism, Behavioral and Endocrine Effects.* Berlin, Springer-Verlag, 1992:195–217.
53. Kato M, Mano H, Ota A, Konomi K, Nakata K. Platelet activating factor degradation in tear fluid from guinea pigs with allergic conjunctivitis. *J Ocul Pharmacol Ther.* 2001;17:83–91.
54. Thakur A, Willcox MDP. Cytokine and lipid inflammatory mediator profile of human tears during contact lens associated inflammatory diseases. *Exp Eye Res.* 1998;67:9–19.

CHAPTER VIII :IDENTIFICATION AND COMPARISON OF RABBIT TEAR PROTEINS OF NORMAL VERSUS A DRY EYE MODEL BY MALDI-TOF MS

8.1 Introduction

The eye is a complex, sensitive component of the human body that has obvious importance, thus extensive study has been conducted on the eye, and particularly the protein components that make up the eye(1-13), for well over at least seventy years for modern testing, and since antiquity for other. The eye structure is divided into three layers, the innermost corneal layer, an intermediate aqueous-mucin(14,15) layer, and an outer most lipid layer(16). One of the functions of the outer lipid layer is to retard the evaporation of the inner aqueous layer through the functionality of the non-polar and polar lipids. The lipids are supplied to the tear film through the meibomian gland. The proteins are supplied to the aqueous portion of the tear layer by the main (orbital) lacrimal gland(17). Exhaustive studies have been performed on human and rabbit tear, and less extensive for dog tear(18) and rat tear(19), for protein quantification and identification, and also for protein expression studies concerning physiological changes that have resulted in the symptoms of dry eye. These types of studies have been accomplished through many standard techniques including 1-D(20) and 2-D(21) gel electrophoresis, capillary electrophoresis(22), HPLC(23,24), immunochemistry(25-27), chip-based micro-fluidic techniques(28), and thin layer chromatography(29). Today's proteomic approaches to protein characterization and identification, through the use of mass spectrometric techniques, have contributed to the information in the study of tear proteins. Some of the mass spectrometric methods used have been gas chromatography-mass spectrometry(29), high-pressure liquid chromatography/electrospray ionization mass spectrometry(30), and matrix assisted laser desorption ionization-time of flight mass spectrometry(31,32). Capillary electrophoresis/electrospray ionization-mass spectrometry has also been applied to the analysis of proteins in whole human blood(33).

Protein profiles, identification, and quantitation have been reported on both normal tear protein content, and protein content for dry eye syndrome, for both human and rabbit. Reported total protein concentrations for rabbit include 12.6 μg/μl in unstimulated tears(34), and 40.0 ± 5.3 μg/μl in lacrimal gland fluid at flow rates < 2 μl/min(35). For normal human tear, a few examples of total reported protein concentrations include 8.1 μg/μl in stimulated tears and 22.7 μg/μl in unstimulated tears(36), 8 ± 2.25 g/l from gentle stimulation(11), and from 6.05 ± 1.58 mg/ml to 11.48 ± 2.32 mg/ml (difference depending on which method was used for calculation, as expressed by the authors) for tears collected by yawn reflex(37). Human tear contains numerous proteins including serum-based proteins such as IgA and IgG, antibacteriolytic components such as lysozyme, transferrin, albumin, lipocalin, and many more. Indeed, Fung, et al(32), recently reported the identification of approximately 500 proteins in normal human basal tear fluid. Rabbit tear contains many of the same types of proteins as are contained in human tear. Boonstra, et al(26), reported the identification of transferrin in rabbit tear, but no lactoferrin, thus indicating that rabbit tear may be substantially different from human tear. Recently, Zhou et al(30), reported the finding of lactoferrin in rabbit tear, demonstrating the differences that may arise from techniques and methods used. Nonetheless, there are many similarities in the types of protein contained in both.

In the past 25 years, many advances in diagnosis, causes, and treatments of the dry eye condition have been made(38). Many are afflicted with the condition *Keratoconjunctivitis sicca* (KCS, also known as “dry eye”), which can be associated with aging, disease, smoke, surgery, or any form of irritation of the eye. The National Eye Institute’s (NEI) definition of dry eye states that KCS is a disorder of the ocular tear film layer usually caused by a tear deficiency, or excessive evaporation of the aqueous layer, resulting in damage of the ocular surface and symptoms of discomfort(39). Some forms of dry eye may be physiologically related, perhaps from the breakdown of the eye tear layer, or to hormones, as demonstrated in a hormone replacement study by Schaumberg, et.al.(40), or to Sjogren syndrom(41). In human dry eye studies, the analytical evaluation of the dry eye condition is performed through the collection of tear samples from individuals who are afflicted with one of the underlying causes of dry eye, and then performing various wet chemistry and instrumental methods for compositions, tear breakup, etc. Studies are also performed on rabbits where the rabbit has been externally given the dry eye condition, and samples are taken and analyzed. The rabbit dry model has been produced through sensory denervation of the lacrimal gland(17,42), and through corneal wounding(43). In this study, the rabbit dry eye model was produced through the removal first of the main lacrimal gland from one of the rabbit's eyes, while the other eye is kept normal as a control. Then, after approximately two weeks, the accessory lacrimal gland and nictitating membrane are removed from the same eye without the lacrimal gland. Tear samples were subsequently taken and analyzed for protein content.

8.2 EXPERIMENTAL

8.2.1 Rabbit tear samples

Baseline tears (representing tears produced under non-irritating conditions used in normal protection and lubrication functions) were collected from normal and surgically induced dry eyes of New Zealand white rabbits using 5 μL silanated microcapillary pipettes(24,37). A usual volume obtained from normal eye is 5 μL, whereas only 2 μL are typically obtained from a dry eye subject. Tear samples were immediately placed into Eppendorf tubes, and preserved by storage at –70 ^{o}C. The rabbit dry eye tear model is created through two surgical procedures. First, the main lacrimal gland is removed from one of the rabbit's eyes, while the other eye is kept normal as a control, and the rabbit is then allowed to heal. After approximately two weeks, the accessory lacrimal gland and nictitating membrane are removed from the same eye without the lacrimal gland. The tear breakup time (TBUT, measured by slit lamp and Tearscope) of the eye is then measured and followed. The TBUT of the surgical eye must be at least half of the control eye to be considered as "dry". The polar and non-polar lipid fractions were extracted from tear samples with a simple chloroform solvent modification procedure(44,45), and the proteins were recovered from the aqueous phase of the extraction.

8.2.2 In-gel reduction, alkylation, digestion, and extraction of peptides

The protein bands that were analyzed by MALDI-TOF mass spectrometry were in-gel digested using an in-lab procedure. The bands of interest are excised from the gel with a scalpel. The bands are chopped into cubes (1 x 1 mm), and placed into separate 1.5 mL Eppendorf tubes. The chopped bands are then washed with 100 – 150 μL of DD water, three times, with five min. soakings. Between each wash, the cubes are centrifuged, and the washing removed. The gels are then dehydrated by the addition of 100 μL of acetonitrile. After approximately 15 minutes, the gels become white and stick together indicating dehydration. The acetonitrile is removed, and the gels are dried in an eppendorf Vacufuge Concentrator 5301 (Brinkman Instruments, Inc.). Reduction is then performed by swelling the gels in 50 μL of a freshly prepared solution containing 10 mM of DTT in a 100 mM NH_4HCO_3 buffer solution. The gels are then incubated for 60 minutes at 56 ^{o}C. After incubation, the gels are centrifuged and the liquid is removed. The gels are again dehydrated in 100 μL of acetonitrile. The acetonitrile is removed and alkylation is performed by the addition of 50 μL of freshly prepared 55 mM iodoacetamide in 100 mM NH_4HCO_3 buffer. The gels are allowed to react, in the dark, for 45 minutes at room temperature. The gels are then centrifuged, and the liquid is removed. The gels are then washed with 100 μL of 100 mM NH_4HCO_3. 100 μL of acetonitrile is added, and the solution is vortexed for 20 minutes. The gels are then centrifuged, the liquid is removed, and dried in the Vacufuge Concentrator. The gels are rehydrated with 10-20 μL of a freshly prepared solution of 50 mM NH_4HCO_3, 5 mM $CaCL_2$, and 12 ng/μL trypsin. The gels are digested for 40 min. at 4 ^oC, then overnight at 37 ^oC. The digestion solution is collected, and the gels are incubated for 15 min. in 30 μL 20 mM NH_4HCO_3 at 37 ^oC, the supernatent is collected, then gels are incubated 3 times for 15 min. in 30 μL of a 60% acetonitrile, 5% formic acid solution. The supernatents are pooled and the volume is reduced to 3 – 10 μL in the Vacufuge Concentrator. For MALDI-TOF mass spectrometry analysis, the peptides are desalted using $ZipTip_{C18}$ (Millipore, Bredford, MA). A basic manufacturer method is followed where 1 μL of 0.1% TFA is added to the sample. The ZipTip is wetted with 2 x 10 μL of 50% acetonitrile, and equilabrated with 3 x 10 μL of 0.1% TFA. The sample is loaded and dispensed for 10 cycles, washed with 3 x 10 μL of 0.1% TFA, and then eluted with 1 to 4 μL of 50% acetonitrile, 0.1% TFA, into a 0.5 mL eppendorf tube by drawing and expelling the elution solution 10 times.

8.2.3 MALDI-TOF MS and MALDI-PSD-TOF MS

MALDI-TOF mass spectra and MALDI-PSD-TOF mass spectra were collected using a Applied Biosystems Voyager Elite BioSpectrometry Research Station with Delayed Extraction Technology, version 5.1 series software (Applied Biosystems, Inc., Framingham, MA). A 337 nm nitrogen laser is used. For peptide analysis, α-cyano-4-hydroxycinnamic acid (α-CHCA) as a saturated solution in 50:50 H_2O:ACN with 0.1% TFA was used by a dry dropplet spotting method. For protein analysis, 3,5-dimethoxy-4-hydroxycinnamic acid (sinapinic acid) as a saturated solution in 30:70 ACN:H_2O with 0.1% TFA was used.

8.3 RESULTS AND DISCUSSION

8.3.1 1D gel electrophoresis

The extracted proteins from the normal-control eye rabbit tear, and the dry eye model rabbit tear, were separated for approximate molecular weight determination using a Mini-PROTEAN Electrophoresis module assembly obtained from Bio-Rad Laboratories, Inc. (Hercules, CA). Figure 8.1 shows the results of the electrophoresis for the low molecular weight standard, the normal-control eye rabbit tear, and the dry eye model rabbit tear, where well over 40 distinct bands are observed. The separation was performed by following the manufacturer's guidelines. Basically, this entails using a 1 mm thick gel with a 12% acrylamide composition. 5 μL of a LMW std and dye mixture was loaded onto the gel along with 10 μL of sample and dye mixtures at dilutions where the second sample well contained one half the concentration of the initial sample loading for comparative purposes (as discussed and illustrated in Figure 8.1). The separation is performed at a constant voltage of 200V. After the electrophoresis separation is complete, the gel is fixed in a solution of 50% methanol (v/v) and 5% acetic acid (v/v). The gel is then rinsed and stained in a solution of 50% methanol (v/v) 5% acetic acid (v/v) and 0.1% blue R250 (w/v). After staining, the gel is rinsed and de-stained in a solution of 5% methanol (v/v) and 5% acetic acid (v/v). For storage, the gel is kept in a fresh solution of 5% methanol (v/v) and 5% acetic acid (v/v). The LMW standard was used to calculate the approximate molecular

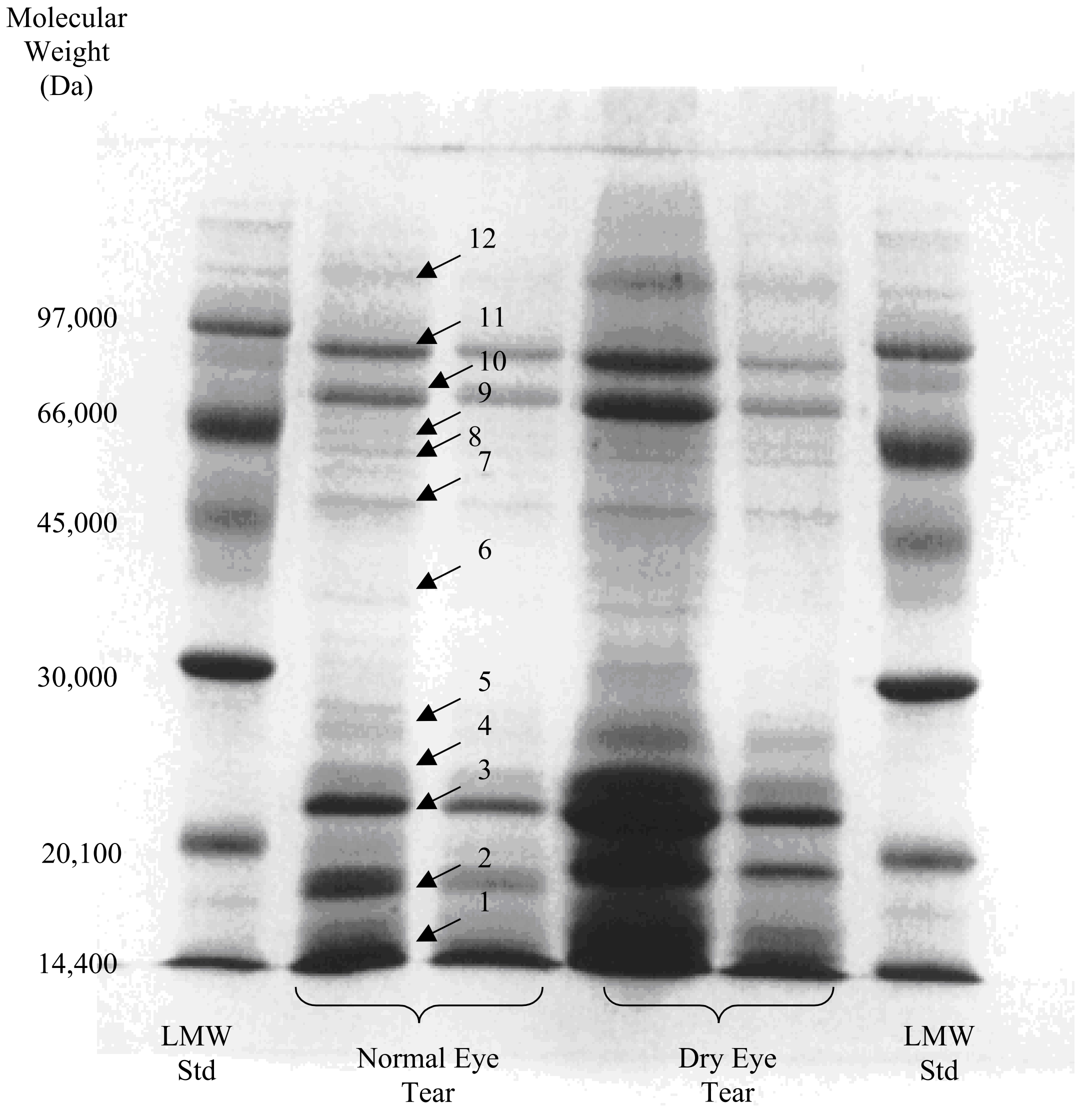

Figure 8.1. 1D SDS-PAGE results of normal eye tear versus dry eye tear.

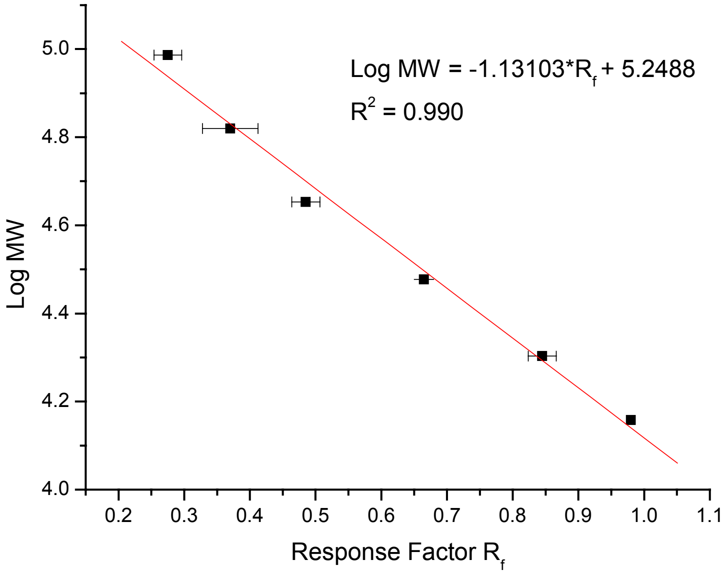

Figure 8.2. Calibration plot used for the molecular weight determinations constructed from the LMW standard's R_f values.

Molecular Weight (Da)	Protein ID from Literature and Mass Spectrometry	Difference in Protein Expression in Dry Eyes Compared to Normal
10,200	Lipophilin	Increased
10456	Lipophilin CL2*	Not Available
11,300	ß-2 microglobulin	Equal
14,113	Apolipoprotein A-1**	Not Available
14,254	Cystatin	Increased
14,390	Lysozyme	Variable
14,559	Unidentified	Increased
16,399	Lipophilin	Variable
17,310	Lipocalin (Tear specific pre-albumin)	Increased
18,500	Platelet-activating growth factor	Equal
20,500	Unidentified	Equal
25,307	T-cell-specific surface glycoprotein CD28 precursor***	Not Available
30,300	Apolipoprotein D monomer	Variable
30,740	Channel protein [1] **	Not Available
37,500	Unidentified	Equal
51,165	Lacrimal lipase**	Not Available
55,721	Cytochrome P450 2C14**	Not Available
56,808	Protein disulfide isomerase precursor (PDI)***	Not Available
68,915	Serum albumin precursor***	Not Available

*Identification determined by MALDI-TOF PSD analysis which did not allow for quantitative comparison.
**Identification determined by ES-MS-MS analysis which did not allow for quantitative comparison.
***Identification determined by MALDI-TOF fingerprint analysis which did not allow for quantitative comparison.
[1] Related to voltage dependent anion-selective channel protein.

Table 8.1. Protein Peaks Found in Rabbit Tear by MALDI-TOF MS and ES-MS-MS with Tentative Assignments.

weights of the extracted rabbit tear proteins. Figure 8.2 is the calibration plot used for the molecular weight determinations constructed from the LMW standard's R_f values. Table 8.1 lists the protein assignments for some of the major bands observed for the extracted proteins.

8.3.2 Tear total protein

Quantitation of total tear protein was determined by the Bradford Assay method (Sigma-Aldrich, St. Louis, MO). The protein, in solution, is complexed with the dye Brilliant Blue G which causes a shift in the dye's maximum absorption from 465 nm to 595 nm. The absorption amount is directly proportional to protein concentration in a linear working range of 1-1.4 mg/mL. Figure 8.3 is a calibration curve showing the linear working range used to quantitate the proteins in both the normal, and the dry eye model tear fluid. Table 8.2 is a tabulation of total tear protein comparative results for normal versus dry eye tear for seven different rabbits. Also included in the table is a 21μL composite sample of normal eye tear total protein.

8.3.3 MALDI-TOF MS of Tear Protein

In the recent literature, there have been numerous amounts of incremental optimizations in sample pretreatment prior to MALDI-TOF MS analysis reported. These include the addition of monobasic ammonium phosphate as a matrix enhancement, and post-crystallization washing with dibasic ammonium citrate, both resulting in suppressing the formation of metal adducts and matrix clusters(46). There has also been the reporting of wax coating MALDI plates prior to sample spotting as a way of improving response(47) in peptide analysis. In the present study of tear proteins, we have evaluated these optimization steps and incorporated certain aspects of

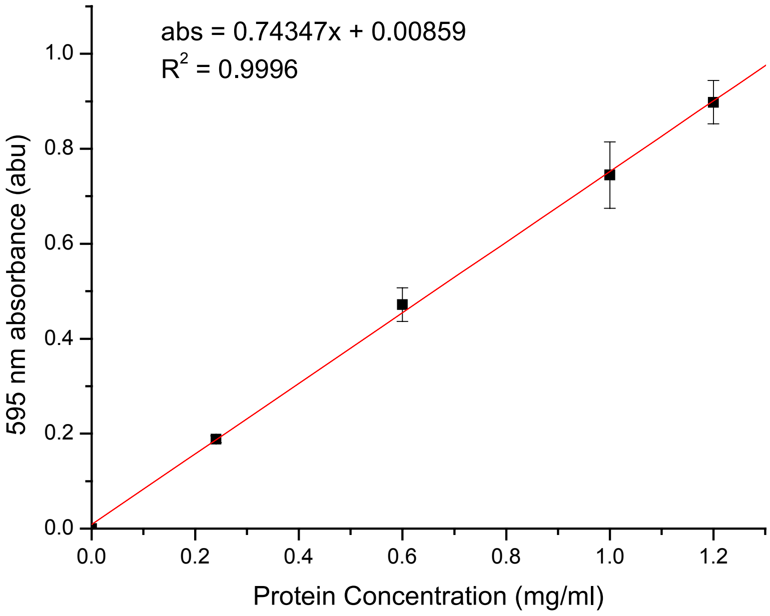

Figure 8.3. Calibration curve for protein quantitation.

Table 8.2. Concentration of protein in normal and dry eye tear

Sample ID	Control Eye (mg/mL)	Dry Model Eye (mg/mL)
SJ-71 (06-01-04)	1.69	3.24
SJ-72 (06-01-04)	4.42	3.45
SJ-73 (06-01-04)	6.95	7.94
SJ-75 (10-09-03)	3.33	[a]NA
SJ-75 (06-01-04)	7.58	5.44
SJ-76 (10-13-03)	[a]NA	3.23
SJ-76 (06-01-04)	4.70	1.43
SJ73-SJ76 21μL Comp.	3.70	NA
Average	4.62	4.12
Std Dev	2.05	2.26

[a]NA: not analyzed.

them into the collection of the presently reported results. Wax coating of the Voyager MALDI plates was observed to decrease the chemical noise in MALDI-TOF spectra, and increase the resolution of the peaks, for the analysis of peptides. The most dramatic effect though of applying the wax coating to the Voyager MALDI plates was observed for protein analysis in linear mode. Figure 8.4a is the MALDI-TOF spectrum for lysozyme with an uncoated plate, and Fig. 8.4b is the MALDI linear mode spectrum of lysozyme collected using a wax coated plate. The S/N ratio increased from 7:1 to 65:1 with the application of the wax coating. A decrease in dimerization is also observed at m/z 28.8 kDa. This same affect was observed with carbonic anhydrase (Figure 8.5a uncoated plate, Fig. 8.5b coated plate) where the S/N ratio increased from 12:1 to 135:1. Figure 8.6a is the MALDI-TOF spectrum for an uncoated plate analysis of BSA (+2 at 33216 Da and +1 at 66431 Da) giving a S/N ratio of 10:1 for the 33 kDa peak, and 15:1 for the 66 kDa peak. Figure 8.6b is the same BSA standard collected using a wax coated plate resulting in a S/N ratio of 39:1 for the 33 kDa peak, and 158:1 for the 66 kDa peak.

A study was performed comparing the tear protein of normal eye tear to the dry eye tear model by depositing a 50:1 ratio of tear (neat) with matrix, and collecting the spectrum in linear mode. Figure 8.7 shows the enhancement effect observed for the tear protein spectrum when employing the wax coated Voyager MALDI plates. Figure 8.7a was collected using an uncoated plate. Figure 8.7b is the MALDI-TOF spectrum collected using the wax coated Voyager plate, illustrating a clear enhancement in the MALDI-TOF MS spectrum of the tear proteins. Because the tear samples contain a considerable amount of salts, the matrix/sample plate spots were washed with a 10 mM diammonium citrate H_2O solution, which was observed to also enhance the response of the proteins.

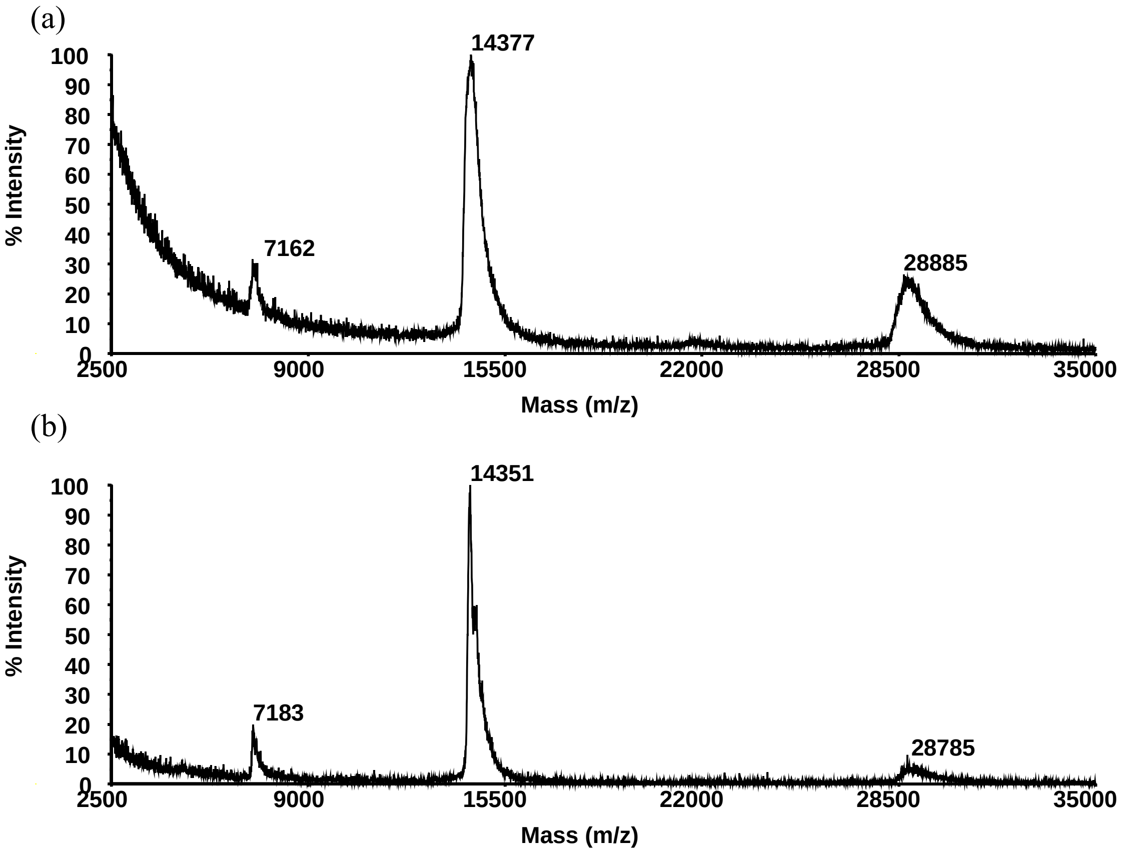

Figure 8.4 (a) MALDI-TOF spectrum of a lysozyme (14376 Da) standard collected using a standard, non-coated Voyager plate with a S/N ratio of 7:1. (b) Lysozyme protein standard spectrum collected using a wax coated plate with a S/N ratio of 65:1. A decrease in dimerization is observed at m/z 28.8 kDa.

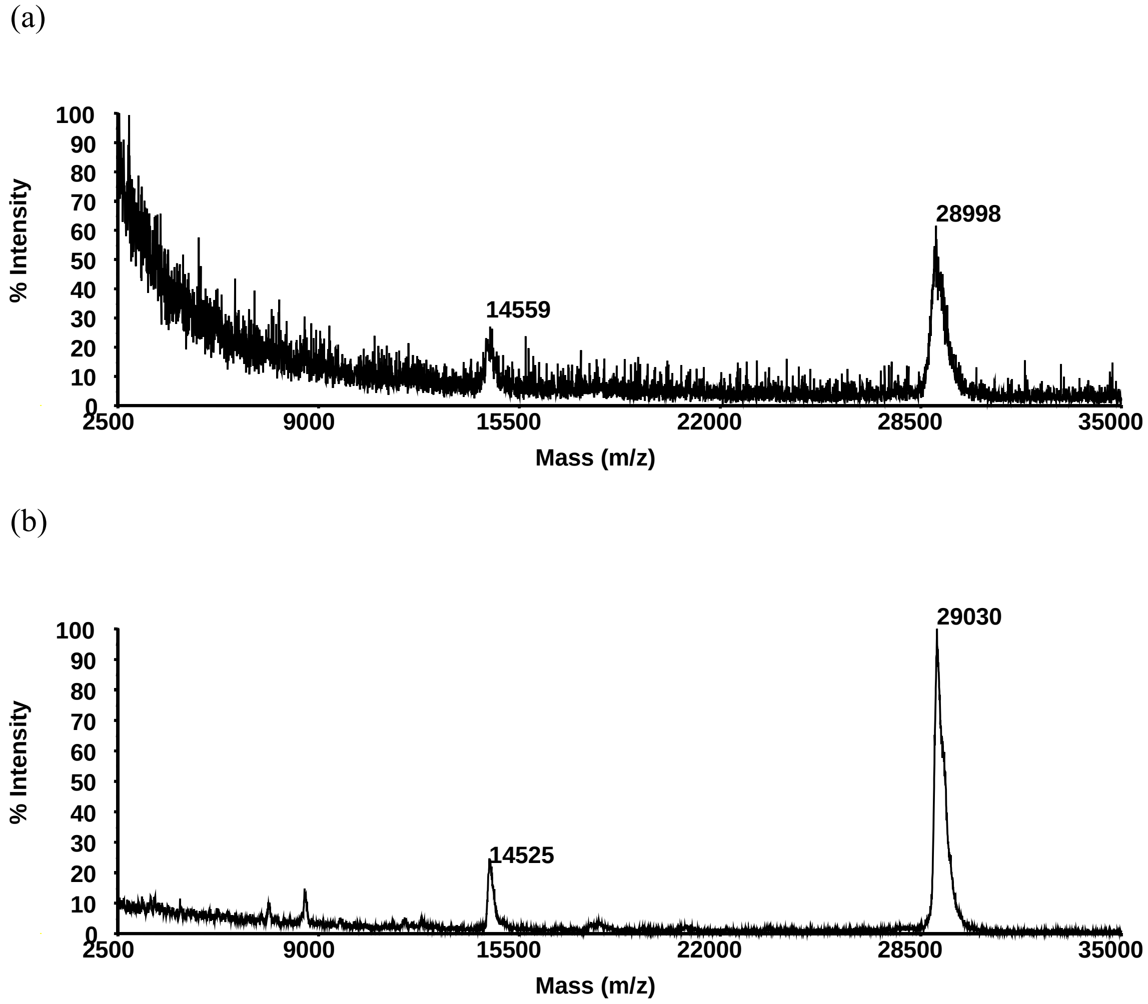

Figure 8.5. (a) MALDI-TOF spectrum of carbonic anhydrase (29024 Da) standard collected using a non-coated plate with a S/N ratio of 12:1. (b) Carbonic anhydrase protein standard spectrum collected using a wax coated plate with S/N ratio of 135:1.

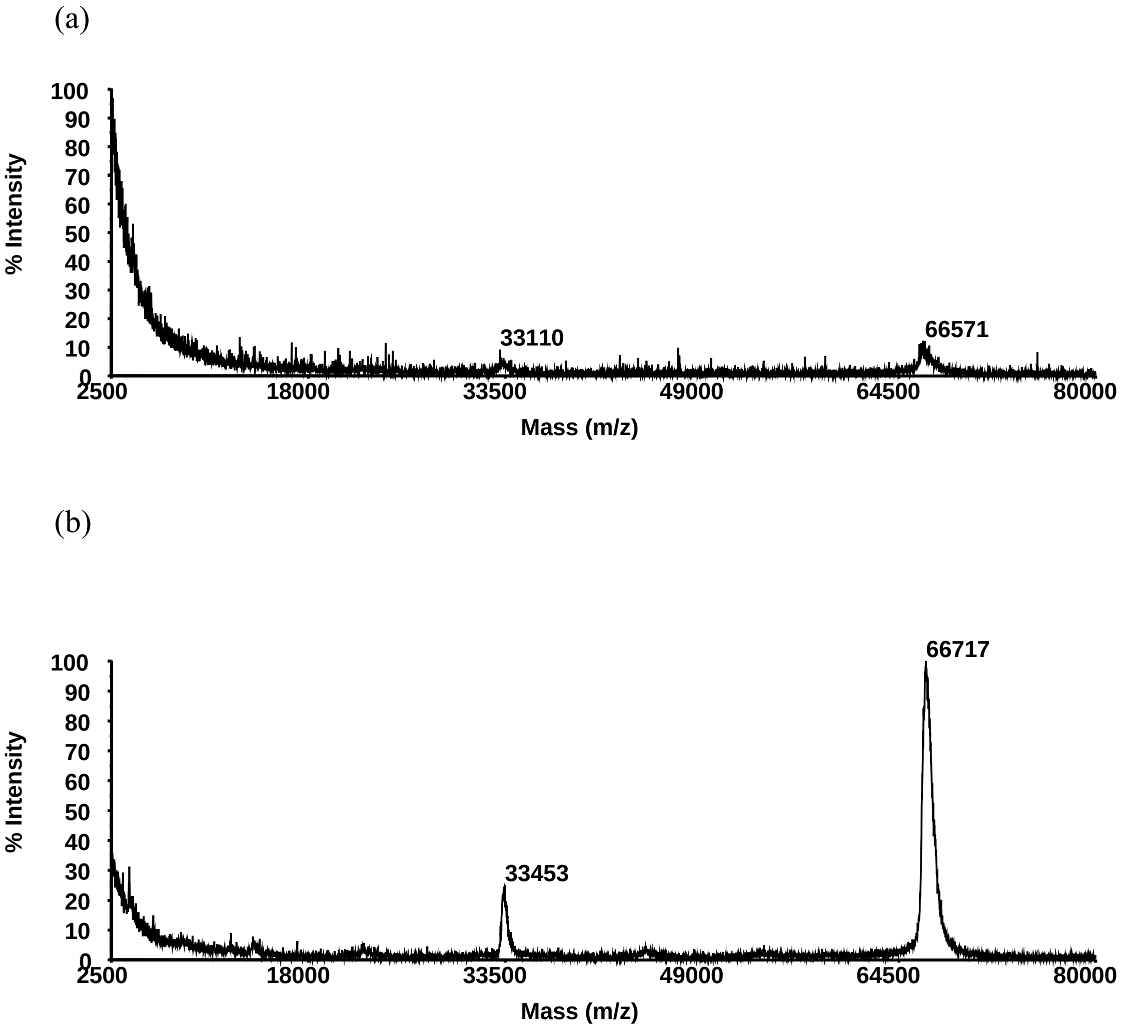

Figure 8.6. (a) MALDI-TOF spectrum of BSA (33216 Da and 66431 Da) standard collected using a non-coated plate. The S/N ratio for the 33 kDa peak is 10:1 and S/N ratio for 66 kDa peak is 15:1. (b) BSA spectrum collected using wax coated plate. The S/N ratio for the 33 kDa peak is 39:1 and S/N ratio for 66 kDa peak is 158:1.

Figures 8.8a and 8.8b are the first comparative spectra of rabbit tear fluid proteins from a rabbit that has been given the dry eye condition. Figure 8.8a is the MALDI-TOF mass spectrum of the left, normal eye of the rabbit. Figure 8.8b is the mass spectrum of the right, dry eye model eye of the rabbit. Of interest in these two spectra is the observance of a decrease in the 14,390 Da protein, a decrease in the 16,454 Da protein, and an increase in the 10,151 Da protein for Fig 8.8b, the dry eye model. From Table 1 it appears that a likely candidate for the assignment of the 14,390 Da protein may be lysozyme. The 16,454 Da protein may be lipophilin, and the 10,151 Da protein is probably the lipophilin protein. The 11,300 Da protein found in both the normal and the dry eye extracts is assigned as a ß-2 microglobulin protein. Figure 8.9 is the post source decay (PSD) spectrum of an m/z 1756 peptide obtained from band 1 in the 1D SDS-PAGE gel. It has been identified as the lipophilin CL2 protein at 10,456 Da. The 1D SDS-PAGE result of the tear proteins illustrated in Figure 8.1 shows that the majority of the proteins are the lower molecular weight proteins ranging from approximately 10 kDa to 25 kDa (bands 1 through 4), followed by the transferrins of bands 10 and 11. These low molecular weight proteins appear to be comprised of many lipid-binding proteins such as the lipophilins, the apolipoproteins, and the lipocalins, and also the globulins, cystatin and lysozyme. Therefore, it would be expected that readily observable changes in the protein expressions would primarily involve these low molecular weight species. Furthermore, previous work done in our lab has shown that the major lipids in the tear film are mono and diacylglycerols(48), while other known tear lipids such as cholesterol, the wax esters, and the phosphorylated lipids, are in much lower abundances. It would seem likely then that the lipid binding proteins in the tear film are the fatty acid chain type binding proteins, for example the human tear lipocalin member tear prealbumin is found in vitro to bind retinol and fatty acids, but not cholesterol, while tear fluid apoD does bind cholesterol

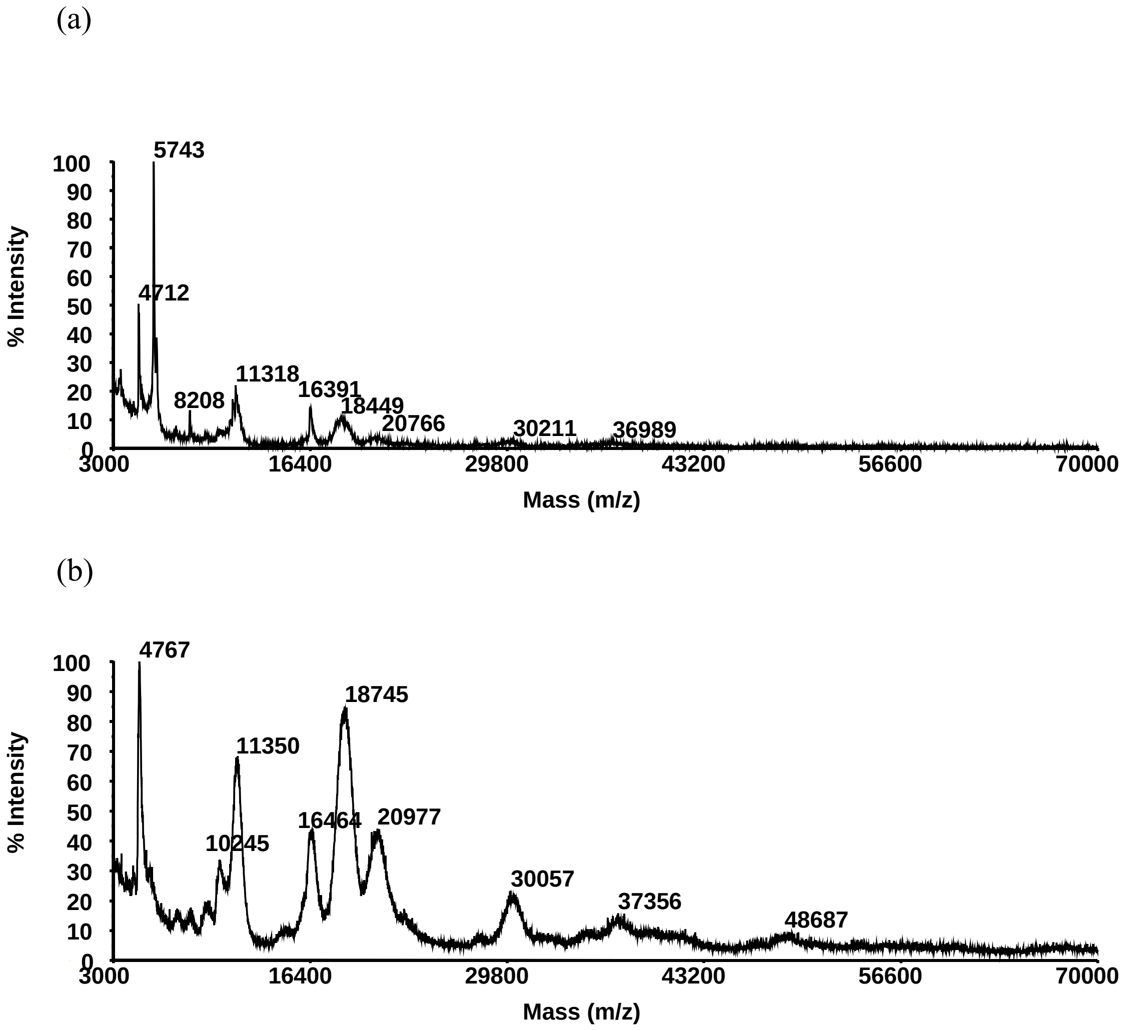

Figure 8.7. Comparison of tear protein MALDI-TOF MS spectral response enhancement using a wax coated Voyager plate. (a) Tear protein spectrum collected using an un-coated plate. (b) Tear protein spectrum collected using a wax coated plate.

and the phosphorylated lipids(49) (apoD possibly bands 6 and 8 which are in low abundances).

A second set of spectra are presented in Figure 8.10 comparing the MALDI-TOF MS protein analysis of the rabbit normal eye versus the dry eye model. The normal eye spectrum in Fig. 8.10a shows a very large abundance of an m/z 17,408 protein which would probably represent tear lipocalin, represented by the the predominant band #2 in Figure 1. Notably, in the dry eye model spectrum of Fig. 8.10b, this protein is absent, but a new protein at m/z 29,002 (unidentified) is now observed. Tear lipocalin is thought to play a major role in tear stability, being solely bound to the lipids, thus providing an anchoring effect between the tear film lipid layer and the tear aqueous region. m/z 30,370 Da apolipoprotein D monomer as compared to the dry eye. Secondly, the dry eye spectrum appears to have added the m/z 17,330 Da lipocalin protein, thirdly, the m/z 11,370 Da ß-2 microglobulin protein appears to have decreased in the dry eye spectrum, and fourthly, the 16,392 Da lipophilin protein has increased in the dry eye spectrum. The next normal versus dry eye model is illustrated in Figure 8.11, where the normal eye spectrum is Fig. 8.11a, and the dry eye model spectrum is Fig. 8.11b. Four differences are observed between the spectra. First, the normal eye spectrum appears to have a more abundant 11 kDa protein expressed. In the dry eye 11b spectrum, the m/z 10 kDa, the m/z 16 kDa, and the m/z 17 kDa protein are observed to be more greatly expressed. In Figure 8.12, the dry eye spectrum in (b) shows an elevation of the m/z 14 kDa protein compared to the normal eye spectrum in Fig. 8.12a. In both Figures 8.13 and 8.14, the dry eye model spectra show an increase in the 10 kDa protein (lipophilin), and the 17 kDa (lipocalin) protein.

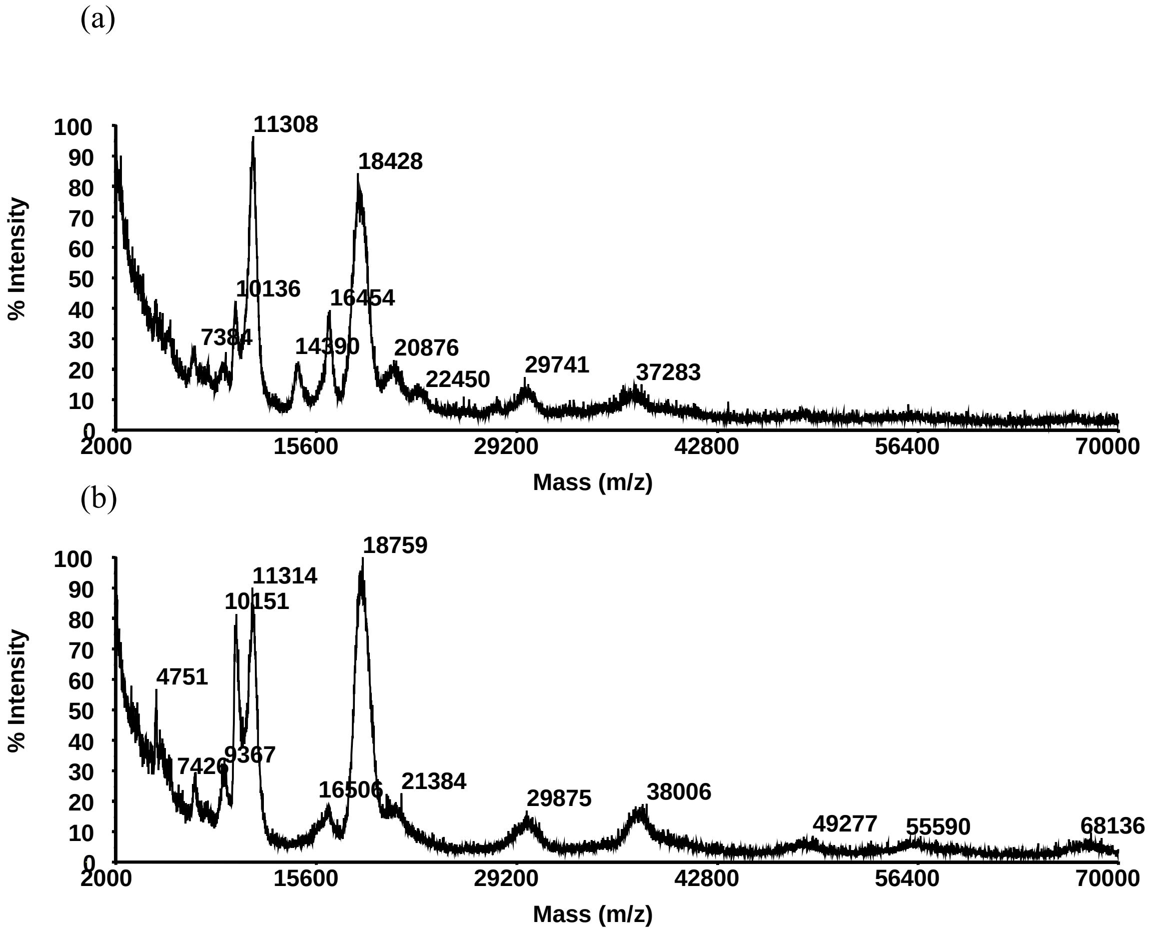

Figure 8.8. MALDI-TOF MS spectra of (a) normal eye tear proteins, and (b) dry eye tear proteins. The bottom dry eye MS spectrum shows an increase in the 10 kDa lipophilin protein, and a decrease in both the 14 kDa lysozyme protein, and the 16 kDa lipophilin protein.

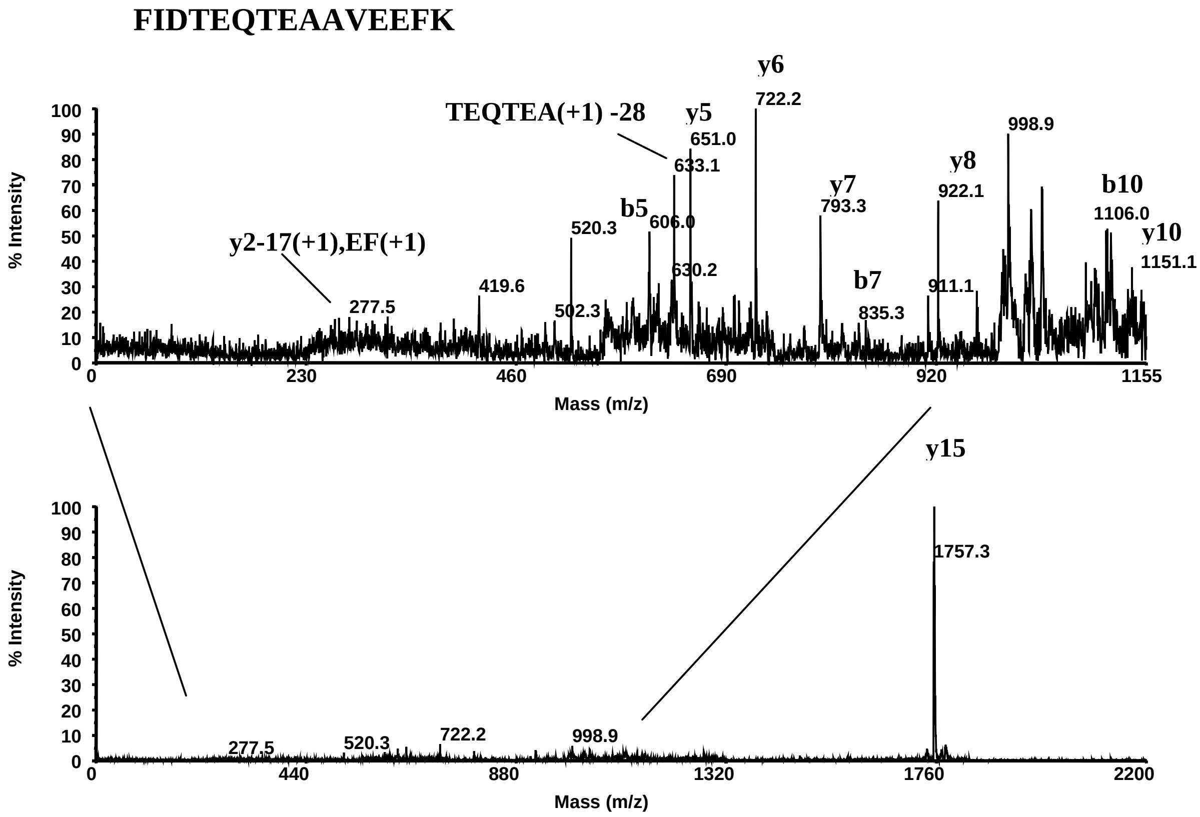

Figure 8.9. PSD spectrum of an m/z 1756 peptide obtained from band 1 in the 1D SDS-PAGE gel, identified as the lipophilin CL2 protein at 10,456 Da.

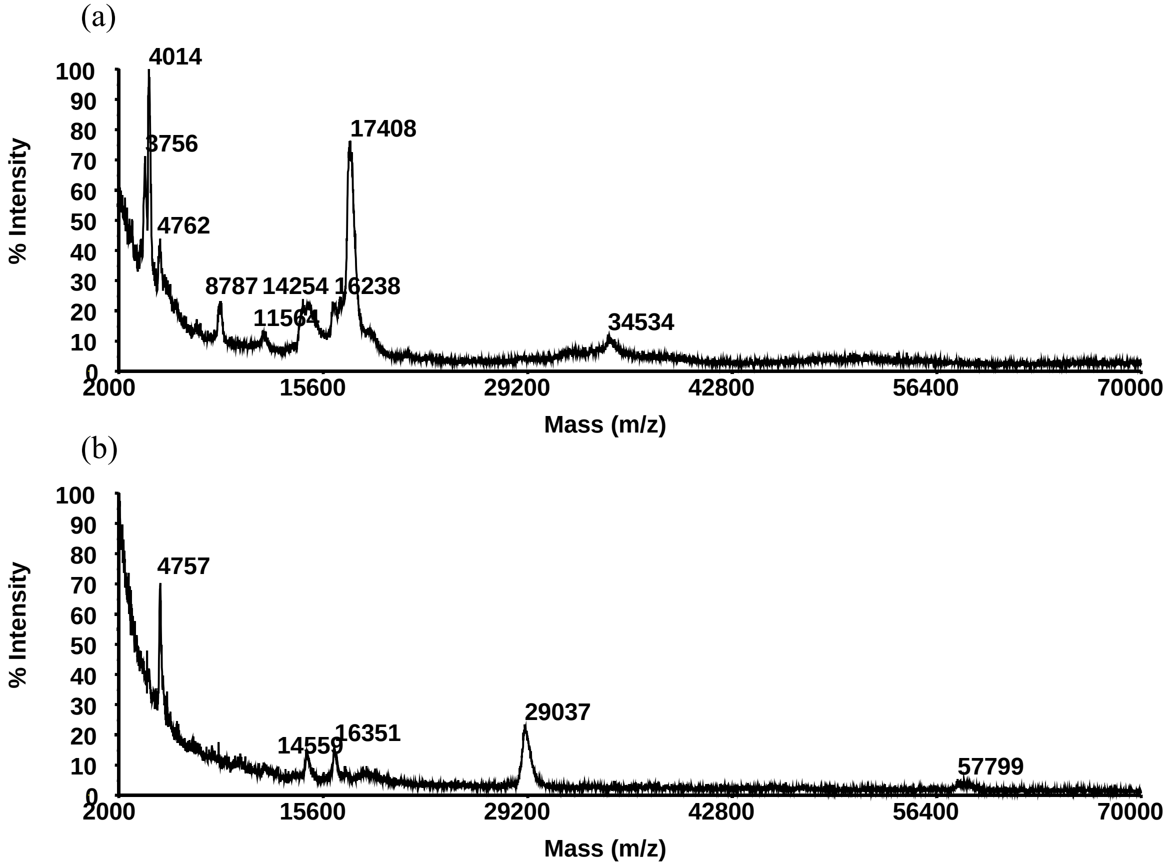

Figure 8.10. MALDI-TOF MS spectra of (a) normal eye tear proteins, and (b) dry eye tear proteins. The top normal eye spectrum contains a strong peak at 17 kDa which is probably lipocalin. The bottom dry eye tear protein spectrum shows a predominant peak at 29 kDa of an unidentified protein.

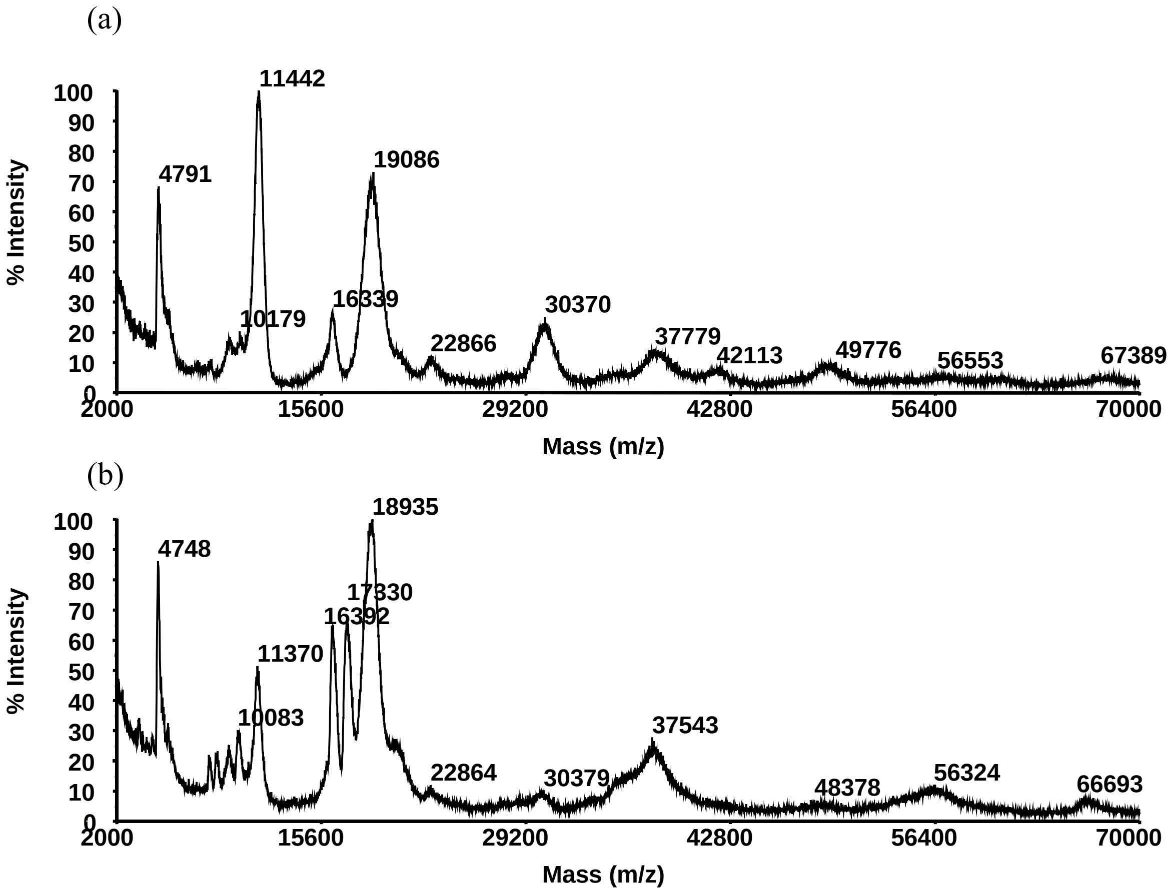

Figure 8.11. MALDI-TOF MS spectra of (a) normal eye tear proteins, and (b) dry eye tear proteins. The bottom dry eye MS spectrum shows an increase in the 17 kDa lipocalin protein, an increase in the 16 kDa lipophilin protein and a decrease in both the 11 kDa ß-2 microglobulin protein, and the 30 kDa apoD protein.

8.3.4 ES Triple Quadrupole MS/MS of Digested Peptides

As a further aid in the identification of the tear proteins, Electrospray Triple Quadrupole tandem mass spectrometry was performed on the most abundant peptides from an in-solution digestion of the tear proteins. The lipid fraction was first removed from the tear fluid following the above modified extraction method. The aqueous tear protein extract was then cleaned using a ProteoPrep^{TM} Protein Precipitation Kit (Sigma, Saint Louis, Missouri) to isolate the proteins and wash off the tear salts. In-solution digestion was then performed on the proteins, and the resulting peptides were infused into the electrospray source using a syringe pump. Figure 8.15a is a single stage spectrum of the normal eye peptides. Figure 8.15b is a single stage spectrum of the dry eye peptides. The most abundant peptides were subjected to collision induced dissociation, and the resultant product ion spectra were searched using Protein Prospector for possible protein identification. Figure 8.16 is a product ion spectrum from the collision induced dissociation of the m/z 661 (+3) peptide. The important product ions include the y_1-NH_3 peak at m/z 158, the y_3^{+2} peak at m/z 187, the a_2 peak at m/z 251, the y_{16}-NH_3^{+2} at m/z 843, the y_8-NH_3 peak at m/z 895, and the a_{12} peak at m/z 1240. The protein was identified as the T-cell receptor alpha chain V region RL-5 precursor with a molecular weight of 14,856 Da.

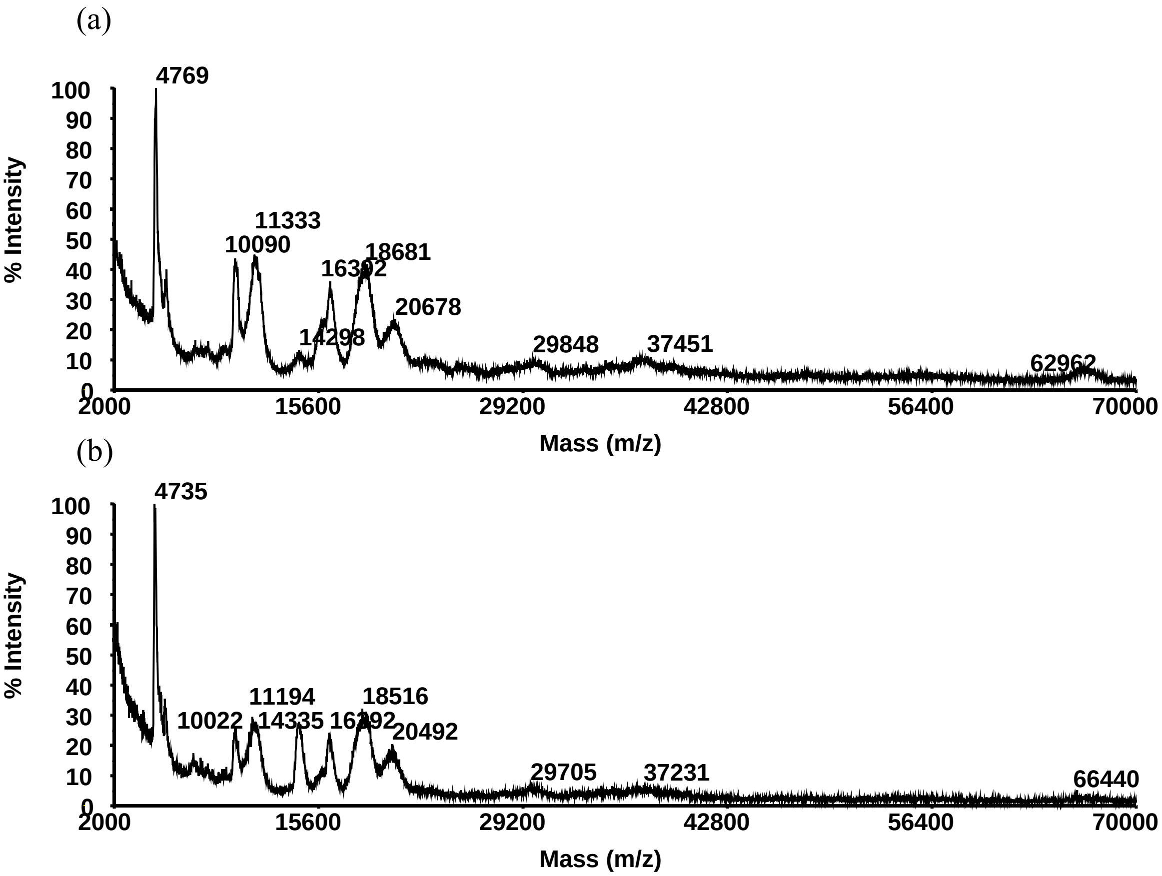

Figure 8.12. MALDI-TOF MS spectra of (a) normal eye tear proteins, and (b) dry eye tear proteins. The bottom dry eye MS spectrum shows an increase in the 14 kDa apolipoprotein.

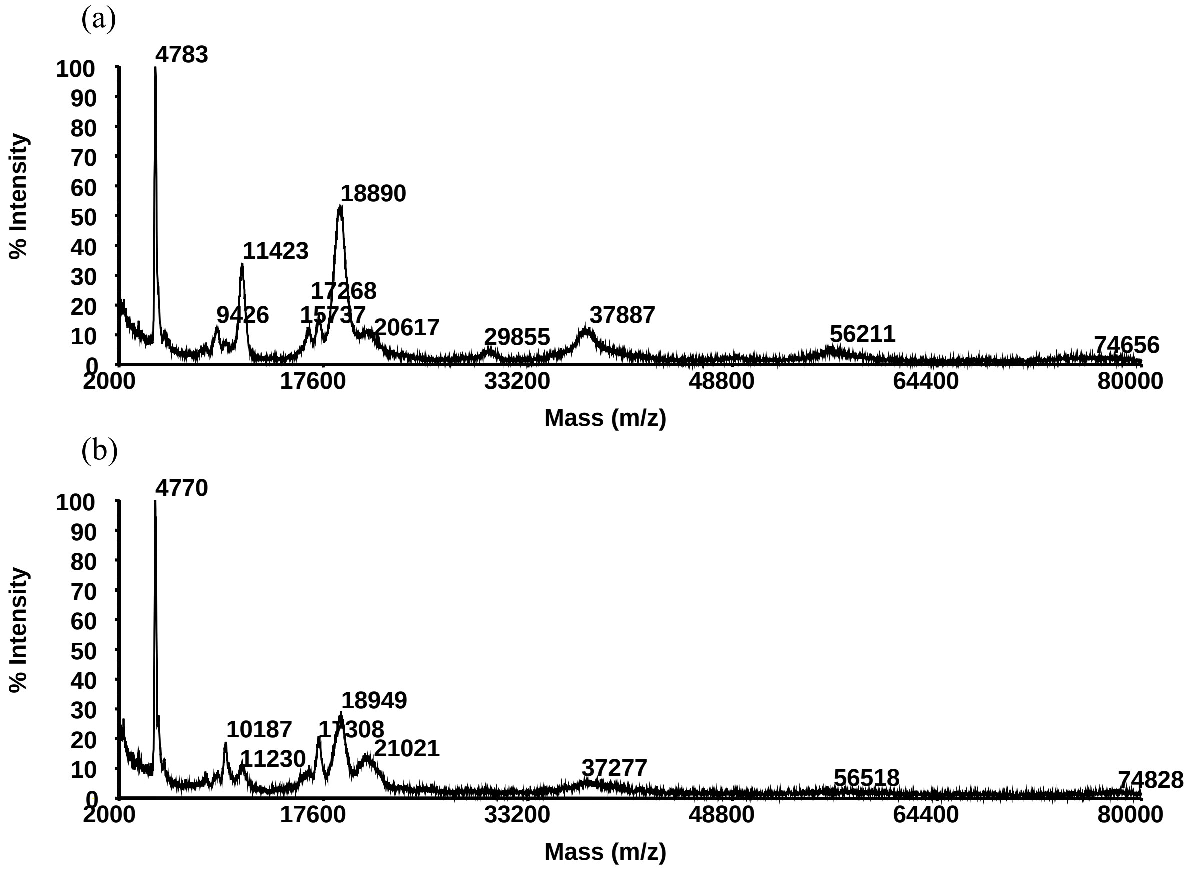

Figure 8.13. MALDI-TOF MS spectra of (a) normal eye tear proteins, and (b) dry eye tear proteins. The bottom dry eye MS spectrum shows an increase in both the 10 kDa lipophilin protein, and the 17 kDa lipocalin protein.

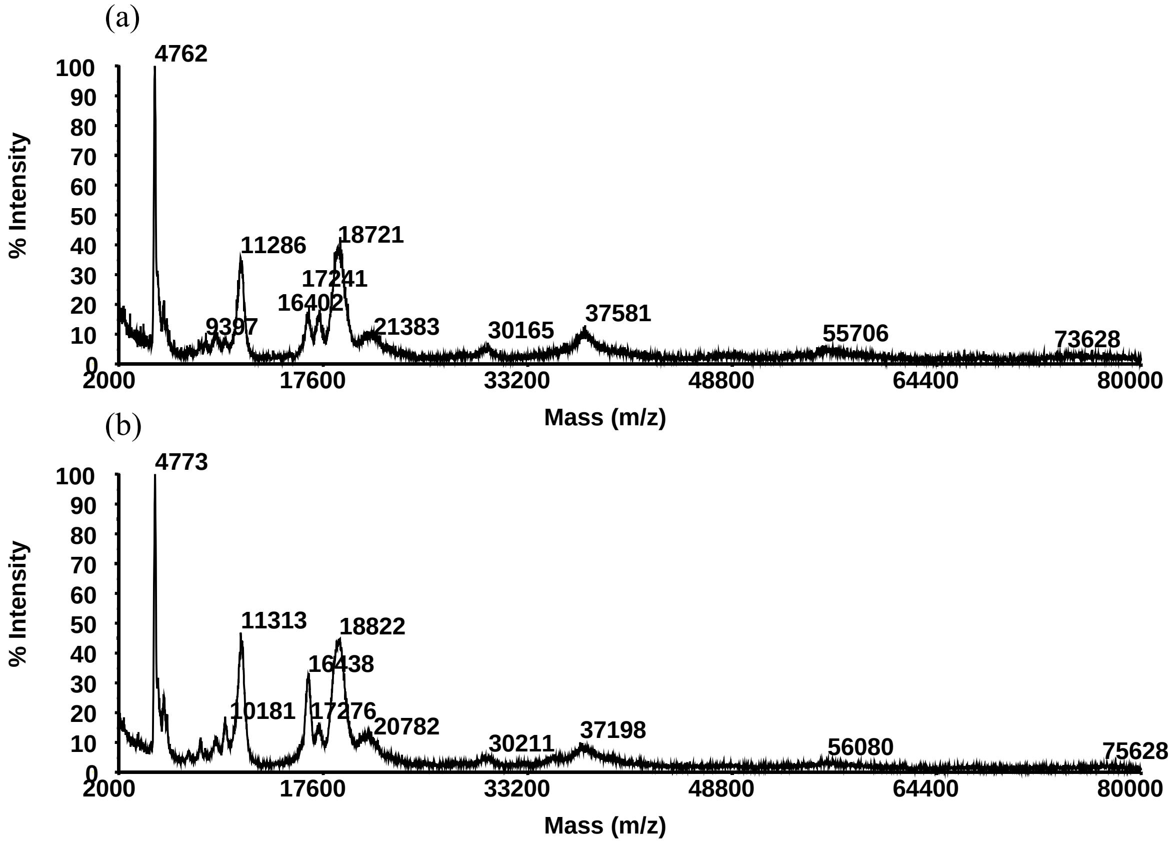

Figure 8.14. MALDI-TOF MS spectra of (a) normal eye tear proteins, and (b) dry eye tear proteins. The bottom dry eye MS spectrum shows an increase in both the 10 kDa lipophilin protein, and the 17 kDa lipocalin protein.

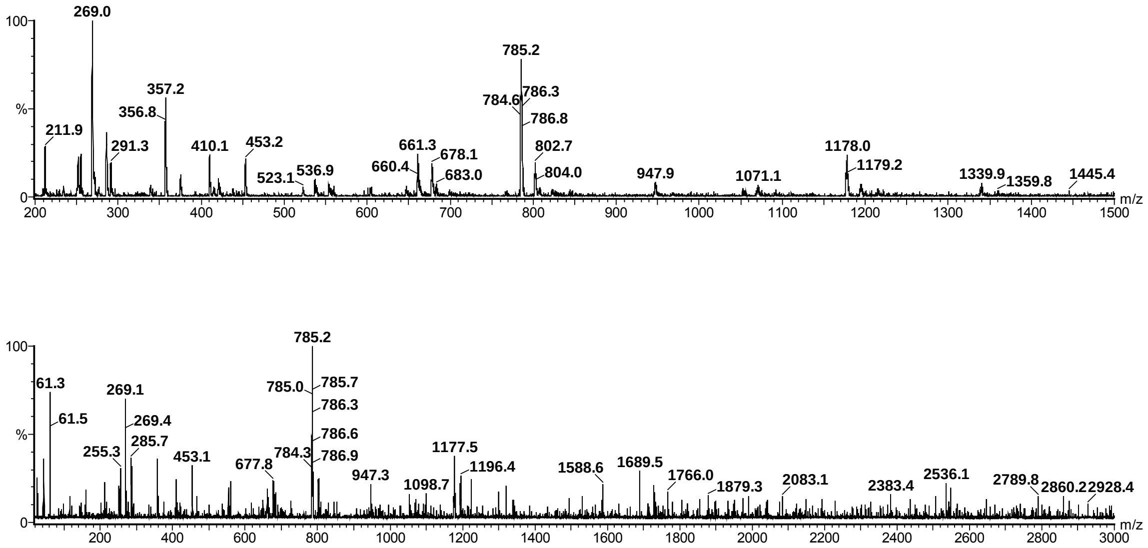

Figure 8.15. (a) Single stage spectrum of the normal eye peptides. (b) Single stage spectrum of the dry eye peptides.

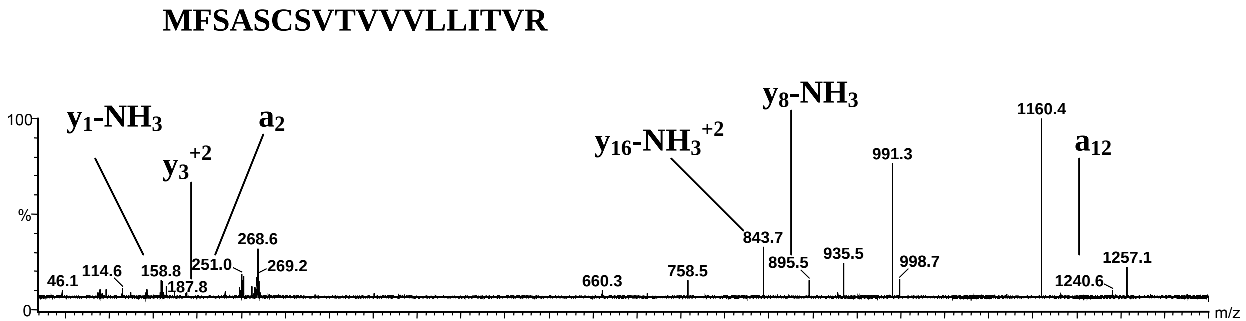

Figure 8.16. Ms/ms spectrum of the m/z 661.3 peptide.

8.4 Conclusion

Wax coating of MALDI plates significantly enhances the response of proteins in linear mode time-of-flight analysis. Tears contain a considerable amount of salts that can be effectively removed through spot washing with an aqueous solution of ammonium citrate, thus reducing the salt suppression effects of the untreated biological sample. Tear protein quantitation and 1D SDS-PAGE gel analysis of the normal versus the dry eye model tears did not show a significant difference. The MALDI-TOF MS linear mode analysis of the intact tear proteins indicated that expression differences exist primarily in the low molecular weight range of the lipid binding proteins. Substantial differences in the observed abundances of lipophilin (m/z 10.2 kDa), lysozyme (14.4 kDa), and lipocalin (m/z 17.3 kDa), in normal versus dry eye tear protein MALDI-TOF MS spectra could indicate a diseased state, and may have an application in diagnosis of the dry eye condition.

8.5 REFERENCES

1. Holly, F. J., and Lemp, M. A. The preocular tear film and dry eye syndromes. *International ophthalmology Clinics*, Vol. 13, No. 1, Little, Brown and Company, Boston, 1973, 29-46.
2. Ellison, Solon A.; Jacobson, Mark; Levine, Michael J. Lacrimal and salivary proteins. Immunol. Eye, Workshop 3: Immunol. Aspects Ocul. Dis.: Infect., Inflammation, Allergy (1981), Meeting Date 1980, 205-19.
3. Frey, W. H., DeSota-Johnson, D. Hoffman, C., and McCall, J. T. Effects of stimulus of the chemical composition of human tears. *Am. J. Ophthalmol.*, 1981; 92: 559-567.
4. Holly, F. J., and Hong, B. S. Biochemical and surface characteristics of human tear proteins. *Am J Optom & Physiol Optics*, 1982; 59: 43-50.
5. Gachon, A. M., Richard, J., and Dastugue, B. Human tears: normal protein pattern and individual protein determinations in adults. *Cur Eye Res*, 1982; 2: 301-308.
6. Suarez, J. C. Significance of postgamma protein fraction in tears. *Ophthalmologica, Basel*, 1986; 193: 75-77.
7. Kuizenga, A., Stolwijk, T. R., van Agtmaal, E. J., van Haeringen, N. J., and Kijlstra, A. Detection of secretory IgM in tears of IgA defecient individuals. *Cur Eye Res*, 1990; 9: 997-1005.

8. Gachon, A. M. F. Human lacrimal gland secretes proteins belonging to the group of hydrophobic molecule transporters. In *Lacrimal Gland, Tear Film, and Dry Eye Syndromes*. Sullivan DA (ed). Plenum Press: New York 1994; 205.
9. Baguet J., Claudon-Eyl, V., Sommer, F., and Chevallier, P. Normal protein and glycoprotein profiles of reflex tears and trace element composition of basal tears from heavy and slight deposits on soft contact lenses. *CLAO J*, 1995; 21: 114-121.
10. Asrani, A. C., Lumsden, A. J., Kumar, R., and Laurie, G. W. Gene cloning of BM180, a lacrimal gland enriched basement membrane protein with a role in stimulated secretion. In *Lacrimal Gland, Tear Film, and Dry Eye Syndromes 2*. Sullivan DA, Dartt DA, Meneray MA (ed). Plenum Press: New York 1998; 49.
11. Lehrer, R. I., Xu, G., Abduragimov, A., Dinh, N. N., Qu, X. D., Martin, D., and Glasgow, B. J. Lipophilin, a novel heterodimeric protein of human tears. *FEBS Letters*, 1998; 432: 163-167.
12. Schoenwald, R. D., Vidvauns, S., Wurster, D. E., and Barfknecht, C. F. The role of tear proteins in tear film stability in the dry eye patient and in the rabbit. In *Lacrimal Gland, Tear Film, and Dry Eye Syndromes 2*. Sullivan DA, Dartt DA, Meneray MA (ed). Plenum Press: New York 1998; 391.
13. Boptom, V. E., Willcox, M. D. P., and Millar, T. J. Modulation of tear film protein secretion with phosphodiesterase inhibitors. *Clin. Exp. Ophthalmol.*, 2000; 28: 208-211.
14. Moore JC, Tiffany JM. Human ocular mucas. Chemical studies. *Exp. Eye Res*. 1981; **33***:* 203.
15. Carrington SD, Hicks SJ, Corfield AP, Kaswan RL, Packer N, Bolis S, Morris CA. In *Lacrimal Gland, Tear Film, and Dry Eye Syndromes 2*. Sullivan DA, Dartt DA, Meneray MA (ed). Plenum Press: New York 1998; 253.
16. McCulley JP, Shine WE. The lipid layer: the outer surface of the ocular surface tear film. *Bioscience Reports*. 2001; **21**: 407.
17. Salvatore, M. F., Pedroza, L., and Beuerman, R. W. Denervation of rabbit lacrimal gland increases levels of transferrin and unidentified tear proteins of 44 and 36 kDa. *Curr Eye Res.* 1999; 18: 455-466.
18. Barrera, R., Jimenez, A., Lopez, R., Mane, M. C., Rodriguez, J. F., and Molleda, J. M. Evaluation of total protein content in tears of dogs by polyacrylamide gel disk electrophoresis. *Am J Vet Res* 1992; 53: 454-456
19. Kondo, Y. Studies on the biochemical marker loci detected with urine, tears, and saliva of rats. *Exp. Anim.* 1994; 43: 1-9.
20. Berta, A. A polyacrylamide-gel electrophoresis study of human tear proteins. *Graefe's Arch Clin Exp Ophthalmol* 1982; 219: 95-99.
21. Joo, W., Lee, D., and Kim, C. Development of an effective sample preparation method for the proteome analysis of body fluids using 2-D Gel electrophoresis. *Biosci. Biotechnol. Biochem.*, 2003; 67: 1574-1577.
22. Varnell, R. J., Maitchouk, D. Y., Beuerman, R. W., Salvatore, M. F., Carlton, J. E., and Haag, A. M. Analysis of rabbit tear fluid using capillary electrophoresis with UV or laser-induced fluorescence detection. *J. Cap. Elec.*, 1997; 1: 1-6.
23. Boonstra, A., and Kijlstra, A. Separation of human tear proteins by high performance liquid chromatography. *Curr. Eye Res.,* 1984; 3: 1461-1469.
24. Wollensak, G., Mur, E., Mayr, A., Baier, G., Gottinger, W., and Stoffler, G. Effective methods for the investigation of human tear film proteins and lipids. *Graefe's Arch Clin Exp Ophthalmol* 1990; 228: 78-82.

25. Gachon, A. M., Verrelle, P., Betail, G., and Dastugue, B. Immunological and electrophoretic studies of human tear proteins. *Exp. Eye Res.*, 1979; 29: 539-553.
26. Boonstra, A., and Kijlstra, A. The identification of transferrin, an iron-binding protein in rabbit tears. *Exp. Eye Res.*, 1984; 38: 561-567.
27. Inada, K., Baba, H., and Okamura, R. Studies of human tear proteins – 1. Analysis of tears from normal subjects by crossed immunoelectrophoresis. *Jpn. J. Ophthalmol.*, 1982; 26: 314-325.
28. Schmut, O., Horwath-Winter, J., Zenker, A., and Trummer, G. The effect of sample treatment on separation profiles of tear fluid proteins: quantitative and semi-quantitative protein determination by an automated analysis system. *Graefe's Arch Clin Exp Ophthalmol,* 2002; 240: 900-905.
29. Glasgow, B. J., Abduragimov, A. R., Farahbakhsh, Z. T., Faull, K. F., and Hubbell, W. L. Tear lipocalins bind a broad array of lipid ligands. *Curr. Eye Res.*, 1995; 14: 363-372.
30. Zhou, L., Beuerman, R. W., Barathi, A., and Tan, D. Analysis of rabbit tear proteins by high-pressure liquid chromatography/electrospray ionization mass spectrometry. *Rapid Commun. Mass Spectrum.*, 2003; 17: 401-412.
31. Mulvenna, I., Stapleton, F., Hains, P. G., Cengiz, A., Tan, M., Walsh, B., and Holden, B. Low molecular weight analysis of tears using matrix assisted laser desorption ionization-time of flight mass spectrometry. *Clinical and Experimental Ophthalmology*, 2000; 28: 205-207.
32. Fung, K., Morris, C., and Duncan, M. *Lacrimal Gland, Tear Film, and Dry Eye Syndromes 3* Edited by D. Sullivan *et al*., Kluwer Academic/Plenum Publishers, 2002, p. 601.
33. Cao, P., and Moini, M. Analysis of peptides, proteins, protein digests, and whole human blood by capillary electrophoresis/electrospray ionization-mass spectrometry using an in-capillary electrode sheathless interface. *J Am Soc Mass Spectrom* 1998; 9: 1081-1088.
34. Bonavida, B., Sapse, A. T., and Sercarz, E. E. Rabbit tear proteins. I. Detection and quantitation of lysozyme in nonstimulated tears. *Invest Ophthalmol*, 1968; 7: 435.
35. Dartt, L. A., and Botelho, S. Y. Protein in rabbit lacrimal gland fluid. *Invest. Ophthalmol. Visual Sci.*, 1979; 18: 1207-1209.
36. Dohlman, C. H., Friend, J., Kalevar, V., Yogoda, D., and Balazs, E. The glycoprotein (mucus) content of tears from normal and dry eye patients. *Exp Eye Res* 1976; 22: 359.
37. Ng, V., Cho, P., and To, C. Tear proteins of normal young Hong Kong Chinese. *Graefe's Arch Clin Exp Ophthalmol,* 2000; 238: 738-745.
38. Pflugfelder, S. C., Solomon, A., and Stern, M. E. The diagnosis and management of dry eye: A twenty-five-year-review. *Cornea*, 2000; 19: 644-649.
39. Lemp, M. A. Report of the National Eye Institute/Industry workshop on clinical trials in dry eyes. *CLAO J*, 1995; 21: 222-232.
40. Schaumberg DA, Buring JE, Sullivan DA, Dana MR. Hormone replacement therapy and dry eye syndrome. *JAMA*. 2001; **286**: 2114.
41. Ohashi, Y., Ishida, R., Kojima, T., Goto, E., Matsumoto, Y., Watanabe, K., Ishida, N., Nakat, K., Takeuchi, T., and Tsubota, K. Abnormal protein profiles in tears with dry eye syndrom. *Am. J. Ophthalmol.*, 2003; 136: 291-299.
42. Nguyen, D. H., Beuerman, R. W., Meneray, M. A., and Maitchouk, D. Sensory denervation leads to deregulated protein synthesis in the lacrimal gland. *Lacrimal Gland, Tear Film, and Dry Eye Syndromes 2* edited by Sullivan *et al*., Plenum Press, New York, 1998.
43. Varnell, R. J., Maitchouk, D. M., Beuerman, R. W., Carlton, J. E., and Haag, A. Small-volume analysis of rabbit tears and effects of a corneal wound on tear protein spectra.

Lacrimal Gland, Tear Film, and Dry Eye Syndromes 2 edited by Sullivan *et al.*, Plenum Press, New York, 1998.

44. Folch, J., Lees, M., and Stanly, G. H. S. A simple method for the isolation and purification of total lipids from animal tissues. *J. Biol. Chem.* 1957; 226: 497.
45. Bligh, E. G., and Dyer, W. J. A rapid method of total lipid extraction and purification. *Can. J. Biochem. Physiol.* 1959; 37: 911.
46. Smirnov, I. P.; Zhu, X.; Taylor, T.; Huang, Y.; Ross, P.; Papayanopoulos, I. A.; Martin, S. A.; Pappin, D. J. Suppression of -Cyano-4-hydroxycinnamic Acid Matrix Clusters and Reduction of Chemical Noise in MALDI-TOF Mass Spectrometry *Anal. Chem.* **2004**, 76, 2958-2965.
47. Terry, D. E., Umstot, E., and Desiderio, D. M. Optimized Sample-Processing Time and Peptide Recovery for the Mass Spectrometric Analysis of Protein Digests *J Am Soc Mass Spectrom* **2004**, 15, 784-794.
48. Ham, B. M.; Jacob, J. T.; Keese, M. M.; Cole, R. B. *J. Mass Spectrom.* **2004**, *39*, 1321-1336.
49. Holzfeind, P., Merschak, P., Dieplinger, H., Bernhard, R. The Human Lacrimal Gland Synthesizes Apolipoprotein D mRNA in Addition to Tear Prealbumin mRNA, Both Species Encoding Members of the Lipocalin Superfamily *Exp. Eye Res.* **1995**, 61, 495-500.

CHAPTER IX: SUMMARY AND CONCLUSIONS

Mass spectrometry has become a powerful tool for the chemist and the biochemist. For the disciplines of the chemist, this includes gas phase thermochemistry studies for the physical chemist, structural elucidation and molecular weight of organic compounds for the organic chemist, qualitative and quantitative analysis for the analytical chemist, and even the inorganic chemist for things such as particle size distributions. An increasingly important application of mass spectrometry has been in the fields of proteomics, lipidomics, and metabalomics. Here, the biologist and biochemist have also found an accurate and precise method for composition studies of complex biological samples.

Methods have been developed by affinity capillary electrophoresis (ACE), and cation exchange liquid chromatography (CELC), for the determination of binding strength coefficients for complexes formed between π-delocalized lymphangitic dyes and an anti-cancer agent 4,4-dihydroxybenzophenone-2,4-dinitrophenylhydrazone (A007). *In vitro* trials have shown that complexes with higher binding affinities can offer improved prospects for tumor treatment. For the three tested carriers, the developed methods established that A007 non-covalent binding strength was greatest for methylene green, followed by methylene blue, and lastly toluidine blue. The developed methodology is general in nature such that it may be used to rank a wide variety of solution binding strengths of drug:carrier pairs.

A new approach for calculating bond dissociation energies (BDE's) from ES/MS-MS measurements has been developed. The new method that features a "derived effective path length" has been applied to measure BDE's of alkali metal adducts (Li^+), and halide adducts (Cl^-), of monoacylglycerol, 1,2-diacylglycerol, and 1,3-diacylglycerol lipids. Also studied were lithium-bound dimers of monoacylglycerols, 1,2-diacylglycerols, and of 1,3-diacylglycerols.

BDE's for the adducts and dimers of the lipids were measured using a triple quadrupole mass spectrometer with electrospray as the ionization source. Mass spectral results were compared to computer generated bond dissociation energies using the Becke-style 3-Parameter Density Functional Theory (B3LYP, using the Lee-Yang-Parr correlation functional) method, with excellent agreement between experimental and theoretical energy values. The newly developed method is general in nature and can be used for the measurement of metal or halide ion adduct bond dissociation energies, covalent bond dissociation energies producing fragment ions, and for the measurement of bond energies of non-covalent interactions such as dimer dissociations. The validity of the method has been rigorously established using a triple quadrupole, but it may also be applied to other mass spectrometers that allow user control of the collision cell potential.

Millions of individuals suffer from a health condition known as *Keratoconjunctivitis sicca* (KCS, also known as "dry eye"). Studies have indicated that the lipids in the tear film layer, which covers the outer portion of the eye, may be directly correlated with the existence of dry eye syndrome. By identifying and comparing the major, non-polar lipids in normal eye tear with a dry eye model, it may be possible to identify a symptom of, or a contributing factor to, dry eye. Electrospray tandem mass spectrometry (ES-MS/MS) was used to identify and compare the non-polar lipids, detected as lithium adducts, from normal and dry eye tear samples obtained from rabbits. A limited number of normal human tear samples were also examined for lipid content, and a close resemblance to rabbit was observed. Three distinct regions were delineated in the ES mass spectra of the non polar lipids, m/z 20 to 500, m/z 500 to 800, and m/z 800 to 1100. A common feature noted among identified lipid components was a glycerol backbone with fatty acyl substituents attached. Product ion spectra were obtained for lithiated mono, 1,2- and 1,3-diacyl, and triacylglyceride standards. Newly proposed structures and fragment pathways for the major product ions are presented for the 1,2- and 1,3-diglycerides, as well as for the monoglyceride. New approaches to distinguish asymmetric 1,2-diglycerides, and 1,2- from 1,3-diglycerides are proposed. For the rabbit tear samples, the m/z 20 to 500 range contains mono-ester diols with empirical formulas of $C_nH_{2n}O_4$, the m/z 500 to 800 range includes diesters with empirical formulas of $C_nH_{2n-2}O_5$, and the m/z 800 to 1100 range contains triesters with empirical formulas of $C_nH_{2n-4}O_6$. Also found in the extracts were three isoprene acetals (terpenoids).

When targeting a certain class of analytes such as the phosphorylated lipids in complex biological extracts, interfering species can pose challenges to qualitative and quantitative analysis. Two aspects of lipid analysis in biological extracts were optimized in order to simplify the isolation and characterization of the phosphorylated lipids. A new solid ionic crystal MALDI matrix was synthesized which combined the lipid response enhancing UV absorber para-nitroaniline, and the strong protonating agent butyric acid. Mass spectra of the extracts containing phosphorylated lipids were simplified by revealing only the protonated species of phosphatidylcholine (PC) head group containing lipids such as lyso PC, PC, and platelet-activating factor (PAF) PC's. Further spectrum simplification is obtained by the appearance of only the sodium adduct species for other phosphorylated lipids such as phosphatidylglycerol (PG), phosphatidic acid (PA), and phosphatidylserine (PS). In addition, a new extraction, isolation, and cleanup procedure has been developed to prepare the phosphorylated lipids for MALDI-TOF analysis by the use of immobilized metal ion affinity chromatography (IMAC) media $\text{ZipTip}_{\text{MC}}$. The latter procedure was successfully applied to a complex biological tear film lipid layer extract in preparation for MALDI-TOF analysis for phospholipid characterization.

The ocular tear fluid, like many biological fluids, is a complex mixture of biomolecules such as proteins, non-polar lipids, and polar phosphorylated lipids whose components interact with one another to perform an important biological function. Irregularities in the tear film can cause a number of ocular problems, including dry eye. Approximately 10 to 14 million people in the United States alone suffer from some form of dry eye. However, without the ability to detect and quantify the nano- to picogram quantities of tear components, identifying the underlying cause of dry eye is impossible. We investigated the use of MALDI-TOF MS to identify the phosphorylated lipids in both normal and dry eye rabbit tears. A solid ionic crystal MALDI matrix comprised of para-nitroaniline and butyric acid was employed for enhanced spectral peak responses of the phospholipids. Additionally, a novel phosphorylated lipid isolation, pre-concentration, and clean-up method using IMAC ZipTip$_{MC}$ chromatography was also used. The combination of the solid ionic crystal matrix and the ZipTip$_{MC}$ chromatography enabled the detection and study of low levels of phosphorylated lipids in the complex tear fluid.

A study of a rabbit's tear protein expression for a dry eye rabbit model was performed to determine if a pattern in the expression of the proteins could be identified. The uniqueness of the model allows the comparison of a normal, left eye tear protein expression to a surgically induced dry, right eye tear protein expression. Quantitation of the tear proteins for the dry and normal eye tears were not observed to change considerably with the dry eye condition. One dimensional mini-gel electrophoresis of the normal versus the dry eye tear proteins did not show substantial differences between band patterns, but was used for general identification of the major protein bands. Specific identification of some of the predominant proteins was obtained by tandem mass spectrometry which showed that the lower molecular weight lipid binding proteins (approximately 10 kDa to 36 kDa) comprise a considerable amount of the observed proteins, followed by the transferrins which have higher molecular weights ranging from 70 kDa to 85 kDa. Enhancement of MALDI-TOF MS linear mode analysis of intact proteins in neat tear fluid was demonstrated through the use of wax coated Voyager plates, and spot washing. MALDI-TOF MS analysis of the expressed tear proteins illustrated that the major differences between normal eye tear and dry eye tear proteins is observed for the lower molecular weight lipid binding proteins.

VITA

The author was born in Lincoln, Nebraska. He attended the University of New Orleans as an undergraduate and received a B.A. in Chemistry in 1989. For the next ten years he worked as a bench chemist performing a wide variety of instrumental analysis. In the spring of 2001 he came back to the University of New Orleans and rejoined the Department of Chemistry selecting Dr. Cole and his mass spectrometry group as his place for graduate study.